Imperial College London

Designing and modelling bio-inspired discontinuous composites

by

Joël Jean Henry

Department of Mechanical Engineering, Imperial College London,
South Kensington Campus, London SW7 2AZ, United Kingdom

This thesis is submitted for the degree of
Doctor of Philosophy of Imperial College London

2018

Abstract

The exponential increase in the use of composites for structural applications in the past decades comes with a constant need to increase their performance for them to remain an attractive substitute to conventional metals. In particular, despite their lightweight and high specific stiffness and specific strength, composites generally suffer from a lack of damage tolerance. Their brittle nature restrains the use of composites in industry, or at least leads to over-conservative designs.

This work aimed at designing and modelling novel discontinuous microstructures, inspired by damage tolerant naturally-occurring discontinuous composites. This was achieved by considering discontinuous hybrid and discontinuous hierarchical microstructures.

In a first part, a virtual testing framework was developed to perform virtual testings of non-hybrid and hybrid aligned-fibre discontinuous composites. The virtual framework, made of analytical models combining statistics and micromechanics, captured and explained different effects such as hybrid effects, size effects, and the effect of variability. The models were used to identify microstructures which maximise the strength, failure strain and stiffness of hybrid discontinuous composites.

In a second part, hierarchical discontinuous carbon-fibre reinforced polymers were designed, modelled numerically and tested experimentally. They exhibited a stable failure mechanism and dissipated energy stably, before failure, through diffuse damage (unlike most conventional composites). This study also showed that non-self-similar microstructures could achieve better damage tolerance and provide a clearer warning before failure than self-similar microstructures.

This work shows the potential for different types of discontinuous composites to overcome the inherent brittleness of conventional composites. The models developed throughout this work can be used to support material design, perform parametric studies and identify optimal designs.

Declaration of originality

The work hereby presented is based on research carried out by the author at the Department of Mechanical Engineering of Imperial College London, and it is all the author's own work except where otherwise acknowledged. No part of the present work has been submitted elsewhere for another degree or qualification.

Copyright declaration

The copyright of this thesis rests with the author and is made available under a Creative Commons Attribution Non-Commercial No Derivatives licence. Researchers are free to copy, distribute or transmit the thesis on the condition that they attribute it, that they do not use it for commercial purposes and that they do not alter, transform or build upon it. For any reuse or redistribution, researchers must make clear to others the licence terms of this work.

Contents

List of Figures **xi**

List of Tables **xv**

Acknowledgements **xvii**

List of Publications **xix**

Acronyms and Abbreviations **xxi**

Notation **xxiii**

1 Introduction **1**

1.1 Motivation for bio-inspiration 1

1.2 Discontinuous composites 2

1.3 Hybrid composites 2

1.4 Hierarchical composites 3

1.5 Objectives 4

1.6 Thesis outline 4

I Virtual testing framework for hybrid aligned discontinuous composites **7**

2 A virtual testing framework for aligned discontinuous composite **9**

2.1 Introduction 9

2.2 Model development 11

2.2.1 Multiscale modelling framework 11

2.2.2 RVE definition 11

2.2.3 Response of an interaction between neighbouring fibres 13

2.2.4 Tensile response of a fibre with stochastic strength 16

2.2.5 Macroscopic response and final failure 19

2.2.6 Matlab implementation 22

2.3 Results 23

2.3.1 Experimental validation . . . 23
2.3.2 Parametric study . . . 24
2.3.3 Study of the characteristics of the critical cluster . . . 26
2.3.4 Effect of variability . . . 27
2.3.5 Size effects . . . 29
2.4 Discussion . . . 29
2.4.1 Response of aligned discontinuous composites . . . 29
2.4.2 Optimal configuration for stiff, strong and less brittle discontinuous composites . . . 30
2.4.3 Model in the scope of literature . . . 31
2.5 Conclusions . . . 32
3 A virtual testing framework for the stiffness of hybrid aligned discontinuous composite 33
3.1 Introduction . . . 33
3.2 Model development for brick-and-mortar architecture . . . 35
3.2.1 Description of the geometry . . . 35
3.2.2 Differential equation . . . 36
3.2.3 Stress and strain fields . . . 37
3.2.4 Boundary conditions . . . 38
3.2.5 Location of the characteristic point . . . 39
3.2.6 Calculation of the Young's modulus . . . 40
3.3 Model development for hybrid aligned discontinuous-fibre architectures . 40
3.3.1 Idealised microstructure of hybrid aligned-fibre discontinuous composites . . . 40
3.3.2 RVE model . . . 44
3.3.3 Analytical model . . . 44
3.4 Results . . . 46
3.4.1 Hybrid brick-and-mortar composites . . . 46
3.4.2 Hybrid aligned-fibre discontinuous composites . . . 49
3.5 Discussion . . . 54
3.5.1 Influence of fibre-ends on the Young's modulus of aligned discontinuous composites . . . 54
3.5.2 Influence of hybridisation on the Young's modulus of discontinuous composites . . . 55
3.6 Conclusions . . . 56
4 A virtual testing framework for the full tensile response of hybrid aligned discontinuous composite 57
4.1 Introduction . . . 57
4.2 Hybrid brick-and-mortar composites . . . 59
4.2.1 Model development . . . 59

4.2.2 Results . . . 68
4.3 Hybrid aligned discontinuous composites . . . 71
4.3.1 Model development . . . 71
4.3.2 Results and discussion . . . 76
4.4 Conclusion . . . 80

II Hierarchical discontinuous composites for increased damage tolerance 83

5 Increasing damage tolerance of composites using hierarchical brick-and-mortar microstructures 85

5.1 Introduction . . . 85
5.2 Design of hierarchical microstructures . . . 87
5.2.1 Non-self-similar numerical model . . . 87
5.2.2 Self-similar analytical model . . . 90
5.2.3 Optimisation of the HiBaM microstructure . . . 93
5.2.4 Comparison of BaM and HiBaM composites . . . 96
5.3 Experimental method . . . 96
5.3.1 Material properties . . . 96
5.3.2 Manufacturing plates and specimens with HiBaM microstructures 97
5.3.3 Testing method . . . 99
5.4 Results . . . 100
5.4.1 Damage tolerance in HiBaM composites . . . 100
5.4.2 Parametric study of HiBaM microstructures . . . 102
5.4.3 Effect of ply-shifts . . . 105
5.5 Conclusions . . . 108

6 Relaxing self-similarity constraints for more damage tolerance in composites 111

6.1 Introduction . . . 111
6.2 Design of non-self-similar microstructures . . . 112
6.2.1 HiBaM microstructures and modelling strategy . . . 112
6.2.2 Mechanical response and limitations of the self-similar HiBaM microstructure . . . 113
6.2.3 Design of NSS microstructures . . . 115
6.3 Manufacturing . . . 120
6.3.1 Manufacturing of hierarchical discontinuous composites . . . 120
6.4 Testing and results . . . 121
6.4.1 Monotonic tensile testing . . . 121
6.4.2 Micro Digital Image Correlation . . . 121
6.4.3 Scanning Electron Microscopy . . . 121

6.4.4 Repetitive loadings . . . 122
6.5 Discussion . . . 122
6.5.1 Tailorable non-linear stress-strain response . . . 122
6.5.2 Permanent deformation and diffuse damage . . . 123
6.5.3 Stable failure mechanism . . . 126
6.6 Conclusions . . . 127

7 Conclusions **129**
7.1 On modelling hybrid aligned discontinuous composites . . . 129
7.2 On the understanding of the mechanics of hybrid aligned discontinuous composites . . . 130
7.3 On the potential of hybrid aligned discontinuous composites . . . 130
7.4 On the use of hierarchies in discontinuous composites . . . 131
7.5 On the role of self-similarity constraints on modelling and designing hierarchical discontinuous composites . . . 131
7.6 Novelty . . . 132
7.7 Impact . . . 133

8 Further work **135**
8.1 Optimising hybrid aligned discontinuous composites . . . 135
8.2 Extending the VTF for HADCs . . . 135
8.3 Hierarchical discontinuous composites . . . 136

Bibliography **139**

A Correction factors for the Weibull strength distribution of fibres in a discontinuous composite **A1**

B Toughness estimation of aligned discontinuous composites **B1**

C Derivation of the Young modulus from the non-hybrid BaM model **C1**

D Derivation of rules-of-mixtures **D1**
D.1 Continuous-fibre RoM . . . D1
D.2 RoM for brick-and-mortar . . . D1
D.3 Discontinuous-fibre RoM . . . D1

E Validation of the analytical model for HyBaM composites against FE simulations **E1**

F Modelling of fibre misalignment **F1**

G Extension of the brick-and-mortar model for non-linear-elastic bricks **G1**

List of Figures

2.1 Overview of the different scales involved in the model for aligned discontinuous composites. 12
2.2 Indexing system of the different matrices of the model and stress fields considered in the fibres. 13
2.3 Failure criterion used to identify final failure of an RVE. 20
2.4 Implementation of the proposed model for aligned discontinuous composites. 22
2.5 Comparison of the stress-strain curves predicted by the model against experiments for 3 mm carbon-fibres embedded in polypropylene. 25
2.6 Comparison of the stress-strain curves predicted by the model against experiments for 3 mm carbon-fibres embedded in epoxy. 26
2.7 Effect of fibre length on the response of aligned discontinuous composites. . 27
2.8 Study of the characteristics of the critical cluster in discontinuous composites. 28
2.9 Effect of the variability on discontinuous composites. 29
2.10 Effect of the specimen length l^{spec} on the response of aligned discontinuous composites. 30

3.1 Overview of the shear-lag model for HyBaM composites. 35
3.2 Overview of the different scales present in the model for aligned hybrid discontinuous composites. 42
3.3 Indexing system of the fibres and interactions in the RVE model. 43
3.4 Effects of global parameters on the overall Young's modulus of a HyBaM composite. (See Eq. 3.3 for the definition of $\frac{\Delta E}{\Sigma E}$). 47
3.5 Effect of hybridisation on the Young's modulus of HyBaM composites. . . . 47
3.6 Evolution of the Young's modulus of a hybrid HMC-Glass discontinuous composite with the volume ratio of the stiffer fibre type (HMC). 50
3.7 Evolution of the Young's modulus with the volume ratio of the stiffer fibre type (HMC). 53

4.1 Overview of the shear-lag model for HyBaM composites. 60
4.2 Definition of the matrix subdomains in the unit-cell of a HyBaM composite. 61
4.3 Algorithm used to define the sequence of the states of active matrix subdomains in a HyBaM composite. 67

4.4 General implementation of the model to predict the stress-strain response of hybrid brick-and-mortar composites. 68
4.5 Results for HyBaM composites, for different aspect ratios. 70
4.6 Overview of the different scales present in the VTF. 72
4.7 Effect of the ratio of LE HMC fibres (V_{HMC}) on the response of HADCs in tension. 77
4.8 Effect of the neighbouring fibres on the fibre peak stress. 79
4.9 Fibre stress peak in intermingled and block configurations. 79

5.1 Microstructures of BaM and HiBaM composites. 88
5.2 Mechanical response of a HiBaM composite, as predicted by a unit-cell numerical model. 90
5.3 Stiffness degradation of the matrix in BaM and HiBaM virtual specimens. . 91
5.4 Comparison of the stress-strain curves predicted by the analytical model against the numerical model, for HiBaM composites. 92
5.5 Tensile stress fields within a level-1 brick calculated by the analytical and numerical models, for the *nominal-a* microstructure. 92
5.6 Effect of the geometry of level-0 bricks on the failure mechanism of a level-1 brick in HiBaM composites. 94
5.7 Mechanical response calculated by the numerical model for HiBaM composites with different geometries of level-0 bricks. 94
5.8 Effect of the geometry of level-1 bricks on the failure mechanism of HiBaM composites. 95
5.9 Mechanical response calculated by the numerical model for HiBaM composites with different geometries of level-1 bricks. 95
5.10 Manufacturing process of HiBaM composites. 98
5.11 Tensile testing set-up used in the experiments. 99
5.12 Diffuse damage and fracture surfaces in representative HiBaM specimens. . 100
5.13 Diffused damage mechanisms observed in the SEM in HiBaM specimens before final failure. 101
5.14 Stress-strain response of *nominal-a* HiBaM specimens. 102
5.15 Experimental fracture surfaces of specimens used in the parametric study of the level-0 brick geometry. 103
5.16 Fracture surfaces and stress-strain curves of HiBaM with different level-1 brick-geometries. 104
5.17 Ply-shifts of each of the level-0 bricks in a level-1 brick, for different microstructures. 105
5.18 Fracture surfaces of HiBaM specimens, as observed in the experiments and predicted by the numerical model considering ply-shifts. 105
5.19 Effect of ply-shifts on the stress-strain curves of HiBaM composites. 107

6.1 The *SS* hierarchical microstructure is obtained by introducing discontinuities at two different hierarchical levels in the microstructure 114
6.2 Limits due to imposing self-similarity in HiBaM composites 115
6.3 New *NSS* hierarchical microstructures designed by relaxing the self-similarity constraints 116
6.4 Mechanical response predicted numerically for different level-1 brick shapes 117
6.5 Stress-strain curves of the *NSS3* unit-cell calculated by the numerical model for different configurations of the microstructure. 119
6.6 Numerical colour maps for three *NSS3* configurations 119
6.7 Stress-strain curves measured experimentally for *SS* and *NSS* HiBaM composites. 122
6.8 Evidence of spread deformation before failure, and permanent deformation after failure. 123
6.9 SEM images of the fracture surfaces of *SS* and *NSS1* specimens. 124
6.10 Diffuse damage during loading, and permanent deformation after failure, in *NSS3* specimens. 125
6.11 Demonstration of stable failure mechanism during loading in tension. 126

B.1 Probability density function of minimum overlap lengths for discontinuous composites with different initial fibre lengths. B2

D.1 Definition of the different rules-of-mixtures (CRoM, RoM-BaM and DRoM). D2

E.1 Example of the FE geometry, mesh and boundary conditions used to validate the analytical model for hybrid BaM composites. E1

G.1 Overview of the extension of the BaM model to non-linear-elastic bricks. . . G2

List of Tables

2.1 Properties of the fibres and matrices used as input for the model. 23

3.1 Comparison between non-hybrid BaM composites and HyBaM composites. 41
3.2 Inputs for the standard configuration of the HyBaM composites. 46
3.3 Properties of the fibres and matrix used for the 3D intermingled model. . . 51

4.1 Local stress and strain fields within a subdomain in a hybrid BaM composite. 62
4.2 Driving stress built along the overlap within a subdomain j. 62
4.3 Lengths of process zones in the j^{th} subdomain. 63
4.4 Inputs of the hybrid BaM composites studied in Sec. 4.2.2. 69
4.5 Material properties of the fibres and matrix used in experiments. 76

5.1 Different HiBaM microstructures microstructures considered. 88
5.2 Material properties of the carbon/epoxy thin ply prepreg. 89
5.3 Layup sequence for each microstructure manufactured. 97

6.1 Material properties of the carbon/epoxy thin ply prepreg 113
6.2 Geometry of the hierarchical microstructures 118

F.1 Inputs parameters used to calculate the reduced stiffness matrix F1

Acknowledgements

To Soraia Pimenta, main supervisor of this PhD, for sharing her time, her knowledge and her support in every single part of my PhD. I feel that I have learnt so much during that PhD thanks to you. Again, thank you very much for everything!

To all the other academics, technicians, and other staffs from Imperial College and from other universities, for teaching me, helping me, and for all the insightful discussions I had with them.

To all the other students with whom I spent some time studying in the department of Mechanical Engineering at Imperial College London, for making all these years of study such a pleasure.

To my friends and my flatmates who supported me during all this time. To my family for visiting me and supporting me throughout the PhD. Bernard, Françoise, David and Débora: merci! Finally, to my Lord and God Jesus Christ for being always there with me.

List of publications

Parts of the work presented in this thesis have been disseminated through a number of written publications and oral communications; these are listed below, as of July 2018.

Peer–reviewed journal publications

[p1] J. Henry, S. Pimenta, "Semi-analytical simulation of aligned discontinuous composites", *Composites Science and Technology*, vol. 144, pp. 230–244, 2017.

[p2] J. Henry, S. Pimenta, "Modelling hybrid effects on the stiffness of aligned discontinuous composites with hybrid fibre-types", *Composites Science and Technology*, vol. 152, pp. 275–289, 2017.

[p3] J. Henry, S. Pimenta, "Virtual testing framework for hybrid aligned discontinuous composites", *Composites Science and Technology*, vol. 159, pp. 259–272, 2018.

[p4] J. Finley, J. Henry, S. Pimenta, M. S. P. Shaffer, "The influence of variability and defects on the structural performance of complex composite microstructures", in preparation, 2018.

[p5] J. Henry, S. Pimenta, "Increasing damage tolerance in composites using hierarchical brick-and-mortar microstructures", *Journal of the Mechanics and Physics of Solids*, vol. 118, pp. 322–340, 2018.

[p6] J. Henry, S. Pimenta, "Bio-inspired non-self-similar hierarchical microstructures for damage tolerance", Submitted to *Composites Part A: Applied Science and Manufacturing*, 2018.

Refereed conference publications

[c1] J. Henry, S. Pimenta, H. Yu, M. Longana, "Prediction of mechanical properties of hybrid discontinuous composites", in *ECCM 2016, 17th European Conference on Composite Materials*, (Munich, Germany), 26–30 June 2016.

[c2] S. Pimenta, J. Henry, "Hierarchical brick-and-mortar composites for damage tolerance and progressive failure", in *ECCM 2016, 17th European Conference on Composite Materials*, (Munich, Germany), 26–30 June 2016.

[c3] J. Henry, S. Pimenta, "Mechanical properties of hierarchical discontinuous composites", in *ASC 2016, 31st Technical Conference on Composite Materials*, (Williamsburg, VA, US), 19–21 September 2016.

[c4] J. Henry, S. Pimenta, "Investing the potential of hierarchical non-self-similar discontinuous composites", in *ICCM 2017, 21st International Conference on Composite Materials*, (Xi'An, China), 20–25 August 2017.

[c5] S. Pimenta, J. Henry, J. Finley "The effect of randomness at the micro-scale on failure of composites", in *ICCM 2017, 21st International Conference on Composite Materials*, (Xi'An, China), 20–25 August 2017.

[c6] J. Henry, S. Pimenta, "Hierarchical discontinuous composite for damage tolerant applications", in *ECCM 2018, 18th European Conference on Composite Materials*, (Athens, Greece), 24–28 June 2018.

[c7] J. Finley, J. Henry, S. Pimenta, M.S.P. Shaffer, "The influence of defects and variability in discontinuous composite materials", in *ECCM 2018, 18th European Conference on Composite Materials*, (Athens, Greece), 24–28 June 2018.

Conference abstracts

[a1] S. Pimenta, J. Henry, "Modelling and designing hybrid aligned discontinuous composites", in *EMMC 2016, 15th European Mechanics of Material Conference*, (Brussels, Belgium), 7–9 September 2016.

[a2] J. Henry, S. Pimenta, "Hybrid effects in hybrid aligned discontinuous composites", in *MECHCOMP 2017, 3rd International Conference on Mechanics of Composites*, (Bologna, Italy), 4–7 July 2017.

[a3] J. Henry, S. Pimenta, "Virtual experiments of aligned discontinuous composites", in *ECCOMAS 2017, 6th Thematic Conference on the Mechanical Response of Composites*, (Eindhoven, Netherlands), 20–22 Septembre 2017.

[a4] J. Henry, S. Pimenta, "The effect of randomness at the micro-scale on failure of discontinuous composites", in *EMMC 2018, 16th European Mechanics of Material Conference*, (Nantes, France), 26–28 March 2018.

[a5] S. Pimenta, J. Henry, "Damage tolerant composites with discontinuous and hierarchical microstructures", in *EMMC 2018, 16th European Mechanics of Material Conference*, (Nantes, France), 26–28 March 2018.

Acronyms and Abbreviations

ADC	Aligned Discontinuous Composite
BaM	Brick-and-Mortar
BCE	Boundary Condition Error
CFRP	Carbon-Fibre Reinforced Composite
CRoM	Continuous Rule-of-Mixtures
CT	Compact Tension
def	definition, defined as
DRoM	Discontinuous Rule-of-Mixtures
ERR	Energy Release Rate
FE	Finite Element
HADC	Hybrid Aligned Discontinuous Composite
HE	High Elongation
HyBaM	Hybrid Brick-and-Mortar
HiBaM	Hierarchical Brick-and-Mortar
LE	Low Elongation
NSS	Non-Self-Similar
PDF	Probability Density Function
RoM	Rule-of-Mixtures
RoM-BaM	Rule-of-Mixtures for Brick-and-Mortar
RVE	Representative Volume Element
SL	Shear-Lag
SS	Self-Similar
UD	Unidirectional
VTF	Virtual Testing Framework

Notation

Uppercase roman variables

E, $\mathbb{E}$	tensile stiffness, Young's modulus
F	failure probability
$\mathbb{F}$	status of fibre breakage (logical values)
G	tangent shear stiffness, shear modulus
$\mathcal{G}, \mathcal{G}_{\mathrm{IIc}}$	fracture toughness
$\mathcal{I}$	interval along an overlap
J	non-linear energy release rate
K	inclusion stiffness, $K = E \cdot T$
L	characteristic length, $L = (L_{\mathrm{L}}+L_{\mathrm{R}})/2$
N	number-ratio; number of matrix subdomains; number of active neighbours
$\mathbb{N}$	number of active neighbours
P	load
S	shear strength
$\mathbb{S}$	list of fibre-end locations in interactions
T	characteristic thickness
$\mathbb{T}$	matrix of fibre-type
V	volume fraction; volume ratio
W	work
X, $\mathbb{X}$	strength, fibre strength
$\mathbb{Z}$	list of broken fibres

Lowercase roman variables

a	cluster size
g	toughness component
i	central subdomain index
j	general subdomain index
l	length
ℓ	virtual overlap length
n	RVE size ($n \times n$ fibres)
n_{a}	cluster size ($n_{\mathrm{a}} \times n_{\mathrm{a}}$ fibres)
$n_{\mathrm{L}}, n_{\mathrm{R}}$	number of actives subdomains
n^{RVE}	number of RVEs in the specimen
$\mathbf{s}$	active subdomains
t	thickness
u	displacement
$x, \mathbb{x}$	location of fibre-breaks/fibre-ends; location along the overlap/fibre

Indices

i, j	location within RVE
k	interaction around a fibre
p	RVEs in a specimen
s	segments in an interaction

Decorations above

$\hat{}$	in local base $\hat{x} = x - x_0$

Operators (defined on variable χ)

$\Delta\chi$	difference, $\Delta\chi = \chi_{\mathcal{B}} - \chi_{\mathcal{A}}$
$\Sigma\chi$	sum, $\Sigma\chi = \chi_{\mathcal{B}} + \chi_{\mathcal{A}}$
$\bar{\chi}$	average, $\bar{\chi} = \frac{\Sigma\chi}{2}$
$\tilde{\chi}$	harmonic mean, $\tilde{\chi} = 2 \cdot \frac{\chi_{\mathcal{A}} \cdot \chi_{\mathcal{B}}}{\chi_{\mathcal{A}} + \chi_{\mathcal{B}}}$

Greek variables

$\bar{\alpha}$	aspect ratio $\bar{\alpha} = L/\bar{T}$
γ	shear strain
ε	deformation, tensile strain
η	stiffness ratio $\eta = K_{\mathcal{A}}/K_{\mathcal{B}}$
θ	angle of rotation
κ	stress factor
λ	characteristic coefficient
μ	friction coefficient
ν	Poisson's ratio
ξ	boundary condition error function
$\sigma, \boldsymbol{\sigma}$	longitudinal stress
τ	shear stress
ϕ, Φ	diameter
ψ, Ψ	driving stress $\psi = \Delta\sigma - \kappa \cdot \sigma^{\infty}$

Superscripts

a	average
b	brick
$\mathcal{C}$	overall composite
f	fibre
I	interaction
m	matrix
N	neighbour
O	overlap
p	peak; platelet
∞	remote

Subscripts

0	initial; value at origin; at hierarchical level 0
1	at hierarchical level 1
a	experimental set a
$\mathcal{A}$	fibre/platelet $\mathcal{A}$
b	experimental set b
$\mathcal{B}$	fibre/platelet $\mathcal{B}$
Br	broken segment
char	characteristic
crit	critical value
deb	interfacial debonding
f	fibre
global	global value
H	horizontal interaction
IIc	mode II
L	left-hand side of the overlap
min	minimum value
NB	next fibre-break
nom	nominal
PB	previous fibre-break
po	pull-out
R	right-hand side of the overlap
SL	shear-lag segment
V	vertical interaction
x	along the x direction
y	along the y direction
z	along the z direction

Blackboard bold symbols (e.g. $\mathbb{F}$, $\boldsymbol{\sigma}$, $\mathbb{X}$) are used to represent matrices.

Chapter 1

Introduction

1.1 Motivation for bio-inspiration

Due to their high specific strength and specific stiffness, the use of composites in industry has increased remarkably over the last decades. Composites are typically used when high performance and lightweight are required. Therefore, they are commonly used in the transport industry [1], renewable energy industry [2,3], and sport goods [4]. Composites are primarily attractive for saving weight (e.g. up to 40% of the weight of an aircraft wing compared to a metallic equivalent) [5], which explains why they are used in more than half of the weight of the last civilian aircraft produced (e.g. 53% of the weight in the new Airbus A350-XWB airliner) [6, 7].

However, conventional metals such as aluminium, steel or titanium continue to improve due to new manufacturing processes [8–10], leading to an increase of their strength, and a decrease of their weight and cost. Therefore, there is a need to continue improving composites for them to remain a competitive alternative to metals in industry.

In particular, a main drawback of composites (compared to conventional metals) lays in their inherent brittleness, triggering catastrophic failure with no damage warning, and leading to over-designed structures. This is mainly due to the microstructure of conventional composites – with continuous stiff and brittle fibres embedded in a soft polymeric matrix – which promotes localisation of damage and leads to brittleness [11]. Great efforts have been made in understanding the mechanics of composites to make them more "ductile" and "damage tolerant" [12], which would not only allow for a more efficient use of composites, but would also expand their range of applications.

One way to improve the damage tolerance of composites is to study naturally-occurring composites (e.g. nacre, bone). Although naturally-occurring composites are

also mostly composed of brittle constituents, they are able to combine competing properties such as strength and toughness [12]. These remarkable, yet not fully explained mechanical properties of natural composites, are believed to be due to their microstructures, and numerous studies have been carried out in the literature to further understand the mechanics of such materials.

1.2 Discontinuous composites

The first feature that can be observed in various naturally-occurring composites is the presence of discontinuities [12–15], which is often seen as an "elegant way to combine stiffness, strength and toughness" [12]. Natural composites with discontinuous microstructures can achieve stiffness and strength properties comparable to those of continuous equivalent composites, but increase significantly their tolerance to damage [14,15]. Nacre, for instance, composed of 95% of stiff mineral platelets embedded in 5% of a soft organic phase, exhibits a 3000-fold increase in toughness compared to the platelets, while maintaining reasonable stiffness and strength [16]. Experiments with man-made discontinuous composites have been successful in showing increased nonlinearity and toughness, and also showed the potential of tailoring the discontinuous architecture to achieve different failure mechanisms [16–19].

Discontinuous composites also have better manufacturability than continuous-fibre composites, as the fibres may be able to flow in the matrix during curing; this allows discontinuous composites to be manufactured through automated processes, it reduces the manufacturing time, and it allows for more complex-shaped components to be manufactured [20]. Moreover, recycled composites – which will become essential as composite production keeps increasing – have inherently discontinuous fibres [21, 22].

The potential of discontinuous composites found both in Nature [16] and in experimental works [16–19] motivated numerous attempts to model such microstructures [23–27]. However, a few challenges remain, among which is the need for models capturing different effects related to discontinuities (size effects, variability, ...) in order to improve their design, as well as the need to scale up existing manufacturing processes for industrial applications.

1.3 Hybrid composites

Another feature observed in natural composites is the use of different types or reinforcement within the microstructure. Hybridisation consists of combining different types of inclusions varying in geometry (e.g. fibre diameter) and mechanical proper-

ties (e.g. fibre strength of stiffness) [28]. This was replicated in man-made composites and became a widely known strategy to achieve ductile and damage tolerant composites. These synthetic hybrid composites can be regrouped in three main categories: (i) Interlayer (or interlaminated) configuration, with a layer by layer arrangement, (ii) Intralayer (or intraply) configuration, with a yarn by yarn arrangement, (iii) intrayarn (or intermingled) configuration, with a fibre by fibre arrangement [28, 29].

Hybridisation offers numerous advantages, among which are the possibility to include a cheaper type of reinforcement to reduce the cost, the ability to tailor the properties of the composite for specific applications, an improved fatigue life, impact resistance [30, 31], and the existence of various synergistic effects within a hybrid composite [28].

However, the mechanical behaviour of hybrid composites often shows hybrid effects which cannot be modelled by simple Rule-of-Mixtures (RoMs) and are therefore challenging to predict and explain. There is a need for models which can capture such effects [28] in order to understand their mechanics and investigate how they can be used to improve the composite further.

1.4 Hierarchical composites

Finally, one last feature largely observed in naturally-occurring composites is the use of hierarchies: these composites are reinforced across a range of scales varying from 2 (e.g in nacre [32–34]) to 7 (e.g. in bone [16, 35, 36]).

The role of hierarchies in these composites is not fully explained yet [37], but is believed to be crucial to achieve damage tolerance [38]. In nacre for instance [39], the combination of hierarchies and discontinuities leads to larger process zones during failure, yielding more damage diffusion and energy absorption.

Hierarchical composites have been intensively modelled in the literature [34, 36, 40–44], but the presence of hierarchies makes the mechanics of composites particularly challenging to understand and model. For instance, hierarchical natural composites seem to have an optimal number of hierarchies, which depends on the material properties [36]. One common way to model and design hierarchical composites is to assume self-similarity, which consists of homogenising the material properties at each hierarchical level [36, 42]. However, although such assumption simplifies both the modelling and the design process, it appears that most natural microstructures are actually non-self-similar [35, 45, 46].

Although hierarchical microstructures have been known and studied for decades, there is still a lack of engineered materials with a true hierarchical microstructure [47].

This is because, even though Nature produces such complex architectures with ease, it remains extremely challenging to produce synthetic hierarchical composites as they combine a large range of scales. There is therefore a need to develop methods to manufacture hierarchical composites for structural applications.

1.5 Objectives

This research project aims to expand the general understanding of discontinuous composites, and to develop routes towards novel discontinuous microstructures. This will be done by addressing the following challenges:

- Develop an analytical Virtual Testing Framework (VTF) to accurately model hybrid and non-hybrid aligned discontinuous composites in a computationally efficient way;
- Use the VTF to understand the behaviour of Hybrid Aligned Discontinuous Composites (HADCs), carry out parametric studies, and provide guidelines for optimisation and material design;
- Develop numerical and experimental methods to explore the effect of hierarchies in discontinuous composites;
- Investigate self-similarity when designing / modelling hierarchical discontinuous composites, and provide insights on the limits of self-similarity.

1.6 Thesis outline

To achieve the objectives presented above, this thesis has been separated in two parts. Part I, consisting of Chapters 2 to 4, presents a set of analytical models for predicting the stress-strain response under tension of hybrid and non-hybrid aligned discontinuous composites.

For that purpose, Chapter 2 develops the VTF for aligned discontinuous composites (ADCs). The VTF is validated against experimental results from the literature, and virtual experiments are carried out to study the effect of fibre length on the stress-strain response. The model suggests that well tailored microstructures can achieve ductility while maintaining relatively high strength and stiffness.

Chapter 3 presents a shear-lag based model to calculate the Young's modulus of different hybrid discontinuous composites. Predictions are experimentally validated, and are used to highlight and explain the presence of a negative hybrid effect on the Young's modulus of HADCs. This model is extended in Chapter 4 to predict the full stress-

strain curve of hybrid discontinuous composites, and captures and gives explanations for other hybrid effects found experimentally in the literature.

Part II of the thesis consists of Chapters 5 and 6, and investigates the potential of hierarchical discontinuous Carbon-Fibre Reinforced Polymers (CFRPs) for damage-tolerance applications. Chapter 5 reveals that well tailored Hierarchical Brick-and-Mortar (HiBaM) composites could diffuse damage throughout the microstructure. Chapter 5 also investigates the validity of the self-similar assumption when modelling morphologically self-similar hierarchical composites. Chapter 6 explores how non-self-similar microstructures could enhance damage tolerance in hierarchical composites.

Finally, the overall conclusions of this work are summarised in Chapter 7, and suggestions for further extensions of the work are listed in Chapter 8. For each part of the thesis, the relevant literature will be introduced at the beginning of each chapter.

Part I

Virtual testing framework for hybrid aligned discontinuous composites

Chapter 2

A virtual testing framework for aligned discontinuous composite

2.1 Introduction

Aligned discontinuous composites are found in Nature, and can provide a combination of hight strength, stiffness and toughness [16]. Moreover, they can lead to better manufacturability [20], cost reduction and recyclability [21, 22] than conventional continuous composites, which make them attractive for industry.

However, many problems arise when modelling discontinuous composites. The first one, also present in continuous-fibre composites, is the stochastic variability of the fibre strength, which can be captured by Weibull's continuous probability distribution [48–50]. However, most models for discontinuous composites either neglect fibre failure [24], use a deterministic fibre strength [51], or assume a uniform stress field in the fibres [49, 50], which is not true in discontinuous composites due to the presence of fibre-ends.

Another challenge while modelling discontinuous composites is the failure of the matrix or fibre/matrix interface. Gao et al. [52] identified two main approaches to this problem: a first group of models [23, 53] considers a maximum shear stress criterion and uses shear-lag models to derive the stress-transfer between neighbouring fibres. The second group of models [54] regards debonding as a particular case of fracture mechanics; however, conventional linear elastic fracture mechanics requires knowing in advance the orientation and the length of a pre-existing initial crack [54], and neglects the non-linearity of the matrix. Recently, Pimenta and Robinson [24] developed an analytical model for the response of discontinuous "brick-and-mortar" composites for any shear constitutive law of the matrix, which bridges the strength and toughness-based approaches.

The issue of modelling the microstructure of discontinuous composites and in particular the location of fibre-ends has been tackled in different ways in the literature [24, 55–62]. A first widely used approach is to consider perfectly staggered fibres [24, 55–57, 61], in which case the overlap length between two neighbouring fibres is half the fibre length. Other authors recommend using an average value for the overlap length, which corresponds to a quarter of the fibre length [58]. However, predicting accurately the effect of overlap lengths in discontinuous composites requires more realistic architectures, considering randomly-located fibre-ends [59, 60, 62, 63].

Most models in the literature [24, 61, 62] consider that the strength of discontinuous composites coincides with the maximum average stress that the material can withstand, but experiments [64] show that composites fail when a cluster of damage reaches a critical size and propagates unstably in the material, leading to catastrophic failure. This observation suggests that final failure of composites can be approached as a fracture mechanics problem [63, 65]. This requires being able to predict the toughness of discontinuous composites [50, 66], which can be done for instance by calculating the energy dissipated through the formation of pull-outs with a given stochastic distribution of lengths [50]. In any case, many authors highlighted the importance of accounting for debonding and friction during the pull-out process [52, 67, 68].

An alternative method to model discontinuous composites is Finite Element (FE) simulations, which have the advantage of representing more realistic stress fields without the assumptions made in analytical models. However, being computationally expensive, FE models are generally limited to the fibre/interface scale [54, 68] or to small Representative Volume Elements (RVEs) [61, 62, 69–71], and cannot be used to model full-sized specimens.

Overall, there is still a need for models able to predict accurately and efficiently the mechanical response of discontinuous composites, in order to better understand their deformation and failure mechanisms, perform virtual experiments on full-scale specimens, and also to identify optimal configurations.

The work presented in this chapter aims at modelling a full-size 3D composite specimen with aligned discontinuous fibres with random location of fibre-ends, and accounting for non-linear matrix response and debonding, stochastic formation of fibre breaks, and catastrophic specimen failure.

The chapter is organised as follows: Sec. 2.2 describes the model development and proposes a roadmap for its numerical implementation. Sec. 2.3 presents the model results, including experimental validation and parametric studies. Sec. 2.4 discusses the model and its results, its relation with literature, and its potential applications. Finally, Sec. 2.5 summarises the main conclusions.

2.2 Model development

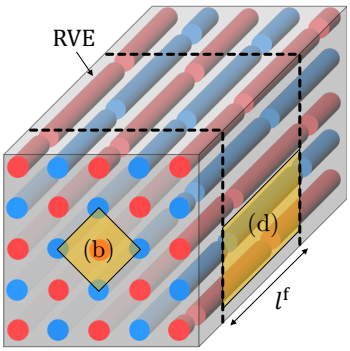
2.2.1 Multiscale modelling framework

The response of aligned discontinuous composites is modelled at different scales [63], as represented in Fig. 2.1. Their implementation in the model is described in the next subsections, and summarised below:

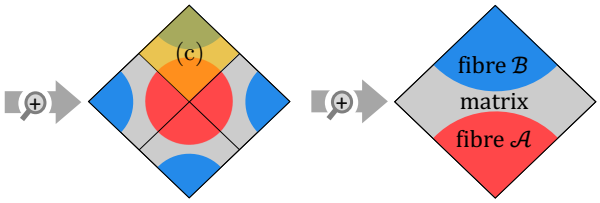
1. **Specimen:** the model considers an aligned short-fibre polymer-matrix composite specimen as a series of $p^{\mathrm{RVE}} \in \{1, ..., n^{\mathrm{RVE}}\}$ *RVEs* (Fig. 2.1a and Sec. 2.2.5).
2. **RVE:** the cross-section of each RVE has $n \times n$ aligned *fibres* in parallel, arranged in a square packing. The length of the RVEs is the fibre length l^{f} (uniform for all fibres in the specimen), and fibre-ends are randomly located along the longitudinal direction of the RVE (Figs. 2.1a and 2.1b and Sec. 2.2.5).
3. **Fibre:** each *fibre* has a stochastic strength and builds stresses through the *interaction* with its four nearest neighbouring fibres (Figs. 2.1b, 2.1c and 2.1d and Sec. 2.2.4).
4. **Interaction:** in each *interaction* between two neighbouring fibres, stresses are transferred through shear in the matrix (Figs. 2.1c, 2.1d and 2.1f and Sec. 2.2.3.4). Each interaction is initially composed by two shear-lag *segments* delimited by fibre-ends (Fig. 2.1d), but can be further divided into more segments due to the formation of fibre-breaks (Fig. 2.1f).
5. **Segment:** each *segment* within an interaction is delimited by fibre-ends and/or fibre-breaks, and can be categorised as shear-lag (subscript SL, Fig. 2.1e) or broken (subscript Br, Fig. 2.1g) (Secs. 2.2.3.1 to 2.2.3.3).

2.2.2 RVE definition

Each fibre in an RVE is identified by the coordinates (i, j) (see Figs. 2.2a and 2.2b). At the beginning of the simulation, each fibre contains one fibre-end along an RVE, whose random location $x \in [0,\ l^{\mathrm{f}}]$ is stored in a matrix $\mathbb{x}_{ij}$. Considering a high fibre-content (and thus small gaps between fibres), the RVEs are assumed to be periodic in the longitudinal direction, and therefore the matrix $\mathbb{x}$ is initially equal for all RVEs. As the simulation progresses, fibre-breaks can be introduced, in which case $\mathbb{x}_{ij}$ becomes a sorted vector $\mathbb{x}_{ij}(1, ..., s_{\max})$, where the smallest value $\mathbb{x}_{ij}(1)$ always corresponds to the fibre-end of fibre (i, j). For example, the vector for fibre $\mathcal{B}$ in Fig. 2.1d is $\mathbb{x}_{\mathcal{B}} = \mathbb{x}_{\mathcal{B}}(1)$

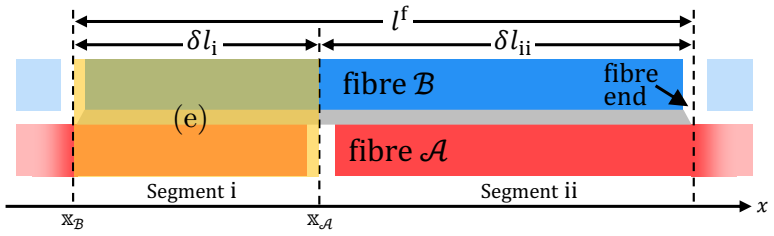


(a) Full 3D structure of the specimen (initial configuration, $n = 5$), with RVEs of length l^{f}.

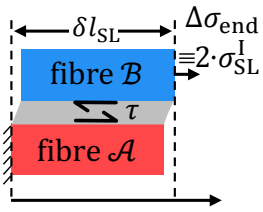


(b) Fibre with its four nearest neighbours.

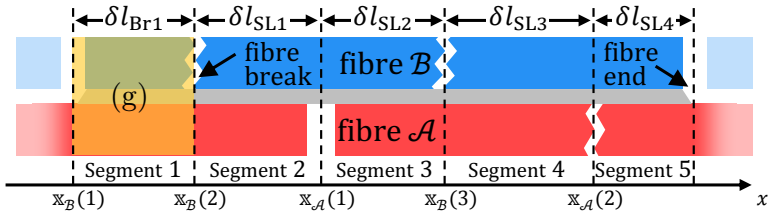
(c) Interaction between two neighbouring fibres (cross-section view).



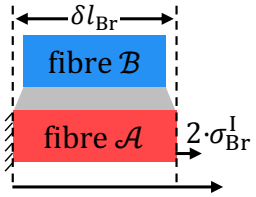
(d) Interaction between two neighbouring fibres (along the longitudinal direction). The interaction is initially composed by two shear-lag segments, with lengths δl_{i} and δl_{ii}.



(e) Shear-lag segment.



(f) Interaction shown in (d) after fibre-breakage. The formation of fibre-breaks creates one broken segment (with length δl_{Br1}) and four shear-lag segments (with lengths δl_{SL1} to δl_{SL4}).

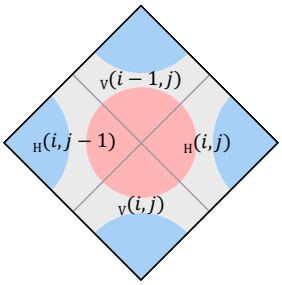


(g) Broken segment.

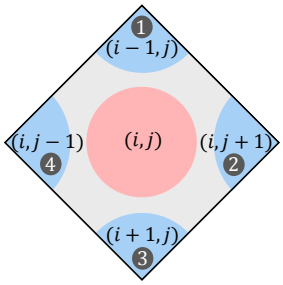
Figure 2.1: Overview of the different scales involved in the model for aligned discontinuous composites.

at the beginning of the simulation, and becomes $\mathbb{x}_{\mathcal{B}} = \{\mathbb{x}_{\mathcal{B}}(1),\ \mathbb{x}_{\mathcal{B}}(2),\ \mathbb{x}_{\mathcal{B}}(3)\}$ after the fibre-breaks occur, in Fig. 2.1f.

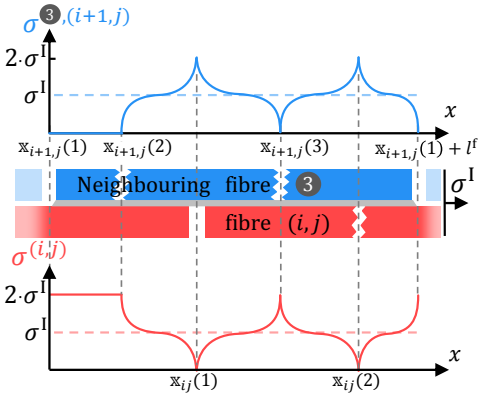
The strength of the fibres is stochastic; different realisations of strengths are used for each RVE, and the values of the fibre strength for each RVE are stored in a matrix $\mathbb{X}_{ij}$ (see Sec. 2.2.4 for further details).



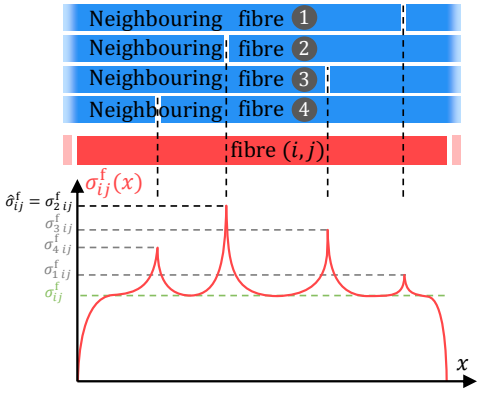
(a) Indices defining the interactions involving fibre (i, j) (in the middle). Subscripts H and V are used respectively for horizontal and vertical interactions. Indices $i \in \{1, ..., n-1\}$ and $j \in \{1, ..., n\}$ for vertical interactions, and $i \in \{1, ..., n\}$ and $j \in \{1, ..., n-1\}$ for horizontal interactions.



(b) Indices defining the fibres and their neighbours, with $i \in \{1, ..., n\}$ and $j \in \{1, ..., n\}$. Circled numbers 1 to 4 are the relative indices of the neighbours of fibre (i, j).



(c) Stress fields in the two quarter-fibres forming the interaction $_{\mathrm{V}}(i, j)$ in Fig. 2.2a, made of one broken segment and four shear-lag segments.



(d) Stress field in fibre (i, j) due to the four neighbouring fibre-ends (Fig. 2.2b) at the initial configuration, and identification of the maximum fibre stress $\hat{\sigma}^{\mathrm{f}}_{ij}$.

Figure 2.2: Indexing system of the different matrices of the model and stress fields considered in the fibres.

2.2.3 Response of an interaction between neighbouring fibres

2.2.3.1 Type and length of segments in an interaction

Consider the horizontal (subscript H) and vertical (subscript V) interactions between a fibre and its four neighbouring fibres (see Figs. 2.2a and 2.2b); the symbol $*$ is used to replace H and V when no orientation is specified for an interaction. Take, for example, the interaction $_{\mathrm{V}}(i, j)$ between fibres (i, j) and $(i+1, j)$, which is also represented in Fig. 2.2c; the location of the fibre-ends involved in that interaction can be collected in a sorted vector $\mathbb{S}_{\mathrm{V}}(i, j) = \{\mathrm{x}_{i+1,j}(1),\ \mathrm{x}_{i+1,j}(2),\ \mathrm{x}_{ij}(1),\ \mathrm{x}_{i+1,j}(3),\ \mathrm{x}_{ij}(2),\ \mathrm{x}_{i+1,j}(1)+l^{\mathrm{f}}\}$. This can be generalised so that, at each stage of the simulation, one can collect a vector with the location of all fibre discontinuities present along each interaction and store

them in two matrices:

$$\begin{aligned}\mathbb{S}_{\mathrm{H}}(i,j) &= \mathrm{sort}\left[\mathbb{x}(i,j)\ ,\ \mathbb{x}(i,j+1)\ ,\ \mathbb{x}(i,j)(1)+l^{\mathrm{f}}\right], \text{for horizontal interactions}\\ \mathbb{S}_{\mathrm{V}}(i,j) &= \mathrm{sort}\left[\mathbb{x}(i,j)\ ,\ \mathbb{x}(i+1,j)\ ,\ \mathbb{x}(i,j)(1)+l^{\mathrm{f}}\right], \text{for vertical interactions.}\end{aligned} \tag{2.1}$$

If the size of a given vector ($\mathbb{S}_{*ij}$) is defined as $s_{\max}+1$ (for instance, $s_{\max}=5$ in the interaction in Figs. 2.1f and 2.2c), then the interaction $_*(i,j)$ will be composed of $s_{\max}$ segments. The s^{th} segment of an interaction has a length equal to $\delta l_s = \mathbb{S}_{*ij}(s+1)-\mathbb{S}_{*ij}(s)$, and will be of one of the two types:

- A segment delimited by discontinuities in the same fibre is a broken segment (see Segment 1 in Figs. 2.1f and 2.2c, and Fig. 2.1g);
- A segment delimited by discontinuities in the two fibres is a shear-lag segment (see Segments 2 to 5 in Figs. 2.1f and 2.2c, and Fig. 2.1e).

The mechanical response of segments and interactions will be calculated in Secs. 2.2.3.2 to 2.2.3.4, using stresses based on the cross-section of the fibres only (i.e. normalised for a volume fraction of 100%).

2.2.3.2 Broken segment

In the case of a broken segment (let us consider Segment 1 from Fig. 2.1f and Fig. 2.1g, where the broken segment is in fibre $\mathcal{B}$), it is assumed that the load is entirely carried by the neighbouring, unbroken fibre element (of fibre $\mathcal{A}$). In that case, the stress ($\sigma^{\mathrm{I}}_{\mathrm{Br}}$) vs. strain ($\varepsilon^{\mathrm{I}}_{\mathrm{Br}}$) response of the broken segment is simply defined by

$$\sigma^{\mathrm{I}}_{\mathrm{Br}} = \varepsilon^{\mathrm{I}}_{\mathrm{Br}} \cdot \frac{E^{\mathrm{f}}}{2}, \tag{2.2}$$

where E^{f} is the stiffness of the fibre. This assumes that no stress is transmitted to the broken element through shear in the matrix, and results in a lower boundary for the stiffness of the composite after fibre breakage.

2.2.3.3 Shear-lag segment

In the case of a shear-lag segment (see for example Segment i in Fig. 2.1d and Fig. 2.1e), let us consider an overlap of length δl_{SL} between two neighbouring fibres, composed of two quarter-fibres $\mathcal{A}$ and $\mathcal{B}$ of diameter ϕ^{f} and stiffness E^{f} with a volume fraction V^{f}. The response of this shear-lag segment can be calculated using Pimenta and Robinson's extended shear-lag model [24], as summarised below. The geometric

inputs (T, t^{m}, L) for the shear-lag model are calculated from the geometry of the shear-lag segment as

$$T = \frac{\phi^{\mathrm{f}}}{4}, \qquad L = \frac{\delta l_{\mathrm{SL}}}{2} \qquad \text{and} \qquad t^{\mathrm{m}} = \left(\sqrt{\frac{\pi}{4 \cdot V^{\mathrm{f}}}} - 1\right) \cdot \phi^{\mathrm{f}}. \tag{2.3}$$

Considering a piecewise-linear constitutive law in shear for the matrix (or fibre-matrix interface), the behaviour of the shear-lag segment is defined by a set of differential equations

$$\begin{aligned} &\frac{\mathrm{d}^2 \Delta\sigma(x)}{\mathrm{d}x^2} = \pm\lambda^2 \cdot \Delta\sigma(x) \quad \text{, with the characteristic coefficient defined as} \\ &\qquad \lambda \overset{\text{def}}{=} \sqrt{\frac{2 \cdot |G^{\mathrm{m}}(x)|}{T \cdot t^{\mathrm{m}} \cdot E^{\mathrm{f}}}}, \end{aligned} \tag{2.4}$$

and where $\Delta\sigma(x) = \sigma_{\mathcal{B}}(x) - \sigma_{\mathcal{A}}(x)$ is the local stress difference between the two fibres $\mathcal{A}$ and $\mathcal{B}$, and $G^{\mathrm{m}}(x) = \mathrm{d}\tau^{\mathrm{m}}(x)/\mathrm{d}\gamma^{\mathrm{m}}(x)$ is the local shear tangent stiffness of the matrix (G^{m} takes a different value at each piece of the constitutive law, and G_0^{m} corresponds to the elastic shear modulus of the matrix). The solutions of these equations enable one to find the shear strain γ_{end} and the stress difference $\Delta\sigma_{\mathrm{end}}$ at the ends of the segment [24]; finally, the remote stress ($\sigma^{\mathrm{I}}_{\mathrm{SL}}$) vs. strain ($\varepsilon^{\mathrm{I}}_{\mathrm{SL}}$) curve of the segment is calculated through

$$\sigma^{\mathrm{I}}_{\mathrm{SL}} = \frac{\Delta\sigma_{\mathrm{end}}}{2} \qquad \text{and} \qquad \varepsilon^{\mathrm{I}}_{\mathrm{SL}} = \frac{\Delta\sigma_{\mathrm{end}}}{2 \cdot E^{\mathrm{f}}} + \frac{t^{\mathrm{m}} \cdot \gamma_{\mathrm{end}}}{\delta l_{\mathrm{SL}}}. \tag{2.5}$$

2.2.3.4 Overall response of an interaction between two neighbouring fibres

Once the full stress-strain curves (σ^{I}_s vs. $\varepsilon^{\mathrm{I}}_s$) of each of the $s \in \{1, ..., s_{\max}\}$ segments forming an interaction between two neighbouring fibres have been calculated (as explained in Secs. 2.2.3.1 to 2.2.3.3), they are combined in series to derive the stress-strain response (σ^{I} vs. $\varepsilon^{\mathrm{RVE}}$) of the overall interaction (Fig. 2.1f). Considering that the length of each segment s is δl_s ($s \in \{1, ..., s_{\max}\}$) such that $\sum_{s=1}^{s_{\max}} \delta l_s = l^{\mathrm{f}}$, and that the remote stress of the interaction (σ^{I}) must be uniform through all segments (hence $\sigma^{\mathrm{I}}_s \equiv \sigma^{\mathrm{I}}\ \forall\ s \in \{1, ..., s_{\max}\}$), the corresponding remote strain of the interaction is

$$\varepsilon^{\mathrm{RVE}}(\sigma^{\mathrm{I}}) = \frac{\sum_{s=1}^{s_{\max}} \delta l_s \cdot \varepsilon^{\mathrm{I}}_s(\sigma^{\mathrm{I}})}{l^{\mathrm{f}}}. \tag{2.6}$$

Eq. 2.6 allows one to populate the rising part of the stress-strain curve of each interaction, and the strength of the interaction is defined as the minimum of the strengths of each segment (since they are arranged in series). As a result, if two neighbouring fibres have a break or an end at the same axial location x, their interaction is considered de-

activated (i.e. no load is carried through this interaction). The stress-strain responses of all horizontal and vertical interactions (i, j) are stored respectively in $\sigma^{\mathrm{I}}_{\mathrm{H}ij}(\varepsilon^{\mathrm{RVE}})$ and $\sigma^{\mathrm{I}}_{\mathrm{V}ij}(\varepsilon^{\mathrm{RVE}})$, where $\varepsilon^{\mathrm{RVE}}$ is the overall strain applied to all interactions and fibres in an RVE.

2.2.4 Tensile response of a fibre with stochastic strength

2.2.4.1 Maximum stress in the fibres

The overall stress field within fibre (i, j) should be calculated by combining the stresses due to the four interactions in each quarter-fibre (see Sec. 2.2.3.4) in parallel. However, calculating these full stress fields would be computationally expensive, and therefore an approximate method is derived as follows.

The average stress in each quarter of fibre (i, j) due to a single interaction is equal to the average stress of the interaction $\sigma^{\mathrm{I}}_{*ij}(\varepsilon^{\mathrm{RVE}})$ (Fig. 2.2c). Combining the four quarter-fibres forming a fibre in parallel, the average stress in the fibre is defined as: $\sigma^{\mathrm{f}}(i, j, \varepsilon^{\mathrm{RVE}}) = \left(\sigma^{\mathrm{I}}_{\mathrm{V}}(i-1, j, \varepsilon^{\mathrm{RVE}}) + \sigma^{\mathrm{I}}_{\mathrm{H}}(i, j, \varepsilon^{\mathrm{RVE}}) + \sigma^{\mathrm{I}}_{\mathrm{V}}(i, j, \varepsilon^{\mathrm{RVE}}) + \sigma^{\mathrm{I}}_{\mathrm{H}}(i, j-1, \varepsilon^{\mathrm{RVE}})\right) / \mathbb{N}^{\mathrm{I}}_{ij}$, where $\mathbb{N}^{\mathrm{I}}_{ij}$ is the number of active neighbours (or interactions) around fibre (i, j); this is initially set up to 4 within the RVE, 3 along the edges and 2 in the corners, but it may decrease as fibres break during the simulation, as will be explained in Sec. 2.2.4.4.

The maximum stress (due to the stress concentrations caused by the neighbouring fibre-ends) in each quarter-fibre (i, j) is equal to $2 \cdot \sigma^{\mathrm{I}}_{*ij}(\varepsilon^{\mathrm{RVE}})$ (Fig. 2.2c). Therefore, for each fibre, four stress peaks are calculated, each representing a combination of (i) the average stress in the fibre and (ii) the stress concentration due to a neighbouring fibre-end (see Fig. 2.2d). As a result, the four values of stress-peaks in each fibre (i, j) are calculated as follow:

$$\begin{aligned}
\sigma^{\mathrm{f}}_1(i, j, \varepsilon^{\mathrm{RVE}}) &= \sigma^{\mathrm{f}}(i, j, \varepsilon^{\mathrm{RVE}}) + \frac{\sigma^{\mathrm{I}}_{\mathrm{V}}(i-1, j, \varepsilon^{\mathrm{RVE}})}{\mathbb{N}^{\mathrm{I}}_{ij}}, \\
\sigma^{\mathrm{f}}_2(i, j, \varepsilon^{\mathrm{RVE}}) &= \sigma^{\mathrm{f}}(i, j, \varepsilon^{\mathrm{RVE}}) + \frac{\sigma^{\mathrm{I}}_{\mathrm{H}}(i, j, \varepsilon^{\mathrm{RVE}})}{\mathbb{N}^{\mathrm{I}}_{ij}}, \\
\sigma^{\mathrm{f}}_3(i, j, \varepsilon^{\mathrm{RVE}}) &= \sigma^{\mathrm{f}}(i, j, \varepsilon^{\mathrm{RVE}}) + \frac{\sigma^{\mathrm{I}}_{\mathrm{V}}(i, j, \varepsilon^{\mathrm{RVE}})}{\mathbb{N}^{\mathrm{I}}_{ij}}, \\
\sigma^{\mathrm{f}}_4(i, j, \varepsilon^{\mathrm{RVE}}) &= \sigma^{\mathrm{f}}(i, j, \varepsilon^{\mathrm{RVE}}) + \frac{\sigma^{\mathrm{I}}_{\mathrm{H}}(i, j-1, \varepsilon^{\mathrm{RVE}})}{\mathbb{N}^{\mathrm{I}}_{ij}}.
\end{aligned} \tag{2.7}$$

Comparing these four values of peaks in the local stresses of fibre (i, j), one can identify the maximum fibre stress $\hat{\sigma}^{\mathrm{f}}_{ij}(\varepsilon^{\mathrm{RVE}})$ (Fig. 2.2d) as well as the relative neighbour

$k_{\text{crit}}(i,j,\varepsilon^{\text{RVE}})$ of fibre (i,j) causing this peak, such that:

$$\hat{\sigma}^{\text{f}}_{ij}(\varepsilon^{\text{RVE}}) = \sigma^{\text{f}}_{k_{\text{crit}}(i,j,\varepsilon^{\text{RVE}})}(i,j,\varepsilon^{\text{RVE}}) = \max\left\{\sigma^{\text{f}}_{k}(i,j,\varepsilon^{\text{RVE}})\right\}_{k=1}^{4}. \tag{2.8}$$

2.2.4.2 Computation of fibre strength

The fibre strength X_{ij} is required to determine whether fibre (i,j) will break under the maximum fibre stress $\hat{\sigma}^{\text{f}}_{ij}(\varepsilon^{\text{RVE}})$ defined in Eq. 2.8. As there is considerable variability in the strength of technical brittle fibres (e.g. carbon and glass), their stochastic strength is modelled using a Weibull distribution [48].

Strength distributions (characterised by a Weibull modulus m and a scale parameter σ_0 measured at the length l_{r}) for technical fibres can be found in the literature, but size and "shape" (of the stress field) effects must be accounted for, as the gauge length l_{r} at which the fibre strength has been measured is not necessarily the same as that of the fibres in the composite (l^{f}), and the stress-fields in the fibres within discontinuous composites are not uniform. Therefore, fibres are assigned strengths following a scaled Weibull distribution with a failure probability given by

$$F(\sigma^{\text{f}}) = 1 - \exp\left(-C_{\text{length}} \cdot C_{\text{shape}} \cdot \left(\frac{\sigma^{\text{f}}}{\sigma_0}\right)^{m}\right), \tag{2.9}$$

where C_{length} and C_{shape} are correction factors accounting for the fibre length and the shape of stress-fields of the fibres in the composite (see App. A). This process creates a matrix containing four ordered strengths for each fibre $\mathbb{X}_{ij}(q)$ ($q \in \{1,...,4\}$), to allow for each fibre to fail once due to each interaction with its four neighbours; the initial strength of the fibre (i,j) is $\mathbb{X}_{ij}(q_{ij})$ where $q_{ij} = 1$. The realisation of fibre strengths is repeated for each RVE, so that different fibres in the same cross-sectional location (i,j) have different values of stochastic strength along the full specimen.

2.2.4.3 Identification of fibre-breaks

At this point, the maximum stress in each fibre (i,j) has been defined for every value of the applied strain as $\hat{\sigma}^{\text{f}}_{ij}(\varepsilon^{\text{RVE}})$ in Eq. 2.8, and also the strength of each fibre as $\mathbb{X}_{ij}(q_{ij})$ in Eq. 2.9. Therefore, one can find out whether a fibre will break or not under a given remote strain ε^{RVE}, and store that information in the matrix of logical values

$$\mathbb{F}_{ij}(\varepsilon^{\text{RVE}}) = \left(\hat{\sigma}^{\text{f}}_{ij}(\varepsilon^{\text{RVE}}) > \mathbb{X}_{ij}(q_{ij})\right) = \begin{cases} 1 : \text{fibre is broken,} \\ 0 : \text{fibre remains in the same configuration.} \end{cases} \tag{2.10}$$

From the values of $\mathbb{F}_{ij}(\varepsilon^{\mathrm{RVE}})$ through the whole RVE, the remote RVE strain at which the first fibre-break occurs in the RVE is defined by

$$\varepsilon_{\mathrm{NB}}^{\mathrm{RVE}} = \min\left\{\varepsilon^{\mathrm{RVE}} \;:\; \left[\exists(i,j) : \mathbb{F}_{ij}(\varepsilon^{\mathrm{RVE}}) > 0\right]\right\}. \tag{2.11}$$

Moreover, the neighbouring fibre causing failure of fibre (i,j) is known (this is defined by the index of the relative neighbour causing the stress concentration $k_{\mathrm{crit}}(i,j,\varepsilon^{\mathrm{RVE}})$ in Eq. 2.8); consequently, a break is introduced in fibre (i,j) at the same location x_{break} as one of the fibre-discontinuities of its critical neighbouring fibre:

$$x_{\mathrm{break}} = \mathbb{x}_{i_{\mathrm{crit}}j_{\mathrm{crit}}}(s_{\mathrm{crit}}), \quad \text{with} \quad \begin{cases} (i_{\mathrm{crit}}, j_{\mathrm{crit}}) = (i-1, j) \text{ for } k_{\mathrm{crit}} = 1 \\ (i_{\mathrm{crit}}, j_{\mathrm{crit}}) = (i, j+1) \text{ for } k_{\mathrm{crit}} = 2 \\ (i_{\mathrm{crit}}, j_{\mathrm{crit}}) = (i+1, j) \text{ for } k_{\mathrm{crit}} = 3 \\ (i_{\mathrm{crit}}, j_{\mathrm{crit}}) = (i, j-1) \text{ for } k_{\mathrm{crit}} = 4 \end{cases} \quad \text{(see Fig. 2.2b)}, \tag{2.12}$$

where the $s_{\mathrm{crit}}^{\mathrm{th}}$ fibre-discontinuity in the critical neighbouring fibre $(i_{\mathrm{crit}}, j_{\mathrm{crit}})$ is located at the end of the longest segment of the interaction between fibres (i,j) and $(i_{\mathrm{crit}}, j_{\mathrm{crit}})$, which is supposed to be the most critical discontinuity for fibre (i,j). For example, in Fig. 2.1f, Segment 4 is the longest shear-lag segment in the interaction between fibres $\mathcal{A}$ and $\mathcal{B}$ and, as a result, fibre $\mathcal{A}$ would break at $x = \mathbb{x}_{\mathcal{B}}(3)$. After this strain $\varepsilon_{\mathrm{NB}}^{\mathrm{RVE}}$, the interaction between fibres (i,j) and $(i_{\mathrm{crit}}, j_{\mathrm{crit}})$ is unable to carry any further stresses.

2.2.4.4 Storing results and updating the configuration after the formation of fibre-breaks

Everything calculated until Eq. 2.12 is valid for each RVE up to the formation of fibre breaks; therefore, the stress-strain curves of the interactions in the $p^{\mathrm{RVE}^{\mathrm{th}}}$ RVE can be stored in matrices $\boldsymbol{\sigma}_{\mathrm{V}}^{\mathrm{RVE}}$ and $\boldsymbol{\sigma}_{\mathrm{H}}^{\mathrm{RVE}}$ up to the strain $\varepsilon_{\mathrm{NB}}^{\mathrm{RVE}}$ defined in Eq. 2.11:

$$\left.\begin{aligned} \sigma_{\mathrm{V}ij}^{\mathrm{RVE}}(\varepsilon^{\mathrm{RVE}}; p^{\mathrm{RVE}}) &= \sigma_{\mathrm{V}ij}^{\mathrm{I}}(\varepsilon^{\mathrm{RVE}}) \\ \sigma_{\mathrm{H}ij}^{\mathrm{RVE}}(\varepsilon^{\mathrm{RVE}}; p^{\mathrm{RVE}}) &= \sigma_{\mathrm{H}ij}^{\mathrm{I}}(\varepsilon^{\mathrm{RVE}}) \end{aligned}\right\} \quad \text{for} \quad \varepsilon^{\mathrm{RVE}} < \varepsilon_{\mathrm{NB}}^{\mathrm{RVE}}. \tag{2.13}$$

Once a fibre breaks, its shear-lag interactions with its neighbours are modified and must be recalculated for strains above $\varepsilon_{\mathrm{NB}}^{\mathrm{RVE}}$. To do this, the list $\mathbb{Z}$ of fibres which broke under the strain $\varepsilon_{\mathrm{NB}}^{\mathrm{RVE}}$ is defined as

$$\mathbb{Z}(\varepsilon_{\mathrm{NB}}^{\mathrm{RVE}}) = \left\{(i,j) \;:\; \mathbb{F}_{ij}(\varepsilon_{\mathrm{NB}}^{\mathrm{RVE}}) = 1\right\}. \tag{2.14}$$

Applying Eq. 2.12 to each fibre (i,j) in $\mathbb{Z}$, the location of the new break in fibre (i,j) x_{break} is calculated and added to the list of fibre-breaks in fibre (i,j), so that

$$\mathbb{x}_{ij} = \text{sort}\left[\mathbb{x}_{ij}\ ,\ x_{\text{break}}\right]. \tag{2.15}$$

Moreover, for the fibres in $\mathbb{Z}$, the interaction between the broken fibre (i,j) and its critical neighbour $(i_{\text{crit}}, j_{\text{crit}})$ is deactivated (because the interaction cannot build-up stresses), and therefore the number of active neighbours (or active interactions) in the two fibres is decreased by one:

$$\begin{aligned} \mathbb{N}_{ij}(\varepsilon^{\text{RVE}} > \varepsilon^{\text{RVE}}_{\text{NB}}) &= \mathbb{N}_{ij}(\varepsilon^{\text{RVE}} < \varepsilon^{\text{RVE}}_{\text{NB}}) - 1, \quad \text{and} \\ \mathbb{N}_{i_{\text{crit}},j_{\text{crit}}}(\varepsilon^{\text{RVE}} > \varepsilon^{\text{RVE}}_{\text{NB}}) &= \mathbb{N}_{i_{\text{crit}},j_{\text{crit}}}(\varepsilon^{\text{RVE}} < \varepsilon^{\text{RVE}}_{\text{NB}}) - 1. \end{aligned} \tag{2.16}$$

Finally, the strength $\mathbb{X}_{ij}(q_{ij})$ of the fibres in $\mathbb{Z}$ must be updated as well, and is increased to $\mathbb{X}_{ij}\left(q_{ij}(\varepsilon^{\text{RVE}} > \varepsilon^{\text{RVE}}_{\text{NB}})\right)$ where $q_{ij}(\varepsilon^{\text{RVE}} > \varepsilon^{\text{RVE}}_{\text{NB}}) = q_{ij}(\varepsilon^{\text{RVE}} < \varepsilon^{\text{RVE}}_{\text{NB}}) + 1$. This is done to account for the fact that, each time a fibre fails, it has one less weak section, and therefore the strength of its segments should increase (see App. A).

Once the configuration of the RVE has been updated (see Eqs. 2.14 to 2.16), the entire process of calculating the stress-strain curves of the interactions in the RVE is repeated for higher values of strain ($\varepsilon^{\text{RVE}} > \varepsilon^{\text{RVE}}_{\text{NB}}$), until new breaks are formed.

2.2.5 Macroscopic response and final failure

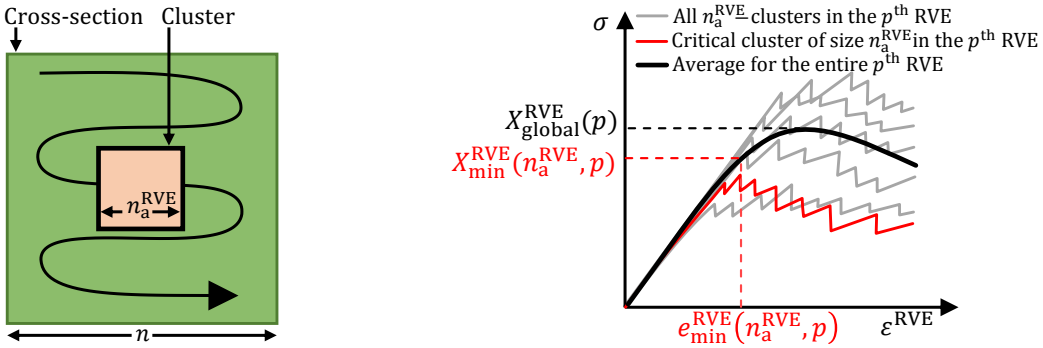
2.2.5.1 Calculation of the overall stress-strain curve of the specimen

Once the stress-strain curves of all $2 \cdot n \cdot (n-1)$ interactions of the p^{th} RVE are calculated (as described in Secs. 2.2.3 and 2.2.4), they can be combined in parallel (i.e. by averaging the stresses of all interactions for each applied strain) and normalised by the fibre volume fraction V^{f} to define the stress-strain curve of the RVE:

$$\sigma^{\text{RVE}}(\varepsilon^{\text{RVE}}; p^{\text{RVE}}) = V^{\text{f}} \cdot \frac{\sum_{i,j}\left(\sigma^{\text{RVE}}_{\text{V}ij}(\varepsilon^{\text{RVE}}; p^{\text{RVE}})\right) + \sum_{i,j}\left(\sigma^{\text{RVE}}_{\text{H}ij}(\varepsilon^{\text{RVE}}; p^{\text{RVE}})\right)}{2 \cdot n \cdot (n-1)}. \tag{2.17}$$

All n^{RVE} RVEs are then combined in series (i.e. by averaging the strains of all RVEs for each applied stress) to obtain the global stress-strain curve of the whole specimen, $\sigma^{\infty}(\varepsilon^{\infty})$:

$$\varepsilon^{\infty} = \frac{\sum_{p^{\text{RVE}}=1}^{n^{\text{RVE}}} \varepsilon^{\text{RVE}}(\sigma^{\infty}; p^{\text{RVE}})}{n^{\text{RVE}}}. \tag{2.18}$$



(a) Scanning of the cross-section of the p^{th} RVE with a window of size $n_{\text{a}}^{\text{RVE}} \times n_{\text{a}}^{\text{RVE}}$.

(b) Derivation of $X_{\text{global}}^{\text{RVE}}$ and $X_{\text{min}}^{\text{RVE}}(n_{\text{a}}^{\text{RVE}}, p)$.

Figure 2.3: Failure criterion used to identify final failure of an RVE.

2.2.5.2 Failure criterion

Eq. 2.17 defines the average stress-strain response of each RVE, and therefore defines the stiffness $E_{\text{global}}^{\text{RVE}}$ and the strength $X_{\text{global}}^{\text{RVE}}$ of each RVE. However, it has been observed [64] that composites typically fail when a cluster of damage (e.g. broken fibres) reaches a critical size and triggers unstable failure of the entire specimen. To account for this possibility of catastrophic failure propagating from a critical flaw in the material, Dugdale's non-linear fracture mechanics criterion [65] was adapted, as described in this section.

A window of $n_{\text{a}}^{\text{RVE}} \times n_{\text{a}}^{\text{RVE}}$ fibres is used to scan each RVE (Fig. 2.3a) to find the weakest cluster of size $n_{\text{a}}^{\text{RVE}}$, which is the cluster in the p^{th} RVE which reaches its maximum stress at the lowest strain ($e_{\text{min}}^{\text{RVE}}(n_{\text{a}}^{\text{RVE}}, p^{\text{RVE}})$, see red curve in Fig. 2.3b). If this cluster is critical, its failure at the strain $e_{\text{min}}^{\text{RVE}}(n_{\text{a}}^{\text{RVE}}, p^{\text{RVE}})$ will trigger catastrophic failure of the entire RVE, at the corresponding stress $X_{\text{min}}^{\text{RVE}}(n_{\text{a}}^{\text{RVE}}) \overset{\text{def}}{=} \sigma^{\text{RVE}}(\varepsilon^{\text{RVE}} = e_{\text{min}}(n_{\text{a}}^{\text{RVE}}))$.

The problem is now to find the critical cluster size $n_{\text{a,crit}}^{\text{RVE}}$ leading to the RVE failure stress $X_{\text{crit}}^{\text{RVE}} \overset{\text{def}}{=} X_{\text{min}}^{\text{RVE}}(n_{\text{a}}^{\text{RVE}} = n_{\text{a,crit}}^{\text{RVE}})$. This problem is analogous to Dugdale's yield-strip model [65] in non-linear fracture mechanics. Considering a centre-crack (length $2a^{\text{RVE}}$) in a linear-elastic – perfectly-plastic plate (with yield strength $X_{\text{global}}^{\text{RVE}}$) under a remote stresses σ^{RVE}, the non-linear energy release rate (ERR) is defined by Dugdale as [65]

$$\begin{aligned} J_{\text{NL}}(\sigma^{\text{RVE}}, a^{\text{RVE}}) &= J_{\text{LE}}(X_{\text{global}}^{\text{RVE}}, a^{\text{RVE}}) \cdot D(\sigma^{\text{RVE}}), \\ \text{with } D(\sigma^{\text{RVE}}) &= \frac{8}{\pi^2} \cdot \ln\left(\sec\left(\frac{\pi}{2} \cdot \frac{\sigma^{\text{RVE}}}{X_{\text{global}}^{\text{RVE}}}\right)\right). \end{aligned} \tag{2.19}$$

In this equation, $D(\sigma^{\text{RVE}})$ is the Dugdale factor and J_{LE} is the ERR for the same structure but considering a linear-elastic material. This relation can be extrapolated for

other geometries [72], and here it is considered that the critical cluster of weak/broken fibres (with an arbitrary shape) can be represented by a penny-shaped crack. For a penny-shaped crack of radius a, $J_{\mathrm{LE}}(\sigma^{\infty}, a) = \left(2/\pi \cdot \sigma^{\infty} \cdot \sqrt{\pi \cdot a}\right)^2 \cdot / E^{\mathrm{RVE}}_{\mathrm{global}}$; therefore, the ERR of a penny-shaped crack in a non-linear material can be calculated as

$$J_{\mathrm{NL}}(\sigma^{\mathrm{RVE}}, a^{\mathrm{RVE}}) = \left(\frac{2}{\pi} \cdot X^{\mathrm{RVE}}_{\mathrm{global}} \cdot \sqrt{\pi \cdot a^{\mathrm{RVE}}}\right)^2 \cdot \frac{1}{E^{\mathrm{RVE}}_{\mathrm{global}}} \cdot \left[\frac{8}{\pi^2} \cdot \ln\left(\sec\left(\frac{\pi}{2} \cdot \frac{\sigma^{\mathrm{RVE}}}{X^{\mathrm{RVE}}_{\mathrm{global}}}\right)\right)\right]. \tag{2.20}$$

In this model, the penny-shaped crack is considered to have the same area as the $n^{\mathrm{RVE}}_{\mathrm{a}} \times n^{\mathrm{RVE}}_{\mathrm{a}}$ cluster, thus $a^{\mathrm{RVE}} = n^{\mathrm{RVE}}_{\mathrm{a}} \cdot \phi^{\mathrm{f}} / \left(2 \cdot \sqrt{V^{\mathrm{f}}}\right)$. Failure will then occur in the RVE when this weakest region of size a^{RVE} gets sufficiently large and satisfies the two conditions

$$\sigma^{\mathrm{RVE}} = X^{\mathrm{RVE}}_{\mathrm{crit}} \equiv X^{\mathrm{RVE}}_{\mathrm{min}}(a^{\mathrm{RVE}}_{\mathrm{crit}}) \wedge J_{\mathrm{NL}}(X^{\mathrm{RVE}}_{\mathrm{crit}}, a^{\mathrm{RVE}}_{\mathrm{crit}}) \geq \mathcal{G}_{\mathrm{crit}}, \tag{2.21}$$

where $\mathcal{G}_{\mathrm{crit}}$ is the fracture toughness of the material. Therefore, the criterion for final failure is

$$\frac{32}{\pi^3} \cdot \frac{{X^{\mathrm{RVE}}_{\mathrm{global}}}^2}{E^{\mathrm{RVE}}_{\mathrm{global}}} \cdot a^{\mathrm{RVE}}_{\mathrm{crit}} \cdot \ln\left(\sec\left(\frac{\pi}{2} \cdot \frac{X^{\mathrm{RVE}}_{\mathrm{crit}}}{X^{\mathrm{RVE}}_{\mathrm{global}}}\right)\right) \geq \mathcal{G}_{\mathrm{crit}}, \quad \text{with} \quad X^{\mathrm{RVE}}_{\mathrm{crit}} = X^{\mathrm{RVE}}_{\mathrm{min}}(a^{\mathrm{RVE}}_{\mathrm{crit}}). \tag{2.22}$$

This criterion is tested for an initial value of a^{RVE} calculated for $n^{\mathrm{RVE}}_{\mathrm{a}} = 1$; if the corresponding ERR is lower than the toughness of the composite, the size of the cluster $n^{\mathrm{RVE}}_{\mathrm{a}}$ is increased progressively, until the criterion in Eq. 2.22 is met. Once $X^{\mathrm{RVE}}_{\mathrm{crit}}$ has been calculated for each RVE, the overall strength of the specimen is defined as

$$X^{\infty}_{\mathrm{crit}} = \min\{X^{\mathrm{RVE}}_{\mathrm{crit}}(p^{\mathrm{RVE}}) \ , \quad p^{\mathrm{RVE}} \in \{1, ..., n^{\mathrm{RVE}}\}\}. \tag{2.23}$$

$X^{\infty}_{\mathrm{crit}}$ is then used as a cut-off in the global response found in Eq. 2.18. A method to estimate the toughness of the material is developed in App. B, assuming that debonding and pull-out occur at the smallest shear-lag segment between each pair of neighbouring fibres.

This failure criterion bridges the two extreme cases of ductile (strength-dominated) and brittle (toughness-dominated) fracture:

- A perfectly brittle material (with finite fracture toughness $\mathcal{G}_{\mathrm{crit}}$ and $X^{\infty}_{\mathrm{crit}} \ll X^{\infty}_{\mathrm{global}}$) will fail when $J_{\mathrm{LE}}(X^{\infty}_{\mathrm{crit}}, a_{\mathrm{crit}}) = \mathcal{G}_{\mathrm{crit}}$, since in this case the Dugdale factor is $D(\sigma^{\infty} \to X^{\infty}_{\mathrm{crit}}) \to (X^{\infty}_{\mathrm{crit}}/X^{\infty}_{\mathrm{global}})^2$;
- A perfectly ductile material (with $\mathcal{G}_{\mathrm{crit}} \to \infty$ and $X^{\infty}_{\mathrm{crit}} \approx X^{\infty}_{\mathrm{global}}$) will fail when $X^{\infty}_{\mathrm{crit}} \to X^{\infty}_{\mathrm{global}}$, since in this case the Dugdale factor is $D(\sigma^{\infty} \to X^{\infty}_{\mathrm{crit}}) \to +\infty$.

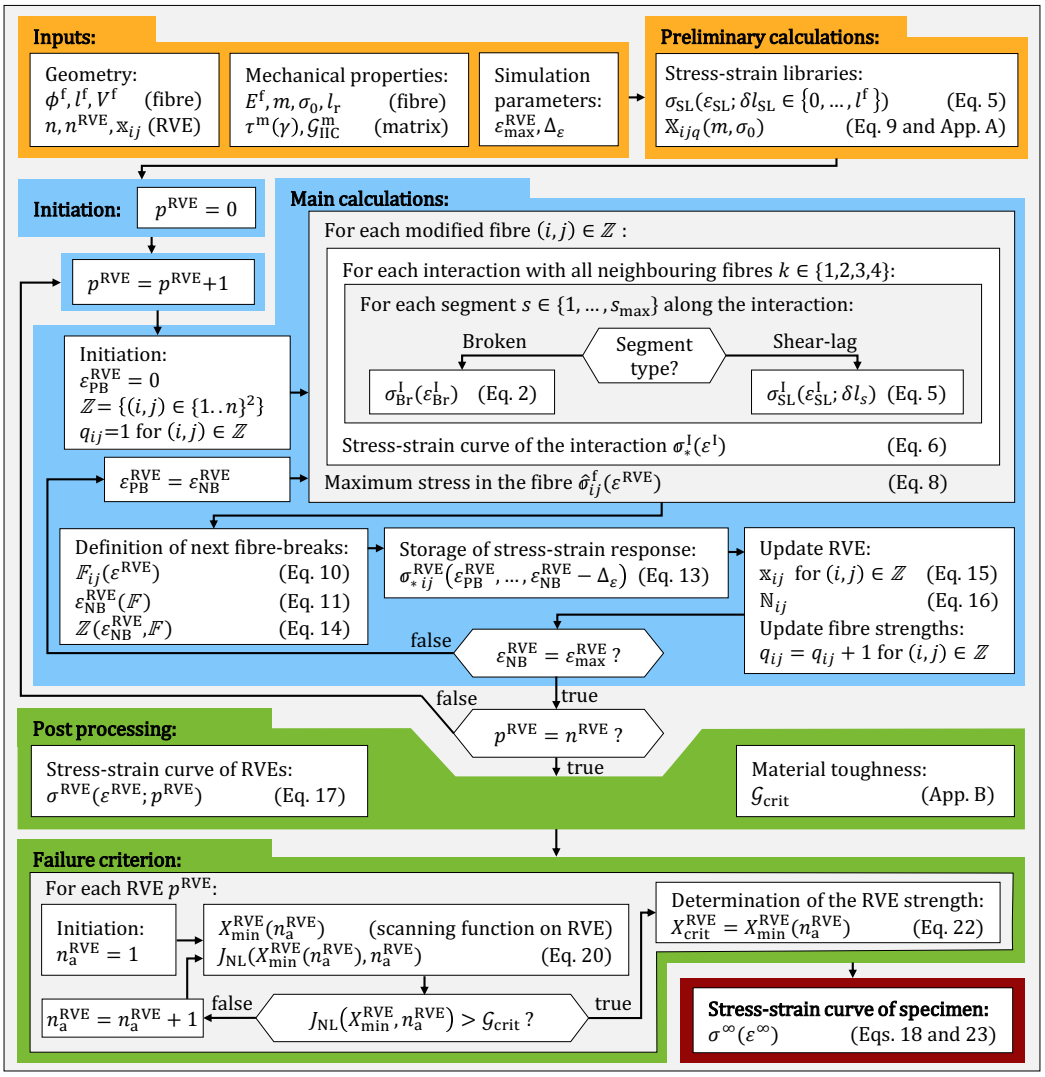


Figure 2.4: Implementation of the proposed model for aligned discontinuous composites.

2.2.6 Matlab implementation

The model described in the previous sections has been implemented in Matlab as summarised in Fig. 2.4. As the mechanical response of segments is called thousands of times during the simulation, a library of stress-strain responses of shear-lag segments (σ^I_{SL} vs. ε^I_{SL}, see Eq. 2.5) is computed prior to the simulation using the Matlab code previously developed [24]. The increase of the segment length (δ_{SL}) in the library is logarithmic (128 values varying from 0 to l^f), as this allows to best capture the evolution of the stress-strain curve with the segment length. This library is then called by the model and returns the stress-strain curve of a shear-lag segment of any length $\sigma^I_{SL}(\varepsilon^I_{SL}; \delta_{SL})$.

The stress-strain responses $\sigma^{\mathrm{I}}_{*ij}$ vs. $\varepsilon^{\mathrm{RVE}}$ of horizontal and vertical interactions (i,j) are stored respectively in the 3D matrices $\boldsymbol{\sigma}^{\mathrm{I}}_{\mathrm{H}}(i,j,\varepsilon^{\mathrm{RVE}})$ and $\boldsymbol{\sigma}^{\mathrm{I}}_{\mathrm{V}}(i,j,\varepsilon^{\mathrm{RVE}})$, where the RVE remote strain $\varepsilon^{\mathrm{RVE}}$ increases from 0 to $\varepsilon^{\mathrm{RVE}}_{\max}$ by steps of $\Delta\varepsilon$.

After fibre-breaks are detected at the strain $\varepsilon^{\mathrm{RVE}}_{\mathrm{NB}}$, the stress-strain curves of the interactions for $\varepsilon > \varepsilon^{\mathrm{RVE}}_{\mathrm{NB}}$ must be recalculated (see Sec. 2.2.4.4). To make the model more efficient, at each increase in the RVE strain for $\varepsilon^{\mathrm{RVE}} > \varepsilon^{\mathrm{RVE}}_{\mathrm{NB}}$ the simulation is re-run only for the interactions in which at least one fibre has just been updated (using the updated fibres (i,j) listed in $\mathbb{Z}(\varepsilon^{\mathrm{RVE}}_{\mathrm{NB}})$). Also, the model computes stress-strain curves within strain intervals where a given configuration is valid (i.e. for $\varepsilon^{\mathrm{RVE}}_{\mathrm{PB}} \leq \varepsilon^{\mathrm{RVE}} < \varepsilon^{\mathrm{RVE}}_{\mathrm{NB}}$, where $\varepsilon^{\mathrm{RVE}}_{\mathrm{PB}}$ is the strain at which the configuration was previously updated), rather than doing it for each strain step, which increases further the efficiency of the implementation.

2.3 Results

2.3.1 Experimental validation

The model is compared against two sets of experimental results measured by Yu et al. [29, 73] in Figs. 2.5 and 2.6. Both sets of specimens (with specifications shown in Tab. 2.1) were manufactured with the same carbon-fibre type [29, 73], but each set was

Table 2.1: Properties of the fibres and matrices used as input for the model. The fibre length $l^{\mathrm{f}} = 3$ mm applies to validation against experiments (Figs. 2.5 and 2.6); it varies in the parametric studies (Figs. 2.7, 2.8 and 2.9), and is fixed to $l^{\mathrm{f}} = 2$ mm to study size effects (Fig. 2.10). The specimen length l^{spec} is equal to 50 mm for all experiments [29, 73] (Figs. 2.5 and 2.6), and set to $l^{\mathrm{spec}} = 10$ mm while studying the effect of l^{f} (Fig. 2.7). The actual friction stress during pull-out is $\tau_\mu = \tau_{\mu 0} \cdot (1 - V^{\mathrm{f}})$ [74].

Fibre properties	l^{f} (mm)	ϕ^{f} (µm)	E^{f} (GPa)	m	σ_0 (MPa)	l_{r} (mm)
High Strength Carbon	$3.0^{*}/2.0$	7^{*}	225^{*}	$5.71^{\dagger}$	$4344^{*,\dagger}$	$25^{\dagger}$
Matrix properties	G^{m}_0 (GPa)	S^{m} (MPa)	$\tau_{\mu 0}$ (MPa)	$\mathcal{G}^{\mathrm{m}}_{\mathrm{IIc}}$ (kJ/m^2)	V^{f} (%)	n
Polypropylene (Fig. 2.5)	$0.7^{\dagger}$	$8^{\dagger}$	$4^{\dagger}$	0.2^{**}	36^{*}	$65^{\ddagger}$
Epoxy, 2 sets (Fig. 2.6)	$1.3^{\dagger}$	$60^{*\dagger}$	$10^{\dagger}$	$0.8^{\ddagger}$	$41^{*}/55^{*}$	$36^{\ddagger}/97^{\ddagger}$
Effect of l^{f} (Fig. 2.7)	1.0	50	10	0.8	36	32
Critical cluster (Fig. 2.8)	1.0	100	10	0.8	36	45
Variability (Fig. 2.9)	1.0	100	10	0.8	36	45
Size effect (Fig. 2.10)	1.0	100	10	0.8	36	45

$*$ Specimen specifications given by Yu et al. [29, 73].

$**$ Estimated considering a weak carbon-fibre/polypropylene bonding.

$\dagger$ Calculated from values found in literature [11, 29, 73, 75–78].

$\ddagger$ Calculated from the size and volume fraction of the specimens tested experimentally [29, 73]).

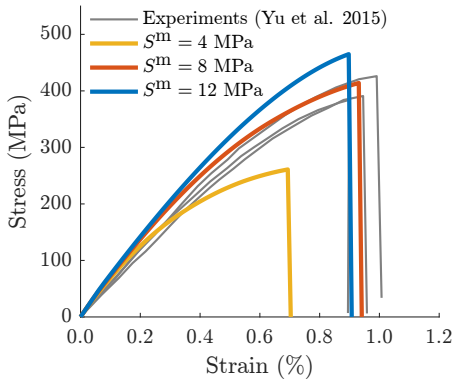
embedded in a different matrix (polypropylene for Set 1 in Fig. 2.5 and epoxy matrix MTM 49-3 for Set 2 in Fig. 2.6 [73], both modelled through bilinear constitutive laws).

As the properties of the polypropylene/carbon-fibre interface were not accurately known, the effects of the shear strength S^{m}, the frictional stress $\tau_{\mu 0}$ and the toughness $\mathcal{G}_{\mathrm{IIc}}^{\mathrm{m}}$ of the fibre/matrix interface on the stress-strain response of the composite are presented in Figs. 2.5a, 2.5b and 2.5c respectively (the nominal values of S^{m} and $\tau_{\mu 0}$ shown in Tab. 2.1 were measured in the literature (using for example single or multiple-overlap debonding tests), and the nominal value of $\mathcal{G}_{\mathrm{IIc}}^{\mathrm{m}}$ was estimated (and could be measured using end notch flexure tests)). Fig. 2.5 shows a good agreement between the model and experiments not only concerning the non-linear shape of the stress-strain curves, but also quantitatively, considering the best estimates for the properties of the fibre/polypropylene interface.

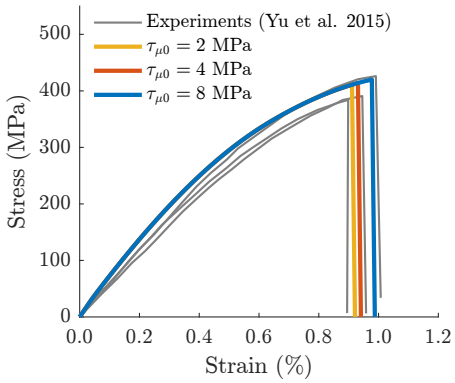
For composites with epoxy matrix (Fig. 2.6), the model predicts a small progressive strain softening, while the experiments show a small progressive strain hardening (especially for $V^{\mathrm{f}} = 55\%$); the latter can be due to (i) the strain-hardening nature of carbon fibres [79], and/or (ii) the re-orientation of misaligned fibres [73] (which are not considered in the model). The final failure is accurately predicted for $V^{\mathrm{f}} = 55\%$ (Fig. 2.6b), but the failure strain and strength of the dataset with $V^{\mathrm{f}} = 41\%$ are lower in the experiments than in the model (Fig. 2.6a). However, the low average and high variability of the strength of the specimens with $V^{\mathrm{f}} = 41\%$ was justified by Yu et al. [73] by the small width of the specimens, which made their strength very sensitive to inaccuracies in specimen cutting. Moreover, the specimens with $V^{\mathrm{f}} = 41\%$ should exhibit a similar failure strain to the specimens with $V^{\mathrm{f}} = 55\%$; overall, the mismatch between model and experiments for the dataset with $V^{\mathrm{f}} = 41\%$ is likely due to experimental problems.

2.3.2 Parametric study

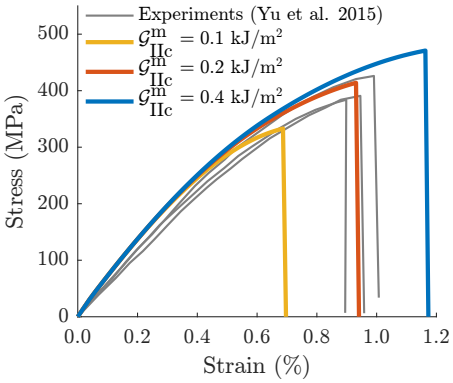
The effect of matrix/interfacial properties on the stress-strain response of discontinuous composites is investigated in Fig. 2.5. Fig. 2.5a shows that a stronger matrix/interface leads to less non-linearity and to an increase in the tensile strength of the composite, as it delays strain-softening and failure of the matrix/interface near fibre-ends. For small values of S^{m}, this leads to an increase in failure strain; however, for higher values of S^{m}, a further increase of the shear strength will actually make the material more brittle, because (i) the effect of the matrix/interface softening will be more confined to the fibre-ends, and (ii) the unstable failure criterion will be triggered for a lower tensile strain (due to shorter fibre pull-outs and the consequent decrease of the toughness of the composite).



(a) Interfacial shear strength S^m.



(b) Interfacial friction stress $\tau_{\mu 0}$.



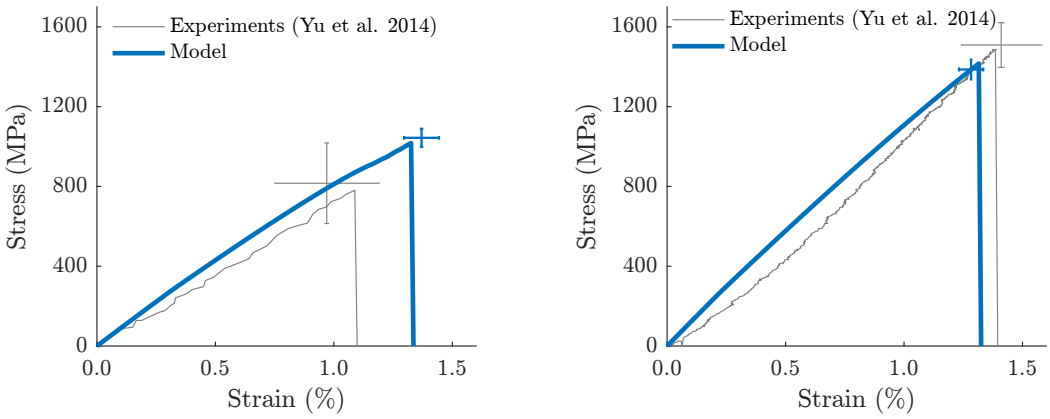
(c) Interfacial toughness $\mathcal{G}^m_{IIc}$.

Figure 2.5: Comparison of the stress-strain curves predicted by the model against experiments [29] (with 3 mm long carbon-fibres embedded in polypropylene, see Tab. 2.1), and influence of matrix/interface input parameters.

The effect of the pull-out friction $\tau_{\mu 0}$ on the stress-strain curve shown in Fig. 2.5b is insignificant, as failure of this particular material is strength-dominated and not affected by the fracture toughness of the composite. Finally, increasing the toughness of the matrix/interface allows the fibres to build-up higher stresses before matrix/interfacial failure (see Fig. 2.5c), therefore delaying failure of the composite.

Fig. 2.7 highlights the different trends for the effect of fibre length on the response of composites with a bilinear (brittle) or a strain-hardening (ductile) matrix (Fig. 2.7a). Up to a threshold ($l^f \approx 1.1$ mm), an increase of fibre length generates an increase of the stiffness and strength of the composite (because the effect of the discontinuities is reduced). Above this threshold, the strength plateaus (because the failure mode changes to fibre-failure), and the stiffness also converges towards that of the continuous-fibre composite (i.e. to $E^f \cdot V^f = 225 \times 0.36 = 81$ GPa).

For the failure strain (Fig. 2.7f), and above the threshold $l^f \approx 1.1$ mm, an increase in fibre length leads to a more brittle material (governed by fibre failure). Below this threshold, matrix/interface ductility starts governing the deformation of the composite, as the two matrices considered generate opposite trends.



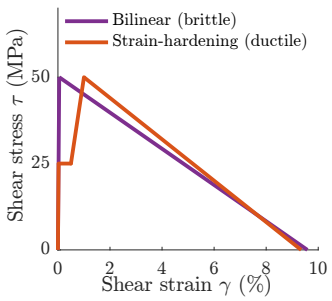
(a) $V^{\mathrm{f}} = 41\%$. **(b)** $V^{\mathrm{f}} = 55\%$.

Figure 2.6: Comparison of the stress-strain curves predicted by the model against experiments [73], for 3 mm carbon-fibres embedded in epoxy matrix and for different fibre volume fractions (see Tab. 2.1). Error bars represent one standard deviation (7 specimens have been tested for $V^{\mathrm{f}} = 41\%$, and 6 for $V^{\mathrm{f}} = 55\%$ [73]).

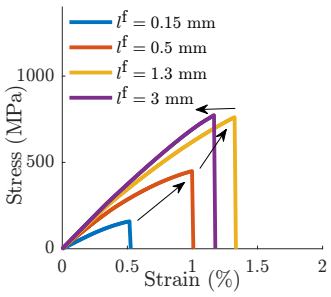
2.3.3 Study of the characteristics of the critical cluster

The characteristics of the critical clusters (which trigger final failure of the specimen) have been studied for three different fibre lengths (0.7, 2.0 and 6.0 mm, see the "critical cluster" specification in Tab. 2.1) using a method proposed by de Geus et al. [80] (see Fig. 2.8). For each fibre length, 1000 RVEs have been analysed and staggered so that their critical clusters are centred on top of each other, as illustrated in Fig. 2.8a. Then, stochastic variables characterising the material locally (e.g. initial fibre-overlapping lengths or fibre strengths) can be averaged at each point of the staggered RVEs; any deviation of the local averages in the centre of the staggered RVEs from the expected value in the entire composite (e.g. shorter overlaps or weaker fibres) will identify a statistically significant source of weakness in the microstructure of the material.

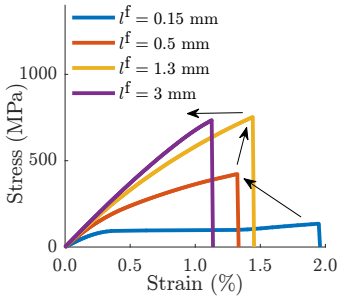
Fig. 2.8 shows that failure of composites with short fibres is triggered by clusters of fibres with minimum overlapping lengths lower than the average (see Fig. 2.8b), with nearly no formation of fibre breaks. On the contrary, failure of composites with long fibres (see Fig. 2.8d) is triggered by clusters of weaker fibres, which fragment before catastrophic failure propagation. Fig. 2.8 also shows that the size of the critical cluster decreases with an increase of the fibre length (from approximatively 9 fibres at $l^{\mathrm{f}} = 0.7$ mm to 4 fibres at $l^{\mathrm{f}} = 6.0$ mm), because the composite becomes more brittle with increasing fibre length.



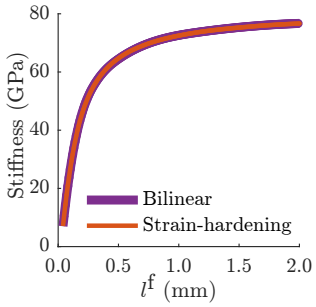
(a) Constitutive laws for the two types of matrix ($G_0^{\mathrm{m}} = 1000$ MPa, $S^{\mathrm{m}} = 50$ MPa and $\mathcal{G}_{\mathrm{IIc}}^{\mathrm{m}} = 0.8$ kJ/m^2).



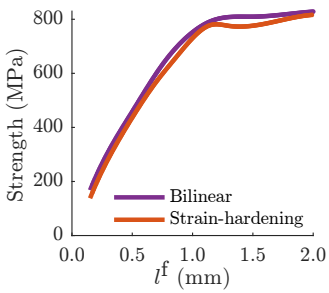
(b) Stress-strain curves of composites with a bilinear matrix, for different fibre lengths.



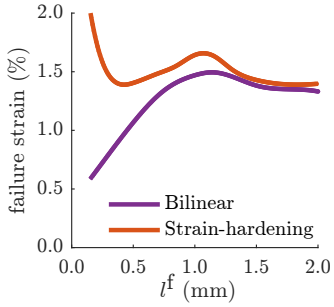
(c) Stress-strain curves of composites with a strain-hardening matrix, for different fibre lengths.



(d) Effect of fibre length on the longitudinal stiffness of the composite, for two types of matrix.



(e) Effect of fibre length on the ultimate strength of the composite, for two types of matrix.



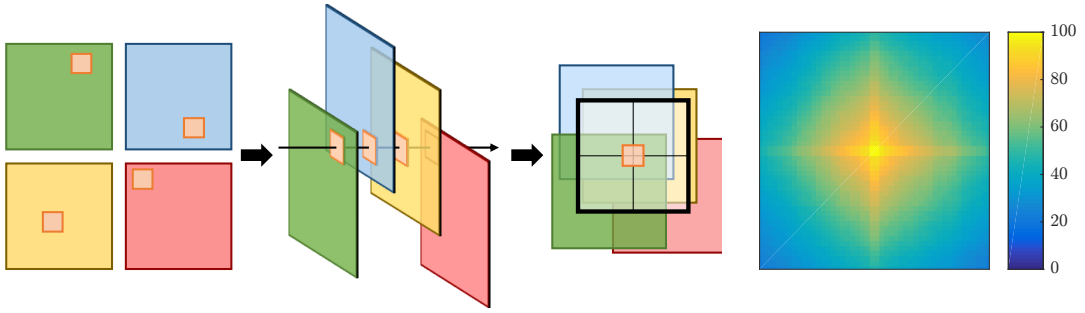
(f) Effect of fibre length on the failure strain of the composite, for two types of matrix.

Figure 2.7: Effect of fibre length on the response of aligned discontinuous composites ($V^{\mathrm{f}} = 36\%$).

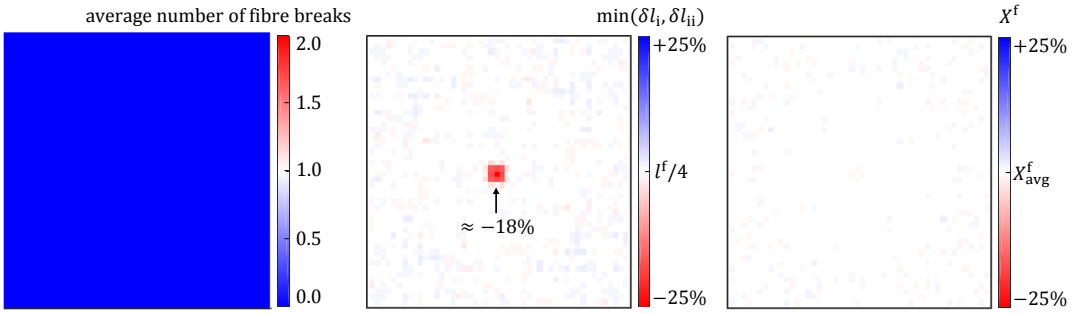
2.3.4 Effect of variability

In Sec. 2.3.3, the model showed that variability was responsible for critical clusters to appear in the material. The model was then used to quantify the effect of variability on the stress-strain curve. Fig. 2.8 suggests that discontinuous composites with shorter fibres are more affected by the overlap length, while discontinuous composites with longer fibres are more affected by fibre strength. Therefore, for both microstructures, the model was used to compute the stress-strain response with and without the relevant source of variability (overlap length for short fibres and fibre strength for long fibres), while keeping the same average value.

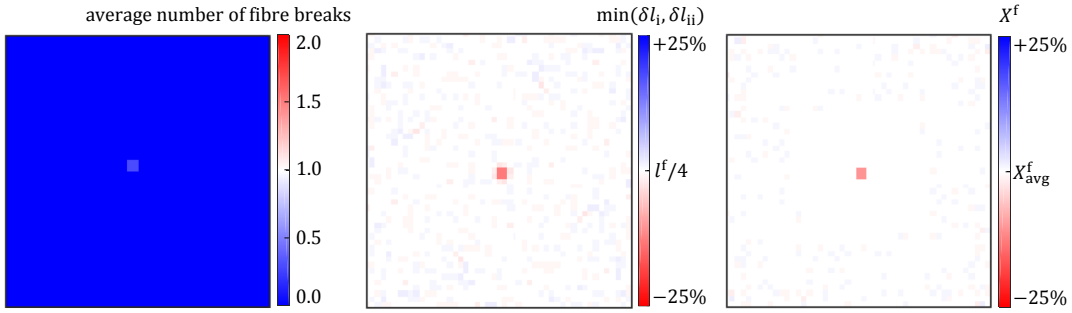
For short-fibre discontinuous composites, Fig. 2.9a shows that softening initiates earlier for a random staggering, and that the strength could be increased by 21% by removing variability in the fibre staggering. Similarly, for long-fibre discontinuous



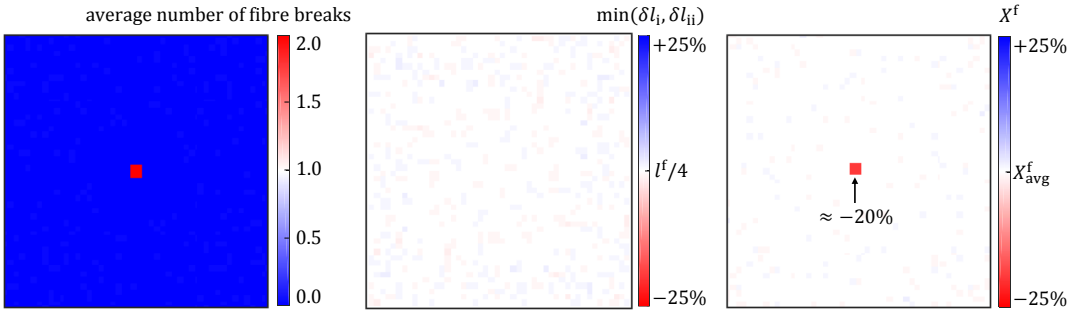
(a) Method for aligning RVEs on their respective critical clusters (left), and percentage of RVEs overlapping on the staggered RVEs (right).



(b) Short fibres ($l^{\mathrm{f}} = 0.7$ mm).

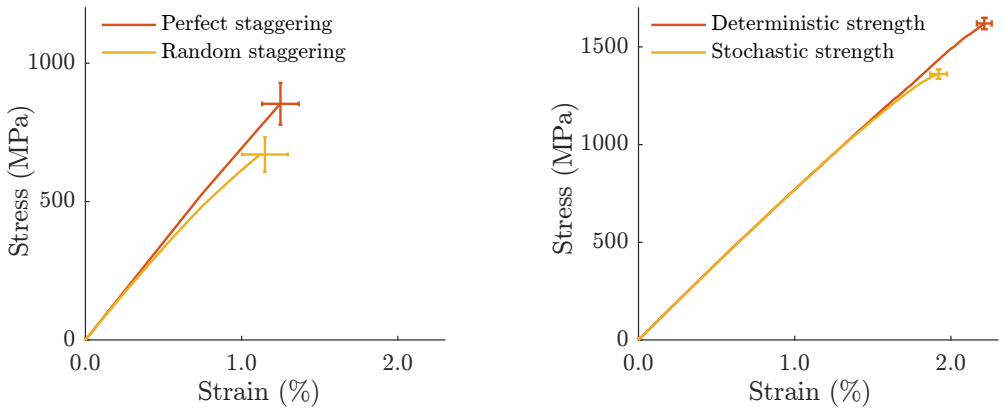


(c) Medium-length fibres ($l^{\mathrm{f}} = 2$ mm).



(d) Long fibres ($l^{\mathrm{f}} = 6$ mm).

Figure 2.8: Study of the characteristics of the critical cluster in discontinuous composites. The following characteristics are shown in figures (b), (c) and (d): number of fibre-breaks per RVE (left), initial overlap length (middle), and fibre strength (right), for different fibre lengths. The staggered RVEs in Figs. (b)-(d) show 45×45 fibres.



(a) Stress-strain curves of short-fibre discontinuous composites with stochastic and deterministic overlap lengths.

(b) Stress-strain curves of long-fibre discontinuous composites with stochastic and deterministic fibre strength.

Figure 2.9: Effect of the variability on discontinuous composites.

composites, Fig. 2.9b suggests that the strength of the composite could be increased by 17% by removing variability in the fibre strength.

2.3.5 Size effects

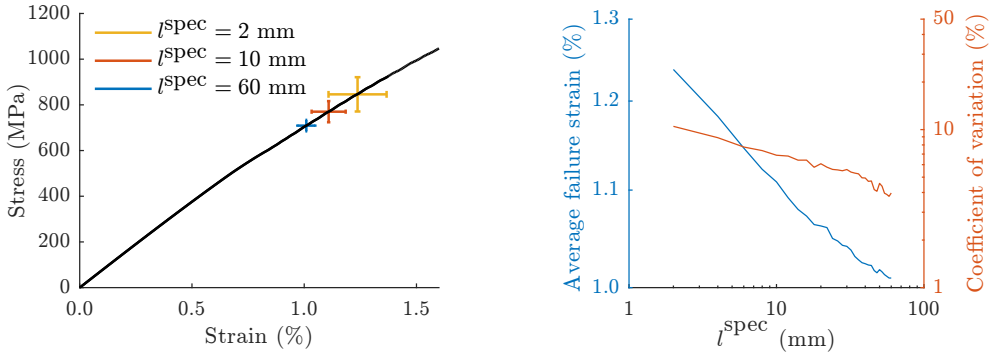
Fig. 2.10 shows that longer specimens become weaker and present less variability than shorter specimens. Moreover, Fig. 2.10b shows a logarithmic relationship between (i) the average strength or the coefficient of variation and (ii) the specimen length, which agrees with Weibull's weakest link theory [48, 81, 82].

2.4 Discussion

2.4.1 Response of aligned discontinuous composites

Fig. 2.8 suggests the presence of two competing failure modes in aligned discontinuous composites:

- Fibre failure, governed by the strength of the fibres, and occurring for long fibres (or for a stronger matrix, as the results show that fibre length and matrix/interfacial strength have a similar impact on the response of the composite). This failure mode triggers brittle failure of the material from small critical clusters.



(a) Stress-strain curve with average failure strains for different specimen lengths l^{spec}.

(b) Variation of the average failure strain and its coefficient of variation with l^{spec} (log-log scale).

Figure 2.10: Effect of the specimen length l^{spec} on the response of aligned discontinuous composites ($l^{f} = 2$ mm; 30 specimens are considered for each length l^{spec}).

- Debonding/pull-out, governed by matrix/interface properties, and occurring for short fibres (or for a weaker matrix). This failure mode triggers a more ductile failure from relatively larger critical clusters.

2.4.2 Optimal configuration for stiff, strong and less brittle discontinuous composites

Figs. 2.5 to 2.8 show that it is possible to tailor the microstructure of aligned discontinuous composites to optimise their mechanical response. The plateau found for the strength (Fig. 2.7e) agrees with numerical models in literature [58,61] and provides a critical fibre length ($l^{f} = 1.1$ mm) to achieve maximum strength of the composite. In the same way, the stiffness is nearly constant for fibres longer than 0.5 mm (Fig. 2.7d). As Fig. 2.7f shows that the final extension will reach a peak for $l^{f} = 1.1$ mm, this is the optimal fibre length to achieve a combination of high strength, high stiffness and high failure strain.

The critical fibre length identified in the present model is larger than those found by other analytical models in the literature [24,83]. For instance, Kelly-Tyson's [83] critical overlap length $\delta l_{K}^{f} = \sigma_0 \cdot \phi / (4S^{m})$ returns 0.15 mm for the configurations in Fig. 2.7 (see Tab. 2.1); this would correspond to a critical fibre length of $l_{K}^{f} = 4 \cdot \delta l_{K}^{f} = 0.60$ mm (to account for random overlap lengths), which is smaller than the value of 1.1 mm found for that configuration in this model. This is explained as:

- The model scales-up the fibre strength to account for size effects in the fibre. Accounting for this strengthening, Kelly-Tyson's critical fibre length becomes $l_{K}^{f} = 0.88$ mm;

- Kelly-Tyson's theory [83] assumes a perfectly-plastic matrix, while the present model considers matrix failure as well (which decreases the ability of the matrix to transfer stresses);
- The model considers that final failure propagates from a weaker cluster (see Sec. 2.2.5). Therefore, although the average overlap length between neighbouring fibres in a specimen is $l^{\mathrm{f}}/4$, Fig. 2.8 shows that the overlap length in the cluster triggering final failure can be much smaller than $l^{\mathrm{f}}/4$ (up to -18% in Sec. 2.3.3), which leads to a higher critical fibre length.

2.4.3 Model in the scope of literature

The model presented in this chapter complements the literature with the following features:

a. This model is one of the first in the literature (along with the model from Pimenta and Robinson [24]) to provide the stress-strain response of aligned discontinuous composites considering a generic non-linear response of the matrix analytically, which makes it suitable to study the effect of different matrices on the response of discontinuous composites (see for instance results in Fig. 2.7).

b. Contrarily to most models in the literature considering idealised microstructures (like perfectly staggered fibres) [24,55–58,61], the present model generates random locations of the fibre-ends throughout the whole specimen. It is shown in Fig. 2.8 that this random staggering is what triggers failure of composites with short fibres; moreover, Trujillo et al. [59] carried out experiments showing that the overlapping pattern in discontinuous composites had a significant impact on the strength of such materials. Therefore, this feature must be included in realistic models for discontinuous composites.

c. This model considers stochastic fibre strengths and accounts for the non-uniform stress fields in the fibres due to neighbouring fibre-ends (see App. A). This is neglected or highly simplified in some models [24,49–51], but Fig. 2.8 reveals that the variability in fibre strength is what triggers failure of composites with long fibres, and therefore must be considered to accurately model aligned discontinuous composites.

d. The model contains a strain-based failure criterion bridging *plasticity* and *fracture mechanics* [65] which captures the failure process observed experimentally in composites [64]: a weak cluster of fibres reaches a critical size and triggers catastrophic failure of the whole specimen. Combined with an analytical expression for estimating the toughness of discontinuous composites (see App. B), this

criterion is able to predict catastrophic failure of the material. Other models in the literature (FE models in particular [61, 62, 71]) consider that the strength of the material is the same as the maximum stress found in the RVE, which can overpredict the composite strength.

e. The model captures size effects in agreement with the weakest link theory [48, 81, 82] and highlights the importance of considering size effects when modelling and designing composite components using allowables measured in small coupons.

f. The semi-analytical character of the model makes it computationally efficient (for instance, a specimen made of 10 000 fibres runs in less than 30 seconds on a standard computer), and is therefore more suitable than FE simulations [54, 61, 62, 68–71] to model full-scale specimens. Moreover, the good agreement with experiments (see Figs. 2.5 and 2.6) makes the model appropriate to support material development and perform virtual experiments.

2.5 Conclusions

A semi-analytical model has been developed to predict the stress-strain response of aligned discontinuous composites. The model is the first in the literature to consider analytically (i) matrix debonding/pull-out using a shear-lag model generalised to any shear constitutive law of the matrix, (ii) fibre fragmentation under the influence of stress concentrations near fibre-ends and stochastic fibre strengths, and (iii) final failure using a strain-based failure criterion combining fracture mechanics and plasticity.

The model suggests that aligned discontinuous composites fail due to a weak cluster of fibres whose criticality depends on (i) the *overlap length* between fibres for short-fibre composites, and (ii) the *fibre strength* for long-fibre composites. Considering the stochastic nature of the location of fibre-ends and of the fibre strengths is therefore fundamental to create representative models and achieve accurate predictions. The model also highlights the importance of size effects when designing full-size composite structures.

The present model is computationally efficient, captures the effect of various parameters on the response of discontinuous composites (matrix properties, fibre length, specimen size), and shows good agreement with experiments in the literature. The model can therefore be used to support the design of structures made with discontinuous composites and to guide the development of optimised discontinuous composites tailored for specific applications. Moreover, this model can also be used to identify the optimal fibre length for a given fibre/matrix combination, which maximises simultaneously the stiffness, the strength and the failure strain of a discontinuous composite.

Chapter 3

A virtual testing framework for the stiffness of hybrid aligned discontinuous composite

3.1 Introduction

Hybrid discontinuous composites combine hybrid fibre-types with a discontinuous microstructure; therefore, this type of composite allows a reduction of material and manufacturing costs, opens new possibilities of hybridisation (e.g. with intimate intermingling of fibre-types), and extends further the ability to tailor the properties of composites in terms of stiffness, strength or toughness [17,29,73]. Hybrid discontinuous composites have already been manufactured [29,73,84,85] and confirmed the advantages listed previously.

However, despite the many advantages of hybrid discontinuous composites, there still is a need to understand these composites better. Indeed, "hybrid effects" can be observed in the experimental data of hybrid discontinuous composites, not only in the measured strength and failure strain, but also on their stiffness [29, 73, 84, 86], and are not fully explained yet. The effects of discontinuities and hybridisation on the stiffness of composites have already been investigated separately. The shear-lag theory developed by Cox [23] predicts the Young's modulus of discontinuous composites $E^{\mathrm{c}}_{\mathrm{Cox}}$, assuming that the inclusions carry longitudinal stresses only, while the matrix transmits stresses through shear:

$$\begin{aligned} E^{\mathrm{c}}_{\mathrm{Cox}} =& V^{\mathrm{f}} \cdot E^{\mathrm{f}} \left(1 - \frac{\tanh(\lambda_{\mathrm{Cox}} \cdot \alpha)}{\lambda_{\mathrm{Cox}} \cdot \alpha}\right) + V^{\mathrm{m}} \cdot E^{\mathrm{m}}, \\ \text{with } \lambda^2_{\mathrm{Cox}} =& \frac{2 \cdot E^{\mathrm{m}}}{E^{\mathrm{f}} \cdot (1 + \nu^{\mathrm{m}}) \cdot \ln(P^{\mathrm{f}}/V^{\mathrm{f}})}, \end{aligned} \tag{3.1}$$

where V^{f} and V^{m} represent the volume fractions, and E^{f} and E^{m} the Young's moduli of the inclusions and the matrix respectively; ν^{m} is the matrix Poisson's ratio, α is the aspect ratio of the inclusions, and P^{f} is a fibre-packing geometric factor [23].

The simplest analytical model to describe the behaviour of hybrid composites is based on the Rule-of-Mixtures (RoM). The Young's modulus of a hybrid composite – reinforced with two types of inclusions $\mathcal{A}$ (Young's modulus $E_{\mathcal{A}}$) and $\mathcal{B}$ (Young's modulus $E_{\mathcal{B}}$) at an overall inclusion volume fraction V^{f}, and with a matrix tensile modulus E^{m} and matrix volume fraction V^{m} – is predicted by the RoM as

$$E^{\mathrm{c}}_{\mathrm{RoM}} = V^{\mathrm{f}} \cdot (E_{\mathcal{A}} \cdot V^{\mathcal{A}} + E_{\mathcal{B}} \cdot V^{\mathcal{B}}) + V^{\mathrm{m}} \cdot E^{\mathrm{m}}, \tag{3.2}$$

where $V^{\mathcal{A}}$ and $V^{\mathcal{B}}$ are the volume-ratio of the inclusions $\mathcal{A}$ and $\mathcal{B}$ respectively (with $V^{\mathcal{A}} + V^{\mathcal{B}} = 1$). Note that the term $V^{\mathrm{m}} \cdot E^{\mathrm{m}}$, corresponding to the matrix contribution, is often neglected. The RoM accurately predicts the Young's modulus of continuous-fibre hybrid composites [28], but not the Young's modulus of discontinuous hybrid composites [73], neither the strength and failure strain of continuous or discontinuous hybrids [87–89].

The Young's modulus of any discontinuous composite – hybrid or not – will be affected by fibre misalignments, since it is (at the moment) impossible to manufacture discontinuous composites with perfectly aligned fibres; the best alignment levels in discontinuous composites have been obtained with the High Performance Discontinuous Fibre (HiPerDiF [73]) method, which is able to align 67% of the fibres within a $\pm 3°$ angle. The effect of this fibre misalignment can be modelled by the classical laminate theory [90, 91], by considering the composite as an equivalent laminate with discrete fibre orientations at each lamina; this requires knowing the transverse properties of the laminates, which can be calculated by a simple rule-of-mixtures, or by Halpin-Tsai [92] or Hashin [93] models.

This chapter aims to predict accurately the Young's modulus of hybrid discontinuous composites, capturing the corresponding hybrid effect which can be observed in recent literature [29, 73, 84]. Sec. 3.2 presents the model development for brick-and-mortar composites, composed of successive layers of linear-elastic inclusions or "bricks" (hereafter named platelets) of high and low Young's moduli, embedded in a linear-elastic soft matrix phase (or "mortar") (Fig. 3.1). In Sec. 3.3, two models are developed to calculate the Young's modulus of aligned discontinuous-fibre hybrid composites with a more realistic 3D microstructure (Fig. 3.2). Sec. 3.4 presents the main results; Sec. 3.5 discusses the models and their results, explains the presence of hybrid effects on the Young's modulus of hybrid discontinuous composites. Finally, Sec. 3.6 summarises the main conclusions.

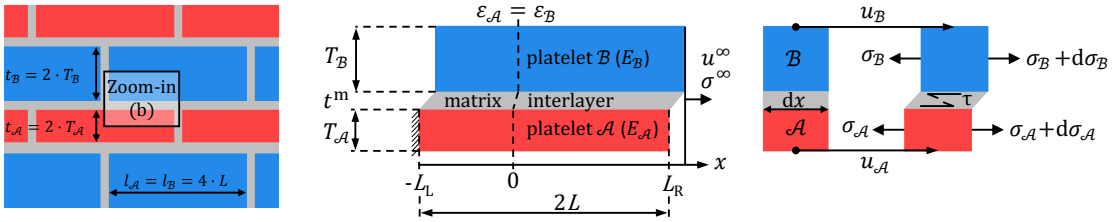
3.2 Model development for brick-and-mortar architecture

3.2.1 Description of the geometry

The Hybrid Brick-and-Mortar (HyBaM) composite considered throughout this section is made of two types of linear-elastic platelets, one with low Young's modulus (material $\mathcal{A}$, with Young's modulus $E_\mathcal{A}$) and the other with high Young's modulus (material $\mathcal{B}$, with Young's modulus $E_\mathcal{B} \geq E_\mathcal{A}$), staggered in alternate layers; both platelets have a uniform length $l_\mathcal{A} = l_\mathcal{B} = l$, and their thicknesses are $t_\mathcal{A}$ and $t_\mathcal{B}$ (with $t_\mathcal{A} \gtreqless t_\mathcal{B}$) (see Fig. 3.1a). These platelets are separated by layers of matrix with shear modulus G^m and thickness t^m. The composite is loaded by a tensile stress σ^∞ or tensile displacement u^∞, applied remotely.

The unit-cell considered for the model is presented in Fig. 3.1b, and consists of an overlap between two quarters of platelet separated by a matrix layer; the characteristic dimensions of the overlap are the half-length $L = l_\mathcal{A}/4 = l_\mathcal{B}/4 = l/4$, and the thicknesses $T_\mathcal{A} = t_\mathcal{A}/2$ and $T_\mathcal{B} = t_\mathcal{B}/2$ (which are independent from each other). Contrarily to the model for discontinuous-fibre hybrids developed in Sec. 3.3, in this model for HyBaM composites the volume ratio of each platelet type is controlled by the thickness of each platelet. The origin of the x-axis is chosen to coincide with the position at which the shear strain in the matrix γ is minimum. However, as the unit-cell is not symmetric, the position of this origin, defined by the variables L_L and L_R (such that $L_\mathrm{L} + L_\mathrm{R} = 2 \cdot L$), is not known *a priori*.

This model assumes a shear-lag behaviour of the composite in which each platelet is loaded under tensile stresses $\sigma_\mathcal{A}(x)$ or $\sigma_\mathcal{B}(x)$, while the matrix transfers shear stresses $\tau(x)$. Considering relatively thin platelets and matrix layers, the stress distributions are assumed to be uniform through the thickness of the platelets and matrix. For the



(a) Hybrid composite with a 'brick-and-mortar' architecture.

(b) Unit-cell considered in the model (zoom-in from (a)).

(c) Infinitesimal element.

Figure 3.1: Overview of the shear-lag model for HyBaM composites.

derivation of the model, the following parameters will be used:

$$\begin{aligned}
\Sigma T &= T_{\mathcal{A}} + T_{\mathcal{B}}, & \Sigma E &= E_{\mathcal{A}} + E_{\mathcal{B}}, & & \\
\Sigma K &= K_{\mathcal{A}} + K_{\mathcal{B}}, & \Sigma\sigma &= \sigma_{\mathcal{A}} + \sigma_{\mathcal{B}}, & & \\
\Delta T &= T_{\mathcal{B}} - T_{\mathcal{A}}, & \Delta E &= E_{\mathcal{B}} - E_{\mathcal{A}}, & & \\
\Delta K &= K_{\mathcal{B}} - K_{\mathcal{A}}, & \Delta\sigma &= \sigma_{\mathcal{B}} - \sigma_{\mathcal{A}}, & & \\
\bar{T} &= \Sigma T/2, & \bar{E} &= \Sigma E/2, & \bar{K} &= \Sigma K/2, \\
\tilde{T} &= 2 \cdot \frac{T_{\mathcal{A}} \cdot T_{\mathcal{B}}}{T_{\mathcal{A}} + T_{\mathcal{B}}}, & \tilde{E} &= 2 \cdot \frac{E_{\mathcal{A}} \cdot E_{\mathcal{B}}}{E_{\mathcal{A}} + E_{\mathcal{B}}}, & \tilde{K} &= 2 \cdot \frac{K_{\mathcal{A}} \cdot K_{\mathcal{B}}}{K_{\mathcal{A}} + K_{\mathcal{B}}},
\end{aligned} \tag{3.3}$$

where $K_{\mathcal{A}} = E_{\mathcal{A}} \cdot T_{\mathcal{A}}$ and $K_{\mathcal{B}} = E_{\mathcal{B}} \cdot T_{\mathcal{B}}$ represent the stiffness of the platelets, and are used to define the stiffness ratio $\eta = K_{\mathcal{A}}/K_{\mathcal{B}}$.

3.2.2 Differential equation

To establish the shear-lag differential equation governing the tensile response of the composite, one needs to consider both the equilibrium of stresses and the compatibility of displacement between the platelets and the matrix [24].

Considering Fig. 3.1c, the equilibrium of stresses between the matrix and the two platelets is given by

$$\mathrm{d}\sigma_{\mathcal{A}}(x) \cdot T_{\mathcal{A}} = -\tau(x) \cdot \mathrm{d}x, \tag{3.4a}$$

$$\mathrm{d}\sigma_{\mathcal{B}}(x) \cdot T_{\mathcal{B}} = \tau(x) \cdot \mathrm{d}x. \tag{3.4b}$$

Using the "sum" and "difference" operators defined in Eq. 3.3 and subtracting Eq. 3.4a to 3.4b leads to

$$(3.4\mathrm{b}) - (3.4\mathrm{a}) \quad \Rightarrow \quad \frac{\mathrm{d}\Delta\sigma(x)}{\mathrm{d}x} = \frac{4 \cdot \Sigma T}{\Sigma T^2 - \Delta T^2} \cdot \tau(x) = \frac{2}{\tilde{T}} \cdot \tau(x). \tag{3.5a}$$

Adding Eqs. 3.4a and 3.4b yields

$$(3.4\mathrm{b}) + (3.4\mathrm{a}) \quad \Rightarrow \quad \Sigma\sigma(x) = 2 \cdot \sigma^{\infty} - \frac{\Delta T}{\Sigma T} \cdot \Delta\sigma(x), \tag{3.5b}$$

where the remote stress σ^{∞} is defined by imposing equilibrium of the entire overlap:

$$\sigma^{\infty} \cdot (T_{\mathcal{A}} + T_{\mathcal{B}}) = \sigma_{\mathcal{A}}(x) \cdot T_{\mathcal{A}} + \sigma_{\mathcal{B}}(x) \cdot T_{\mathcal{B}}, \text{ constant for all } x \in [-L_{\mathrm{L}}, L_{\mathrm{R}}]. \tag{3.6}$$

Imposing compatibility of the displacements in Fig. 3.1c and using the linear-elastic constitutive equations ($\sigma = E \cdot \mathrm{d}u/\mathrm{d}x$) for each platelet leads to

$$\gamma(x) = \frac{u_{\mathcal{B}}(x) - u_{\mathcal{A}}(x)}{t^{\mathrm{m}}} \Rightarrow \frac{\mathrm{d}\gamma(x)}{\mathrm{d}x} = \frac{\dfrac{\sigma_{\mathcal{B}}(x)}{E_{\mathcal{B}}} - \dfrac{\sigma_{\mathcal{A}}(x)}{E_{\mathcal{A}}}}{t^{\mathrm{m}}}, \tag{3.7a}$$

where $u_{\mathcal{A}}$ and $u_{\mathcal{B}}$ are the longitudinal displacements in platelets $\mathcal{A}$ and $\mathcal{B}$. Using the operators defined in Eq. 3.3 and the boundary condition on $\Sigma\sigma(x)$ defined in Eq. 3.5b, Eq. 3.7a becomes

$$\frac{\mathrm{d}\gamma(x)}{\mathrm{d}x} = \frac{1}{t^{\mathrm{m}} \cdot \Sigma T} \cdot \frac{\Sigma K}{E_{\mathcal{A}} \cdot E_{\mathcal{B}}} \cdot \left[\Delta\sigma(x) - \frac{\Delta E \cdot \Sigma T}{\Sigma K} \cdot \sigma^{\infty}\right]. \tag{3.7b}$$

As the shear modulus of the matrix is $G^{\mathrm{m}} = \mathrm{d}\tau/\mathrm{d}\gamma$, Eqs. 3.5a and 3.7b can be combined in a single equation:

$$\begin{aligned} \frac{\mathrm{d}^2\Delta\sigma(x)}{\mathrm{d}x^2} =& \lambda^2 \cdot (\Delta\sigma(x) - \kappa \cdot \sigma^{\infty}), \\ \text{where} \quad & \begin{cases} \kappa = \dfrac{\Delta E \cdot \Sigma T}{\Sigma K} = \dfrac{2 \cdot \Delta E \cdot \Sigma T}{\Sigma E \cdot \Sigma T + \Delta E \cdot \Delta T}, \\ \lambda = \sqrt{\dfrac{2 \cdot G^{\mathrm{m}}}{t^{\mathrm{m}} \cdot \tilde{K}}} = \sqrt{\dfrac{8 \cdot G^{\mathrm{m}} \cdot (\Sigma E \cdot \Sigma T + \Delta E \cdot \Delta T)}{t^{\mathrm{m}} \cdot (\Sigma E^2 - \Delta E^2) \cdot (\Sigma T^2 - \Delta T^2)}}. \end{cases} \end{aligned} \tag{3.8}$$

This equation shows similarities with one derived in the literature for non-hybrid brick-and-mortar composites [24]; the differences between the two models are summarised in Tab. 3.1.

3.2.3 Stress and strain fields

The governing differential equation in $\Delta\sigma(x)$ (Eq. 3.8) can be solved analytically. Once $\Delta\sigma(x)$ is defined, Eqs. 3.5a and 3.7b give the expressions for the shear stress $\tau(x)$ and shear strain $\gamma(x)$ in the matrix, under the boundary conditions $\Delta\sigma(0) = \Delta\sigma_0$, $\gamma(0) = \gamma_0$ and $\tau(0) = G^{\mathrm{m}} \cdot \gamma_0$:

$$\Delta\sigma(x) = \Delta\sigma_0 + \frac{2}{\tilde{T}} \cdot \frac{G^{\mathrm{m}} \cdot \gamma_0}{\lambda} \cdot \sinh(\lambda \cdot x) = \Delta\sigma_0 + \frac{4 \cdot \Sigma T}{\Sigma T^2 - \Delta T^2} \cdot \frac{G^{\mathrm{m}} \cdot \gamma_0}{\lambda} \cdot \sinh(\lambda \cdot x), \tag{3.9a}$$

$$\gamma(x) = \gamma_0 \cdot \cosh(\lambda \cdot x), \tag{3.9b}$$

$$\tau(x) = G^{\mathrm{m}} \cdot \gamma_0 \cdot \cosh(\lambda \cdot x). \tag{3.9c}$$

The constant $\Delta\sigma_0$, which is currently unknown, will be determined in Sec. 3.2.4.

3.2.4 Boundary conditions

One boundary condition for Eq. 3.8 concerns the value of $\Delta\sigma(0) = \Delta\sigma_0$ at the characteristic point ($x = 0$ in Fig. 3.1b). This is the point at which the shear strain in the matrix is minimal (Fig. 3.1b), and is defined by

$$\frac{\mathrm{d}\gamma}{\mathrm{d}x}\Big|_{x=0} = 0 \qquad \Rightarrow \qquad \frac{\mathrm{d}u_{\mathcal{A}}}{\mathrm{d}x}\Big|_{x=0} = \frac{\mathrm{d}u_{\mathcal{B}}}{\mathrm{d}x}\Big|_{x=0} \qquad \Rightarrow \qquad \sigma_{\mathcal{A}}(0) = \sigma_{\mathcal{B}}(0) \cdot \frac{E_{\mathcal{A}}}{E_{\mathcal{B}}}. \tag{3.10}$$

Eq. 3.6 can be used to impose equilibrium of stresses at the characteristic point ($x = 0$) and applied remotely:

$$T_{\mathcal{A}} \cdot \sigma_{\mathcal{A}}(0) + T_{\mathcal{B}} \cdot \sigma_{\mathcal{B}}(0) = \sigma^{\infty} \cdot \Sigma T; \tag{3.11}$$

using this equality, Eq. 3.10 can be expressed as a boundary condition for $\Delta\sigma(x)$:

$$\Delta\sigma(0) = \kappa \cdot \sigma^{\infty}, \quad \text{with} \quad \kappa = \frac{\Delta E \cdot \Sigma T}{\Sigma K} = \frac{2 \cdot \Delta E \cdot \Sigma T}{\Sigma E \cdot \Sigma T + \Delta E \cdot \Delta T}. \tag{3.12}$$

Furthermore, considering the value of $\gamma(x)$ at the edge of the platelets (with $\gamma_{\mathrm{L}} = \gamma(-L_{\mathrm{L}})$ and $\gamma_{\mathrm{R}} = \gamma(L_{\mathrm{R}})$), the overall displacement u^{∞} can be derived either (i) by considering the extension of platelet $\mathcal{A}$ and the shear deformation of the matrix at $x = L_{\mathrm{R}}$, or (ii) by considering the shear deformation of the matrix at $x = -L_{\mathrm{L}}$ and the extension of platelet $\mathcal{B}$ (see Fig. 3.1b):

$$u^{\infty} = u^{\infty}_{\mathcal{A}} \overset{\text{(i)}}{=} \int_{-L_{\mathrm{L}}}^{L_{\mathrm{R}}} \varepsilon_{\mathcal{A}}(x)\mathrm{d}x + \gamma_{\mathrm{R}} \cdot t^{\mathrm{m}} \quad \text{and} \quad u^{\infty} = u^{\infty}_{\mathcal{B}} \overset{\text{(ii)}}{=} \gamma_{\mathrm{L}} \cdot t^{\mathrm{m}} + \int_{-L_{\mathrm{L}}}^{L_{\mathrm{R}}} \varepsilon_{\mathcal{B}}(x)\mathrm{d}x. \tag{3.13}$$

Therefore, averaging these two definitions for u^{∞} leads to

$$u^{\infty} = \frac{u^{\infty}_{\mathcal{A}} + u^{\infty}_{\mathcal{B}}}{2} = \frac{1}{2}\left[t^{\mathrm{m}} \cdot (\gamma_{\mathrm{L}} + \gamma_{\mathrm{R}}) + \int_{-L_{\mathrm{L}}}^{L_{\mathrm{R}}} \frac{\sigma_{\mathcal{A}}(x)}{E_{\mathcal{A}}} + \frac{\sigma_{\mathcal{B}}(x)}{E_{\mathcal{B}}}\mathrm{d}x\right]. \tag{3.14}$$

Moreover, considering that the integrand in Eq. 3.14 is

$$\frac{\sigma_{\mathcal{A}}(x)}{E_{\mathcal{A}}} + \frac{\sigma_{\mathcal{B}}(x)}{E_{\mathcal{B}}} = \frac{\Sigma\sigma(x) - \Delta\sigma(x)}{\Sigma E - \Delta E} + \frac{\Sigma\sigma(x) + \Delta\sigma(x)}{\Sigma E + \Delta E} = \frac{2 \cdot \Sigma E \cdot \Sigma\sigma(x) - 2 \cdot \Delta E \cdot \Delta\sigma(x)}{\Sigma E^2 - \Delta E^2}, \tag{3.15}$$

and using Eq. 3.5b to replace $\Sigma\sigma(x)$ in Eq. 3.15, u^{∞} becomes

$$u^{\infty} = \frac{1}{2}\left[t^{\mathrm{m}} \cdot (\gamma_{\mathrm{L}} + \gamma_{\mathrm{R}}) + \frac{8 \cdot L \cdot \Sigma E \cdot \sigma^{\infty}}{E_{\mathcal{A}} \cdot E_{\mathcal{B}}} - \frac{1}{\Sigma T} \cdot \frac{\Delta K}{E_{\mathcal{A}} \cdot E_{\mathcal{B}}} \cdot \int_{-L_{\mathrm{L}}}^{L_{\mathrm{R}}} \Delta\sigma(x)\mathrm{d}x\right]. \tag{3.16}$$

In order to remove the integral on $\Delta\sigma(x)$ from Eq. 3.16, let us start by integrating the derivative of matrix shear strains in Eq. 3.7b between $-L_{\mathrm{L}}$ and L_{R}:

$$\gamma_{\mathrm{R}} - \gamma_{\mathrm{L}} = \int_{-L_{\mathrm{L}}}^{L_{\mathrm{R}}} \frac{1}{t^{\mathrm{m}} \cdot \Sigma T} \cdot \frac{\Sigma K}{E_{\mathcal{A}} \cdot E_{\mathcal{B}}} \cdot [\Delta\sigma(x) - \kappa \cdot \sigma^{\infty}]\,\mathrm{d}x. \tag{3.17a}$$

Isolating the integral on $\Delta\sigma(x)$ in Eq. 3.17a and re-arranging gives

$$\frac{1}{\Sigma T} \cdot \frac{\Delta K}{E_{\mathcal{A}} \cdot E_{\mathcal{B}}} \cdot \int_{-L_{\mathrm{L}}}^{L_{\mathrm{R}}} \Delta\sigma(x)\mathrm{d}x = (\gamma_{\mathrm{R}} - \gamma_{\mathrm{L}}) \cdot t^{\mathrm{m}} \cdot \frac{\Delta K}{\Sigma K} + \frac{2}{\Sigma T} \cdot \frac{\Delta K}{E_{\mathcal{A}} \cdot E_{\mathcal{B}}} \cdot \kappa \cdot L \cdot \sigma^{\infty}. \tag{3.17b}$$

From Eqs. 3.16 and 3.17b, and defining the remote strain as $\varepsilon^{\infty} = u^{\infty}/(2 \cdot L)$,

$$\begin{aligned} \varepsilon^{\infty} =& \frac{t^{\mathrm{m}}}{4 \cdot L}\left[(\gamma_{\mathrm{R}} + \gamma_{\mathrm{L}}) - (\gamma_{\mathrm{R}} - \gamma_{\mathrm{L}}) \cdot \frac{\Delta K}{\Sigma K}\right] + \frac{\sigma^{\infty} \cdot \Sigma T}{\Sigma K}, \\ \Rightarrow \varepsilon^{\infty} =& \frac{\frac{t^{\mathrm{m}}}{2 \cdot L} \cdot [\gamma_{\mathrm{L}} \cdot K_{\mathcal{B}} + \gamma_{\mathrm{R}} \cdot K_{\mathcal{A}}] + \sigma^{\infty} \cdot \Sigma T}{\Sigma K}, \end{aligned} \tag{3.18}$$

where γ_{L} and γ_{R} are the only unknowns so far.

3.2.5 Location of the characteristic point

In addition to stress and strain fields, to find the overall Young's modulus of the HyBaM composite it is also necessary to know the position of the characteristic point $x = 0$, defined by the lengths L_{L} and L_{R}. Imposing equilibrium of stresses at $x = -L_{\mathrm{L}}$ and $x = L_{\mathrm{R}}$ gives

$$\begin{cases} \sigma^{\infty} \cdot \Sigma T = \Delta\sigma(L_{\mathrm{R}}) \cdot T_{\mathcal{B}}, \\ \sigma^{\infty} \cdot \Sigma T = -\Delta\sigma(-L_{\mathrm{L}}) \cdot T_{\mathcal{A}}. \end{cases} \tag{3.19}$$

Using the definition of $\Delta\sigma(x)$ (Eq. 3.9), the remote stress σ^{∞} can be isolated in each part of Eq. 3.19, which gives

$$\begin{cases} \sigma^{\infty} \cdot (\Sigma T - \kappa \cdot T_{\mathcal{B}}) = \dfrac{4 \cdot \Sigma T}{\Sigma T - \Delta T} \cdot \dfrac{G^{\mathrm{m}} \cdot \gamma_0}{\lambda} \cdot \sinh(\lambda \cdot L_{\mathrm{R}}), \\ \sigma^{\infty} \cdot (\Sigma T + \kappa \cdot T_{\mathcal{A}}) = \dfrac{4 \cdot \Sigma T}{\Sigma T + \Delta T} \cdot \dfrac{G^{\mathrm{m}} \cdot \gamma_0}{\lambda} \cdot \sinh(\lambda \cdot L_{\mathrm{L}}). \end{cases} \tag{3.20}$$

Equalising the two expressions for σ^{∞} in Eq. 3.20 and using the definitions of $T_{\mathcal{A}}$, $T_{\mathcal{B}}$ (Eq. 3.3) and κ (Eq. 3.8) yields

$$\frac{\sinh(\lambda \cdot L_{\mathrm{R}})}{\sinh(\lambda \cdot L_{\mathrm{L}})} = \frac{K_{\mathcal{A}}}{K_{\mathcal{B}}} = \eta. \tag{3.21}$$

Using the relationship $L_{\mathrm{L}} + L_{\mathrm{R}} = 2 \cdot L$, Eq. 3.21 can be solved to find the location of the characteristic point:

$$L_{\mathrm{L}} = \frac{1}{2 \cdot \lambda} \cdot \log \left[\frac{\eta + \exp(2 \cdot \lambda \cdot L)}{\eta + \exp(-2 \cdot \lambda \cdot L)} \right]. \tag{3.22}$$

3.2.6 Calculation of the Young's modulus

The remote stress σ^{∞} can now be derived from the second line of Eq. 3.20:

$$\begin{aligned} \sigma^{\infty} &= -\left[\sigma^{\infty} \cdot \kappa + \frac{4 \cdot \Sigma T}{\Sigma T^2 - \Delta T^2} \cdot \frac{\gamma_0 \cdot G^{\mathrm{m}}}{\lambda} \cdot \sinh(-\lambda \cdot L_{\mathrm{L}}) \right] \cdot \frac{T_{\mathcal{A}}}{\Sigma T} \\ \Rightarrow \sigma^{\infty} &= \frac{\gamma_0 \cdot G^{\mathrm{m}} \cdot \Sigma T}{\lambda \cdot T_{\mathcal{B}}} \cdot \frac{\sinh(\lambda \cdot L_{\mathrm{L}})}{\Sigma T + \kappa \cdot T_{\mathcal{A}}}. \end{aligned} \tag{3.23}$$

Knowing σ^{∞} and ε^{∞} from Eqs. 3.23 and 3.18, and γ_{L} and γ_{R} from Eqs. 3.9b and 3.22, the overall Young's modulus of the composite is a function of the geometry of the microstructure and the mechanical properties of the platelets and the matrix, defined by

$$E^{\mathcal{C}} = \frac{\sigma^{\infty}}{\varepsilon^{\infty}} = \bar{E} \cdot \frac{\beta}{1 + \frac{\delta}{\lambda \cdot L \cdot \tanh(\lambda \cdot L_{\mathrm{L}})}},$$

$$\text{where} \quad \begin{cases} \beta = & 1 + \frac{\Delta E \cdot \Delta T}{\Sigma E \cdot \Sigma T}, \\ \delta = & \frac{1}{2}\left[\frac{1}{\eta} + \cosh(2 \cdot \lambda \cdot L) \right. \\ & \left. - \sinh(2 \cdot \lambda \cdot L) \cdot \tanh(\lambda \cdot L_{\mathrm{L}}) \right], \end{cases} \tag{3.24}$$

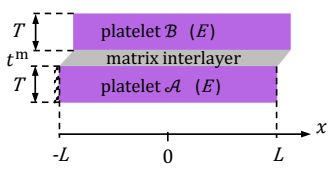
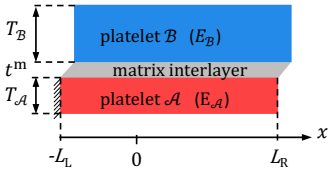
and where $\bar{E}$ is the RoM Young's modulus as defined in Eq. 3.3. This expression of the composite Young's modulus is compared to the one derived for non-hybrid brick-and-mortar composites in Tab. 3.1 (see App. C and [24]).

3.3 Model development for hybrid aligned discontinuous-fibre architectures

3.3.1 Idealised microstructure of hybrid aligned-fibre discontinuous composites

This section uses the model described in Sec. 3.2 to calculate the Young's modulus of aligned hybrid discontinuous composites with a more realistic architecture, featuring

Table 3.1: Comparison of main results between the model for non-hybrid BaM composites [24] and the current model for HyBaM composites.

	Non-hybrid [24]	Hybrid
Unit-cell:		
Differential equation:		
$\frac{d^2\Delta\sigma(x)}{dx^2} = \lambda^2 \cdot [\Delta\sigma(x) - \kappa \cdot \sigma^\infty]$ (a)	$\begin{cases} \kappa = 0 \\ \lambda = \sqrt{\frac{2 \cdot G^m}{t^m \cdot K}} \end{cases}$	$\begin{cases} \kappa = \frac{\Delta E \cdot \Sigma T}{\Sigma K} \\ \lambda = \sqrt{\frac{2 \cdot G^m}{t^m \cdot \tilde{K}}} \end{cases}$
Young's modulus:		
$E^c = \bar{E} \cdot \frac{\beta}{1 + \frac{\delta}{\lambda \cdot L \cdot \tanh(\lambda \cdot L_L)}}$ (b)	$\begin{cases} \beta = 1 \\ \delta = 1 \end{cases}$	$\begin{cases} \beta = 1 + \frac{\Delta E \cdot \Delta T}{\Sigma E \cdot \Sigma T} \\ \delta = \frac{1}{2}\left[\frac{1}{\eta} + \cosh(2 \cdot \lambda \cdot L)\right. \\ \qquad \left. - \sinh(2 \cdot \lambda \cdot L) \cdot \tanh(\lambda \cdot L_L)\right] \end{cases}$

circular fibres, random locations of fibre-ends, and random intermingling of fibre-types. To do so, the model developed in Chapter 2 is adapted as follows:

- The largest scale consists of an *RVE* whose cross-section contains a grid of *fibres* of types $\mathcal{A}$ and $\mathcal{B}$, arranged in parallel in a square packing (see Fig. 3.2a). Here, it is important to understand that the grid defining the RVE is only used to identify neighbouring fibres and interactions; this grid does not aim to represent the physical microstructure (like a FE simulation would do), and it is not used to define geometrical parameters (such as fibre spacing or matrix thickness).

  The length of the RVE is equal to the fibre length l^f, and fibre-ends are randomly located (Fig. 3.2a). The model assumes that there is no longitudinal gap between two consecutive fibres in the fibre direction (i.e. a fibre ends where the next fibre starts); this is a reasonable assumption for composites with moderate to high fibre content, where the reduction of overlap lengths due to the longitudinal gap between fibres is negligible (when compared to the average overlap length $l^f/4$).

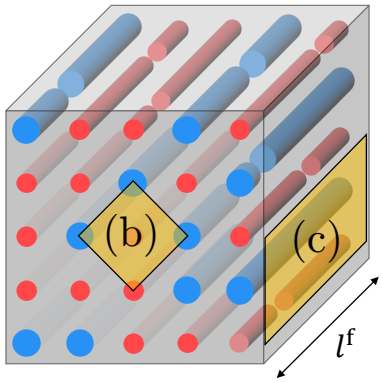
- Contrarily to the model developed for HyBaM composites in Sec. 3.2, in this model for discontinuous-fibre hybrids the volume ratio of each fibre type is controlled by the number of fibres of each type in the RVE. From the volume-ratio of each fibre type ($V_\mathcal{A}$ and $V_\mathcal{B}$, with $V_\mathcal{A} + V_\mathcal{B} = 1$) and the fibre diameters $\phi_\mathcal{A}$ and $\phi_\mathcal{B}$, it is possible to define $N_\mathcal{A}$ and $N_\mathcal{B}$ as the number-ratios of fibres of types $\mathcal{A}$

and $\mathcal{B}$ respectively:

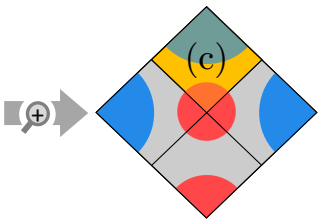
$$N_{\mathcal{A}} = \frac{1}{1 + \frac{V_{\mathcal{B}}}{V_{\mathcal{A}}} \cdot \left(\frac{\phi_{\mathcal{A}}}{\phi_{\mathcal{B}}}\right)^2} \text{ and } N_{\mathcal{B}} = \frac{1}{1 + \frac{V_{\mathcal{A}}}{V_{\mathcal{B}}} \cdot \left(\frac{\phi_{\mathcal{B}}}{\phi_{\mathcal{A}}}\right)^2}, \text{ with } N_{\mathcal{A}} + N_{\mathcal{B}} = 1. \quad (3.25)$$

The type of each fibre ($\mathcal{A}$ or $\mathcal{B}$) is randomly allocated to each position of the grid, in order to match the desired number-ratios $N_{\mathcal{A}}$ and $N_{\mathcal{B}}$ of each fibre type in the cross-section of the RVE.

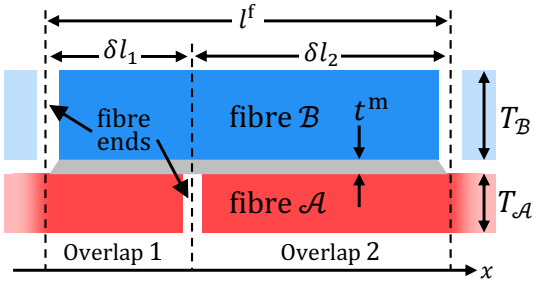
- Each quarter-*fibre* interacts with one of its four neighbouring fibres through an *interaction* (Fig. 3.2b). Each *interaction* is made of two shear-lag *overlaps* of length δl_1 and δl_2 (Fig. 3.2c); the length of Overlap 1 (δl_1) is randomly sampled from a uniform distribution between zero and l^{f}, and the length of Overlap 2 is



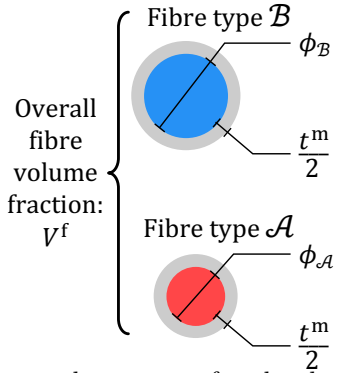
(a) Full 3D structure of the RVE.



(b) Central fibre and the four interactions with its four neighbouring fibres.



(c) Interaction between two fibres made of two overlaps 1 and 2.



(d) Assumed geometry for the derivation of t^{m}.

Figure 3.2: Overview of the different scales present in the model for aligned hybrid discontinuous composites.



(a) Indices defining the interactions involving fibre (i, j) (in the middle). Subscripts H and V are used respectively for horizontal and vertical interactions. Indices $i \in \{1, ..., n-1\}$ and $j \in \{1, ..., n\}$ for vertical interactions, and $i \in \{1, ..., n\}$ and $j \in \{1, ..., n-1\}$ for horizontal interactions.

(b) Indices defining the fibres and their neighbours, with $i \in \{1, ..., n\}$ and $j \in \{1, ..., n\}$.

Figure 3.3: Indexing system of the fibres and interactions in the RVE model.

$\delta l_2 = l^{\mathrm{f}} - \delta l_1$. The effective Young's moduli of the two overlaps can be found by applying the shear-lag model presented in Sec. 3.2, along with the following changes:

$$\begin{aligned} T_{\mathcal{A}} &= \frac{\phi^{\mathrm{f}}_{\mathcal{A}}}{4} \text{ and } T_{\mathcal{B}} = \frac{\phi^{\mathrm{f}}_{\mathcal{B}}}{4}, \\ L_1 &= \frac{\delta l_1}{2} \text{ (Overlap 1) and } L_2 = \frac{\delta l_2}{2} \text{ (Overlap 2).} \end{aligned} \tag{3.26}$$

In Eq. 3.26, the value of the characteristic thickness T of a quarter-fibre in one interaction is calculated as the ratio between the cross-section of the quarter-fibre resisting to tensile stresses ($\pi \cdot (\phi^{\mathrm{f}})^2/16$) and the quarter-fibre perimeter transferring shear stress ($\pi \cdot \phi^{\mathrm{f}}/4$).

For the shear-lag model, it is assumed that each fibre – either of type $\mathcal{A}$ or $\mathcal{B}$ – is surrounded by a matrix layer of uniform thickness t^{m} (see Fig. 3.2d); this enables one to consider hybridisation of fibres with very different diameters. As a result, imposing a total fibre volume fraction V^{f} in the composite leads to

$$\begin{aligned} V^{\mathrm{f}} &= \frac{N_{\mathcal{A}} \cdot \phi^2_{\mathcal{A}} + N_{\mathcal{B}} \cdot \phi^2_{\mathcal{B}}}{N_{\mathcal{A}} \cdot (\phi_{\mathcal{A}} + t^{\mathrm{m}})^2 + N_{\mathcal{B}} \cdot (\phi_{\mathcal{B}} + t^{\mathrm{m}})^2}, \quad \text{and therefore} \\ t^{\mathrm{m}} &= \sqrt{\frac{1}{V^{\mathrm{f}}} \cdot (N_{\mathcal{A}} \cdot \phi^2_{\mathcal{A}} + N_{\mathcal{B}} \cdot \phi^2_{\mathcal{B}}) - (N_{\mathcal{A}} \cdot N_{\mathcal{B}}) \cdot (\phi_{\mathcal{A}} - \phi_{\mathcal{B}})^2} - N_{\mathcal{A}} \cdot \phi_{\mathcal{A}} - N_{\mathcal{B}} \cdot \phi_{\mathcal{B}}. \end{aligned} \tag{3.27}$$

This definition of t^{m} is independent of the arrangement of the fibres in the RVE grid, and allows the fibre volume fraction to reach very high values even if the two fibres types have significantly different diameters (as could happen in reality). Moreover, the matrix thickness t^{m} defined in Eq. 3.27 is the same for all interac-

tions in a given composite, and is assumed to be uniform along the perimeter of the fibre, as done in most models in literature [94–96].

3.3.2 RVE model

A first option to calculate the Young's modulus of hybrid discontinuous aligned-fibre composites is to actually simulate the full microstructure of the composite. To do so, the RVE's cross-section is considered to be a square containing $n \times n$ fibres. Consequently, each fibre and interaction can be defined by their location (i, j) within the cross-section (see Figs. 3.3a and 3.3b). Each fibre is involved in two horizontal (subscript H) and two vertical (subscript V) interactions.

In an interaction (i, j), the effective Young's moduli of its two overlaps $E_1^{\mathrm{O}}(i, j)$ and $E_2^{\mathrm{O}}(i, j)$ can be calculated from Eq. 3.24 (see Sec. 3.2 and Fig. 3.2c); the two overlaps are subsequently combined in series to obtain the Young's modulus of the interaction E^{I}:

$$E^{\mathrm{I}}(i,j) = \frac{1}{\dfrac{\delta l_1}{E_1^{\mathrm{O}}(i,j)} + \dfrac{\delta l_2}{E_2^{\mathrm{O}}(i,j)}}. \tag{3.28}$$

Note that this formulation is applied to both hybrid ($\mathcal{AB}$) and non-hybrid ($\mathcal{AA}/\mathcal{BB}$) interactions.

Finally, the Young's modulus of the discontinuous hybrid composite $E^{\mathcal{C}}$ is calculated by combining all horizontal and vertical interactions (i, j) in parallel, weighted by their respective cross-section areas:

$$E^{\mathcal{C}} = \frac{\sum_{i,j} E^{\mathrm{I}}(i,j) \cdot \mathcal{A}^{\mathrm{I}}(i,j)}{\sum_{i,j} \mathcal{A}^{\mathrm{I}}(i,j)}, \tag{3.29}$$

where the area of an interaction $\mathcal{A}^{\mathrm{I}}$ between two fibres is either $\mathcal{A}^{\mathrm{I}}_{\mathcal{AA}} = \pi \cdot \phi_{\mathcal{A}}^2 / \left(8 \cdot V^{\mathrm{f}}\right)$, $\mathcal{A}^{\mathrm{I}}_{\mathcal{BB}} = \pi \cdot \phi_{\mathcal{B}}^2 / \left(8 \cdot V^{\mathrm{f}}\right)$, or $\mathcal{A}^{\mathrm{I}}_{\mathcal{AB}} = \pi \cdot \left(\phi_{\mathcal{A}}^2 + \phi_{\mathcal{B}}^2\right) / \left(16 \cdot V^{\mathrm{f}}\right)$ (see Fig. 3.2d).

3.3.3 Analytical model

Assuming the RVE to be sufficiently large compared to the fibre/interaction scales, it is possible to consider analytical statistical distributions for the two stochastic variables characterising an interaction: (i) the type of the two fibres ($\mathcal{A}$ or $\mathcal{B}$) and (ii) the overlap length δl_1. This enables one to calculate the expected value of the Young's modulus of hybrid-fibre aligned discontinuous composites analytically, as described in this section.

3.3.3.1 Probability of occurrence of the different interactions $\mathcal{AA}$, $\mathcal{AB}$, $\mathcal{BB}$

As the RVE is assumed to be large compared to the fibre scale, finding the probability of occurrence of the three possible types of interactions ($\mathcal{AA}$, $\mathcal{AB}$ and $\mathcal{BB}$) is equivalent to the probability of sampling the type of two random fibres in the composite. This leads to the following probabilities:

$$\begin{aligned} \mathbb{P}_{\mathcal{AA}} &= N_{\mathcal{A}}^2, && \text{probability of occurrence of an interaction } \mathcal{AA}, \\ \mathbb{P}_{\mathcal{AB}} &= 2 \cdot N_{\mathcal{A}} \cdot N_{\mathcal{B}}, && \text{probability of occurrence of an interaction } \mathcal{AB}, \\ \mathbb{P}_{\mathcal{BB}} &= N_{\mathcal{B}}^2, && \text{probability of occurrence of an interaction } \mathcal{BB}. \end{aligned} \tag{3.30}$$

From Eq. 3.25, one can verify that $\mathbb{P}_{\mathcal{AA}} + \mathbb{P}_{\mathcal{AB}} + \mathbb{P}_{\mathcal{BB}} = (N_{\mathcal{A}} + N_{\mathcal{B}})^2 = 1$.

3.3.3.2 Young's modulus for the interaction between two fibres with randomly-located fibre-ends

For a fixed fibre length l^{f} and for a given type of interaction ($\mathcal{AA}$, $\mathcal{AB}$ or $\mathcal{BB}$, generally represented by $**$), the analytical expression for the effective Young's modulus derived in Eq. 3.24 can be expressed as a function of the ratio $\rho = \delta l_1 / l^{\mathrm{f}}$, with $\rho \in [0,\ 1]$, uniformly distributed (see Fig. 3.2c). From Eqs. 3.22 and 3.24, the effective Young's modulus of an overlap can be expressed as

$$E_{**}^{\mathrm{O}}(\rho) = \bar{E} \cdot \frac{\beta}{1 + \dfrac{2 \cdot \delta(\rho)}{\lambda \cdot \rho \cdot l^{\mathrm{f}} \cdot \tanh(\lambda \cdot L_{\mathrm{L}}(\rho))}},$$

$$\text{with} \begin{cases} \beta = & 1 + \dfrac{\Delta E \cdot \Delta T}{\Sigma E \cdot \Sigma T}, \\ \delta(\rho) = & \dfrac{1}{2}\left[\dfrac{1}{\eta} + \cosh(\lambda \cdot \rho \cdot l^{\mathrm{f}}) \right. \\ & \left. - \sinh(\lambda \cdot \rho \cdot l^{\mathrm{f}}) \cdot \tanh(\lambda \cdot L_{\mathrm{L}}(\rho))\right], \\ L_{\mathrm{L}}(\rho) = & \dfrac{1}{2 \cdot \lambda} \cdot \log\left[\dfrac{\eta + \exp(\lambda \cdot \rho \cdot l^{\mathrm{f}})}{\eta + \exp(\lambda \cdot \rho \cdot l^{\mathrm{f}})}\right], \end{cases} \tag{3.31}$$

where $\bar{E}$, η, λ, ΔE, ΣE, ΔT, ΣT are parameters fixed for a given interaction $**$ (see Sec. 3.2). Note that, in Eq. 3.31, δ and L_{L} both become functions of ρ, as the length of Overlap 1 ($\delta l_1 = \rho \cdot l^{\mathrm{f}}$) of each interaction is now a statistical variable. Consequently, the effective Young's modulus of an interaction E_{**}^{I} can be calculated by combining the two overlaps (Overlap 1 with ratio ρ and Overlap 2 with ratio $1 - \rho$) in series:

$$E_{**}^{\mathrm{I}}(\rho) = \frac{1}{\dfrac{\rho}{E_{**}^{\mathrm{O}}(\rho)} + \dfrac{1-\rho}{E_{**}^{\mathrm{O}}(1-\rho)}}. \tag{3.32}$$

3.3.3.3 Expression for the Young's modulus of a hybrid discontinuous composite

The average effective Young's modulus of an interaction of type $**$ can be found by integrating $E^{\mathrm{I}}_{**}(\rho)$ with respect to ρ:

$$\bar{E}^{\mathrm{I}}_{**} = \int_{\rho=0}^{1} E^{\mathrm{I}}_{**}(\rho)\mathrm{d}\rho \ , \quad \text{which can be evaluated numerically.} \tag{3.33}$$

Finally, the expected Young's modulus of an HADC ($E^{\mathcal{C}}$) can be calculated by combining the three types of interactions ($\mathcal{AA}$, $\mathcal{AB}$ and $\mathcal{BB}$) in parallel, weighted by their probability of occurrence in the composite and their respective cross-section areas:

$$E^{\mathcal{C}} = V^{\mathrm{f}} \cdot \frac{\mathbb{P}_{\mathcal{AA}} \cdot \phi^2_{\mathcal{A}} \cdot \bar{E}^{\mathrm{I}}_{\mathcal{AA}} + \mathbb{P}_{\mathcal{AB}} \cdot \left(\phi^2_{\mathcal{A}} + \phi^2_{\mathcal{B}}\right)/2 \cdot \bar{E}^{\mathrm{I}}_{\mathcal{AB}} + \mathbb{P}_{\mathcal{BB}} \cdot \phi^2_{\mathcal{B}} \cdot \bar{E}^{\mathrm{I}}_{\mathcal{BB}}}{\mathbb{P}_{\mathcal{AA}} \cdot \phi^2_{\mathcal{A}} + \mathbb{P}_{\mathcal{AB}} \cdot \left(\phi^2_{\mathcal{A}} + \phi^2_{\mathcal{B}}\right)/2 + \mathbb{P}_{\mathcal{BB}} \cdot \phi^2_{\mathcal{B}}}. \tag{3.34}$$

3.4 Results

This section presents the results from the models developed in the two previous sections. Some of the results are compared with several rules-of-mixtures for hybrid composites, which are defined in App. D.

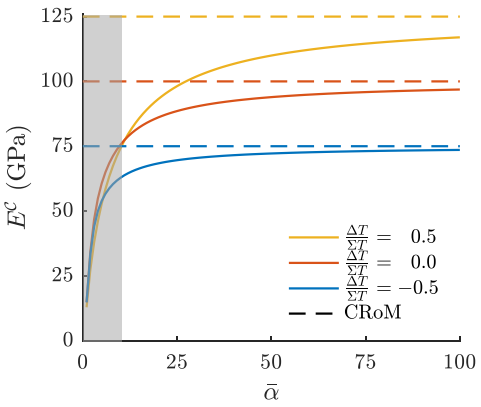
3.4.1 Hybrid brick-and-mortar composites

The model derived in Sec. 3.2 was used to calculate the Young's modulus $E^{\mathcal{C}}$ of HyBaM composites. The standard inputs for the model (which fully define all variables required) are defined in Tab. 3.2, and results are shown in Figs. 3.4 and 3.5.

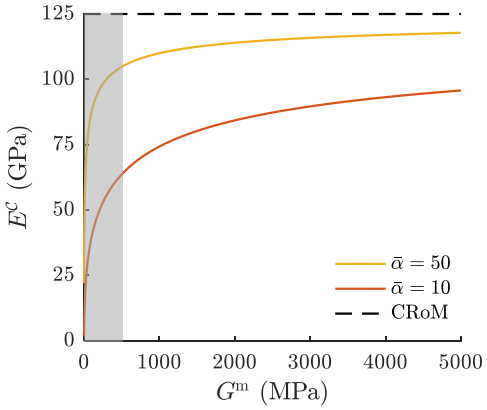
Due to the shear-lag assumptions of the model, the results shown in Figs. 3.4 and 3.5 are not physically meaningful for small aspect ratios, small values of G^{m}, and for $\frac{\Delta E}{\Sigma E} \to \pm 1$ or $\frac{\Delta T}{\Sigma T} \to \pm 1$ (meaning that either $K_{\mathcal{A}}$ or $K_{\mathcal{B}}$ converge towards 0). These regions where model results are mathematically correct but not physically meaningful are shown by shaded areas in Figs. 3.4 and 3.5.

Table 3.2: Inputs for the standard configuration (geometry and mechanical properties of the platelets and the matrix) of the HyBaM composites studied in Sec. 3.4.1.

Parameter	L (mm)	$\bar{T}$ (mm)	t^{m} (mm)	G^{m} (MPa)	$\bar{E}$ (GPa)
Value	1.0	0.1	0.01	1000	100

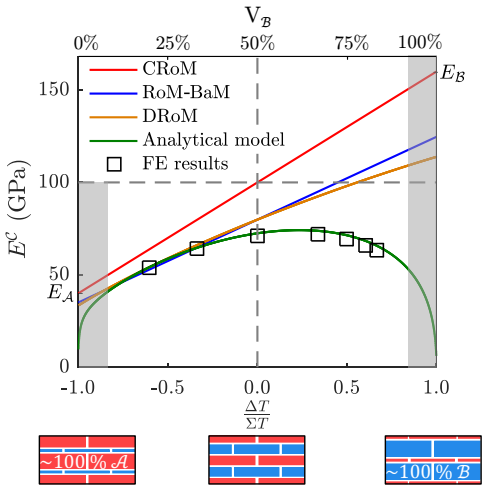


(a) Effect of average platelet aspect-ratio on $E^{\mathcal{C}}$. $\frac{\Delta E}{\Sigma E} = 0.5$.

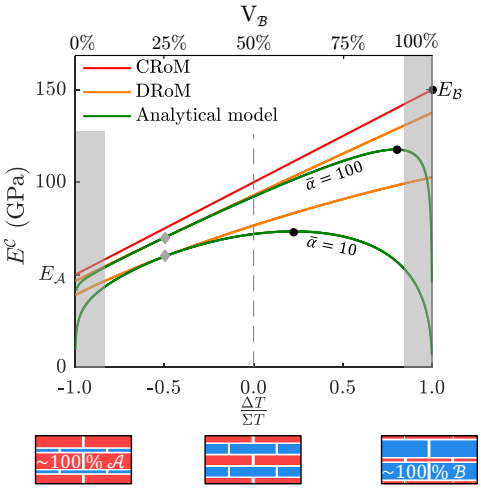


(b) Effect of the matrix shear modulus on $E^{\mathcal{C}}$. $\frac{\Delta E}{\Sigma E} = 0.5$.

Figure 3.4: Effects of global parameters on the overall Young's modulus of a HyBaM composite. (See Eq. 3.3 for the definition of $\frac{\Delta E}{\Sigma E}$).



(a) Comparison of the analytical model against the rules-of-mixtures and FE solutions, for $\bar{\alpha} = 10$ and $\frac{\Delta E}{\Sigma E} = 0.6$.



(b) Convergence of $E^{\mathcal{C}}$ toward the rules-of-mixtures with increasing $\bar{\alpha}$, for $\frac{\Delta E}{\Sigma E} = 0.5$. Black points represent the maximum stiffness, and grey diamonds show the configurations at which the analytical model coincides with the DRoM, corresponding to $\frac{\Delta T}{\Sigma T} = -\frac{\Delta E}{\Sigma E}$, or $K_{\mathcal{A}} = K_{\mathcal{B}}$.

Figure 3.5: Effect of hybridisation on the Young's modulus of HyBaM composites. The RoMs are defined in App. D, and details on the FE validation are given in App. E. (See Eq. 3.3 for the definition of $\frac{\Delta E}{\Sigma E}$ and $\frac{\Delta T}{\Sigma T}$).

3.4.1.1 Effect of discontinuities in a hybrid brick-and-mortar composite

Fig. 3.4a shows the evolution of the Young's modulus of a hybrid brick-and-mortar composite $E^{\mathcal{C}}$ with the average aspect ratio $\bar{\alpha} = L/\bar{T}$, for different hybrid configurations (each defined by a given value of $\frac{\Delta T}{\Sigma T}$, and with $\frac{\Delta E}{\Sigma E} = 0.5$). For each configuration, when $\bar{\alpha}$ increases, the Young's modulus of the composite increases and converges to that predicted by the Continuous Rule-of-Mixtures (CRoM, see App. D), following an exponential trend; however, the rate of convergence decreases as the stiffer platelet becomes thicker (see line for $\frac{\Delta T}{\Sigma T} = 0.5$ in Fig. 3.4a).

Fig. 3.4b shows the evolution of the composite Young's modulus $E^{\mathcal{C}}$ with the matrix shear modulus G^{m}, for different aspect ratios $\bar{\alpha}$. This graph shows that the composite Young's modulus is strongly dependent on the stiffness of the matrix, especially for short platelets (small $\bar{\alpha}$).

3.4.1.2 Hybrid effect depending on the difference of thickness and of Young's modulus between the two types of platelets

The effect of the difference in platelet thickness ($\frac{\Delta T}{\Sigma T}$) and platelet Young's modulus ($\frac{\Delta E}{\Sigma E}$) on the Young's modulus of HyBaM composites is studied in Figs. 3.5. All plots display the Young's modulus of the HyBaM composite against the platelet thickness ratio $\frac{\Delta T}{\Sigma T}$, so that the left-hand side of the plot corresponds to $T_{\mathcal{B}} = 0$ (i.e. $\frac{\Delta T}{\Sigma T} = -1$, no type-$\mathcal{B}$ platelet), while the right-hand side corresponds to $T_{\mathcal{A}} = 0$ (i.e. $\frac{\Delta T}{\Sigma T} = +1$, no type-$\mathcal{A}$ platelet); the sum (or average) of the thickness of the two platelets is kept constant at $\Sigma T = 0.2$ mm ($\bar{T} = 0.1$ mm). For the inputs defined in Tab. 3.2, selecting a given $\frac{\Delta T}{\Sigma T}$ directly defines the volume ratio of each platelet type (for instance, $V_{\mathcal{B}} = 1/2 \cdot (1 + \frac{\Delta T}{\Sigma T})$); for this reason, the plots in Fig. 3.5 also show the volume fraction of $\mathcal{B}$-platelets in the x-axis. However, it must be clear that, for the HyBaM microstructure, this fraction is controlled by the relative thickness (and not by the number) of the two platelets; in contrast, the volume fraction of $\mathcal{B}$-fibres in the intermingled composite (Secs. 3.3 and 3.4.2) will be controlled by the relative number of the two fibre-types (each with a fixed diameter).

Figs. 3.5a and 3.5b display the Young's modulus of hybrid brick-and-mortar composites calculated by different rules-of-mixtures (see App. D), the present analytical model (see Eq. 3.24), and FE simulations (see App. E). The following observations can be made:

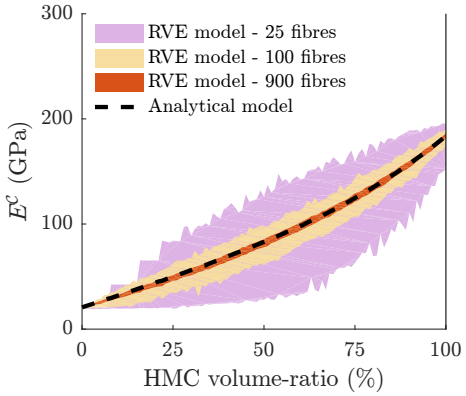
- The CRoM (Continuous Rule-of-Mixtures) approximation returns a linear interpolation between the Young's moduli of the platelets $E_{\mathcal{A}}$ and $E_{\mathcal{B}}$, and does not account for discontinuities in the platelets (see Fig. 3.5a);

- The RoM-BaM (Rule-of-Mixtures for Brick-and-Mortar) interpolates linearly between the Young's moduli of non-hybrid BaM composites with platelets of type $\mathcal{A}$ or $\mathcal{B}$, and uniform characteristic thickness $T_\mathcal{A} = T_\mathcal{B} = \bar{T}$. Accounting for the discontinuities of the platelets reduces the composite's Young's modulus, especially for stiffer platelets (compare the results for CRoM and RoM-BaM in Fig. 3.5a);
- The DRoM (Discontinuous Rule-of-Mixtures) accounts for the actual platelet thicknesses ($T_\mathcal{A}$ and $T_\mathcal{B}$) at each value of $\frac{\Delta T}{\Sigma T}$, and is therefore not linear (see Figs. 3.5a and 3.5b). Consequently, the end-points of the DRoM curve (corresponding to $T_\mathcal{A} = \Sigma T$ or $T_\mathcal{B} = \Sigma T$) are slightly different to those of the RoM-BaM (corresponding to $T_\mathcal{A} = \bar{T}$ or $T_\mathcal{B} = \bar{T}$);
- The analytical model returns Young's moduli converging to zero for $T_\mathcal{A} \to 0$ or $T_\mathcal{B} \to 0$ (see Figs. 3.5a and 3.5b). In these cases, one of the platelets becomes too thin for stress to be built-up and transferred between the two different platelets effectively, which leads to a complete loss of stiffness in the composite; these cases are not realistic and would not be observed in real composite microstructures.
- The analytical model predicts a significant hybrid effect on the Young's modulus of HyBaM composites, which strongly deviates from the RoMs (especially for small aspect ratios, see $\bar{\alpha} = 10$ in Fig. 3.5b), but agrees with FE simulations (see Fig. 3.5a). In particular, unlike the RoMs, the actual Young's modulus of the composite does not increase monotonically with $\frac{\Delta T}{\Sigma T}$, and the configuration which maximises the Young's modulus of the composite is $\frac{\Delta T}{\Sigma T} < 1$;
- The analytical model predicts composite Young's moduli always lower than those predicted by the CRoM, and converges towards the CRoM only when the platelets become infinitely long (see Fig.3.5b). In this case only ($\bar{\alpha} \to \infty$), the Young's modulus of the HyBaM composite is maximised when $\frac{\Delta T}{\Sigma T} \to 1$ (i.e. when the softer platelets become infinitely thin).
- The analytical model predicts a lower Young's modulus of HyBaM composites than the DRoM, for all values of $\frac{\Delta T}{\Sigma T} \neq -\frac{\Delta E}{\Sigma E}$ (see Fig. 3.5b). At $\frac{\Delta T}{\Sigma T} = -\frac{\Delta E}{\Sigma E}$, the difference in platelet thicknesses is balanced by a symmetric difference in the Young's moduli of the platelets, so that the two platelet types have the same overall stiffness $K_\mathcal{A} = K_\mathcal{B} = \bar{K} = \bar{T} \cdot \bar{E}$.

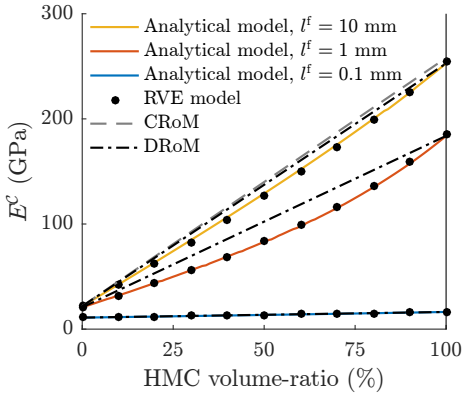
3.4.2 Hybrid aligned-fibre discontinuous composites

3.4.2.1 Parametric study on aligned-fibre discontinuous composites

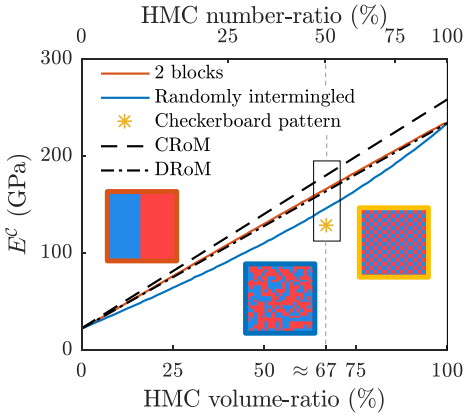
The RVE model proposed for hybrid aligned-fibre discontinuous composites (see Sec. 3.3.2) is compared against the analytical model (see Sec. 3.3.3) in Figs. 3.6a and 3.6b (see material properties in Tab. 3.3). Fig. 3.6a shows that, for a low number of



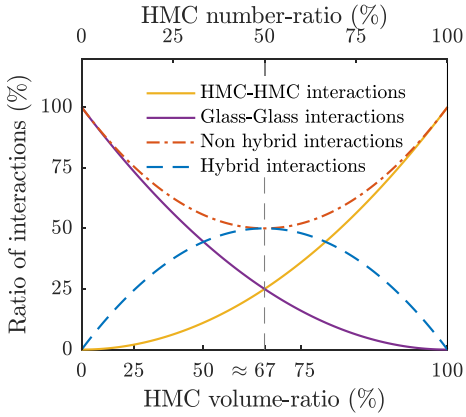
(a) Scatter in the composite Young's modulus for 1000 predictions of the RVE model, for different RVE sizes, compared with the analytical model ($l^f = 1$ mm).



(b) Comparison of the predictions of the different models (DRoM, RVE and full analytical model), for different fibre lengths.



(c) Effect of the fibre architecture on the Young's modulus of HADCs ($l^f = 3$ mm).



(d) Distribution of interactions vs. HMC volume-ratio (top scale) and HMC fibre-ratio (bottom scale) for a randomly intermingled hybrid composite.

Figure 3.6: Evolution of the Young's modulus of a hybrid HMC-Glass discontinuous composite with the volume ratio of the stiffer fibre type (HMC). For this parametric study, the standard properties of the fibres are listed in Tab. 3.3 (with overall fibre volume fraction $V^f = 30\%$), and changes in fibre length are specified in the plots.

fibres in the RVE, the Young's modulus of hybrid discontinuous composites predicted by the RVE model presents a high variability; however, the results of the RVE model converge towards the analytical model as the RVE simulated gets larger (a good agreement is found for 900 or more fibres ($n \geq 30$) in the RVE model). This good agreement between the RVE and analytical model is verified for both long and short fibres (see Fig. 3.6b)

Fig. 3.6c shows that, for a fixed combination of fibre types (with given length, diameters and Young's moduli), the fibre architecture within the RVE has an effect on the Young's modulus of the composite. The composite with fibres arranged in a checkerboard pattern has the lowest Young's modulus, while the composite with the two fibre-types clustered in two separated blocks has the maximum stiffness (which matches the one predicted by the DRoM).

3.4.2.2 Experimental validation

The predictions of the RVE model have been compared against experimental results provided by HaNa Yu and Marco L. Longana from the University of Bristol [84, 86], as shown in Fig. 3.7. The specimens were manufactured through the HiPerDif method [29, 73], and the specifications of the hybrid discontinuous composites are given in Tab. 3.3; the overall fibre volume fraction was estimated to be $30-35\%$, and therefore predictions are plotted for these two values.

Moreover, although the HiPerDif method provides a very good level of fibre alignment when compared to previous manufacturing methods [73, 97], there is still a small degree of fibre misalignment in the specimens. Consequently, a method based on the laminate plate analogue [90, 91] is used to calculate the Young's modulus of hybrid discontinuous composites, with a given fibre orientation distribution, as explained in App. F. The model results shown in Figs. 3.7a and 3.7b are thus corrected for the fibre

Table 3.3: Properties of the fibres and matrix used as input for the 3D intermingled model. The values of the fibre length l^{f} and the fibre diameter ϕ^{f} apply to the validation against experiments (Fig. 3.7) only, and vary in the parametric studies (Fig. 3.6).

Fibre properties	l^{f} (mm)	ϕ^{f} (µm)	E^{f} (GPa)
High Modulus Carbon (HMC)	3.0^{*}	10^{*}	860^{*}
High Strength Carbon (HSC)	3.0^{*}	7^{*}	225^{*}
Glass (G)	3.0^{*}	7^{*}	73^{*}

Composite/matrix properties	
G^{m} (GPa)	1.5^{**}
V^{f} (%)	$30-35^{**}$
$n \times n$	$\approx 7000^{**}$

$*$ Material properties found in literature [29].

$**$ Specifications of the experimental data given by HaNa Yu and Marco L. Longana from the University of Bristol [84].

orientation distribution (shown in Fig. 3.7c) obtained by Yu et al., using the HiPerDiF process [73].

It can be concluded that, for the fibre orientation distribution previously measured for the HiPerDiF process, the effect of fibre misalignment on the Young's modulus of the material produced is negligible. It should be noted that the method used here considers full stiffness matrices [90,91] (as detailed in Appendix F), and should therefore be more accurate than simpler methods which neglect the contribution of the transverse and shear moduli of misaligned fibres (as the latter, consequently, overpredict the stiffness loss due to small levels of misalignments [90, 91]). Nevertheless, Fig. 3.7d shows the potential effect that more severe misalignment levels would have on the Young's modulus of HADCs.

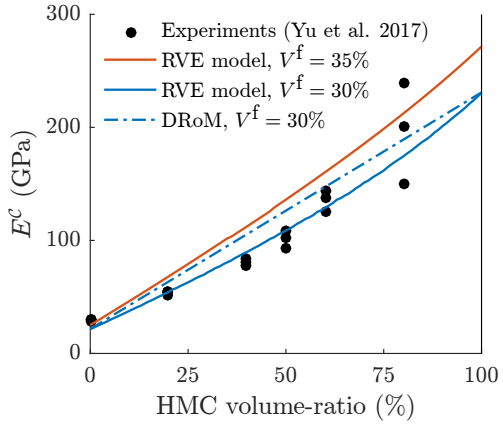
The full model developed in Sec. 3.3 predicts a non-linear trend in the relationship between the hybrid composite Young's modulus and the ratio of fibre types (Figs. 3.7a and 3.7b); although the experimental data contain only three measurements for each fibre-ratio and present a large amount of scatter, a similarly non-linear trend appears to be present as well. This non-linear hybrid effect cannot be captured by the DRoM; to quantify the improvement of the experimental fitting obtained with the full model, a normalised standard deviation was calculated between all N_{exp} experimental points and (i) the DRoM (Σ_{DRoM}), and (ii) the model developed in this chapter (Σ_{model}):

$$\begin{aligned} \Sigma_{\text{RoM}} &= \sqrt{\frac{1}{N_{\text{exp}}} \cdot \sum_{i=1}^{N_{\text{exp}}} \frac{(E_{\text{exp}}(i) - E_{\text{DRoM}}(i))^2}{E_{\text{exp}}(i)^2}}, \text{ and} \\ \Sigma_{\text{model}} &= \sqrt{\frac{1}{N_{\text{exp}}} \cdot \sum_{i=1}^{N_{\text{exp}}} \frac{(E_{\text{exp}}(i) - E_{\text{model}}(i))^2}{E_{\text{exp}}(i)^2}}. \end{aligned} \tag{3.35}$$

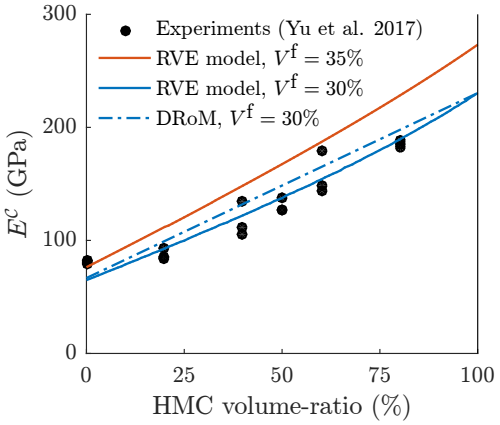
Eq. 3.35 returns the values $\Sigma_{\text{model}} = 0.109$ and $\Sigma_{\text{DRoM}} = 0.148$ for the HMC-HSC composite, and $\Sigma_{\text{model}} = 0.154$ and $\Sigma_{\text{DRoM}} = 0.233$ for the HMC-Glass composite. This suggests that, in both cases, the model better captures the trend of the Young's modulus with the HMC-volume ratio; it also shows that the DRoM becomes even less suitable for HMC-Glass than for the HMC-HSC composites, as the non-linear trend is more pronounced for the former (see Fig. 3.7).

Fig. 3.6a shows that the variability of the Young's modulus of the composite should be negligible for the specimen size used in the experiments ($\approx$ 7000 fibres in the cross-section, see Tab. 3.3). This implies that the variability found in the experiments cannot be explained by the finite size of the specimens alone, and is likely due to (i) variations of the overall fibre volume fraction V^{f}, (ii) variations of the HMC ratio, and (iii) variations on the misalignment of the fibres. To investigate this last hypothesis, three normal distributions of fibre misalignments were generated, based on experimental res-

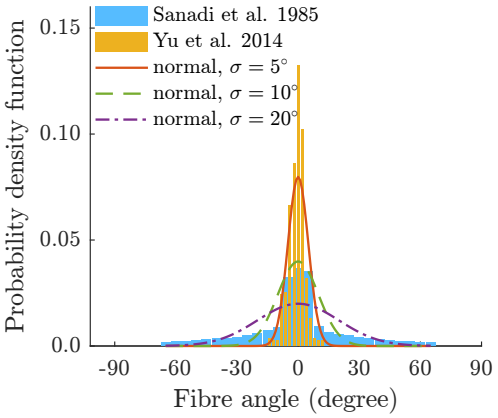
ults found in the literature (see Fig. 3.7c); their effect on the Young's modulus of hybrid discontinuous composites is shown in Fig. 3.7d. The results suggest that the effect of fibre misalignments on the Young's modulus of hybrid discontinuous composites becomes more pronounced when the proportion of high modulus fibres (HMC in this case) increases, which agrees with the experimental trend.



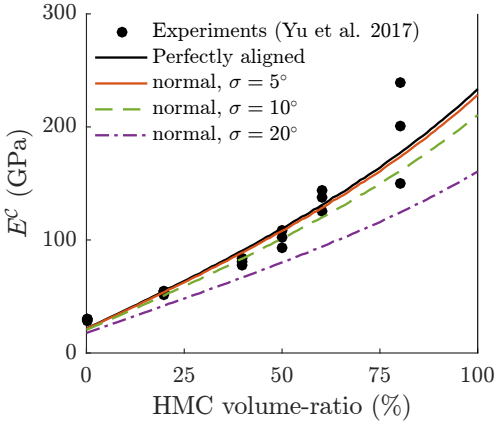
(a) HMC-Glass configuration.



(b) HMC-HSC configuration.



(c) Fibre alignment distributions from the literature [73, 97] and normal distributions with different standard deviations σ. The distribution from [73] shows in-plane angles, but the alignment method used causes through the thickness misalignments to be negligible.



(d) Effect of fibre misalignments on the stiffness of HMC-Glass discontinuous composites ($V^f = 30\%$).

Figure 3.7: Evolution of the Young's modulus with the volume ratio of the stiffer fibre type (HMC), and comparison between the results of the RVE model, the rules-of-mixtures, and experiments (material specifications given in Tab. 3.3). Model predictions in Figs. 3.7a and 3.7b include the effect of fibre misalignments, using the distribution measured by Yu et al. [73] shown in Fig. 3.7c.

3.5 Discussion

3.5.1 Influence of fibre-ends on the Young's modulus of aligned discontinuous composites

Results show that, even for a relatively large platelet or fibre aspect-ratio (e.g. $L/\bar{T} = 100$ and $l^{\mathrm{f}}/\phi^{\mathrm{f}} = 300$), the effect of fibre-ends on the Young's modulus of discontinuous composites is significant, particularly for stiffer fibres (see Fig. 3.4 and compare CRoM and DRoM in Fig. 3.5a for BaM, and compare CRoM and DRoM in Fig. 3.7 for intermingled composites). For instance, for a non-hybrid discontinuous composite made of 3 mm long HMC fibres, the proposed model predicts a Young's modulus of 230 GPa, which represents a significant reduction compared to the expected value of 261 GPa for *continuous*-fibre composites (as predicted by the rule-of-mixtures).

The presence of discontinuous fibres in the composite creates interactions between the fibres around the fibre-ends, where the load is transferred from a fibre to another through shear in the matrix. However, at fibre-sections far from the fibre-ends, an equilibrium is reached and stresses are not transferred through the matrix any more. This results in of two different behaviours:

- For short fibres, the entire length of a fibre is affected by fibre-ends. As a result, the overall Young's modulus of the composite is governed by the ability of the matrix to transmit load from a fibre to another, which explains the deviation of the actual Young's modulus of a non-hybrid discontinuous composite from that of a continuous-fibre composites (see for instance Fig. 3.6b for a HMC-ratio of 100% and $l^{\mathrm{f}} = 1$ mm). Moreover, increasing the fibre-to-matrix modulus ratio $E^{\mathrm{f}}/G^{\mathrm{m}}$ enlarges the region affected by fibre-ends (see Fig. 3.4b); therefore, increasing $E^{\mathrm{f}}/G^{\mathrm{m}}$ will have a similar effect to shortening the fibres, as both cases would increase the effects of fibre-ends;
- For long fibres (or lower $E^{\mathrm{f}}/G^{\mathrm{m}}$ ratio), the regions disturbed by fibre-ends are negligible, and the Young's modulus of the composite is mainly governed by the Young's modulus of the fibres. As a direct result, the Young's modulus of a discontinuous composite with long-fibres will converge to the one predicted by the rule-of-mixtures for continuous-fibre composite (see for instance Fig. 3.6b for a HMC-ratio of 100% and $l^{\mathrm{f}} = 10$ mm).

3.5.2 Influence of hybridisation on the Young's modulus of discontinuous composites

The analytical model for HyBaM composites always predicts a Young's modulus lower than the CRoM and the DRoM (see Fig. 3.5b). This is due to the fact that an overlap between two platelets can be divided in two parts, separated by the characteristic point (where the shear-strain of the matrix is minimum). In a non-hybrid composite, this characteristic point is located at the centre of the overlap, meaning that both parts of the overlap have the same length and, consequently, the same contribution towards the Young's modulus of the composite. However, in a hybrid overlap, the matrix shear strain is not minimum at the middle of each overlap, and therefore the overlap is split in two unequal lengths (Fig. 3.1b); as the Young's modulus grows non-linearly with the overlap length (Fig. 3.4a), the Young's modulus drop generated by the shorter part of the overlap will not be overcome by the smaller increase due to the longer part of the overlap. One can note that the proposed model will coincide with the DRoM only when the minimum shear strain of the matrix actually occurs at the middle of the overlap (i.e. when the stiffness of both platelets are equal ($K_{\mathcal{A}} = K_{\mathcal{B}}$), see grey diamonds in Fig. 3.5b).

Consequently, Fig. 3.6c shows that hybrid interactions (i.e. interactions between fibres of different types, see Fig. 3.6d) lower the stiffness of hybrid discontinuous composites and govern the corresponding hybrid effects. This is concluded because:

- the 2-blocks architecture has nearly no hybrid interactions, and its Young's modulus matches the prediction of the DRoM (i.e. no hybrid effect);
- the intermingled architecture has varying proportions of hybrid interactions (see Fig. 3.6d) and varying degrees of hybrid effects (relatively to the DRoM, see Fig. 3.6c), both showing the same trend (maximised at $V_{\mathrm{HMC}} = 67\%$, and minimised at $V_{\mathrm{HMC}} = 0$ or 100%);
- the checkerboard pattern has 100% hybrid interactions, and has the lowest stiffness as well as the largest hybrid effect (relatively to the DRoM) of all architectures studied in Fig. 3.6c.

This hybrid effect on the Young's modulus of hybrid discontinuous composites is also increased by increasing the difference between the Young's moduli of the two types of inclusion (the hybrid effect is more pronounced in Fig. 3.7a than in Fig. 3.7b), and by shortening the inclusions (compare $\bar{\alpha} = 100$ and $\bar{\alpha} = 10$ in Fig. 3.5b, and compare $l^{\mathrm{f}} = 1$ mm and $l^{\mathrm{f}} = 10$ mm in Fig. 3.6b).

The combined effect of discontinuities and hybridisation on the Young's modulus of composites is highlighted in Fig. 3.6c. For a randomly intermingled composite with a HMC volume-ratio of $\approx 67\%$, neglecting hybrid effects (compare results for randomly intermingled and DRoM in Fig. 3.6c) and the presence of discontinuities (compare

CRoM and DRoM in Fig. 3.6c) would lead to an overestimation of around 23% of the composite Young's modulus.

3.6 Conclusions

Shear-lag based analytical and numerical models were developed to calculate the Young's modulus of hybrid discontinuous composites, considering platelets/fibres with different cross-sections and different Young's moduli. Two different microstructures were modelled: one represents a hybrid, perfectly-staggered brick-and-mortar composite, and the other represents hybrid aligned discontinuous-fibre composites with random locations of fibre-ends. The following conclusions can be reached:

- Both brick-and-mortar and intermingled models agreed remarkably well with FE and experimental results. Also, the randomly-intermingled architecture of HADCs can be successfully modelled either through Monte Carlo analyses of RVE simulations (replicating the actual microstructure of the composite) or through an analytical statistical representation of the microstructure, as the two methods return similar results for sufficiently large composites (with more than 900 fibres in the cross-section).
- Fibre-ends may have a significant impact on the Young's modulus of hybrid and non-hybrid discontinuous composites. This effect is more pronounced for composites with shorter fibres, and with stiffer fibres and/or a softer matrix.
- A *negative hybrid effect* further reduces the Young's modulus of hybrid discontinuous composites below the predictions of the rules-of-mixtures, and leads to a non-linear relationship between the Young's modulus of the hybrid discontinuous composite and the volume-ratio of the two fibre types.
- The hybrid effect is amplified with (i) a higher Young's moduli difference between the two fibre types, (ii) shorter fibres, and (iii) an increase of the degree of intermingling in the hybrid discontinuous composite.

The RVE model presented in this chapter can be used to study the response of various hybrid architectures (not only with random intermingling, but also with blocks or layers of the two fibre-types), and will be adapted in Chapter 4 to calculate the entire stress-strain curve of HADCs.

Chapter 4

A virtual testing framework for the full tensile response of hybrid aligned discontinuous composite

4.1 Introduction

The potential advantages of hybridisation led to numerous studies on hybrid composites [88,98–101]. While manufacturing technologies used to be limited to hybridisation at the layer [102] or at the yarn [103] level, Yu et al. [29, 84] recently developed a new manufacturing process capable of producing, for the first time, *intermingled* (i.e. hybridisation at the fibre-level) *discontinuous* hybrid composites. The microstructure of such an intimate intermingling is believed to provide advantages and for instance promote further hybrid effects [28].

Hybrid composites are affected by non-linear hybrid effects (deviations from the rule-of-mixtures), which are challenging to understand and predict, as recognised in a recent review [28]. These effects are magnified with the use of intimate intermingled of the fibre-types [28, 103], and also by the use of discontinuous fibres [29, 84]. Moreover, the design space of intermingled hybrid discontinuous composites is very wide (including different fibre diameters and lengths, fibre strengths, volume ratio between the fibre types, fibre arrangements, matrix properties, ...), and therefore experiments cannot provide an exhaustive analysis of the effects of all parameters. Therefore, virtual testing models can provide a more effective way to (i) predict the mechanical response and hybrid effects in hybrid discontinuous composites, and (ii) provide guidance for the design of optimised hybrid microstructures.

A first challenge in modelling hybrid discontinuous composites is correctly capturing the effect of the discontinuities due to the fibre-ends. One widely-used approach is shear-lag models [24, 38, 104–109]. Although most shear-lag models in the literature consider a purely elastic [33, 38, 110] (see also Chapter 3) or perfectly plastic [109–112] matrix, the shear-lag framework developed for brick-and-mortar [24] and aligned discontinuous (Chapter 2) composites considers the full matrix constitutive law in shear, including strain-hardening and progressive failure; this framework also considers the random placement of fibre-ends (Chapter 2), contrarily to most analytical models which assume perfectly staggered fibres [24, 55, 61] or regularly spaced fibre-ends [58]. However, the framework developed in Chapter 2 is only valid for non-hybrid aligned discontinuous composites, and it cannot be directly applied to predict the full response of hybrid composites as the shear-lag stress transfer is affected by hybridisation of fibre-types (as shown in Chapter 3, for a purely elastic domain).

A second challenge in modelling hybrid discontinuous composites is predicting *the hybrid effect* [31, 88, 102, 113–117], which has been first observed in the early 70s by Hayashi [114] and is described as an increase of the apparent failure strain of the low-elongation fibres when mixed with another fibre-type in a composite. This hybrid effect cannot be predicted by the rules-of-mixtures [28,31,88,102,113,115–117]; although several models have explained and predicted the existence of hybrid effects in continuous composite [28, 87], it has never been explored whether the presence of fibre-ends in discontinuous composites affects hybrid effects.

The strength variability of the fibres is an important feature to account for in hybrid composites, as it is responsible for some effects of hybridisation. Some authors. [87,116–118] showed that no variability in the strength of the low-elongation fibres would lead to no hybrid effect. Moreover, neglecting the strength variability in hybrids [100, 119] results in the prediction of stress plateaus during fragmentation of the low-elongation fibres, which is contradicted by experimental evidence [29, 84].

Although much attention has been given to the study of failure of the low-elongation phase and the associated hybrid effect, hybrid composites with a sufficiently high fraction of high-elongation fibres can present a pseudo-ductile response, in which the high-elongation fibres carry the load for higher strains and until failure; in this case, the strength variability of the high-elongation fibres is likely to affect the final failure of the material, although this is neglected in most models [100]. Chapter 2 proposed a fracture mechanics failure for non-hybrid aligned discontinuous composites, which showed good agreement with experiments; for hybrid composites, Swolfs et al. [28] observed that there is still a need to propose methods which can predict final failure accurately.

This chapter aims to provide a modelling framework for intermingled hybrid aligned discontinuous composites, and is divided in two parts. Firstly, the shear-lag-based

analytical model developed in Sec. 3.2 is extended in Sec. 4.2 to calculate the stress-strain response of a hybrid brick-and-mortar composite (with two types of platelet with different thicknesses and moduli), considering a generic matrix constitutive law (including fracture). This model and those developed in Chapter 2 and Sec. 3.3 are then further developed and used in Sec. 4.3 to calculate the response of aligned hybrid discontinuous composites, considering a more realistic 3D microstructure of a specimen, as well as fibre failure under stochastic strength distributions, and using a fracture mechanics criterion to predict final failure of the composite. Finally, Sec. 4.4 draws the main conclusions of the work.

4.2 Hybrid brick-and-mortar composites

4.2.1 Model development

4.2.1.1 Microstructure and micromechanical properties

The HyBaM composite considered in this section is made of two types of linear-elastic platelets $\mathcal{A}$ and $\mathcal{B}$ of half-thicknesses $T_{\mathcal{A}}$ and $T_{\mathcal{B}}$, and Young's moduli $E_{\mathcal{A}}$ and $E_{\mathcal{B}}$ respectively (see Chapter 3). These platelets are perfectly staggered and separated by a matrix layer of thickness t^{m} (see Fig. 4.1a).

The unit-cell considered in the model is presented in Fig. 4.1b and consists of an overlap of total length $2 \cdot L = L_{\mathrm{L}} + L_{\mathrm{R}}$ between two quarters of platelet separated by the matrix layer; the origin of the x-coordinate (which is defined by L_{L} or L_{R}) is unknown *a priori* and evolves with progressive tensile loading, and will be calculated in Sec. 4.2.1.4. The fact that the origin $x = 0$ of the overlap is not constant is a major change compared to the models previously developed for the stress-strain response of non-hybrid BaM composites (where $L_{\mathrm{L}} = L_{\mathrm{R}} = L/2$) [24] and for the Young's modulus of HyBaM (where $L_{\mathrm{L}} \neq L_{\mathrm{R}}$, but both L_{L} and L_{R} are constant and can be determined by an analytical expression, as explained in Chapter 3).

The entire shear stress (τ) versus strain (γ) response of the matrix of fibre-matrix interaction is considered, and approximated by a non-linear elastic piecewise linear curve with N linear *subdomains* of tangent shear modulus G_j^{m}, $j \in \{1, ..., N\}$, with $G_j^{\mathrm{m}} \gtreqless 0$ (see for instance Fig. 4.2a, which is an example of a constitutive law where $N = 3$). Each subdomain $j \in \{1, ..., N\}$ is defined within a shear strain interval $\gamma \in [\gamma_{j-1}^{\mathrm{m}},\ \gamma_j^{\mathrm{m}}]$; subdomain $N + 1$, for $\gamma > \gamma_N^{\mathrm{m}}$, corresponds to the fully debonded state of the matrix, where the debonding strain γ_N^{m} can be calculated from the fracture toughness of the matrix, by ensuring that the total area below the curve of the constitutive law is equal to $\mathcal{G}_{\mathrm{IIc}}^{\mathrm{m}}/t^{\mathrm{m}}$ [24].

This model assumes a shear-lag behaviour of the composite in which each platelet will be loaded by tensile stresses $\sigma_{\mathcal{A}}(x)$ and $\sigma_{\mathcal{B}}(x)$, while the matrix will be loaded by shear stresses $\tau(x)$. Considering relatively thin platelets and matrix layers, the stress distributions are assumed uniform through the thickness. Like in Chapter 3, the following parameters will be used for the derivation of the model:

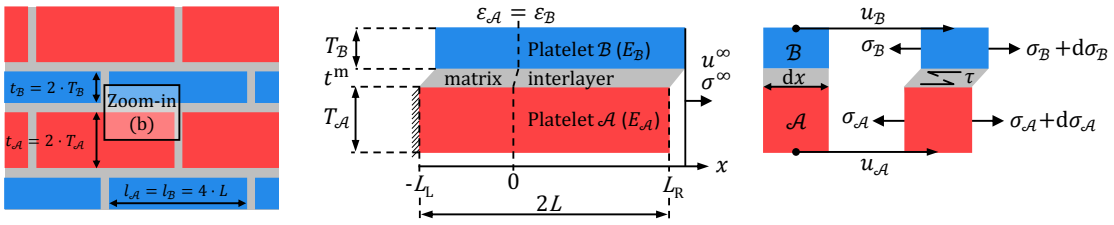
$$\begin{aligned}
\Sigma T &= T_{\mathcal{A}} + T_{\mathcal{B}}, & \Sigma E &= E_{\mathcal{A}} + E_{\mathcal{B}}, & & \\
\Sigma K &= K_{\mathcal{A}} + K_{\mathcal{B}}, & \Sigma \sigma &= \sigma_{\mathcal{A}} + \sigma_{\mathcal{B}}, & & \\
\Delta T &= T_{\mathcal{B}} - T_{\mathcal{A}}, & \Delta E &= E_{\mathcal{B}} - E_{\mathcal{A}}, & & \\
\Delta K &= K_{\mathcal{B}} - K_{\mathcal{A}}, & \Delta \sigma &= \sigma_{\mathcal{B}} - \sigma_{\mathcal{A}}, & & \\
\bar{T} &= \Sigma T/2, & \bar{E} &= \Sigma E/2, & \bar{K} &= \Sigma K/2, \\
\tilde{T} &= 2 \cdot \frac{T_{\mathcal{A}} \cdot T_{\mathcal{B}}}{T_{\mathcal{A}} + T_{\mathcal{B}}}, & \tilde{E} &= 2 \cdot \frac{E_{\mathcal{A}} \cdot E_{\mathcal{B}}}{E_{\mathcal{A}} + E_{\mathcal{B}}}, & \tilde{K} &= 2 \cdot \frac{K_{\mathcal{A}} \cdot K_{\mathcal{B}}}{K_{\mathcal{A}} + K_{\mathcal{B}}},
\end{aligned} \tag{4.1}$$

where $K_{\mathcal{A}} = E_{\mathcal{A}} \cdot T_{\mathcal{A}}$ and $K_{\mathcal{B}} = E_{\mathcal{B}} \cdot T_{\mathcal{B}}$ represent the stiffness of the platelets, and define the stiffness ratio $\eta = K_{\mathcal{A}}/K_{\mathcal{B}}$. In this chapter, platelets $\mathcal{A}$ and $\mathcal{B}$ are chosen so that $K_{\mathcal{A}} \geq K_{\mathcal{B}}$ (or $\eta \geq 1$).

4.2.1.2 Differential equation

Considering that the matrix layer in Fig. 4.1c is in the j^{th} subdomain (where $\gamma \in [\gamma_{j-1}^{\text{m}},\ \gamma_j^{\text{m}}]$ and where the tangent shear modulus is G_j^{m}), the equilibrium of stresses and the compatibility of the displacements between the matrix and the two platelets lead to the following differential equation for $\psi(x)$ (see Chapter 3):

$$\begin{aligned}
&\frac{\mathrm{d}^2\psi(x)}{\mathrm{d}x^2} = \operatorname{sign}(G_j^{\text{m}}) \cdot \lambda_j^2 \cdot \psi(x), \\
&\text{where} \begin{cases}
\psi(x) \overset{\text{def}}{=} \Delta\sigma(x) - \kappa \cdot \sigma^{\infty} & \text{is the } \textit{driving stress}, \\
\kappa \overset{\text{def}}{=} \Delta E \cdot \Sigma T / \Sigma K & \text{is the stress factor}, \\
\lambda_j \overset{\text{def}}{=} \sqrt{2 \cdot |G_j^{\text{m}}| / (t^{\text{m}} \cdot \tilde{K})} & \text{is the characteristic coefficient}.
\end{cases}
\end{aligned} \tag{4.2}$$

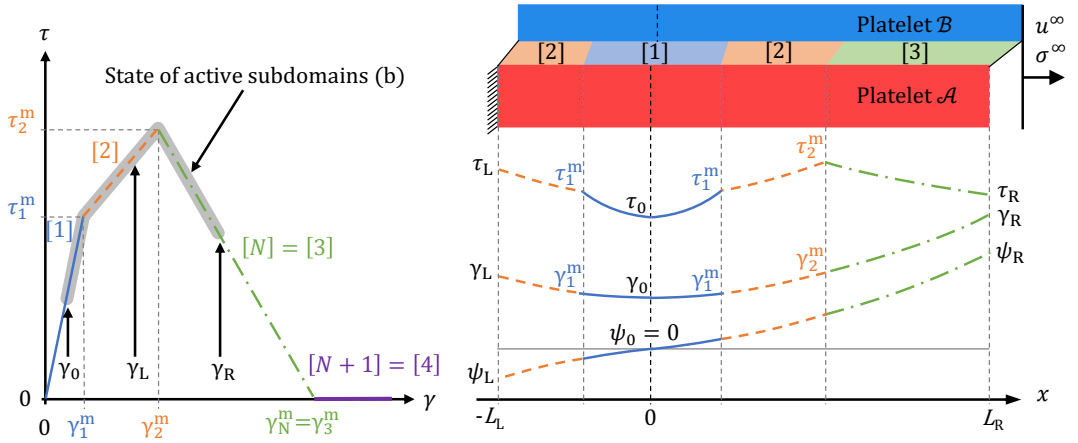


(a) Hybrid composite with a "brick-and-mortar" architecture.

(b) Unit-cell considered in the model (zoom-in from (a)).

(c) Infinitesimal element.

Figure 4.1: Overview of the shear-lag model for HyBaM composites (see Chapter 3).



(a) Constitutive law in shear of the matrix (with $N = 3$ subdomains). The active subdomains in Fig. 4.2b are highlighted in grey.

(b) Overlapping region with the state $\mathbf{s}$ of active subdomains: $\mathbf{s}_\mathrm{L} = \{1, 2\}$ and $\mathbf{s}_\mathrm{R} = \{1, 2, 3\}$, or $\mathbf{s} = \{2, 1, 2, 3\}$.

Figure 4.2: Definition of the matrix subdomains in the unit-cell (overlap) of a HyBaM composite.

Eq. 4.2 is solved for the different types of subdomains (with positive, zero, and negative G_j^m) to find the expression of the driving stress $\psi(x)$ along the overlap. The matrix shear stress $\tau(x)$ and shear strain $\gamma(x)$ fields can then be calculated from the following equations (see also Chapter 3):

$$\frac{\mathrm{d}\psi(x)}{\mathrm{d}x} = \frac{4 \cdot \Sigma T}{\Sigma T^2 - \Delta T^2} \cdot \tau(x) = \frac{2}{\bar{T}} \cdot \tau(x), \tag{4.3a}$$

$$\frac{\mathrm{d}\gamma(x)}{\mathrm{d}x} = \frac{2}{t^\mathrm{m} \cdot \Sigma T} \cdot \frac{\Sigma E \cdot \Sigma T + \Delta E \cdot \Delta T}{\Sigma E^2 - \Delta E^2} \cdot \psi(x) = \frac{\Sigma K}{t^\mathrm{m} \cdot \Sigma T \cdot E_\mathcal{A} \cdot E_\mathcal{B}} \cdot \psi(x). \tag{4.3b}$$

The fields $\psi(x)$, $\tau(x)$, $\gamma(x)$ are shown in Tab. 4.1 for all different types of subdomains. The differential equation in Tab. 4.1(a) is identical to that used to derive the Young's modulus of HyBaM composites (Chapter 3), although it is solved for more generic boundary conditions in Tab. 4.1(b) to account for non-linear-elastic matrix subdomains with positive tangent stiffness. Also, the differential equations and fields in Tab. 4.1 are formally similar to those derived for non-hybrid BaM composites [24], but with the "driving stress" $\psi(x)$ replacing the "stress difference" $\Delta\sigma(x)$, and with much more complex coefficients due to the hybrid configuration (i.e. $\Delta T \neq 0$, $\Delta E \neq 0$, and/or $\Delta K \neq 0$).

4.2.1.3 Boundary conditions

A first boundary condition for the stress and strain fields defined in Tab. 4.1 relates to the origin of the x-axis (see Fig. 4.2b) in the overlap, which is defined such that the

Table 4.1: Local stress and strain fields within a subdomain in a hybrid BaM composite; the local coordinate is defined as $\hat{x} = x - x_0$.

Differential equation ($\hat{G}^{\mathrm{m}} = G_j^{\mathrm{m}}$ and $\hat{\lambda} = \lambda_j$)	Local stress and strain fields under the following boundary conditions: $\gamma(x_0) = \hat{\gamma}_0$, $\tau(x_0) = \hat{\tau}_0 = \tau(\hat{\gamma}_0)$ and $\psi(x_0) = \hat{\psi}_0$
Positive stiffness, $\hat{G}^{\mathrm{m}} > 0$: $\frac{\mathrm{d}^2\psi(x)}{\mathrm{d}x^2} = \hat{\lambda}^2 \cdot \psi(x)$ (a)	$\hat{\psi}(\hat{x}) = \hat{\psi}_0 \cdot \cosh(\hat{\lambda} \cdot \hat{x}) + \frac{2}{\hat{\lambda} \cdot \tilde{T}} \cdot \hat{\tau}_0 \cdot \sinh(\hat{\lambda} \cdot \hat{x})$ $\hat{\tau}(\hat{x}) = \hat{\tau}_0 \cdot \cosh(\hat{\lambda} \cdot \hat{x}) + \hat{\psi}_0 \cdot \frac{\hat{\lambda} \cdot \tilde{T}}{2} \cdot \sinh(\hat{\lambda} \cdot \hat{x})$ (b) $\hat{\gamma}(\hat{x}) = \hat{\gamma}_0 + \frac{\Sigma K}{\hat{\lambda} \cdot t^{\mathrm{m}} \cdot \Sigma T \cdot E_{\mathcal{A}} \cdot E_{\mathcal{B}}} \cdot \left[\hat{\psi}_0 \cdot \sinh(\hat{\lambda} \cdot \hat{x}) + \frac{2}{\hat{\lambda} \cdot \tilde{T}} \cdot \hat{\tau}_0 \cdot (\cosh(\hat{\lambda} \cdot \hat{x}) - 1)\right]$
Zero stiffness, $\hat{G}^{\mathrm{m}} = 0$: $\frac{\mathrm{d}^2\psi(x)}{\mathrm{d}x^2} = 0$ (c)	$\hat{\psi}(\hat{x}) = \hat{\psi}_0 + \frac{2}{\tilde{T}} \cdot \hat{\tau}_0 \cdot \hat{x}$ $\hat{\tau}(\hat{x}) = \hat{\tau}_0$ (d) $\hat{\gamma}(\hat{x}) = \hat{\gamma}_0 + \frac{\Sigma K}{t^{\mathrm{m}} \cdot \Sigma T \cdot E_{\mathcal{A}} \cdot E_{\mathcal{B}}} \cdot \left[\hat{\psi}_0 \cdot \hat{x} + \frac{1}{\tilde{T}} \cdot \hat{\tau}_0 \cdot \hat{x}^2\right]$
Negative stiffness, $\hat{G}^{\mathrm{m}} < 0$: $\frac{\mathrm{d}^2\psi(x)}{\mathrm{d}x^2} = -\hat{\lambda}^2 \cdot \psi(x)$ (e)	$\hat{\psi}(\hat{x}) = \hat{\psi}_0 \cdot \cos(\hat{\lambda} \cdot \hat{x}) + \frac{2}{\hat{\lambda} \cdot \tilde{T}} \cdot \hat{\tau}_0 \cdot \sin(\hat{\lambda} \cdot \hat{x})$ $\hat{\tau}(\hat{x}) = -\hat{\psi}_0 \cdot \frac{\hat{\lambda} \cdot \tilde{T}}{2} \cdot \sin(\hat{\lambda} \cdot \hat{x}) + \hat{\tau}_0 \cdot \cos(\hat{\lambda} \cdot \hat{x})$ (f) $\hat{\gamma}(\hat{x}) = \hat{\gamma}_0 + \frac{\Sigma K}{\hat{\lambda} \cdot t^{\mathrm{m}} \cdot \Sigma T \cdot E_{\mathcal{A}} \cdot E_{\mathcal{B}}} \cdot \left[\hat{\psi}_0 \cdot \sin(\hat{\lambda} \cdot \hat{x}) + \frac{2}{\hat{\lambda}\tilde{T}} \cdot \hat{\tau}_0 \cdot (1 - \cos(\hat{\lambda} \cdot \hat{x}))\right]$
Fully debonded, $\hat{G}^{\mathrm{m}} = 0 \wedge \tau = 0$: $\frac{\mathrm{d}^2\psi(x)}{\mathrm{d}x^2} = 0$ (g)	$\hat{\psi}(\hat{x}) = \hat{\psi}_0$ $\hat{\tau}(\hat{x}) = 0$ (h) $\hat{\gamma}(\hat{x}) = \hat{\gamma}_0 + \frac{\Sigma K}{t^{\mathrm{m}} \cdot \Sigma T \cdot E_{\mathcal{A}} \cdot E_{\mathcal{B}}} \cdot \hat{\psi}_0 \cdot \hat{x}$

Table 4.2: Driving stress built along the overlap within a subdomain j, for a variation of the shear strains from $\hat{\gamma}_0$ to $\hat{\gamma}_l$ and an initial driving stress $\hat{\psi}_0$.

Type of subdomain ($\hat{G}^{\mathrm{m}} = G_j^{\mathrm{m}}$ and $\hat{\lambda} = \lambda_j$)	Local driving stress at the end of the interval $\hat{\gamma} \in [\hat{\gamma}_0, \hat{\gamma}_l]$.	
Positive stiffness $\hat{G}^{\mathrm{m}} = G_j^{\mathrm{m}} > 0$	$\psi(\hat{\gamma}_0, \hat{\gamma}_l, \hat{\psi}_0) = \sqrt{\hat{\psi}_0^2 + \left(\frac{2}{\hat{\lambda} \cdot \tilde{T}}\right)^2 \cdot [\hat{\tau}_l^2 - \hat{\tau}_0^2]}$	(a)
Zero stiffness $\hat{G}^{\mathrm{m}} = G_j^{\mathrm{m}} = 0$	$\psi(\hat{\gamma}_0, \hat{\gamma}_l, \hat{\psi}_0) = \sqrt{\hat{\psi}_0^2 + \frac{4 \cdot t^{\mathrm{m}} \cdot \Sigma T}{\tilde{T}} \cdot \frac{E_{\mathcal{A}} \cdot E_{\mathcal{B}}}{\Sigma K} \cdot \hat{\tau}_0^2 \cdot (\hat{\gamma}_l - \hat{\gamma}_0)}$	(b)
Negative stiffness $\hat{G}^{\mathrm{m}} = G_j^{\mathrm{m}} < 0$	$\psi(\hat{\gamma}_0, \hat{\gamma}_l, \hat{\psi}_0) = \sqrt{\hat{\psi}_0^2 + \left(\frac{2}{\hat{\lambda} \cdot \tilde{T}}\right)^2 \cdot [\hat{\tau}_0^2 - \hat{\tau}_l^2]}$	(c)
Fully debonded $\hat{G}^{\mathrm{m}} = G_j^{\mathrm{m}} = 0 \ \wedge \ \tau^{\mathrm{m}} = 0$	$\psi(\hat{\gamma}_0, \hat{\gamma}_l, \hat{\psi}_0) = \hat{\psi}_0$	(d)

Table 4.3: Lengths of process zones required to develop the shear strains from $\hat{\gamma}_0$ to $\hat{\gamma}_l$ in the j^{th} subdomain, and for an initial driving stress $\hat{\psi}_0$.

Type of subdomain ($\tilde{G}^{\text{m}} = G_j^{\text{m}}$ and $\hat{\lambda} = \lambda_j$)	Length required to develop the shear strain interval $\hat{\gamma} \in [\hat{\gamma}_0, \hat{\gamma}_l]$.	
Positive stiffness	$l(\hat{\gamma}_0, \hat{\gamma}_l, \hat{\psi}_0) = \frac{2}{\hat{\lambda}} \cdot \text{atanh}\left[\frac{\hat{\lambda}\cdot\tilde{T}}{2\cdot(\hat{\tau}_0+\hat{\tau}_l)} \cdot \left(\sqrt{\hat{\psi}_0^2 + \left(\frac{2}{\hat{\lambda}\cdot\tilde{T}}\right)^2 \cdot (\hat{\tau}_l^2 - \hat{\tau}_0^2)} - \hat{\psi}_0\right)\right]$	(a)
Zero stiffness	$l(\hat{\gamma}_0, \hat{\gamma}_l, \hat{\psi}_0) = \frac{\tilde{T}}{2\cdot\hat{\tau}_0} \cdot \left[\sqrt{\hat{\psi}_0^2 + \frac{2\cdot t^{\text{m}}\cdot\Sigma T^2}{\Sigma K} \cdot \frac{E_{\mathcal{A}}\cdot E_{\mathcal{B}}}{T_{\mathcal{A}}\cdot T_{\mathcal{B}}} \cdot \hat{\tau}_0^2 \cdot (\hat{\gamma}_l - \hat{\gamma}_0)} - \hat{\psi}_0\right]$	(b)
Negative stiffness	$l(\hat{\gamma}_0, \hat{\gamma}_l, \hat{\psi}_0) = \frac{2}{\hat{\lambda}} \cdot \text{atan}\left[\frac{\hat{\lambda}\cdot\tilde{T}}{2\cdot(\hat{\tau}_0+\hat{\tau}_l)} \cdot \left(\sqrt{\hat{\psi}_0^2 + \left(\frac{2}{\hat{\lambda}\cdot\tilde{T}}\right)^2 \cdot (\hat{\tau}_0^2 - \hat{\tau}_l^2)} - \hat{\psi}_0\right)\right]$	(c)
Fully debonded	$l(\hat{\gamma}_0, \hat{\gamma}_l, \hat{\psi}_0) = \frac{2\cdot t^{\text{m}}\cdot\Sigma T}{\hat{\psi}_0} \cdot \frac{2\cdot T_{\mathcal{A}}\cdot T_{\mathcal{B}}}{\Sigma K} \cdot (\hat{\gamma}_l - \hat{\gamma}_0)$	(d)

shear strain is minimum at $x = 0$:

$$\gamma(0) \overset{\text{def}}{=} \min\{\gamma(x)\} \Rightarrow \frac{\mathrm{d}\gamma}{\mathrm{d}x}\Big|_{x=0} = 0 \overset{\text{def}}{=} \psi(0) = 0. \tag{4.4}$$

Considering that the overall load carried by the platelets remains constant along the overlap, a second boundary condition for the driving stress at the ends of the overlap can be expressed by

$$\begin{cases} \Delta\sigma_{\text{R}} \overset{\text{def}}{=} \Delta\sigma(L_{\text{R}}) = \frac{\Sigma T}{T_{\mathcal{B}}} \cdot \sigma^{\infty} \\ \Delta\sigma_{\text{L}} \overset{\text{def}}{=} \Delta\sigma(-L_{\text{L}}) = -\frac{\Sigma T}{T_{\mathcal{A}}} \cdot \sigma^{\infty} \end{cases} \Rightarrow \begin{cases} \psi_{\text{R}} \overset{\text{def}}{=} \psi(L_{\text{R}}) = \left(\frac{\Sigma T}{T_{\mathcal{B}}} - \kappa\right) \cdot \sigma^{\infty} \\ \psi_{\text{L}} \overset{\text{def}}{=} \psi(-L_{\text{L}}) = -\left(\frac{\Sigma T}{T_{\mathcal{A}}} + \kappa\right) \cdot \sigma^{\infty}. \end{cases} \tag{4.5a}$$

Eq. 4.5a yields the following relationship between ψ_{L} and ψ_{R}:

$$\frac{\psi_{\text{R}}}{\psi_{\text{L}}} = -\frac{\Sigma T/T_{\mathcal{B}} - \kappa}{\Sigma T/T_{\mathcal{A}} + \kappa} \;\Leftrightarrow\; \psi_{\text{R}} = -\eta\cdot\psi_{\text{L}}, \quad \text{where} \quad \eta \overset{\text{def}}{=} \frac{\Sigma T/T_{\mathcal{B}} - \kappa}{\Sigma T/T_{\mathcal{A}} + \kappa} = \frac{T_{\mathcal{A}}\cdot E_{\mathcal{A}}}{T_{\mathcal{B}}\cdot E_{\mathcal{B}}} = \frac{K_{\mathcal{A}}}{K_{\mathcal{B}}}. \tag{4.5b}$$

One can therefore define the *Boundary Condition Error* (BCE) function as

$$\xi(\gamma_0, L_{\text{L}}, L_{\text{R}}) \overset{\text{def}}{=} \eta\cdot\psi(\gamma_0, -L_{\text{L}}) + \psi(\gamma_0, L_{\text{R}}), \tag{4.6}$$

where $\psi(\gamma_0, x)$ is the driving stress at coordinate x, with $\gamma(0) = \gamma_0$. From Eq. 4.5b, equilibrium of stresses is reached in the overlap when the condition $\xi(\gamma_0, L_{\text{L}}, L_{\text{R}}) = 0$ is satisfied.

The remote stress σ^{∞} applied to the overlap can be derived from the driving stresses through Eq. 4.5a (where σ^{∞}, ψ_{L} and ψ_{R} are all functions of γ_0):

$$\sigma^{\infty} = \frac{\psi_{\mathrm{R}}}{\frac{\Sigma T}{T_{\mathcal{B}}} - \kappa} \quad \text{or} \quad \sigma^{\infty} = \frac{-\psi_{\mathrm{L}}}{\frac{\Sigma T}{T_{\mathcal{A}}} + \kappa}. \tag{4.7}$$

The remote strain ε^{∞} can be calculated by integrating the local tensile strain of each platelet along the overlap; taking $\gamma_{\mathrm{L}} \overset{\text{def}}{=} \gamma(-L_{\mathrm{L}})$ and $\gamma_{\mathrm{R}} \overset{\text{def}}{=} \gamma(L_{\mathrm{R}})$ as the matrix shear strains at the ends of the overlap, this yields (see Chapter 3)

$$\varepsilon^{\infty} = \frac{t^{\mathrm{m}}}{2 \cdot L} \cdot \frac{\gamma_{\mathrm{L}} \cdot K_{\mathcal{B}} + \gamma_{\mathrm{R}} \cdot K_{\mathcal{A}}}{\Sigma K} + \sigma^{\infty} \cdot \frac{\Sigma T}{\Sigma K}. \tag{4.8}$$

4.2.1.4 Model implementation

The main challenge of the model for HyBaM composites is now to use the fields and boundary conditions derived in Secs. 4.2.1.2-4.2.1.3 to obtain the full equilibrium stress-strain curve of the overlap, considering a piecewise matrix response. The method implemented here is inspired on that previously proposed for non-hybrid BaM composites [24]; however, the fact that the origin of the hybrid overlap ($x = 0$) is not known *a priori* and does not stay constant with progressive loading makes the implementation significantly more challenging and necessarily different from that for the non-hybrid composite.

The implementation is based on driving the minimum matrix shear strain in the overlap (γ_0) from zero to γ_N^{m}, and defining how the *state* of active subdomains of the matrix in the overlap – represented as $\mathbf{s}^k = \{i + n_{\mathrm{L}}, ..., i+1, i, i+1, ..., i + n_{\mathrm{R}}\}$ – evolves with γ_0. This representation of the active subdomains implies that subdomain i is active at the origin of the overlap (hence $\gamma_0 \in [\gamma_{i-1}^{\mathrm{m}},\ \gamma_i^{\mathrm{m}}]$), subdomain $i + n_{\mathrm{L}}$ is active at the left end of the overlap (hence $\gamma_{\mathrm{L}} \in [\gamma_{i+n_{\mathrm{L}}-1}^{\mathrm{m}},\ \gamma_{i+n_{\mathrm{L}}}^{\mathrm{m}}]$), and subdomain $i + n_{\mathrm{R}}$ is active at the right end of the overlap (hence $\gamma_{\mathrm{R}} \in [\gamma_{i+n_{\mathrm{R}}-1}^{\mathrm{m}},\ \gamma_{i+n_{\mathrm{R}}}^{\mathrm{m}}]$). The method described hereafter is summarised in Fig. 4.4 for a fully generic matrix constitutive law, but for clarity it will be explained using a particular case (illustrated in Fig. 4.3).

Let us consider the trilinear matrix constitutive law shown in Fig. 4.2. Assume that the state of active subdomains at the given shear strain γ_0 is $\mathbf{s}^k = \{2, 1, 2, 3\}$ (with $i = 1$, $n_{\mathrm{L}} = 1$, $n_{\mathrm{R}} = 2$), which is highlighted in black in Fig. 4.3a and shown as ① in Fig. 4.3b. The next possible states $\mathbf{s}^{k+1}$ (highlighted in yellow in Fig. 4.3a) correspond to:

- $\mathbf{s}^{k+1} = \{2, 3\}$, due to the deactivation of matrix subdomain $[i = 1]$ at the origin of the overlap (at $x = 0$), which will happen if γ_0 reaches $\gamma_{i=1}^{\mathrm{m}}$ before γ_{L} reaches $\gamma_{i+n_{\mathrm{L}}=2}^{\mathrm{m}}$ and before γ_{R} reaches $\gamma_{i+n_{\mathrm{R}}=3}^{\mathrm{m}}$. This deactivation cannot happen when there is only one active subdomain on one side (i.e. if $n_{\mathrm{L}} = 0$ or $n_{\mathrm{R}} = 0$);

- $\mathbf{s}^{k+1} = \{3, 2, 1, 2, 3\}$, due to the activation of matrix subdomain $[i + n_{\mathrm{L}} + 1 = 3]$ at the left end (at $x = -L_{\mathrm{L}}$), which will happen if γ_{L} reaches $\gamma^{\mathrm{m}}_{i+n_{\mathrm{L}}=2}$ before γ_0 reaches $\gamma^{\mathrm{m}}_{i=1}$ and before γ_{R} reaches $\gamma^{\mathrm{m}}_{i+n_{\mathrm{R}}=3}$. The assumption that platelet $\mathcal{A}$ is the stiffest ($\eta > 1$) implies that $\gamma_{\mathrm{R}} \geq \gamma_{\mathrm{L}}$; as a result, $n_{\mathrm{L}} \leq n_{\mathrm{R}}$, and an activation at the left end cannot happen when $n_{\mathrm{L}} = n_{\mathrm{R}}$;
- $\mathbf{s}^{k+1} = \{2, 1, 2, 3, 4\}$, due to the activation of matrix subdomain $[i + n_{\mathrm{R}} + 1 = 4]$ at the right end (at $x = L_{\mathrm{R}}$), which will happen if γ_{R} reaches $\gamma^{\mathrm{m}}_{i+n_{\mathrm{R}}=3}$ before γ_0 reaches $\gamma^{\mathrm{m}}_{i=1}$ and before γ_{L} reaches $\gamma^{\mathrm{m}}_{i+n_{\mathrm{L}}=2}$.

The algorithm to select the correct next state $\mathbf{s}^{k+1}$ from the three possibilities listed above works as follows:

1. Two matrices $\mathbf{\Psi}$ (containing all values of the driving stress $\psi_{[j,j+n]}$ at the end of fully-developed matrix subdomains) and $\mathbf{L}$ (containing the lengths of process zones $l_{[j,j+n]}$ needed to fully develop active matrix subdomains) are populated using the expressions shown in Tabs. 4.2 and 4.3 respectively:

$$\mathbf{\Psi} = \begin{bmatrix} \psi_{[2,2]} & \psi_{[2,3]} & \cdots & \psi_{[2,N]} \\ \psi_{[3,3]} & \psi_{[3,4]} & \iddots & \\ \vdots & \iddots & & \\ \psi_{[N,N]} & & & \end{bmatrix} \text{ (Tab. 4.2), and} \tag{4.9a}$$

$$\mathbf{L} = \begin{bmatrix} l_{[2,2]} & l_{[2,3]} & \cdots & l_{[2,N]} \\ l_{[3,3]} & l_{[3,4]} & \iddots & \\ \vdots & \iddots & & \\ l_{[N,N]} & & & \end{bmatrix} \text{ (Tab. 4.3), where} \tag{4.9b}$$

$$\psi_{[j,j+n]} \stackrel{\mathsf{def}}{=} \psi(\gamma^{\mathrm{m}}_{j+n-1}, \gamma^{\mathrm{m}}_{j+n}, \psi_{[j,j+n-1]}), \text{ and} \tag{4.9c}$$

$$l_{[j,j+n]} \stackrel{\mathsf{def}}{=} l_{[j,j+n-1]} + l(\gamma^{\mathrm{m}}_{j+n-1}, \gamma^{\mathrm{m}}_{j+n}, \psi_{[j,j+n-1]}) \tag{4.9d}$$

   are defined recursively, and where $\psi_{[j,j-1]} = 0$. The two matrices $\mathbf{\Psi}$ and $\mathbf{L}$ do not depend on the overlap length $(2 \cdot L)$ nor on the applied load to the overlap, and therefore they are populated only once, at the beginning of the analysis.

2. For the current state $\mathbf{s}^k = \{2, 1, 2, 3\}$, the model identifies whether a new subdomain would activate first on the right-end or on the left-end. To do this, the actual length of the overlap $(2 \cdot L)$ was initially ignored, virtual values (identified by the superscript $*$) were imposed to variables $\gamma^*_0 = \gamma^{\mathrm{m}}_{i=1}$ and $L^*_{\mathrm{L}} = l_{[i+1,i+n_{\mathrm{L}}]=[2,2]}$ (which implies that $\gamma^*_{\mathrm{L}} = \gamma^{\mathrm{m}}_{i+n_{\mathrm{L}}=2}$ and $\psi^*_{\mathrm{L}} = -\psi_{[i+1,i+n_{\mathrm{L}}]=[2,2]}$), and the boundary condition error ($\xi^*(\gamma^*_0, L^*_{\mathrm{L}}, L^*_{\mathrm{R}})$, see Eq. 4.6) was calculated for the following cases:

   (i) when $L^*_{\mathrm{R}} = l_{[i+1,i+n_{\mathrm{R}}-1]=[2,2]}$ (which implies that $\gamma^*_{\mathrm{R}} = \gamma^{\mathrm{m}}_{i+n_{\mathrm{R}}-1=2}$, and $\psi^*_{\mathrm{R}} = \psi_{[i+1,i+n_{\mathrm{R}}-1]=[2,2]}$), which is represented as $\xi^*(\gamma^*_0, L^*_{\mathrm{L}}, L^*_{\mathrm{R}}) = \xi^*(\gamma^{\mathrm{m}}_{i=1}, l_{[i+1,i+n_{\mathrm{L}}]=[2,2]}, l_{[i+1,i+n_{\mathrm{R}}-1]=[2,2]})$;

(ii) when $L^*_{\rm R} = l_{[i+1,i+n_{\rm R}]=[2,3]}$ (which implies that $\gamma^*_{\rm R} = \gamma^{\rm m}_{i+n_{\rm R}=3}$, and $\psi^*_{\rm R} = \psi_{[i+1,i+n_{\rm R}]=[2,3]}$), which is represented as $\xi^*(\gamma^*_0, L^*_{\rm L}, L^*_{\rm R}) = \xi^*(\gamma^{\rm m}_{i=1}, l_{[i+1,i+n_{\rm L}]=[2,2]}, l_{[i+1,i+n_{\rm R}]=[2,3]})$.

Therefore, because the function $\xi(\gamma_0, x_{\rm L}, x_{\rm R})$ is continuous and monotonic in $x_{\rm R}$, it is possible to determine whether equilibrium ($\xi^* = 0$) can be found at a point $x^*_{\rm R} \in [l_{[i+1,i+n_{\rm R}-1]=[2]}, l_{[i+1,i+n_{\rm R}]=[2,3]}]$ (interval $\mathcal{I}$ in point ② of Fig. 4.3b) by looking at the sign of (see point ③ in Fig. 4.3b)

$$\begin{aligned}\bar{\xi} \stackrel{\text{def}}{=} \xi^*(\gamma^{\rm m}_{i=1}, l_{[i+1,i+n_{\rm L}]=[2,2]}, l_{[i+1,i+n_{\rm R}-1]=[2,2]}) \\ \times \xi^*(\gamma^{\rm m}_{i=1}, l_{[i+1,i+n_{\rm L}]=[2,2]}, l_{[i+1,i+n_{\rm R}]=[2,3]}) :\end{aligned} \tag{4.10}$$

(a) if $\bar{\xi} < 0$, there exists a unique point $x^*_{\rm R} \in \mathcal{I}$ satisfying the BCE condition $\bar{\xi}^*(\gamma^{\rm m}_{i=1}, L^*_{\rm L}, x^*_{\rm R}) = 0$. Therefore, a new subdomain $[i + n_{\rm L} + 1 = 3]$ would activate at $x = -L^*_{\rm L}$ (i.e. at the left virtual edge) before subdomain $[i + n_{\rm R} + 1 = 4]$ could activate at the corresponding equilibrium point $x = x^*_{\rm R} \in \mathcal{I}$. This will lead to an Assumed Left Activation (ALA) of subdomain $[i + n_{\rm L} + 1 = 3]$;

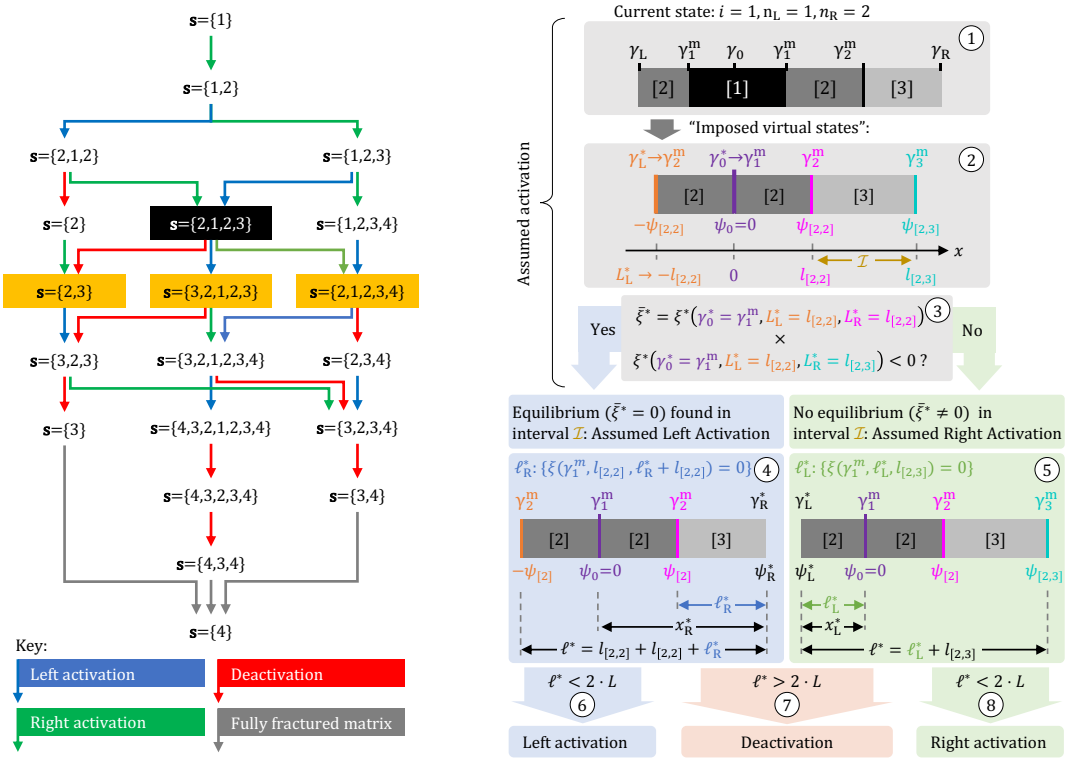
(b) if $\bar{\xi} > 0$, a point satisfying the BCE condition $\xi^*(\gamma^{\rm m}_{i=1}, L^*_{\rm L}, x^*_{\rm R}) = 0$ cannot be found in the interval $x^*_{\rm R} \in \mathcal{I}$. Therefore, before subdomain $[i + n_{\rm L} + 1 = 3]$ could activate at the left virtual edge $x = -L^*_{\rm L}$, a new subdomain $[i + n_{\rm R} + 1 = 4]$ would activate at $x = L^*_{\rm R}$ (i.e. at the right virtual edge). This will lead to an Assumed Right Activation (ARA) of subdomain $[i + n_{\rm R} + 1 = 4]$.

3. Let us assume the case of ALA defined in case (a) above, so that one can determine whether this assumed activation of subdomain $[i + n_{\rm L} + 1 = 3]$ may actually happen, or whether deactivation of the central subdomain $[i = 1]$ will happen first. The location of the equilibrium point $x^*_{\rm R}$ can be determined by imposing the BCE condition ($\xi^*(\gamma^*_0, L^*_{\rm L}, x^*_{\rm R}) = 0$, Eq. 4.6), using the process zones of the fully-developed active subdomains defined in matrix $\mathbf{L}$ (see point ④ in Fig. 4.3b):

$$x^*_{\rm R} \stackrel{\text{def}}{=} l_{[i+1,i+n_{\rm R}-1]=[2,2]} + \ell^*_{\rm R} : \{\xi^*(\gamma^{\rm m}_{i=1}, L^*_{\rm L}, x^*_{\rm R}) = 0\}. \tag{4.11}$$

This defines the virtual overlap length $\ell^* = L^*_{\rm L} + x^*_{\rm R}$ required to simultaneously activate the next matrix subdomain on the left (i.e. have $\gamma^*_{\rm L} = \gamma^{\rm m}_{i+n_{\rm L}=2}$) and deactivate the subdomain at the origin of the overlap (i.e. have $\gamma^*_0 = \gamma^{\rm m}_{i=1}$). Consequently,

– If $\ell^* < 2 \cdot L$, the overlap is long enough to accommodate the entire process zone of subdomains $\{i + n_{\rm L}, ..., i + 1\}$ on the left of the origin of the overlap, and therefore the ALA must happen before the central subdomain is



(a) Possible evolutions of the active matrix subdomains in a hybrid overlap.

(b) Illustration of the algorithm to identify the next state of active subdomains (highlighted in black in Fig. 4.3a). The current state is $\mathbf{s}^k = \{2, 1, 2, 3\}$ and the 3 possible next states $\mathbf{s}^{k+1}$ shown in yellow in Fig. 4.3a).

Figure 4.3: Algorithm used to define the sequence of the states of active matrix subdomains in a HyBaM composite, considering the trilinear matrix constitutive law given in Fig. 4.2a, for $\eta > 1$.

deactivated. The transition shear strain to the next state $k+1$ is given by

$$\gamma_0^{k+1} = \gamma_0 \ : \ \{\xi(\gamma_0, L_L, 2 \cdot L - L_L) = 0\} \tag{4.12}$$

where L_L is the process length required to develop shear strains from $\gamma(0) = \gamma_0$ to $\gamma(-L_L) = \gamma^m_{i+n_L}$, and Eq. 4.12 is solved numerically with respect to γ_0. The new state of active matrix subdomains will be given by $\mathbf{s}^{k+1} = \{i + n_L + 1, ..., i + 1, i, i + 1, ..., i + n_R\} = \{3, 2, 1, 2, 3\}$ (see point ⑥ in Fig. 4.3b).

– If $\ell^* > 2 \cdot L$, the overlap is not long enough to allow for an ALA to happen, and the next transition to a different state will be the deactivation of the central subdomain $[i = 1]$ which will occur at the transition shear strain

$$\gamma_0^{k+1} = \gamma_i^m. \tag{4.13}$$

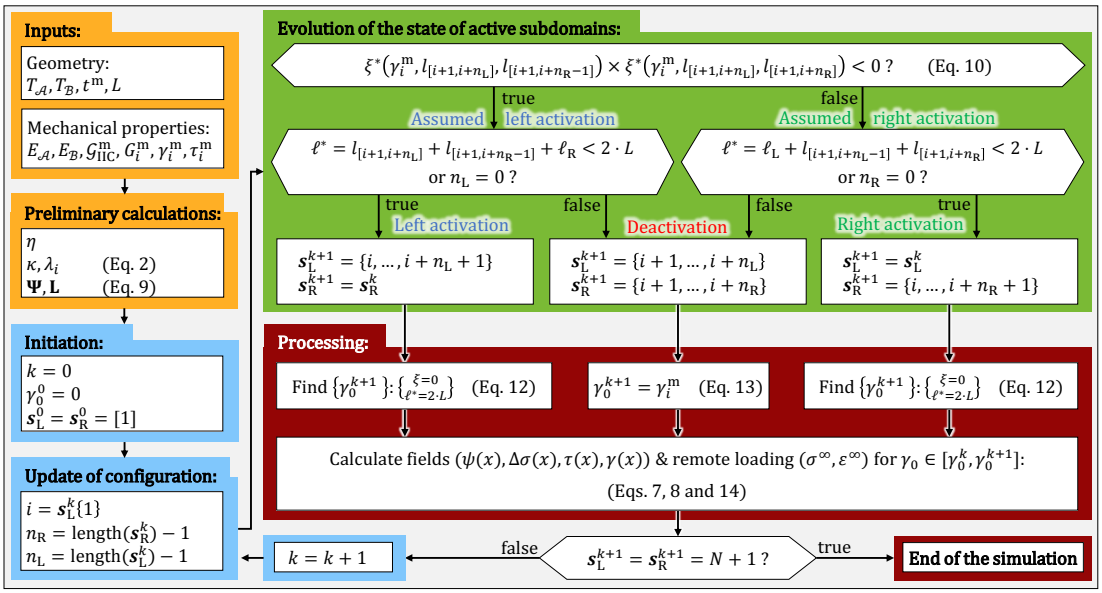


Figure 4.4: General implementation of the model to predict the stress-strain response of hybrid brick-and-mortar composites.

The new state of active subdomains will be given by $\mathbf{s}^{k+1} = \{i + n_{\mathrm{L}}, ..., i + 2, i + 1, i + 2, ..., i + n_{\mathrm{R}}\} = \{2, 3\}$ (see point ⑦ in Fig. 4.3b).

4. Finally, the fields $\psi(x)$ and $\gamma(x)$ are calculated for $\gamma_0 \in [\gamma_0^k,\ \gamma_0^{k+1}]$, and used to find the remote stress σ^∞ and strain ε^∞ using Eqs. 4.7 and 4.8 respectively. The value of the shear strains γ_{L} and γ_{R} required in Eqs. 4.7 and 4.8 are given by

$$\{\gamma_{\mathrm{L}} \overset{\text{def}}{=} \gamma(-L_{\mathrm{L}}), \gamma_{\mathrm{R}} \overset{\text{def}}{=} \gamma(2 \cdot L - L_{\mathrm{L}})\} \ : \ \{\xi(\gamma_0, L_{\mathrm{L}}, 2 \cdot L - L_{\mathrm{L}}) = 0\}\,. \tag{4.14}$$

This process allows one to calculate the full stress-strain response of a HyBaM composite with a generic matrix constitutive law, without a need for an iterative process.

4.2.2 Results

4.2.2.1 Overview of results

Figs. 4.5a and 4.5b display the stress-strain curves of HyBaM composites with different average platelet aspect ratios ($\bar{\alpha} = 5$ and $\bar{\alpha} = 25$), considering a trilinear matrix constitutive law and the inputs given in Tab. 4.4: note that this trilinear constitutive law (with $N = 3$, and shown in Fig. 4.2a) is just one example that illustrates the capabilities of the model, but other constitutive laws (e.g. bilinear, trapezoidal, strain-hardening, etc.) can equally be considered by the implementation described in Sec. 4.2.1.4. Figs. 4.5c and 4.5d show the shear stress fields along a short ($\bar{\alpha} = 5$)

and long ($\bar{\alpha} = 25$) overlap respectively, for all transitions between the different matrix states; these transition points are reported on the corresponding stress-strain curve in Figs. 4.5a and 4.5b. It must be noted that the results in Fig. 4.5 assume that the platelets are linear-elastic (i.e. do not fail in tension under the stresses applied).

The model has been validated against FE simulations (using the method previously applied to validate predictions for the full stress-strain curve of non-hybrid BaM composites [24] and the stiffness of HyBaM composites (see Chapter 3), using a plasticity model to represent the non-linear response of the matrix); the results reported in Fig. 4.5 show a very good agreement both for the shear stress-field in the matrix along the overlap, and for the overall stress-strain curve of the HyBaM composite.

4.2.2.2 Effect of hybrid reinforcement on matrix failure in hybrid discontinuous composites

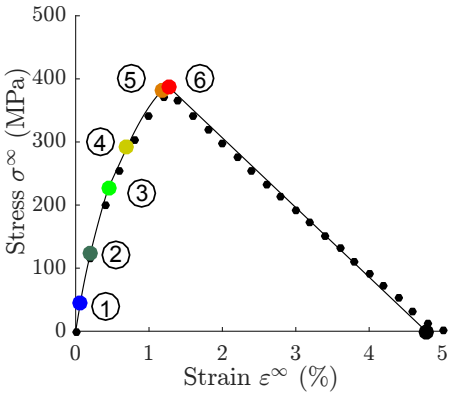
Both Figs. 4.5c and 4.5d show a non-symmetrical distribution of shear stresses in the matrix along hybrid overlaps. This asymmetry of matrix stress and strain fields is due to the difference in overall stiffness ($K = E \cdot T$) between the two platelet types, which causes the matrix shear strain to be larger at the end of the stiffer platelet ($\mathcal{A}$ in Fig. 4.5) than at the end of the softer platelet ($\mathcal{B}$ in Fig. 4.5). Consequently, the origin of the overlap (where the shear strain is minimum, represented by the grey diamonds in the Figs. 4.5c-4.5d) is shifted towards the end of the softest platelet at the beginning of the loading, and shifted further as the loading progresses.

Fig. 4.5 also shows the different effects of hybridisation for different platelet geometries. While the overlap with short platelets ($\bar{\alpha} = 5$) presents relatively homogeneous shear stress fields, slender platelets ($\bar{\alpha} = 25$) allow for more matrix subdomains to be simultaneously active in the overlap. Moreover, for slender configurations, having very

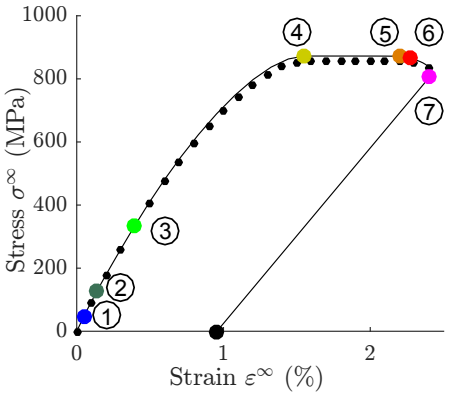
Table 4.4: Inputs (geometry and mechanical properties of the platelets and the matrix) of the hybrid BaM composites studied in Sec. 4.2.2.

Parameter	L	$\bar{T}$	t^{m}	$\bar{E}$	$\frac{\Delta E}{\Sigma E}$	$\frac{\Delta T}{\Sigma T}$	G^{m}	$\mathcal{G}^{\mathrm{m}}_{\mathrm{IIc}}$
Unit	(mm)	(mm)	(mm)	(GPa)			(MPa)	(kJ/m^2)
Value	0.5 or 2.5	0.1	0.01	100	-0.2	-0.3	1500	2

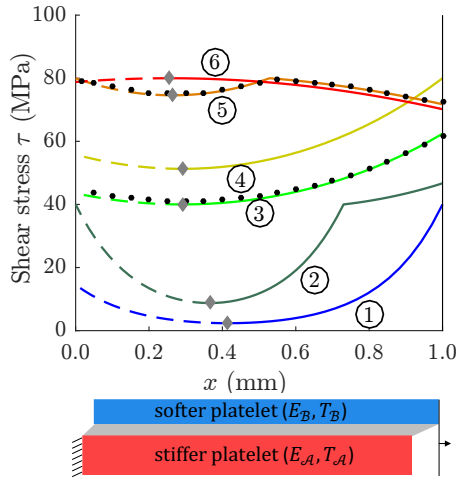
Matrix type	N	Points of the constitutive law (γ^{m} [$-$], τ^{m} [MPa])
Trilinear (Fig. 4.5)	3	$(0, 0)$, $(0.0267, 40)$, $(0.50, 80)$, $(4.777, 0)$



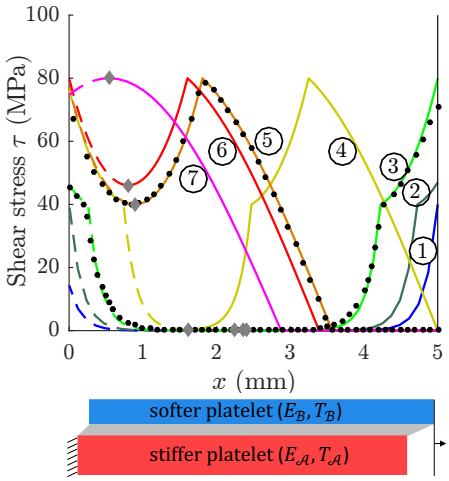
(a) Stress-strain curve for short platelets ($\bar{\alpha} = 5$).



(b) Stress-strain curve for long platelets ($\bar{\alpha} = 25$).



(c) Shear stress along short platelets ($\bar{\alpha} = 5$) for all states s^k shown by the coloured points defined in the $\sigma^\infty(\varepsilon^\infty)$ curve in Fig. 4.5a.



(d) Shear stress along long platelets ($\bar{\alpha} = 25$) for all states s^k shown by the coloured points defined in the $\sigma^\infty(\varepsilon^\infty)$ curve in Fig. 4.5b.

Figure 4.5: Results for HyBaM composites, for different aspect ratios ($\bar{\alpha} = 5$ on the left, and $\bar{\alpha} = 25$ on the right), for a given hybrid configuration and a trilinear matrix shear constitutive law (see Tab. 4.4). FE results are represented by black dots (for the stress-strain curves in Figs. (a) and (b), and for the stress-fields in Figs. (c) and (d)). The origin of the overlap (where the matrix shear strain is minimum) is shown by grey diamonds, for each stress field in Figs. (c) and (d).

different platelet stiffnesses could trigger delamination from the end of the stiffest platelet only (between steps ④ and ⑤ in Figs 4.5b and 4.5d), while delamination would be expected to occur at either end of an overlap in a non-hybrid BaM composite.

This asymmetry in the matrix shear stress field means that the load carrying capacity of the matrix is reduced due to hybridisation. As a direct result, the matrix-

dominated (i.e. assuming no platelet failure) strength of a HyBaM composite is lower than the non-hybrid equivalent.

4.3 Hybrid aligned discontinuous composites

4.3.1 Model development

4.3.1.1 Microstructure of hybrid aligned discontinuous composites

This section proposes a VTF for aligned discontinuous composites with intermingled hybrid fibre-types. The microstructure considered here is the same as that used in Chapter 3 to determine the Young's modulus of HADCs. The specimen is modelled as a chain of n^{RVE} *RVEs* (Fig. 4.6a), where each RVE is made of $n \times n$ fibres, and the RVE length is the same as the fibre length l^{f} (uniform throughout the specimen).

In an RVE, each fibre is identified by the coordinates (i, j) in a square arrangement (see Fig. 4.6b). The grid defining the RVE in Fig. 4.6a has no physical meaning and is used to define neighbouring fibres and interactions only; in particular, it does not define fibre spacing or the matrix thickness (this will be done in Eq. 4.15) (see Chapter 3). The locations of fibre-ends are stored in the matrix $\mathbb{x}_{ij}$ (see Chapter 2). Each fibre is affected a fibre-type ($\mathcal{A}$, Young's modulus $E_{\mathcal{A}}$ and diameter $\phi_{\mathcal{A}}$, or $\mathcal{B}$, Young's modulus $E_{\mathcal{B}}$ and diameter $\phi_{\mathcal{B}}$) in the matrix of fibre-types $\mathbb{T}_{ij}$, so as to achieve the desired volume or number ratio of type-$\mathcal{A}$ and type-$\mathcal{B}$ fibres (respectively $V_{\mathcal{A}}$ or $N_{\mathcal{A}}$ and $V_{\mathcal{B}}$ or $N_{\mathcal{B}}$, with $V_{\mathcal{A}} + V_{\mathcal{B}} = 100\%$ and $N_{\mathcal{A}} + N_{\mathcal{B}} = 100\%$); the matrix of fibre-types is defined so that $\mathbb{T}_{ij} = 1$ when fibre (i, j) is of type $\mathcal{A}$, and $\mathbb{T}_{ij} = 0$ when fibre (i, j) is of type $\mathcal{B}$. This allows one to define two additional matrices:

- $\Phi_{ij} = \phi_{\mathcal{A}} \cdot \mathbb{T}_{ij} + \phi_{\mathcal{B}} \cdot (1 - \mathbb{T}_{ij})$, where Φ_{ij} returns the diameter of fibre (i, j);
- $\mathbb{E}_{ij} = E_{\mathcal{A}} \cdot \mathbb{T}_{ij} + E_{\mathcal{B}} \cdot (1 - \mathbb{T}_{ij})$, where $\mathbb{E}_{ij}$ returns the Young's modulus of fibre (i, j).

The novelty of this section compared to Chapter 3 consists on extending the analysis of hybrid discontinuous composites to the non-linear-elastic domain, by considering the non-linear response of the matrix (using the shear-lag formulation presented in Sec. 4.2), stochastic fibre strength distributions, and unstable specimen fracture. These new developments are detailed in Secs. 4.3.1.2-4.3.1.4, and are inspired by the VTF for non-hybrid discontinuous composites presented in Chapter 2.

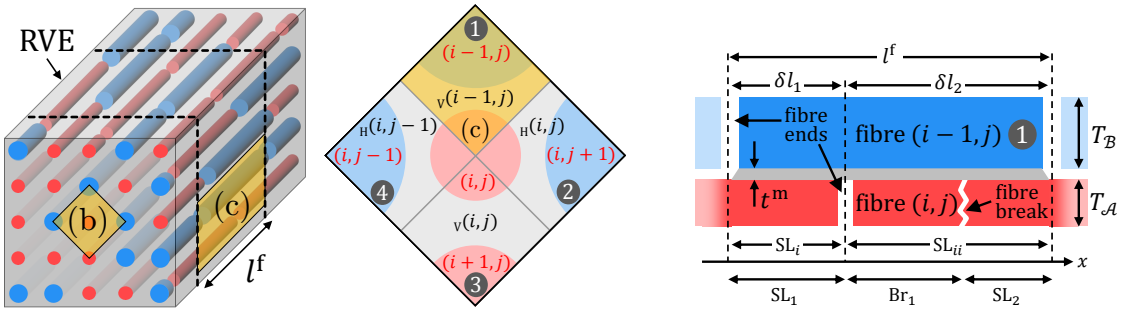
It is worth noting that the fibres are considered to be perfectly aligned in this model. Previous studies showed that it is now possible to manufacture hybrid discontinuous composites with an outstanding level of alignment [73], on which the effect of

fibre misalignment (estimated through classical laminate theory (App. F)) should be negligible.

4.3.1.2 Response of an interaction between two neighbouring fibres

Consider that a fibre interacts with its four nearest neighbours through horizontal (subscript H) and vertical (subscript V) interactions (see Figs. 4.6b); the symbol $*$ is used to replace H and V when no orientation is specified for an interaction. An interaction is initially decomposed in two *shear-lag segments* (see Fig. 4.6c), although the occurrence of fibre-breaks may decompose it further:

- A segment delimited by discontinuities (i.e. fibre-ends or fibre-breaks) in the two interacting fibres is a *shear-lag segment* (subscript 'SL', see for instance Segment SL_1 in Fig. 4.6c). For a shear-lag segment of length δl_{SL}, the shear-lag model developed in Sec. 4.2 is used to calculate the stress ($\sigma^{\mathrm{I}}_{\mathrm{SL}}$) vs. strain ($\varepsilon^{\mathrm{I}}_{\mathrm{SL}}$) response



(a) Full 3D structure of a specimen made of a combination in series of n^{RVE} RVEs of length l^{f}.

(b) Indices defining the fibres (in red) and the interactions involving fibre (i,j) (in black). Subscripts H and V are used respectively for horizontal and vertical interactions. Circled numbers ① to ④ are the relative indices of the neighbours of fibre (i,j).

(c) Interaction $_{V}(i-1,j)$ between quarter-fibres $(i-1,j)$ and (i,j) (see Fig. 4.6b) initially made of two shear-lag segments SL_i and SL_{ii}, and then of two shear-lag segments SL_1 and SL_2 and one broken segment Br_1.

Figure 4.6: Overview of the different scales present in the VTF for aligned hybrid discontinuous composites and indexing system of the different matrices of the model.

of the segment, considering the following geometrical inputs (see Chapter 3):

$$T_{\mathcal{A}} \overset{\text{def}}{=} \frac{\phi^{\text{f}}_{\mathcal{A}}}{4}, \qquad T_{\mathcal{B}} \overset{\text{def}}{=} \frac{\phi^{\text{f}}_{\mathcal{B}}}{4}, \qquad L = \frac{\delta l_{\text{SL}}}{2}, \text{ and}$$
$$t^{\text{m}} \overset{\text{def}}{=} \sqrt{\frac{1}{V^{\text{f}}} \cdot (N_{\mathcal{A}} \cdot \phi^2_{\mathcal{A}} + N_{\mathcal{B}} \cdot \phi^2_{\mathcal{B}}) - (N_{\mathcal{A}} \cdot N_{\mathcal{B}}) \cdot (\phi_{\mathcal{A}} - \phi_{\mathcal{B}})^2} - N_{\mathcal{A}} \cdot \phi_{\mathcal{A}} - N_{\mathcal{B}} \cdot \phi_{\mathcal{B}}, \tag{4.15}$$

where t^{m} is the equivalent matrix thickness (considered to be uniform for all interactions in the specimen), calculated from the overall fibre volume fraction V^{f} (see Chapter 3).

- A segment delimited by two discontinuities in the same fibre is a *broken segment* (subscript 'Br', see for instance the broken segment Br_1 in the centre of the interaction in Fig. 4.6c after the introduction of the fibre break). In that case, the surviving fibre (fibre $(i-1, j)$ in Fig. 4.6c) carries the total load corresponding to that interaction, and the stress ($\sigma^{\text{I}}_{\text{Br}}$) vs. strain ($\varepsilon^{\text{I}}_{\text{Br}}$) response of the broken segment is given by
$$\sigma^{\text{I}}_{\text{Br}} = \varepsilon^{\text{I}}_{\text{Br}} \cdot E_{\text{s}} \cdot \frac{\phi^2_{\text{s}} + \phi^2_{\text{b}}}{\phi^2_{\text{s}}}, \tag{4.16}$$
where the subscripts 's' and 'b' correspond to the 'surviving fibre' (fibre $(i-1, j)$ in Fig. 4.6c) and the 'broken fibre' (fibre (i, j) in Fig. 4.6c) respectively.

The $s_{\max} \geq 2$ segments of an interaction are then combined in series to find the remote stress (σ^{I}) vs. strain (ε^{RVE}) response of the interaction (see Chapter 2):

$$\varepsilon^{\text{RVE}}(\sigma^{\text{I}}) = \frac{\sum_{s=1}^{s_{\max}} \delta l_s \cdot \varepsilon^{\text{I}}_s(\sigma^{\text{I}})}{l^{\text{f}}}. \tag{4.17}$$

4.3.1.3 Tensile response of a fibre

Due to the discontinuous nature of the composite, the tensile stresses in each fibre will be built from the interaction with its four nearest neighbours. The stress field along a fibre therefore consists of two components: an average stress, and stress peaks due to discontinuities in neighbouring fibres. These are calculated by extending the previous model for non-hybrid (Chapter 2) to hybrid fibre-types:

- The *average stress* (superscript 'a') $\sigma^{\text{a}}_k(i, j, \varepsilon^{\text{RVE}})$ seen by the quarter-fibre (i, j) in the interaction with its k^{th} neighbour is calculated by imposing compatibility of displacements and equilibrium of stresses in the two fibres. These conditions

yield

$$\sigma_1^{\mathrm{a}}(i,j,\varepsilon^{\mathrm{RVE}}) = \sigma_{\mathrm{V}}^{\mathrm{I}}(i-1,j)\cdot\frac{\mathbb{E}_{i,j}\cdot(\Phi_{i,j}^2+\Phi_{i-1,j}^2)}{\mathbb{E}_{i,j}\cdot\Phi_{i,j}^2+\mathbb{E}_{i-1,j}\cdot\Phi_{i-1,j}^2}, \tag{4.18a}$$

$$\sigma_2^{\mathrm{a}}(i,j,\varepsilon^{\mathrm{RVE}}) = \sigma_{\mathrm{H}}^{\mathrm{I}}(i,j)\cdot\frac{\mathbb{E}_{i,j}\cdot(\Phi_{i,j}^2+\Phi_{i,j+1}^2)}{\mathbb{E}_{i,j}\cdot\Phi_{i,j}^2+\mathbb{E}_{i,j+1}\cdot\Phi_{i,j+1}^2}, \tag{4.18b}$$

$$\sigma_3^{\mathrm{a}}(i,j,\varepsilon^{\mathrm{RVE}}) = \sigma_{\mathrm{V}}^{\mathrm{I}}(i,j)\cdot\frac{\mathbb{E}_{i,j}\cdot(\Phi_{i,j}^2+\Phi_{i+1,j}^2)}{\mathbb{E}_{i,j}\cdot\Phi_{i,j}^2+\mathbb{E}_{i+1,j}\cdot\Phi_{i+1,j}^2}, \tag{4.18c}$$

$$\sigma_4^{\mathrm{a}}(i,j,\varepsilon^{\mathrm{RVE}}) = \sigma_{\mathrm{H}}^{\mathrm{I}}(i,j-1)\cdot\frac{\mathbb{E}_{i,j}\cdot(\Phi_{i,j}^2+\Phi_{i,j-1}^2)}{\mathbb{E}_{i,j}\cdot\Phi_{i,j}^2+\mathbb{E}_{i,j-1}\cdot\Phi_{i,j-1}^2}. \tag{4.18d}$$

- Additional *stress peaks* (superscript 'p') $\sigma_k^{\mathrm{p}}(i,j,\varepsilon^{\mathrm{RVE}})$ in fibre (i,j) due to discontinuities in its k^{th} neighbouring fibre can be calculated through equilibrium of stresses at the location of those discontinuities:

$$\sigma_1^{\mathrm{p}}(i,j,\varepsilon^{\mathrm{RVE}}) = \sigma_{\mathrm{V}}^{\mathrm{I}}(i-1,j)\cdot\frac{\Phi_{i,j}^2+\Phi_{i-1,j}^2}{\Phi_{i,j}^2}, \tag{4.19a}$$

$$\sigma_2^{\mathrm{p}}(i,j,\varepsilon^{\mathrm{RVE}}) = \sigma_{\mathrm{H}}^{\mathrm{I}}(i,j)\cdot\frac{\Phi_{i,j}^2+\Phi_{i,j+1}^2}{\Phi_{i,j}^2}, \tag{4.19b}$$

$$\sigma_3^{\mathrm{p}}(i,j,\varepsilon^{\mathrm{RVE}}) = \sigma_{\mathrm{V}}^{\mathrm{I}}(i,j)\cdot\frac{\Phi_{i,j}^2+\Phi_{i+1,j}^2}{\Phi_{i,j}^2}, \tag{4.19c}$$

$$\sigma_4^{\mathrm{p}}(i,j,\varepsilon^{\mathrm{RVE}}) = \sigma_{\mathrm{H}}^{\mathrm{I}}(i,j-1)\cdot\frac{\Phi_{i,j}^2+\Phi_{i,j-1}^2}{\Phi_{i,j}^2}. \tag{4.19d}$$

The maximum stress $\hat{\sigma}_{ij}^{\mathrm{f}}(\varepsilon^{\mathrm{RVE}})$ in fibre (i,j), as well as the relative neighbour $k_{\mathrm{crit}}(i,j,\varepsilon^{\mathrm{RVE}})$ responsible for the corresponding peak, can be identified such that:

$$\begin{aligned}\hat{\sigma}_{ij}^{\mathrm{f}}(\varepsilon^{\mathrm{RVE}}) &= \hat{\sigma}_{k_{\mathrm{crit}}(i,j,\varepsilon^{\mathrm{RVE}})}^{\mathrm{f}}(i,j,\varepsilon^{\mathrm{RVE}}) \\ &= \frac{1}{\mathbb{N}_{ij}^{\mathrm{I}}}\cdot\max\left\{\sigma_k^{\mathrm{p}}(i,j,\varepsilon^{\mathrm{RVE}})+\sum_{\substack{k^*=1\\k^*\neq k}}^{4}\sigma_{k^*}^{\mathrm{a}}(i,j,\varepsilon^{\mathrm{RVE}})\right\}_{k=1}^{4},\end{aligned} \tag{4.20}$$

where $\mathbb{N}_{\mathbb{ij}}^{\mathrm{I}}$ is the number of active neighbours interacting with fibre (i,j) (Chapter 2).

Once the maximum stress is calculated using Eq. 4.20, this stress is compared against the individual strength $\mathbb{X}_{ij}$ of each fibre. The strength of each fibre is sampled from a Weibull distribution (Chapter 2), using two failure probabilities for the two fibre

types:

$$F_{\mathcal{A}}(\sigma^{\mathrm{f}}) = 1 - \exp\left(-C_{\mathcal{A}}^{\mathrm{length}} \cdot C_{\mathcal{A}}^{\mathrm{shape}} \cdot \left(\frac{\sigma^{\mathrm{f}}}{\sigma_{0_{\mathcal{A}}}}\right)^{m_{\mathcal{A}}}\right), \tag{4.21a}$$

$$F_{\mathcal{B}}(\sigma^{\mathrm{f}}) = 1 - \exp\left(-C_{\mathcal{B}}^{\mathrm{length}} \cdot C_{\mathcal{B}}^{\mathrm{shape}} \cdot \left(\frac{\sigma^{\mathrm{f}}}{\sigma_{0_{\mathcal{B}}}}\right)^{m_{\mathcal{B}}}\right). \tag{4.21b}$$

In these distributions, $m_{\mathcal{A}}$ and $m_{\mathcal{B}}$ are the Weibull moduli, and $\sigma_{0_{\mathcal{A}}}$ and $\sigma_{0_{\mathcal{B}}}$ are the scale parameters measured with fibres of length l_0 under uniform stresses (scale parameters σ are calculated from the average strengths X_0 and the Weibull moduli m). C_*^{length} and C_*^{shape} are correction factors accounting for the actual fibre length $l^{\mathrm{f}} \gtreqless l_0$ in the discontinuous composite, and for the non-uniform shape of the stress fields along the fibres (Chapter 2).

Once a fibre-break is detected at an applied remote strain $\varepsilon_{\mathrm{PB}}^{\mathrm{RVE}}$ (i.e. when $\hat{\sigma}_{ij}^{\mathrm{f}}(\varepsilon_{\mathrm{PB}}^{\mathrm{RVE}}) \geq \mathbb{X}_{ij}$), the model adds a fibre-break to the vector of fibre discontinuities $\mathbb{x}_{ij}$ and updates the calculations of the stress-strain response of all interactions and fibres affected by the new fibre-break, for $\varepsilon^{\mathrm{RVE}} > \varepsilon_{\mathrm{PB}}^{\mathrm{RVE}}$.

4.3.1.4 Macroscopic response and final failure

Once the stress-strain responses of all $2 \cdot n \cdot (n-1)$ interactions in the p^{th} RVE are calculated, they are combined in parallel (weighted by the respective fibre cross-sections) to give the stress-strain curve of the p^{th} RVE:

$$\begin{aligned}\sigma^{\mathrm{RVE}}(\varepsilon^{\mathrm{RVE}}; p^{\mathrm{RVE}}) = V^{\mathrm{f}} \cdot \Bigg(& \frac{\sum_{i,j} \sigma_{\mathrm{V}ij}^{\mathrm{RVE}}(\varepsilon^{\mathrm{RVE}}; p^{\mathrm{RVE}}) \cdot [\Phi^2(i,j) + \Phi^2(i+1,j)]}{\sum_{i,j} \Phi^2(i,j) + \Phi^2(i+1,j)} \\ & + \frac{\sum_{i,j} \sigma_{\mathrm{H}ij}^{\mathrm{RVE}}(\varepsilon^{\mathrm{RVE}}; p^{\mathrm{RVE}}) \cdot [\Phi^2(i,j) + \Phi^2(i,j+1)]}{\sum_{i,j} \Phi^2(i,j) + \Phi^2(i,j+1)} \Bigg).\end{aligned} \tag{4.22}$$

Then, the n^{RVE} RVEs are combined in series to find the global stress (σ^{∞}) vs. strain (ε^{∞}) curve of the specimen:

$$\varepsilon^{\infty} = \frac{\sum_{p^{\mathrm{RVE}}=1}^{n^{\mathrm{RVE}}} \varepsilon^{\mathrm{RVE}}(\sigma^{\infty}; p^{\mathrm{RVE}})}{n^{\mathrm{RVE}}}. \tag{4.23}$$

The global stress-strain curve calculated through Eq. 4.23 is then capped by a criterion based on fracture mechanics, which aims to simulate unstable crack propagation from a broken cluster of a critical size. This criterion is similar to that previously developed for non-hybrid fibre types (see Chapter 2), and requires the fracture toughness of the composite as an input; for the hybrid-fibre case, this fracture toughness is es-

timated by calculating the debonding and pull-out works associated with the minimum shear-lag length at each interaction in an RVE (full details are provided in App. B).

4.3.1.5 Matlab implementation

The VTF described in Secs. 4.3.1.1-4.3.1.4 has been implemented in Matlab in a way similar to the previous non-hybrid model (see Chapter 2). However, for the hybrid-fibre-composite, three libraries are created for stress-strain responses $\sigma^{\mathrm{I}}_{\mathrm{SL}}(\varepsilon^{\mathrm{I}}_{\mathrm{SL}})$ of the three types of interactions (for the three different fibre combinations at an interface: $\mathcal{AA}$, $\mathcal{AB}$ and $\mathcal{BB}$), and for discrete overlap lengths ranging from 0 to l^{f}. These libraries are called during the simulation in order to eliminate the need to re-calculate the stress-strain response for each shear-lag segment throughout the analysis.

4.3.2 Results and discussion

4.3.2.1 Stress-strain response of hybrid intermingled composites

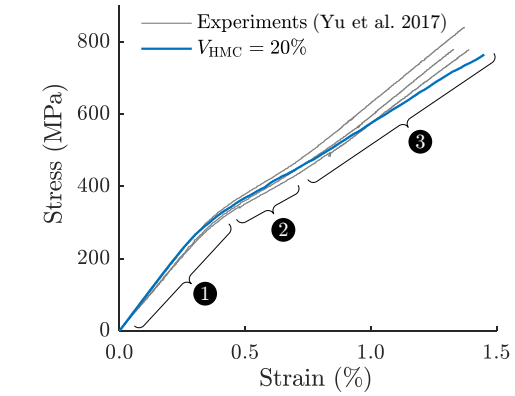
Figs. 4.7a-4.7c show the stress-strain curves predicted by the VTF for HADCs with epoxy matrix, High Modulus Carbon (HMC, corresponding to Low Elongation (LE) fibres), and High Strength Carbon (HSC, corresponding to High Elongation (HE) fibres), for different volume ratios of HMC fibres. Model inputs are given in Tab. 4.5 and were selected to represent the material experimentally tested by Yu et al. [84] (note that for these results, a bilinear law has been chosen as it better represents the brittle epoxy matrix used in the experiments). Model predictions have a very good agreement with experimental results [84,86]; both the model and the experiments show three main regions on the stress-strain curves:

Table 4.5: Material properties of the fibres and matrix used in experiments, taken as inputs for the VTF for hybrid intermingled aligned discontinuous composites (Fig. 4.7).

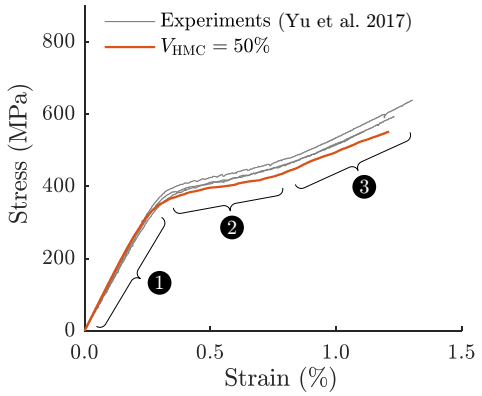
Fibre properties						
	l^{f} * (mm)	ϕ * (μm)	E * (GPa)	$m^{\dagger}$	X_0^{*} (MPa)	l_0 *,† (mm)
High Strength Carbon	3.0	7	225	5.71	4344	25
High Modulus Carbon	3.0	10	860	5.00	3430	1

Matrix properties (bilinear law)	
G^{m} (GPa)	1.5 *
S^{m} (MPa)	60 †
$\mathcal{G}^{\mathrm{m}}_{\mathrm{IIc}}$ (kJ/m^2)	0.8 *,†
V^{f} (%)	30 *

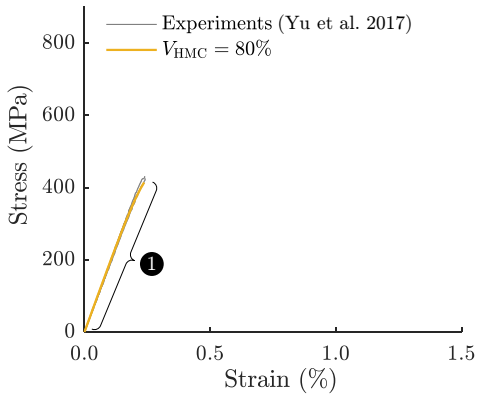
$*$ Specifications of the experimental data [29, 84, 120].
† Calculated from experimental results from literature [11, 75–78, 121].



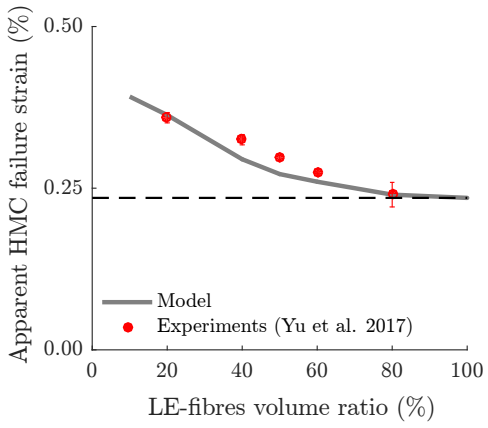
(a) $V_{HMC} = 20\%$.



(b) $V_{HMC} = 50\%$.



(c) $V_{HMC} = 80\%$.



(d) Evolution of the failure strain of the LE fibres with the volume-ratio of LE fibres.

Figure 4.7: Effect of the ratio of LE HMC fibres (V_{HMC}) on the response of HADCs in tension. The three different regions in the stress-strain curves of Figs. (a)-(c) are: (1) linear, (2) fragmentation, and (3) strain-hardening. The experimental data have been provided by HaNa Yu and Marco L. Longana from University of Bristol [84].

- a *linear region*, which appears in all cases, and whose stiffness increases (as expected) with the ratio of HMC fibres;
- a *fragmentation region*, which corresponds to the progressive failure of the LE fibres (HMC). This regions becomes more evident (with more pronounced knees and increased strain-range) as the ratio of LE fibres increases. This agrees with experiments as well as model predictions from the literature [29, 84, 100];
- a *strain-hardening region*, in which the surviving HE fibres (HSC) carry most of the load, after the LE fibres are fragmented to saturation. As the LE fibre ratio

increases (from Fig. 4.7a to 4.7b), this region becomes smaller, and eventually disappears when the ratio of LE fibres is so high that their failure triggers failure of the HE fibres as well (Fig. 4.7c).

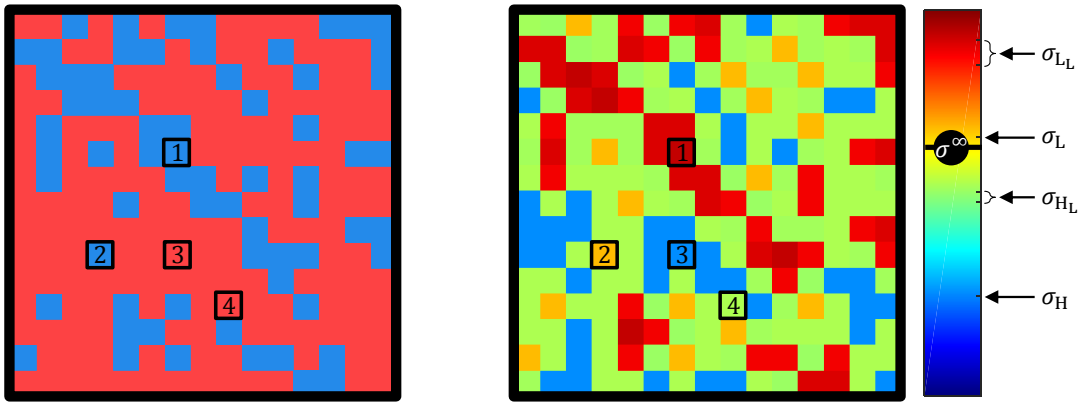
4.3.2.2 Hybrid effects on the apparent failure initiation

In Fig. 4.7d, both the experiments and the VTF suggest that a reduction of the ratio of low-elongation fibres leads to an increase of their apparent failure strain. This apparent failure strain corresponds to the failure point of the composite with a brittle response (as shown in Fig. 4.7c); for a hybrid composite with a pseudo-ductile response (as shown in Figs. 4.7a and 4.7b), the apparent failure strain corresponds to the first knee in the stress-strain curve, and is determined from the intersection of the linear and the fragmentation regions [84, 122]. This hybrid effect leads to an increase to up to 50% in the apparent failure strain of the low-elongation fibre type, which is at the high end of the typical values found for continuous-fibre hybrid composites (around $10 - 50\%$ [28]); although this high value might be due to the particular method used to define the onset of failure of the LE fibres, it could also suggest that the presence of discontinuities in the fibres magnifies the hybrid effect further.

Three reasons can explain this hybrid effect in aligned discontinuous composites. Firstly, as the HE fibres can undergo much higher strains than the LE fibres, HE fibres surrounding LE fibres prevent the propagation of fibre-breaks, thus delaying the gradual fragmentation of LE fibres; this agrees with literature for continuous hybrid composites, where HE fibres have been reported to behave like "crack arrestors" [117]. Secondly, the ability of the matrix to transfer stresses is reduced for hybrid interactions (see Sec. 4.2), and therefore the LE fibres surrounded by HE fibres are expected to have a lower average stress than the LE fibres surrounded by other LE fibres. Thirdly, the ends or breaks in the neighbouring HE fibres will cause stress-concentrations smaller than those due to the LE fibres, as the diameter of the former is smaller; as a result, the stress peaks in a LE fibre (see Eq. 4.19) will be reduced when it only interacts with HE fibres, which delays failure of the LE fibres.

While the first reason given for the hybrid effect should be equally observed in continuous and discontinuous hybrid composites, the last two reasons should have a more significant effect in hybrid composites with discontinuous fibres, which may justify the magnitude of the hybrid effects shown in Fig. 4.7. Hybrid effects are also likely to be magnified by the intimate intermingling obtained with discontinuous composites.

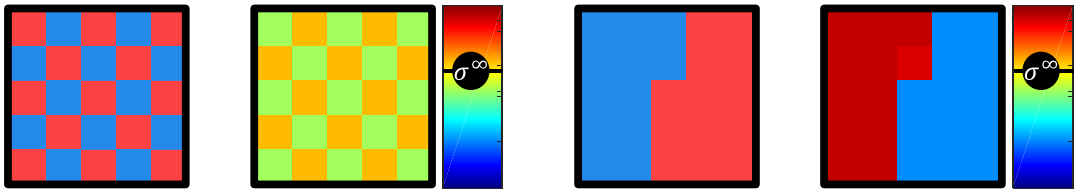
In order to understand better the hybrid effect and the effect of neighbouring fibres, the normalised peak stress of each fibre for an intermingled hybrid microstructure was calculated (see Fig. 4.8). For this study, the length of all overlaps was fixed to $l^{\mathrm{f}}/2$, to



(a) Hybrid intermingled RVE (blue: carbon, red: glass).

(b) Stress peak in each fibre of the RVE shown in Fig. 4.8a.

Figure 4.8: Effect of the neighbouring fibres on the fibre peak stress. Subscripts L and H refer to LE and HL fibres respectively, and subscripts L_L and H_L refer to LE and HE fibres with at least one neighbouring LE fibre.



(a) Fully intermingled RVE (left) and corresponding fibre stress peak (right).

(b) Block RVE (left) and corresponding fibre stress peak (right).

Figure 4.9: Fibre stress peak in intermingled and block configurations.

ensure that the value of the fibre stress peak was only due to the neighbouring fibre types and not to the variability in the overlap length.

Fig. 4.8 shows that LE fibres surrounded only by HE fibres (see box 2) have a much lower peak stress than LE fibres having at least one neighbouring LE fibre (see box 1). In a similar way, HE fibres undergo higher peak stresses when they have at least one neighbouring LE fibres (compare boxes 3 and 4). This result confirms that, for a given remote stress σ^∞, isolating LE fibres "protects" them from higher peak stress and therefore increases their apparent failure strain.

From that observation, Fig. 4.9 shows that LE fibres will undergo lower stresses in a perfectly intermingled microstructure (Fig. 4.9a) than in a "block" microstructure (Fig. 4.9b). This "shielding effect" could not only delay the apparent failure strain of the LE fibres, but also delay the final failure of the composites. This potential of fully intermingled HADCs was investigated further in [123].

4.3.2.3 Contribution to the state of the art

The results obtained with the models for HyBaM and HADCs can be discussed in the scope of the literature in hybrid and discontinuous composite materials:

a. This work addresses two families of composites (discontinuous [24, 33, 36, 38, 42, 105, 108, 110, 124–126] and hybrid [29, 99, 100, 103, 114, 116, 117, 119, 127]) which had been modelled independently until now, and allows one to understand and predict the combined effect of discontinuous architectures and hybridisation in composites.

b. The shear lag model developed in Sec. 4.2 is the first one in the literature to extend the widely-used shear-lag approach [24, 38, 104–109] to discontinuous hybrid composites, considering a generic non-linear response of the matrix. In particular, the model shows that the stresses in the matrix of a hybrid overlap are not symmetric, which decreases the load transmissible from a platelet/fibre to another, and may therefore reduce the strength of a hybrid discontinuous composite when compared to a non-hybrid equivalent.

c. The VTF developed in Sec. 4.3 for HADCs captures features observed in experiments but not predicted by existing models in the literature [29, 99, 100, 119]:
   - The VTF predicts that fragmentation of the LE fibres is gradual and occurs with an increase in the remote stress, and that the fragmentation region becomes steeper as the LE-fibres volume ratio decreases (see Figs. 4.7a and 4.7b), as observed in experiments. On the contrary, most models from the literature assume that fragmentation of the LE fibres occurs at a constant stress [100, 119].
   - The VTF predicts the hybrid effect on the failure strain of the LE fibres (Fig. 4.7d) as reported in the literature, due to the ratio of low-elongation to high-elongation fibres and to the degree of intermingling of the two fibre types.

d. The VTF can predict the tensile response of HADCs accurately (see Fig. 4.7) and quickly (the model for a specimen with 10 000 fibres runs in less than 30 seconds), and therefore bridges simpler analytical models [99, 100, 119] and more realistic but computationally expensive FE models [128, 129] in the literature.

4.4 Conclusion

Analytical and numerical models have been developed to calculate the stress-strain response of aligned hybrid discontinuous composites in tension. The following conclusions can be reached:

- A shear-lag model for hybrid brick-and-mortar composites, considering a generic non-linear matrix response (including fracture), shows that hybridisation promotes earlier yielding and fracture of the matrix, and therefore reduces the load carrying capability of HADCs.
- A virtual testing framework for intermingled HADCs was developed and validated against experiments from the literature, and it was able to predict the non-linear stress-strain curves observed in the experiments. In particular, the model captures the pseudo-ductile response of HADC with a high ratio of high-elongation fibres (with a linear region, a fragmentation region and a strain-hardening region), as well as the brittle response of hybrid composites with a high ratio of low-elongation fibres.
- The virtual testing framework is able to capture the hybrid effect on the apparent failure strain of the low-elongation fibres. The model suggests that the presence of high-elongation fibres shields the low-elongation fibres from stress-concentrations, thus delaying the accumulation of breaks in the low-elongation fibres and the corresponding loss of stiffness.

The virtual testing framework is computationally efficient and has been validated experimentally; consequently, it can be used to perform virtual tests and to identify the effect of the microstructure and micromechanical properties on the stiffness, stress-strain non-linearity and ultimate failure of HADCs.

Part II

Hierarchical discontinuous composites for increased damage tolerance

Chapter 5

Increasing damage tolerance of composites using hierarchical brick-and-mortar microstructures

5.1 Introduction

The damage tolerance found in naturally-occurring composites was found to be mainly due to the presence of discontinuities and hierarchies in their microstructures. The fascinating properties of such composites motivated numerous attempts to model and mimic their microstructure and mechanical response. Gorbatikh et al. [41] showed, with their model, that carefully engineered hierarchical microstructures (with different sizes of inclusions) could eliminate the stress concentrations at the larger inclusions, hence changing the failure mechanism to a more stable one. Experimentally, nacre-like synthetic composites achieved a 700-fold increase in the toughness of the brittle constituent [130], and crack deflection capabilities [131]. Other synthetic hierarchical discontinuous composites displayed damage diffusion, preventing catastrophic failure and increasing damage tolerance [132].

Various methods have been developed to synthesise composites with bio-inspired hierarchical discontinuous microstructures, and can be classified in two categories [43]. The "bottom-up" strategy creates the composite by assembling the different constituents together; this strategy includes, amongst others, multimaterial 3D printing [132] which provides fast prototyping of samples, and polymer-coating process methods [47] suitable for large-scale production. The second approach is the "top-down" strategy, in which an existing block of material is modified to create the discontinuities and hierarchies in the microstructure; this includes 3D laser engraving [130] and laser micro-cutting of prepregs [131, 133].

Unlike conventional composites, hierarchical discontinuous microstructures are more challenging to model, as they involve reinforcements of very different scales [134, 135]. Full FE models and Molecular Dynamics Simulations have been considered [136] but, being computationally expensive, they are limited in the size of the RVE that they can study. This is also a problem for the Embedded Region (ER) technique, in which two independent FE meshes (representing host and embedded regions) are created and tied together [134], allowing for instance to model carbon nanotubes within a polymeric matrix. Another solution is multi-scale FE models of RVEs [43, 44, 137, 138], where the homogenised mechanical properties of RVEs are calculated in smaller-scale FE models, and then applied as inputs to larger-scale FE models.

An alternative approach to model hierarchical discontinuous composites is to replace FE with simplified analytical methods, applied to an explicit representation of the microstructure [40, 41]. For instance, Gorbatikh et al. [41] developed a model for composites reinforced by inclusions with two very distinct sizes, which were modelled by rigid lines.

Another common way to model hierarchical materials is to view them as self-similar [34, 42, 139] or quasi-self-similar [36] microstructures. The self-similar assumption considers that all hierarchical levels of the microstructure are morphologically and mechanically similar, and differ only on the absolute value of a characteristic length; as a result, homogenised mechanical properties (e.g. strength, flaw tolerance) can be calculated by the same approach at all hierarchical levels [42, 74, 140]. However, it has been shown [36] that, in some cases, the assumption of self-similarity fails to correctly predict and mimic the mechanical response of hierarchical composites, even when their microstructure is morphologically self-similar.

This chapter proposes, designs and demonstrates the potential of combining discontinuities and hierarchies in a microstructure, to promote stable energy dissipation mechanisms and achieve damage tolerance. This is achieved through modelling, manufacturing and testing of Hierarchical Brick-and-Mortar (HiBaM) composites, which are realised through the "top-down" modification of (originally brittle) Carbon-Fibre Reinforced Polymers.

The chapter is organised as follows: Sec. 5.2 proposes and compares two models (analytical and numerical) to predict the tensile response of HiBaM composites, and designs microstructures to be manufactured and tested. Sec. 5.3 explains the experimental methods used for the manufacturing and the testing of the HiBaM specimens. Sec. 5.4 presents the experimental results and discusses the potential of hierarchical discontinuous composites to achieve increased damage-tolerance. Finally, Sec. 5.5 draws the main conclusions of this work.

5.2 Design of hierarchical microstructures

5.2.1 Non-self-similar numerical model

5.2.1.1 Model definition

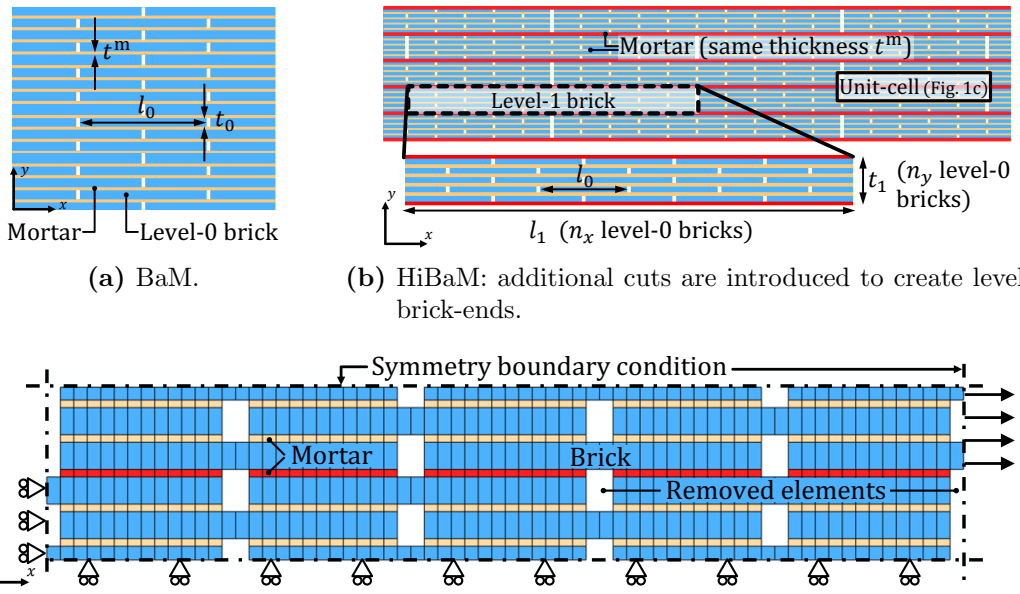
The model system studied in this work is a HiBaM composite with two levels of hierarchy. Simple BaM microstructures are composed by bricks of one single size and, therefore, display a single level of hierarchy (with perfectly staggered bricks as shown in Fig. 5.1a); HiBaM composites use the simple BaM microstructure (hereafter identified as level-0) as the building blocks of a larger BaM microstructure (hereafter identified as level-1), as shown in Fig. 5.1b. The lengths and thicknesses of level-0 and level-1 bricks are respectively l_0, t_0, l_1, t_1; the size of a level-1 brick can also be defined by the number of level-0 bricks it is made of $(n_x \times n_y)$. The thickness of the mortar layer between bricks is t^{m} which, in this work, remains equal at both hierarchical levels. Tab. 5.1 describes the geometry of the HiBaM microstructures used throughout this chapter.

This HiBaM microstructure was modelled *numerically*, with FE simulations using the Abaqus software [141]. The symmetries and the periodicity of the microstructure allow the entire material to be modelled by the unit-cell shown in Fig. 5.1c. The level-0 bricks are modelled using orthotropic linear-elastic plane-stress elements and Hashin failure criteria, with properties representative of a unidirectional (UD) carbon-epoxy thin ply (see Tab. 5.2). The mortar – hereafter designated as "matrix" – of both level-0 and level-1 is assumed to be created by an epoxy-rich interply region between the bricks, which is modelled using cohesive elements (see Tab. 5.2). The cuts defining the ends of the level-0 and level-1 bricks were represented by removing elements at the appropriate locations (see Fig. 5.1c). The structure was loaded in longitudinal tension by applying the boundary conditions shown in Fig. 5.1c.

It is important to notice that this numerical model does not assume self-similarity, as the unit-cell represents each level-0 "brick" of the microstructure explicitly, rather than homogenising the mechanical response of the level-0 BaM material within the level-1 bricks.

5.2.1.2 Mechanical response of HiBaM composite

The tensile response observed in the numerical model of the HiBaM microstructures is composed of three different stages, which are explained bellow and illustrated in Fig. 5.2 for the *nominal-a* microstructure (see Tab. 5.1):



(a) BaM.

(b) HiBaM: additional cuts are introduced to create level-1 brick-ends.

(c) Unit-cell of the numerical model for HiBaM composites (zoom-in from (b)).

Figure 5.1: Microstructures of BaM and HiBaM composites.

Table 5.1: Different microstructures considered in the design (Sec. 5.2) and testing (Sec. 5.4) of HiBaM microstructures. Parameters n_x and n_y are defined in Fig. 5.1b.

	Microstructure	$l_0/l_{0\text{nom}}$	$t_0/t_{0\text{nom}}$	n_x	n_y
($l_{0\text{nom}} = 460$ μm, $t_{0\text{nom}} = t_{0\text{nom-a}} = 22$ μm)	*BaM-a*	1	1	1	1
Parametric study on geometry of level-0 bricks ($l_{0\text{nom}} = 460$ μm, $t_{0\text{nom}} = t_{0\text{nom-a}} = 22$ μm)	*Nominal-a*	1	1	5	5
	Short-a	1/2	1	5	5
	Long-a	2	1	5	5
	Scaled-up-a	2	2	5	5
Parametric study on geometry of level-1 bricks ($l_{0\text{nom}} = 460$ μm, $t_{0\text{nom}} = t_{0\text{nom-b}} = 28$ μm)	*Nominal-b*	1	1	5	5
	Thick-b	1	1	5	11
	Long-b	1	1	11	5
	Large-b	1	1	11	11

i. *Linear–elastic stage* (up to point I in Fig. 5.2). This stage ends with damage initiation in the matrix, starting from the corners of neighbouring level-1 bricks (as shown by the stiffness degradation of the matrix in Fig. 5.2d, point I). Up to that point, the energy stored in the material is purely elastic, and there is no energy dissipated through damage (see Fig. 5.2b);

ii. *Damage accumulation stage* (between points I and III in Fig. 5.2). The longitudinal stresses in the bricks increase further (as shown by the stress fields in Fig. 5.2c, points II and III), but damage in the matrix propagates from the corners of level-1 bricks towards the centre of level-1 bricks, following the overlaps between level-0 bricks in a staircase pattern (as shown in Fig. 5.2d, points II

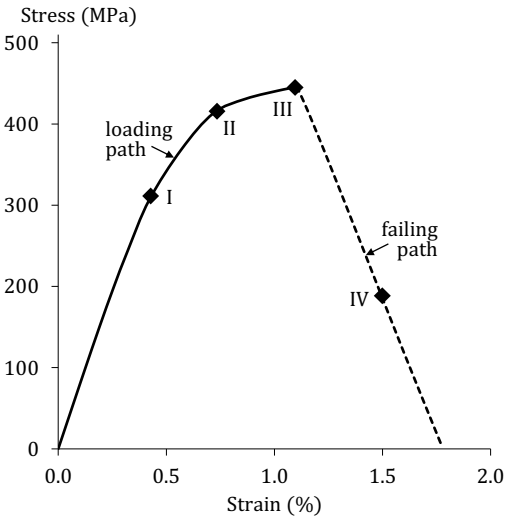
Table 5.2: Material properties of the carbon/epoxy thin ply prepreg used in the models and the experiments [131, 142]. Superscripts 'b', 'm', and 'p' refer to the 'brick', 'matrix', and 'ply' properties respectively. The two ply-thickness values correspond to two prepregs used experimentally, with two different fibre volume fractions.The longitudinal Young's modulus and strength of the bricks are calculated from values for the ply ($t^{p0} = 23$ µm, $E^{p0} = 102$ GPa, and $X^{p0} = 1892$ MPa [131]), using $E^{b} = E^{p0} \cdot t^{p0}/t_{0nom}$, and $X^{b} = X^{p0} \cdot t^{p0}/t_{0nom}$. The mode-I strength and toughness of the cohesive elements representing the matrix were set to unrealistically high values to mimic mode-II dominated failure.

Property	Variable	Unit	Set a	Set b
Prepreg ply thickness	t^{p}	µm	23	29
Level-0 brick thickness	t_{0nom}	µm	22	28
Thickness of the rich resin region between plies	t^{m}	µm	1	1
Fibre volume fraction in the ply	V^{f}	%	43	34
Longitudinal Young's modulus of the level-0 bricks	E^{b}	GPa	106.6	83.8
Longitudinal tensile strength of the level-0 bricks	X^{b}	MPa	1978	1554
Matrix mode II fracture toughness	$\mathcal{G}^{m}_{IIc}$	kJ/m^2	0.90	0.90
Matrix shear strength	S^{m}	MPa	88.5	88.5

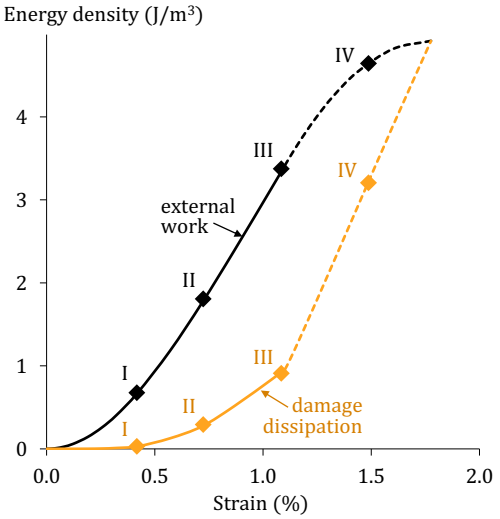
and III). Consequently, the material loses tangent stiffness in an almost discrete way (see different slopes up to point I, between points I and II, and between points II and III in Fig. 5.2a), corresponding to damage propagation in each individual step of this staircase pattern. Moreover, Fig. 5.2b indicates that energy is being dissipated through damage of the matrix during this stage;

iii. *Post–failure stage* (after point III in Fig. 5.2). The maximum load–bearing capacity of the composite (at point III) is defined when a crack tip develops in the matrix (i.e. when damage equals 1 at the interface with the corners of neighbouring bricks); for the *nominal-a* geometry analysed in Fig. 5.2, this also corresponds to the moment when matrix damage within a level-1 brick creates a full rhombus shape. Subsequently, damage localises in one of the two level-1 bricks in the unit-cell (as shown in Fig. 5.2d, point IV), and the level-0 bricks unload elastically (as shown in Fig 5.2c, point IV).

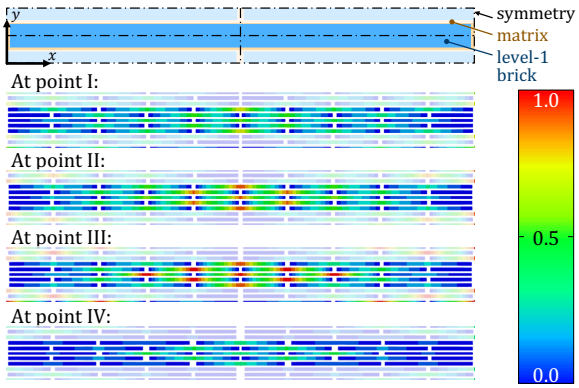
The results from Fig. 5.2 show a high amount of energy dissipated stably through diffused damage and significant non-linearity in the overall stress-strain response of the HiBaM composite, but one has to keep in mind that these results were obtained from a unit-cell model, which may not be representative of a full-scale specimen where damage could localise. To explore the possibility of damage localisation, a full scale HiBaM composite specimen with 48 unit-cells was modelled as shown in Fig. 5.3, with no symmetry or periodicity imposed. Fig. 5.3a shows that the introduction of hierarchies prevents damage localisation: indeed, the rhombus shape of matrix damage found in the unit-cell model (Fig. 5.2d) is also observed throughout the full composite specimen,



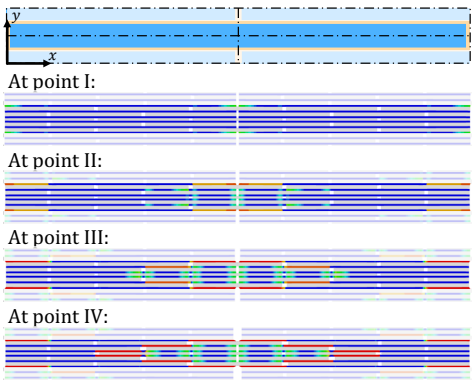
(a) Stress-Strain curve of the HiBaM composite.



(b) Energy dissipation in the HiBaM composite.



(c) Pattern of longitudinal tensile stresses in the level-0 bricks (normalised by the maximum value observed), mapped on 4 unit-cells for clarity.



(d) Pattern of stiffness degradation in the matrix, mapped on 4 unit-cells for clarity.

Figure 5.2: Mechanical response of a HiBaM composite (with a *nominal-a* microstructure, defined in Tab. 5.1), as predicted by a unit-cell numerical model.

not only at the failure site (where the rhombus pattern is fully closed, leading to final failure of the composite), but also away from the failure site.

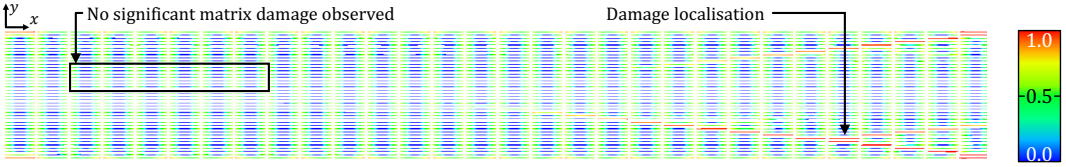
5.2.2 Self-similar analytical model

5.2.2.1 Model definition

An *analytical* model was also developed for the HiBaM composite microstructures described in Sec. 5.2.1.1. However, unlike the numerical model detailed in Sec. 5.2.1.2,



(a) In a HiBaM virtual specimen, matrix damage is dispersed in all level-1 bricks, throughout the entire microstructure.



(b) In a BaM virtual specimen, matrix damage localises (on the right) and is not diffused throughout the microstructure.

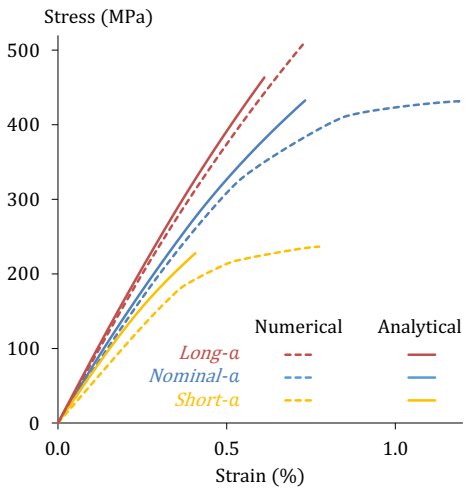
Figure 5.3: Stiffness degradation of the matrix in BaM and HiBaM virtual specimens.

this analytical model uses the self-similar assumption which, for this particular microstructure, is defined as follows: bricks of each hierarchical level (level-0, level-1, ...) are assumed to have homogeneous material properties, with a homogenised stress-strain response, and with a uniform response through the thickness of the brick.

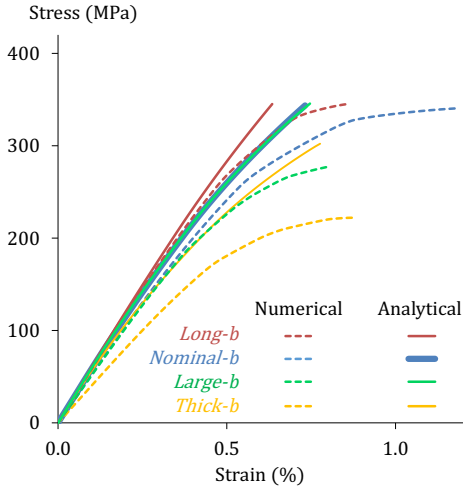
The analytical self-similar model predicts the response of the level-0 BaM microstructure using a shear-lag approach for simple BaM composites with linear-elastic bricks and bilinear matrix response [24]. Subsequently, the non-linear stress-strain curve of the level-0 BaM microstructure is approximated by a piecewise linear curve, and is used as the input for the brick material response of the BaM structure of level-1; this required extending the existing formulation for linear-elastic bricks [24] to non-linear elastic bricks (see App. G). Therefore, assuming that the level-0 bricks have a linear elastic response, the model is used recursively to calculate the homogenised stress-strain responses of the different hierarchical levels of a HiBaM microstructure.

5.2.2.2 Comparison of numerical and analytical models

The results of the analytical model for HiBaM composites with two hierarchical levels are compared to the numerical results in Fig. 5.4, for different brick geometries (described in Tab. 5.1). Although the trend for how the initial stiffness of a HiBaM composite changes with different level-0 brick geometries seems to be correctly captured by the analytical model (Fig. 5.4), the loss of tangential stiffness due do damage dissipation is not well predicted by the analytical model, whose results present very little non-linearity compared to the numerical model. Since the same material properties and constitutive laws were used in both models, this suggests that the analytical model



(a) Stress-strain curves for different geometries of the level-0 bricks.



(b) Stress-strain curves for different geometries of the level-1 bricks.

Figure 5.4: Comparison of the stress-strain curves predicted by the analytical model (using the self-similar assumption) against the numerical model, for HiBaM composites with two levels and geometries defined in Tab. 5.1. The stress fields for the *nominal-a* microstructure are shown in Fig. 5.5.



(a) Analytical model.

(b) Numerical model.

Figure 5.5: Tensile stress fields within a level-1 brick calculated by the analytical and numerical models, for the *nominal-a* microstructure. The colour scale is normalised to the maximum stress reached in the numerical model.

is not able to account for the progressive damage propagation within each level-1 brick. Therefore, the analytical model cannot correctly calculate the stress-strain response of HiBaM composites, and becomes progressively more inaccurate as the level-0 bricks become shorter (Fig. 5.4a), and as level-1 bricks become thicker and larger (Fig. 5.4b).

The results of Fig. 5.4 show the limitation of the self-similar assumption, as it neglects that the real failure mechanism in HiBaM composites (as predicted by the numerical model) requires the interaction between the different hierarchical levels: the level-1 brick-ends trigger stress-concentrations in the neighbouring level-1 bricks, initiating damage in the matrix which propagates between the level-0 bricks. Moreover, the assumption of self-similarity implies a homogenisation of the stress, and therefore a uniform stress through the thickness of the bricks of all levels (compare the stress fields calculated by the analytical model (Fig. 5.5a) and by the numerical model (Fig. 5.5b)); although this seems acceptable for level-0 bricks, Fig. 5.5b shows that the stress fields in the level-1 bricks is complex and not uniform through the thickness. Therefore, the

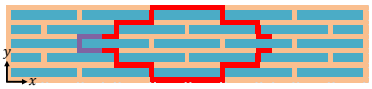
remaining of this work will use the numerical model (although computationally more expensive) to investigate the behaviour of HiBaM composites.

5.2.3 Optimisation of the HiBaM microstructure

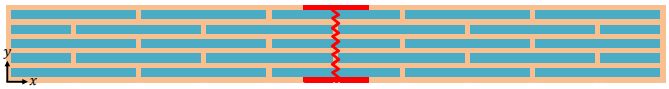
Intuitively, Sec. 5.2.1.2 suggests the existence of an optimal microstructure for HiBaM composites, to maximize the non-linearity of the stress-strain curve and the stable energy dissipation through damage diffusion. Let us first explore how the geometry of the level-0 bricks affects the response of HiBaM composites (i) qualitatively, looking at the failure mechanisms (Fig. 5.6), and (ii) quantitatively, looking at the stress-strain curves and the energy dissipated (Fig. 5.7). This will be done by comparing the response of HiBaM composites with different level-0 brick geometries against the *nominal-a* microstructure (as specified in Tab. 5.1), while keeping the number of level-0 bricks in each level-1 brick unchanged (to preserve the rhombus shape of matrix damage):

- Increasing the length of level-0 bricks (Fig. 5.6b) leads to fracture of the level-0 bricks and, consequently, premature and brittle failure of the HiBaM composite, leading to a quasi-linear response (see *long-a* in Fig. 5.7a) and very little damage energy dissipated (see *long-a* in Fig. 5.7b);
- However, decreasing the length of level-0 bricks (Fig. 5.6c) leads to a decrease in the stiffness and the strength of the HiBaM composite (see *short-a* in Fig. 5.7a), as the shear-lag stress transfer becomes less effective. Consequently, although the ratio of damage to elastic energy remains the same as in the *nominal-a* case, the absolute value of both energies is reduced in the *short-a* microstructure (see *short-a* in Fig. 5.7b);
- Scaling-up both the length and the thickness of level-0 bricks (Fig. 5.6d) increases the energy release rate for delamination between the bricks, and triggers premature unstable failure of the overlaps between bricks [24]. Therefore, the stress-strain curve of the HiBaM composite will stop before the maximum non-linear stage is reached (compare *scaled-up-a* and *nominal-a* in Fig. 5.7a), and less energy will be dissipated through diffuse damage of the matrix (see *scaled-up-a* in Fig. 5.7b). This agrees with existing literature, which stresses the importance of using small-scale building blocks in hierarchical structures [25, 32, 143].

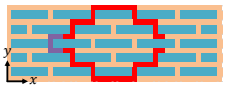
Let us now investigate how the geometry of the level-1 bricks affects the response of the HiBaM composite (i) qualitatively, looking at the failure mechanisms (Fig. 5.8), and (ii) quantitatively, looking at the stress-strain curves and the energy dissipated (Fig. 5.9). This will be done by comparing the response of HiBaM with different level-1 brick geometries (achieved by changing the number of level-0 bricks inside a level-1 brick) against the *nominal-b* microstructure (as specified in Tab. 5.1), while keeping the size of level-0 bricks unchanged:



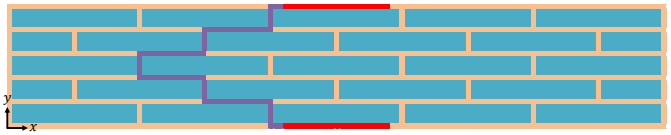
(a) *Nominal-a* level-0 brick length, with formation of a full rhombus pattern of damage in the matrix.



(b) *Long-a* level-0 brick geometry, with fracture of level-0 bricks.



(c) *Short-a* level-0 brick geometry, with a smaller shear-lag stress-transfer length.



(d) *Scaled-up-a* level-0 brick geometry, with earlier unstable delamination.

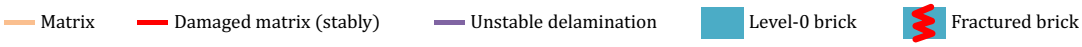
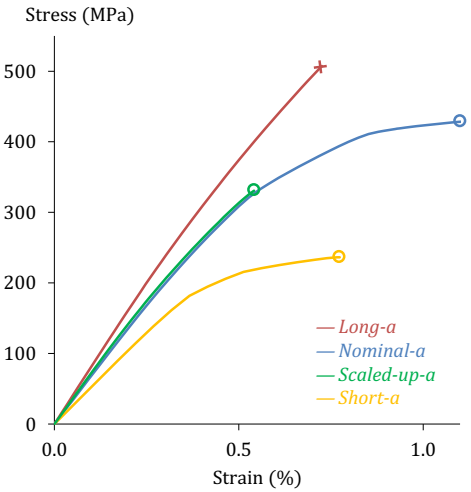
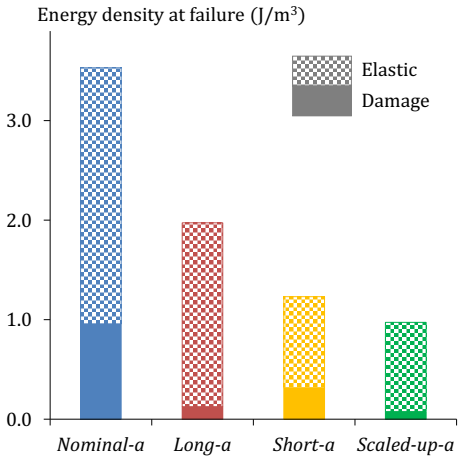


Figure 5.6: Effect of the geometry of level-0 bricks on the failure mechanism of a level-1 brick in HiBaM composites.



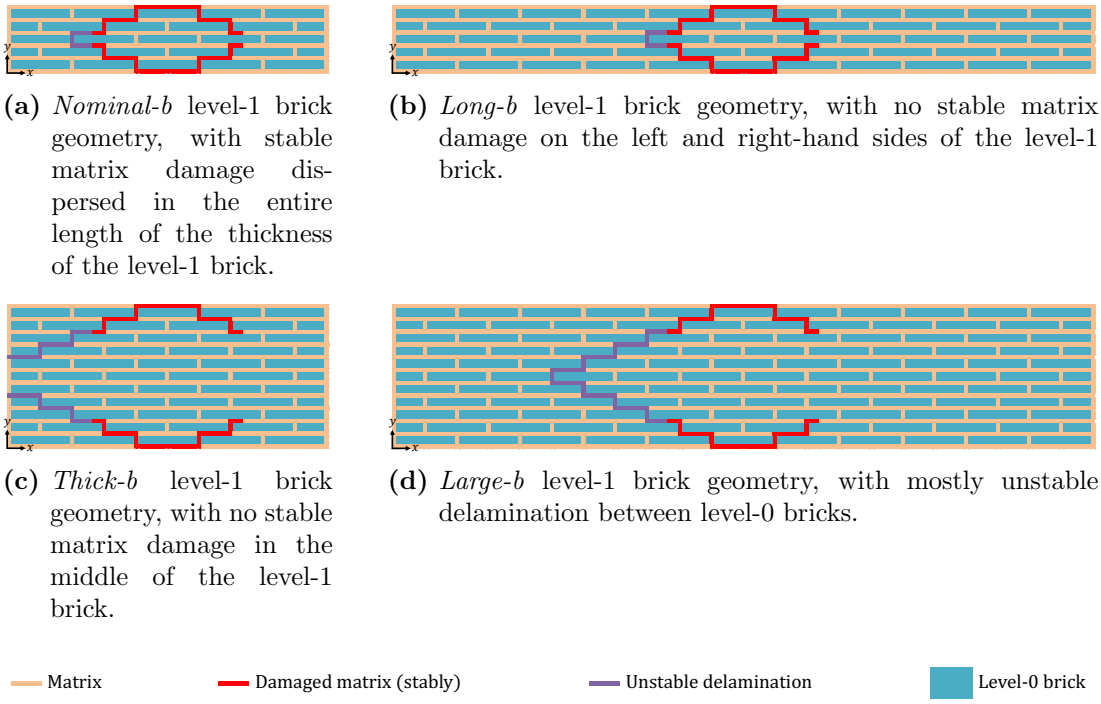
(a) Stress-strain curves. Final failure modes: matrix delamination (○), level-0 brick fracture (×).



(b) Internal energy at the point of maximum stress.

Figure 5.7: Mechanical response calculated by the numerical model for HiBaM composites with different geometries of level-0 bricks.

- When the length of level-1 bricks is increased (i.e. when n_x increases, see Fig. 5.8b), both the failure mechanism (i.e. damage of the matrix along a rhombus pattern) and the strength of the HiBaM composite remain unchanged; however, only the matrix nearer the centre (horizontally) of each level-1 brick is affected by damage degradation, as the rhombus pattern of damage does not reach the ends of the level-1 bricks; this yields little strain at failure (see *long-b* in Fig. 5.9a)



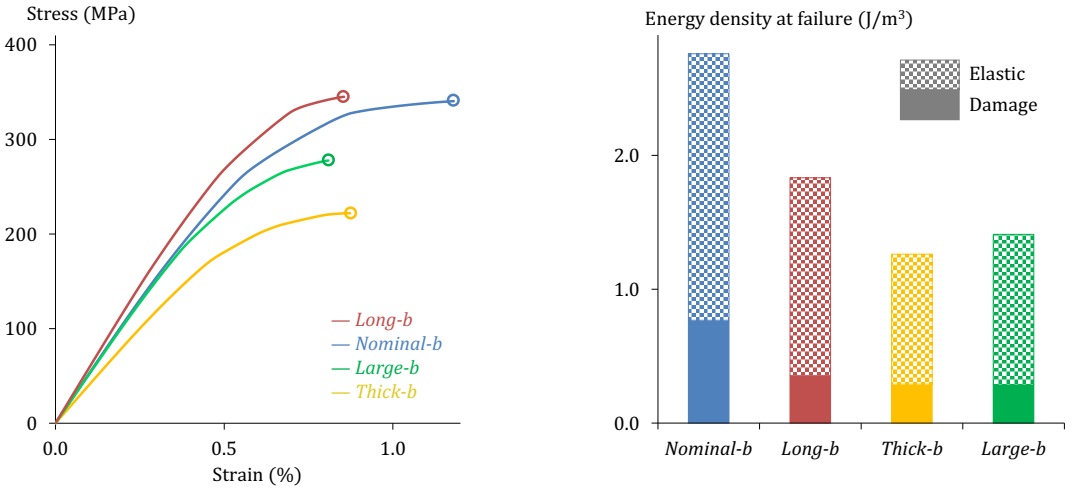
(a) *Nominal-b* level-1 brick geometry, with stable matrix damage dispersed in the entire length of the thickness of the level-1 brick.

(b) *Long-b* level-1 brick geometry, with no stable matrix damage on the left and right-hand sides of the level-1 brick.

(c) *Thick-b* level-1 brick geometry, with no stable matrix damage in the middle of the level-1 brick.

(d) *Large-b* level-1 brick geometry, with mostly unstable delamination between level-0 bricks.

Figure 5.8: Effect of the geometry of level-1 bricks on the failure mechanism of HiBaM composites.



(a) Stress-strain curves. Failure mode: matrix delamination (○).

(b) Internal energy at the point of maximum stress.

Figure 5.9: Mechanical response calculated by the numerical model for HiBaM composites with different geometries of level-1 bricks.

and much less damage energy dissipated (see *long-b* in Fig. 5.9b) than for the *nominal-b* level-1 brick length;

- When the thickness of level-1 bricks is increased (i.e. when n_y increases, see Fig. 5.8c), the middle (vertically) of each level-1 brick is not loaded, and therefore

the stiffness and the strength of the HiBaM composite are reduced (see *thick-b* in Fig. 5.9a). As the rhombus damage pattern cannot fully close within one level-1 brick (as it reaches the vertical boundary with the neighbouring bricks), less energy is dissipated stably through damage (see *thick-b* in Fig. 5.9b) than for the *nominal-b* level-1 brick thickness;

- When both the length and the thickness of the level-1 bricks are scaled-up (i.e. both n_x and n_y increase, see Fig. 5.8d), the length of the rhombus damage pattern reaches a critical size above which the delamination propagates unstably, yielding premature failure of the level-1 brick (compare *large-b* to *nominal-b* in Fig. 5.9a). Moreover, the ratio of debonded-matrix-length to level-1 brick-area is smaller than for the *nominal-b* geometry, and therefore the energy dissipated by matrix damage is reduced (see *large-b* in Fig. 5.9b).

5.2.4 Comparison of BaM and HiBaM composites

Let us now compare the *nominal-a* HiBaM microstructure with the *BaM-a* architecture. As already mentioned in Sec. 5.2.1, Fig. 5.3a suggests that energy is dissipated through matrix damage throughout the entire virtual specimen when hierarchies are used. On the contrary, for a simple BaM virtual specimen of the same size, Fig. 5.3b suggests that the regions with significant matrix damage are localised at a few brick interfaces only, and damage propagates unstably in a specific region of the material, causing catastrophic failure of the composite specimen with no significant accumulation of damage away from the failure site. These different patterns of matrix damage suggest that HiBaM composites do not suffer from damage localisation, unlike BaM composites.

Quantitatively, the energy dissipated through damage by the HiBaM microstructure is two times higher than that of the BaM equivalent. Moreover, the energy dissipated through damage represents only 9% of the total energy for BaM composites, against 27% for the HiBaM composites.

5.3 Experimental method

5.3.1 Material properties

All microstructures identified in Tab. 5.1 (except *scaled-up-a*) have been manufactured using SkyFlex USN020A carbon/epoxy prepregs, whose properties are given in Tab. 5.2. Note that the thicknesses of the plies used for the parametric studies of

the level-0 brick geometry ($t_{0\text{nom}-\text{a}}$) and of the level-1 brick geometry ($t_{0\text{nom}-\text{b}}$) are different, because the plies were cut from two different rolls (see Tab. 5.2).

5.3.2 Manufacturing plates and specimens with HiBaM microstructures

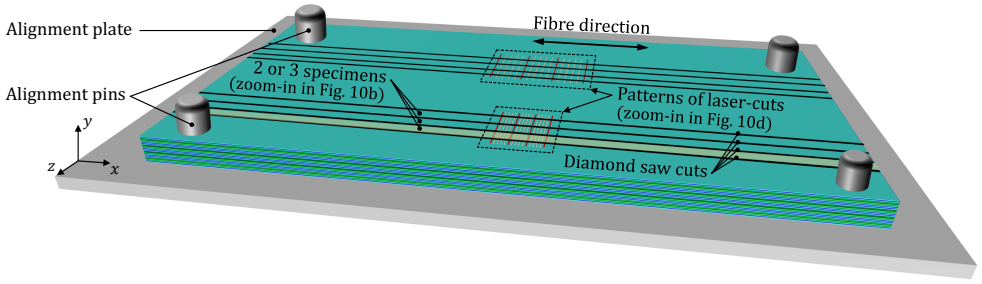
The hierarchical microstructures identified in Sec. 5.2 were manufactured using the following process [133]:

a. The discontinuities in the HiBaM microstructures were laser-cut in thin CFRP prepreg plies using a Diode Pumped Solid State (DPSS) micromachining system, which provided sufficient accuracy for the microstructures to be manufactured [131]. The cuts were introduced perpendicularly to the fibre direction in each prepreg ply, according to the patterns shown in Figs. 5.10b and 5.10c, to create the brick-ends. Two patterns of cuts (A and C, as shown in Fig. 5.10c) were required to manufacture a simple BaM microstructure (in which the cuts generated the end of the level-0 bricks); to create the ends of the level-1 bricks in the HiBaM microstructures, two additional patterns of cuts (B and D shown in Fig. 5.10c) were required.

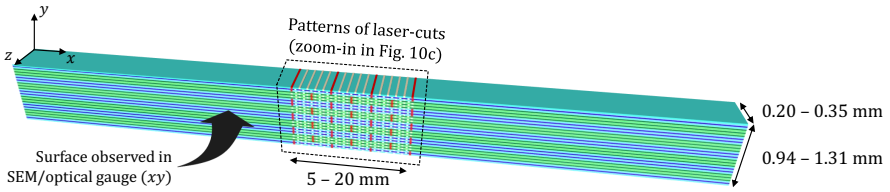
b. In order to achieve high precision in the through-the-thickness alignment of the laser-cut patterns in the microstructure, alignment holes were also laser-cut from the prepreg plies. The plies with the laser-cut patterns were then laid-up as shown in Fig. 5.10 and as specified in Tab. 5.3, using the alignment holes along with an alignment rig with pins (used to keep the same reference frame for all plies [133]) to align the patterns of cuts as accurately as possible. This created uncured plates with HiBaM microstructures (see Fig. 5.10a).

Table 5.3: Layup sequence for each microstructure manufactured.

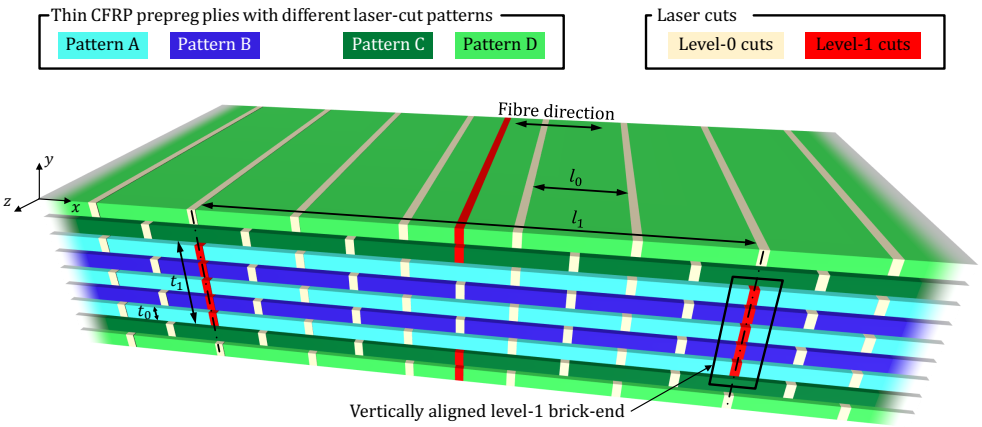
Microstructure	Number of plies through the thickness	Layup sequence (see Sec. 5.3.2 and Fig. 5.10c)	Plate thickness (mm)
BaM-a	41	$(AC)_{20}A$	0.94
Nominal-a	41	$(ABA)(CDCDCABABA)_3(CDCDC)(ABA)$	0.94
Short-a	41	$(ABA)(CDCDCABABA)_3(CDCDC)(ABA)$	0.94
Long-a	41	$(ABA)(CDCDCABABA)_3(CDCDC)(ABA)$	0.94
Nominal-b	41	$(ABA)(CDCDCABABA)_3(CDCDC)(ABA)$	1.19
Thick-b	45	$(BA)_3((CD)_5C)((AB)_5A)((CD)_5C)(AB)_3$	1.31
Long-b	41	$(ABA)(CDCDCABABA)_3(CDCDC)(ABA)$	1.19
Large-b	45	$(BA)_3((CD)_5C)((AB)_5A)((CD)_5C)(AB)_3$	1.31



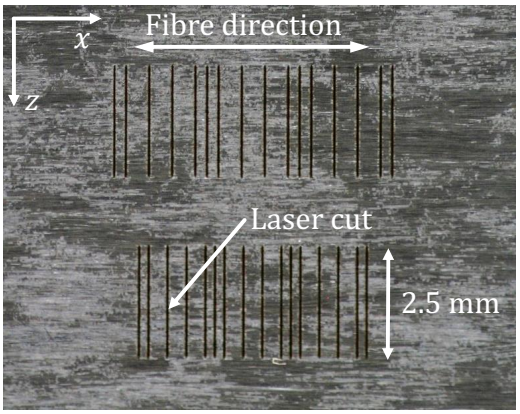
(a) Lay-up and alignment of the prepreg plies using the alignment rig (not to scale).



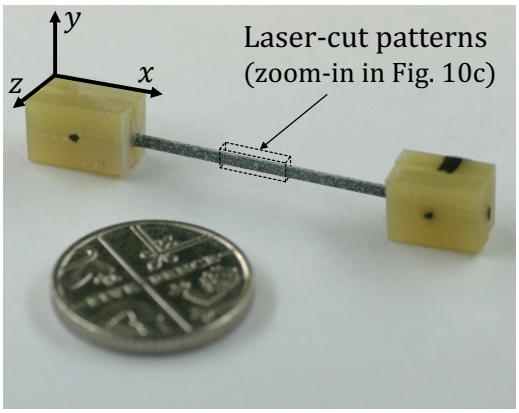
(b) Overview of one HiBaM specimen (not to scale).



(c) Level-1 brick of a *Nominal-a* HiBaM microstructure, manufactured with thin plies with four different laser-cut patterns (not to scale). The layup sequence shown here is $DC(ABABA)CD$ (the complete layup sequence is given in Tab. 5.3).



(d) Hierarchical patterns of laser-cuts in a thin prepreg ply.



(e) End-tabbed specimen. The hierarchical microstructure is in the centre of the specimen, facing the z-direction.

Figure 5.10: Manufacturing process of HiBaM composites.

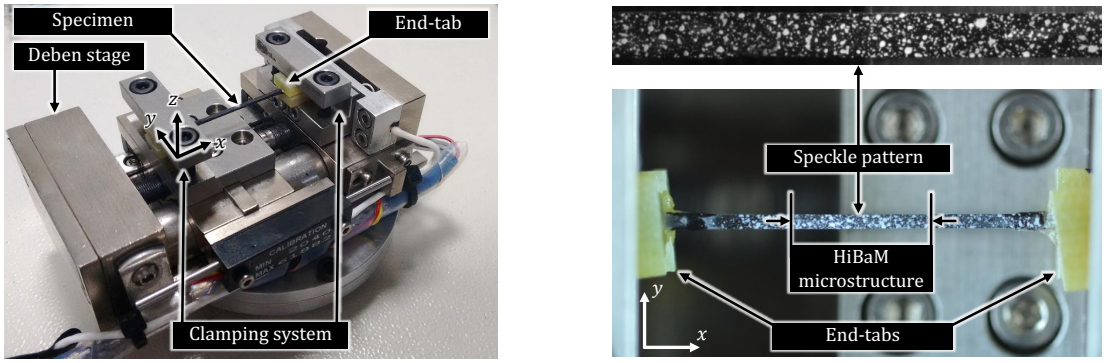
c. The plates with the HiBaM microstructures were cured in an autoclave, according to the temperature and pressure cycle specified by the manufacturer [142].

Once the plates were cured, specimens were cut to a $0.20 - 0.35$ mm width (defined in the z-direction, see Fig. 5.10a), using a high-precision diamond saw. The length of the laser-cut pattern (2.5 mm also defined in the z-direction, see Fig. 5.10d) ensured that at least two specimens with a hierarchical microstructure throughout their entire z-direction could be cut out of each pattern of laser-cuts. The specimens were then end-tabbed using glass/epoxy plates (Fig. 5.10e). The dimensions of the specimens, given in Tab. 5.3 and Fig. 5.10b, were chosen to ensure that failure occurred before the testing rig reached its maximum load capacity (Sec. 5.3.3).

It will be shown in Sec. 5.4.3 that the alignment rig described above in Point b allowed to obtain an accuracy in the relative placement of the laser-cut patterns better than 50 μm. Nevertheless, the manual lay-up process still induced small shifts of the plies relatively to the perfectly-aligned lay-up idealised in Sec. 5.2. The magnitude of the ply-shifts and their effect on the mechanical response of the HiBaM specimens manufactured will be discussed in Sec. 5.4.3.

5.3.3 Testing method

For each HiBaM microstructure, one set of specimens was tested in a Scanning Electron Microscope (SEM), to observe the damage and failure mechanisms occurring during tensile loading. Those specimens were polished using grinding papers and a diamond suspension on polishing cloths, and gold-coated, to ensure good-quality SEM pictures. Another set of specimens was sprayed with a speckle pattern and tested using an optical strain gauge [144], to accurately measure their stress-strain response (Fig. 5.11b).



(a) HiBaM specimen in the Deben tensile stage.

(b) Speckle pattern on a clamped HiBaM specimen.

Figure 5.11: Tensile testing set-up used in the experiments.

The two sets of specimens were both tested in tension using a Deben in-situ MT300 tensile stage [145] (see Fig. 5.11a). The specimens were tested under displacement control, at a speed rate of 0.1 mm/min to ensure quasi-static conditions. The maximum permissible load in the Deben stage is 300 N.

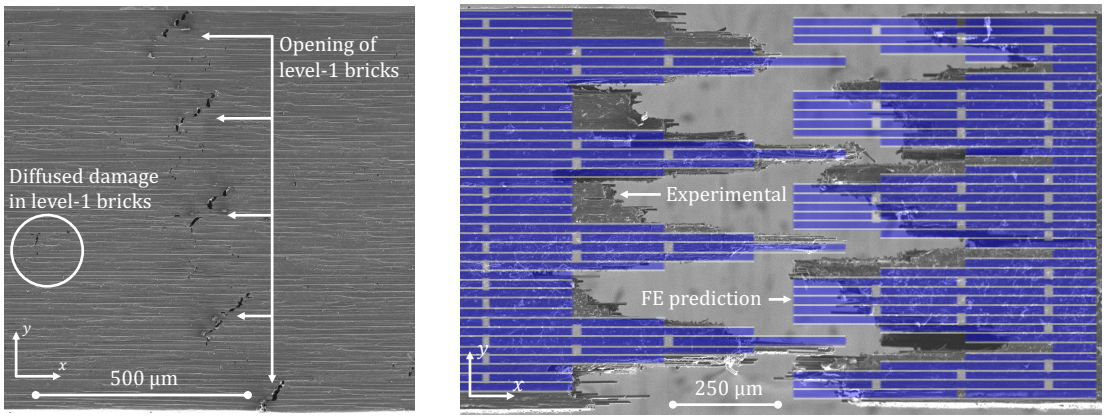
5.4 Results

5.4.1 Damage tolerance in HiBaM composites

5.4.1.1 Damage diffusion in the microstructure

Fig. 5.12a reveals diffused damage formed during tensile loading of a HiBaM specimen, observed as opening of the ends of level-1 bricks. This pattern of damage was observed throughout the entire microstructures of the HiBaM specimens (i.e. not only at the failure site, but also away from the failure site).

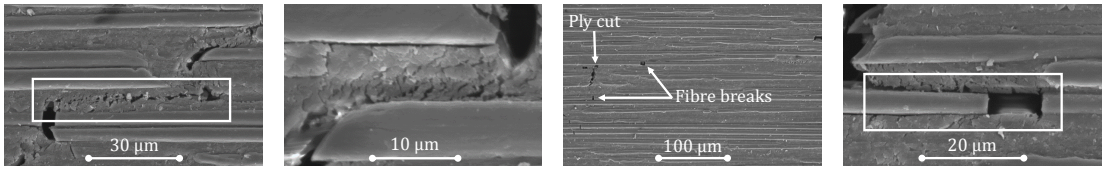
The diffuse damage pattern observed in the HiBaM microstructure (Fig. 5.12a) was not seen in the non-hierarchical BaM composite specimens, demonstrating that the diffusion of damage throughout the specimen is triggered by the use of hierarchical microstructures. This supports the numerical results from Sec. 5.2.4, which predict twice as much damage energy dissipation in the HiBaM specimens, compared to the non-hierarchical ones. This also corroborates experimental results from the literature [47, 132], which observed diffused damage in hierarchical microstructures.



(a) Diffused damage at 89% of the maximum load.

(b) Comparison between the fracture surfaces observed experimentally and predicted by the numerical model.

Figure 5.12: Diffuse damage and fracture surfaces in representative HiBaM specimens, observed in the experiments and predicted by the numerical model.



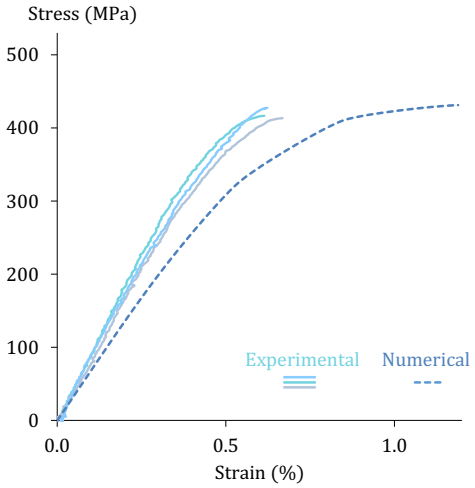
(a) Matrix failure. **(b)** Matrix/fibre interface failure. **(c)** Fibre breaks. **(d)** Fibre pull out.

Figure 5.13: Diffused damage mechanisms observed in the SEM in HiBaM specimens before final failure.

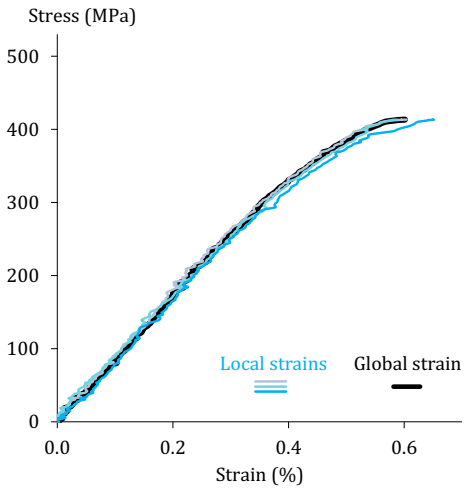
Different mechanisms were found to contribute to stable energy dissipation before final failure of the specimens (see Fig. 5.13):

- *Matrix/interface failure* (Figs. 5.13a and 5.13b): this is the main mechanism for which the microstructure was developed and designed. Matrix (Fig. 5.13a) and interface (Fig. 5.13b) failure occurred between level-0 bricks, either following the rhombus pattern predicted by numerical models (see Sec. 5.2.1.2 and Fig. 5.2d), but also in other smaller brick overlaps created by random ply-shifts which occurred during the lay-up process (to be discussed in Sec. 5.4.3).
- *Fibre breakage*: due to the stochastic nature of the strength of the fibres and to the occurrence of random ply shifts (to be discussed in Sec. 5.4.3), some fibres failed in the experimental specimens, although this was not predicted by the numerical model (Fig. 5.13c). This fibre breakage not only dissipates some energy directly, but it also triggers further energy dissipation through failure of the matrix/interface (as mentioned in the previous point) and pull-out of fibre-ends (as will be explained in the next point);
- *Fibre pull-out*: at relatively high strains (i.e. close to final failure of the specimen), broken fibres and pre-cut brick-ends started to pull out (Fig. 5.13d), hence dissipating energy through friction with the surrounding material.

Fig. 5.12b shows an overall good agreement between the fracture surfaces predicted by the numerical model and observed experimentally, as the rhombus staircase pattern of damage at the interface between level-0 bricks, predicted in Sec. 5.2.1.2, is also seen in the experiments. Nevertheless, small discrepancies between the fracture surfaces predicted by the numerical model and observed experimentally can be noticed in Fig. 5.12b; this is due to small random shifts between the CFRP plies, which occurred during the lay-up process, as will be discussed in Sec. 5.4.3.



(a) Stress-strain curves predicted by the numerical virtual specimen compared against those obtained experimentally with three nominally identical specimens.



(b) Local (from 3 strain gauges) and global (from 1 strain gauge) stress-strain responses of one single HiBaM specimen.

Figure 5.14: Stress-strain response of *nominal-a* HiBaM specimens.

5.4.1.2 Non-linear stress-strain response of HiBaM microstructures

The experimentally-measured stress-strain responses of three *nominal-a* specimens are compared against the prediction of the numerical model in Fig. 5.14a. In both cases, non-linearity is observed, but the experimental specimens failed prematurely in comparison with the simulated specimen; moreover, the experimental specimen was also stiffer than predicted by the model. Random ply-shifts were hypothesised to be the main responsible for these deviations, as will be discussed in Sec. 5.4.3.

In order to ensure that the non-linearity observed in the global stress-strain curve of specimens (as shown in Fig. 5.14a) was due to uniformly large strains in the entire gauge length of a specimen (rather than due to large strains localised at a small portion of the gauge length), strains were also measured in three distinct sub-regions of the gauge length of a specimen. Fig. 5.14b shows that the amount of non-linearity in the experimental stress-strain curves is similar in all sub-regions within a specimen, including the sub-region of final specimen failure as well as the sub-regions away from the failure site. This corroborates the results from Fig. 5.3a, predicting diffuse damage (and, consequently, stress-strain non-linearity) across the entire HiBaM specimen.

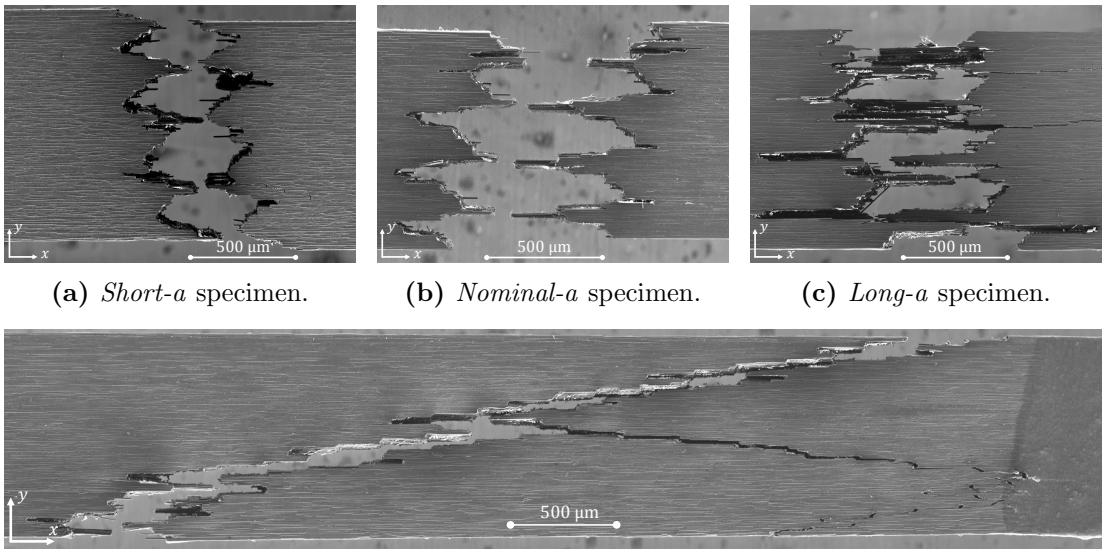
5.4.2 Parametric study of HiBaM microstructures

Figs. 5.15a-5.15c show the effect of level-0 brick length on the fracture surface of HiBaM experimental specimens. Figs. 5.15a-5.15b show that, below the *nominal-a*

level-0 brick length, the fracture surface of HiBaM specimens still follows the rhombus pattern of matrix damage predicted by the numerical model (as identified in Fig. 5.6a), with limited fibre-breakage; however, the effect of random ply-shifts (which occurred during manufacturing, see Sec. 5.4.3) on the fracture surface becomes more evident as the level-0 brick length decreases, which leads to a less well-defined HiBaM pattern in the fracture surface of the *short-a* microstructure (Fig. 5.15a), when compared to that of the *nominal-a* specimen (Fig. 5.15b).

As the level-0 brick length increases to sufficiently large values to cause extensive brick failure (as shown in Fig. 5.15c), the fracture surface of HiBaM specimens becomes more chaotic, although some features of the rhombus pattern of matrix damage predicted by the numerical model for shorter level-0 bricks are still visible. The mismatch between the fracture surfaces of the *long-a* microstructure observed experimentally (in Fig. 5.15c) and predicted numerically (in Fig. 5.6b) is likely due to the stochastic variability of the strength of the individual fibres, which makes some level-0 bricks able to withstand higher loads than those predicted by the (deterministic) numerical model; these statistically stronger level-0 bricks were then able to fail by debonding and pull-out rather than tensile brick failure.

For non-hierarchical BaM microstructures, the fracture surface of each specimen followed a different random pattern across each specimen (see example in Fig. 5.15d), as expected. While the fracture surface of the *BaM-a* specimens is also dominated by debonding between level-0 bricks along a staircase pattern, the damage accumulation mechanism is significantly different from that observed in the HiBaM *nominal-a* speci-



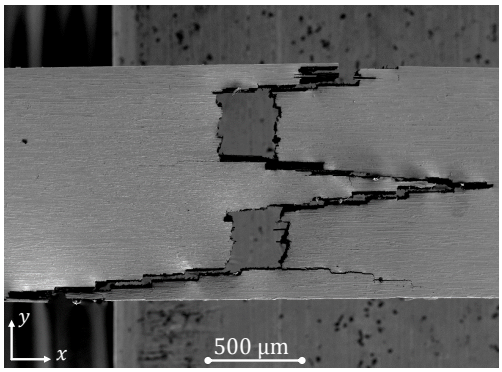
(a) *Short-a* specimen. **(b)** *Nominal-a* specimen. **(c)** *Long-a* specimen.

(d) *BaM-a* specimen.

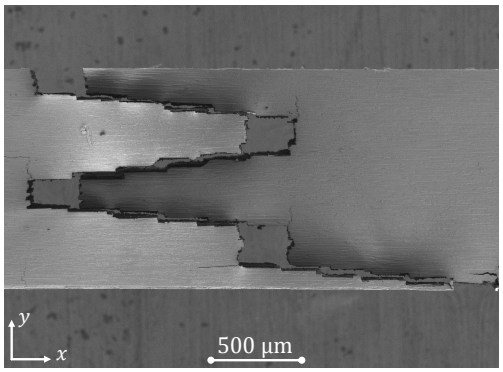
Figure 5.15: Experimental fracture surfaces of specimens used in the parametric study of the level-0 brick geometry.

men, and the former does not evidence the same pattern of damage accumulation away from the final fracture surface as observed at the failure site.

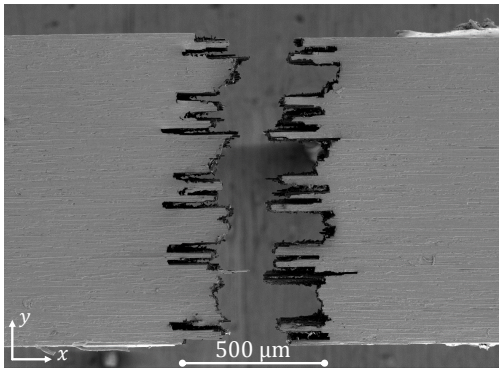
Fig. 5.16 summarises the influence of the dimensions of level-1 bricks on the fracture surface and stress-strain curve of HiBaM specimens. The fracture surfaces of *large-b* (Fig. 5.16a) and *thick-b* (Fig. 5.16b) specimens agree very well with the numerical predictions (shown in Figs. 5.8d and 5.8c respectively). The relative trends between the stress-strain curves predicted by the numerical models for the different level-1 brick geometries are also observed in the experimental results (see Fig. 5.16d). The quantitative discrepancies between the experimental and numerical stress-strain curves, as well as the differences between the observed (Fig. 5.16c) and predicted (Fig. 5.8b) fracture



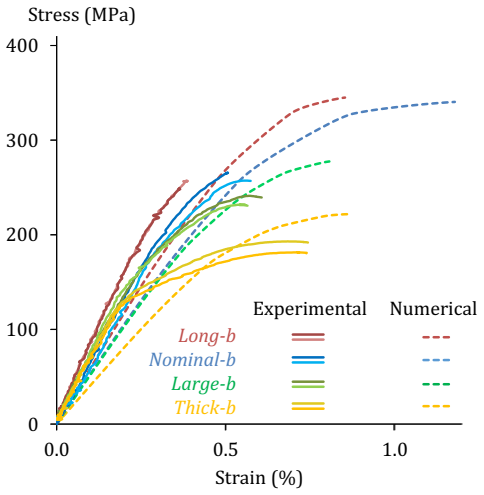
(a) Fracture surface of a *large-b* specimen.



(b) Fracture surface of a *thick-b* specimen.



(c) Fracture surface of a *long-b* specimen.



(d) Stress-strain curves of the HiBaM microstructures with different level-1 brick geometries.

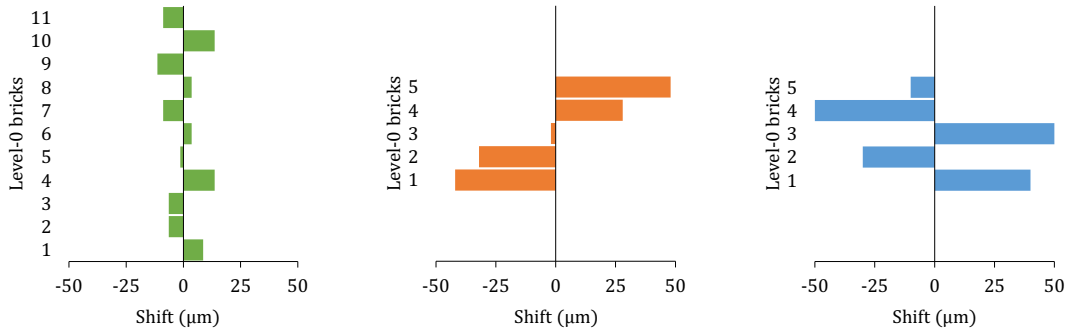
Figure 5.16: Fracture surfaces and stress-strain curves of HiBaM with different level-1 brick-geometries. *Nominal-b* specimens had a similar fracture surface as the *nominal-a* specimens (shown in Fig. 5.15b).

surfaces of *long-b* specimens, are believed to be due to random ply-shifts, which will be discussed in Sec. 5.4.3.

5.4.3 Effect of ply-shifts

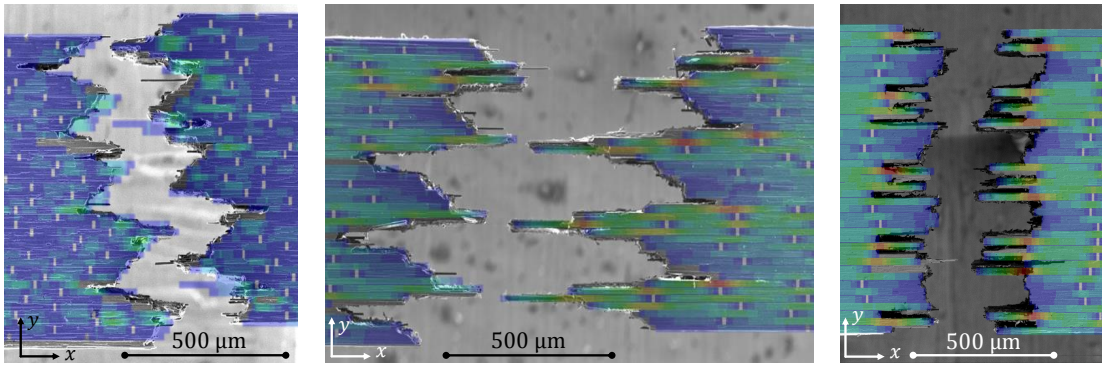
Throughout Secs. 5.4.1 and 5.4.2, it has been hypothesised that random ply-shifts occurred during the lay-up process (due to the finite tolerance between the diameter of the alignment pins and the diameter of the laser-cut ply holes, see Fig. 5.10a), and that these ply-shifts are one of the main reasons for the differences observed between the numerical and the experimental results, both in terms of fracture surfaces and stress-strain curves.

To verify this hypothesis, SEM pictures of specimens in which the opening of brick-ends was clear (such as Fig. 5.12a) were used to estimate the shift (in the x-direction)



(a) *Thick-b* specimen. **(b)** *Nominal-a* specimen. **(c)** *Long-b* specimen.

Figure 5.17: Ply-shifts of each of the level-0 bricks in a level-1 brick, for different microstructures.



(a) *Short-a* specimen. **(b)** *Nominal-a* specimen. **(c)** *Long-b* specimen.

Figure 5.18: Fracture surfaces of HiBaM specimens, as observed in the experiments and predicted by the numerical model considering ply-shifts.

between (i) the experimentally-observed position of the level-1 brick-ends (which, in Fig. 5.12a, are not vertically aligned) and (ii) the expected position of the level-1 brick-ends (which, as shown in Fig. 5.10c, should be vertically aligned, both within a level-1 brick and throughout the thickness of the specimen). The resulting shift measured within a level-1 *nominal-a* brick within Fig. 5.12a is illustrated in Fig. 5.17b; a similar process was carried out for other HiBaM specimens, as shown in Fig. 5.17a and Fig. 5.17c.

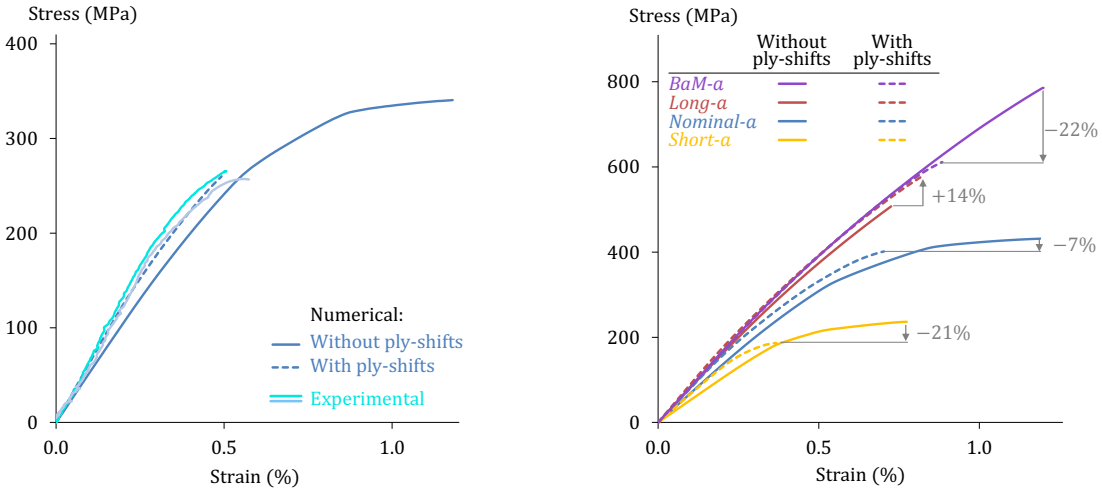
This quantification of ply-shifts revealed that the *thick-b* (Fig. 5.17a) and *large-b* specimens had the smallest amount of ply-shifts of all specimens analysed. Interestingly, these specimens also showed the best agreement between experimental results and model predictions, both in terms of (i) fracture surfaces (compare Figs. 5.8c vs. 5.16b, and 5.8d vs. 5.16a), and (ii) the strains at failure (Fig. 5.16d).

Assuming that the shift of a ply remains uniform along the whole ply length (x-axis) and depth (z-axis), the measured ply-shifts were then introduced in the numerical models for the specimens which were most affected by ply-shifts. The fracture surfaces predicted by the modified numerical models compare extremely well with the experiments (see Figs. 5.18a, 5.18b, and 5.18c).

Fig. 5.19a shows that accounting for ply-shifts in the numerical model of the *nominal-b* specimens would reduce the predicted failure strain down to the value observed experimentally. These results suggest that ply-shifts are responsible for a significant loss of stress-strain non-linearity and, therefore, energy dissipation. This also explains why natural composites tend to have perfectly staggered microstructures (rather than microstructures with random shifts), as it maximises their ability to dissipate energy before failure and, consequently, their damage tolerance [125].

Fig. 5.19b shows the effect that the ply-shifts measured in the *nominal-a* specimen would have had in the different BaM microstructures. Let us first compare the effect of ply-shifts on BaM and HiBaM microstructures: for the same ply-shifts, the strength of BaM composites is reduced by 22% compared with the perfectly-staggered microstructure, while only by 7% for the *nominal-a* HiBaM, suggesting that the addition of hierarchies reduces the dependence of the strength on the level of alignment. This is because ply-shifts in level-0 bricks reduce the overlap length between neighbouring bricks and trigger an even earlier damage localisation in the BaM microstructure, hence considerably diminishing the strength; however, for HiBaM composites, despite ply-shifts in level-0 bricks, matrix failure still has to follow a rhombus pattern (which, for the *nominal-a* microstructure, contains the interface along three consecutive bricks) before final failure, which explains why most of the strength is maintained.

The strength reduction observed with ply-shifts in the simple BaM microstructure agrees with previous works from the literature [26, 146]; these studies concluded that



(a) Stress-strain curves of the *nominal-b* specimens measured experimentally, and predicted numerically with and without accounting for ply-shifts.

(b) Stress-strain curves for different geometries of the level-0 bricks, with and without considering the effect of the ply-shifts shown in Fig. 5.17b.

Figure 5.19: Effect of ply-shifts on the stress-strain curves of HiBaM composites.

randomness and statistical variations in the overlap length between fibres and platelets would trigger the localisation of damage, therefore lowering the strength (up to 40%), the ductility and energy absorption of discontinuous composites; however, the present study suggests that HiBaM microstructures can delay this localisation of damage.

Let us now look at how varying the length of level-0 bricks modifies the effect of ply-shifts (see Fig. 5.19b). Failure of microstructures *nominal-a* and *short-a* is governed by brick debonding and pull-out, and both microstructures are weakened by the presence of ply-shifts. However, the *short-a* microstructure exhibits a strength reduction of 21% when ply-shifts are considered, compared to the perfectly-staggered case, while the strength reduction for the *nominal-a* specimens is only 7%. This is because *short-a* specimens have shorter level-0 bricks, and therefore the same absolute value of ply-shifts as in the *nominal-a* microstructure will have a stronger relative effect in *short-a* specimens.

On the contrary, the strength of the *long-a* microstructure improves by 14% with the presence of ply-shifts. This improvement occurs because the *long-a* microstructure fails when level-0 bricks fracture under tension, as a result of the stress concentrations due to the ends of the neighbouring level-0 bricks; in the perfectly-staggered microstructure, these level-0 brick-ends are aligned at the same location, which maximises the total stress concentration at the middle of a brick. Consequently, ply-shifts eliminate the perfect alignment of neighbouring brick-ends, hence reducing the stress concentrations

at the middle of a level-0 brick, and allowing for a higher strength to be reached by specimens dominated by tensile failure of level-0 bricks (Fig. 5.19b).

Optimal HiBaM microstructures can still be designed even if the alignment of the microstructure is subjected to variability (as observed with the present manufacturing process). To achieve this optimal design, level-0 bricks should be slightly longer than the ones designed for perfectly aligned microstructures, in order to increase the shortest overlap length between neighbouring bricks.

5.5 Conclusions

In this work, hierarchical brick-and-mortar composites with two levels of hierarchy have been designed, manufactured and tested. The following conclusions can be reached:

- Although the microstructure of a HiBaM composite is self-similar (with two morphologically identical hierarchical levels), the assumption of self-similarity cannot be used to accurately calculate the mechanical response of the composite, as the failure mechanism involves an interaction between the two hierarchical scales: failure initiation is triggered in the composite via features *at the larger scale*, while propagation occurs via damage in the matrix following a rhombus pattern *in the smaller scale*. Moreover, the stress fields also vary within a given level of hierarchy.

- The hierarchical microstructure ensures that damage initiates and propagates throughout the entire specimen before damage localisation, hence promoting (i) *non-linearity*, providing a warning before failure, and (ii) *stable energy dissipation* via diffused damage throughout the material before failure (which was quantified by numerical simulations, and verified qualitatively in experiments).

- The HiBaM microstructure can be optimised by tailoring both the aspect-ratio and the absolute dimensions of the bricks, at each hierarchical level. These parameters are governed by different mechanisms at each scale:
  - At the *smaller scale*: (i) the brick aspect-ratio is selected to maximise the force carried and transmitted between the level-0 bricks, while preventing fracture of the bricks; (ii) the brick absolute thickness should be minimised, in order to ensure stable and diffused delamination of the bricks, instead of localising damage due to premature delamination.
  - At the *larger scale*: (i) the brick aspect-ratio is selected to ensure that the rhombus pattern of matrix damage can fully develop, while maximising the efficiency of each level-1 brick to dissipate energy; (ii) the absolute brick di-

mensions are selected in order to avoid both damage localisation (which will occur if the level-1 bricks are too small), and unstable damage propagation (which will occur if the level-1 bricks are too large).

- Ply-shifts created during the manufacturing process have different effects on different level-0 brick geometries. On the one hand, ply-shifts reduce the overlap length between bricks, which triggers premature final failure of HiBaM microstructures with relatively short level-0 bricks. On the other hand, ply-shifts reduce the stress concentrations due to brick-ends, which will delay final failure of HiBaM microstructure with relatively long level-0 bricks. Moreover, random ply-shifts also stiffen HiBaM microstructures. Therefore, ply-shifts have to be accounted for when optimising the microstructure of hierarchical discontinuous materials.

Compared to non-hierarchical BaM microstructures, it was shown that HiBaM microstructures (i) dissipate more energy stably before failure, (ii) present a more non-linear response, (iii) delay damage localisation further, and (iv) are less sensitive to microstructural imperfections such as ply-shifts. Consequently, this study shows that combining discontinuous and hierarchical features in the microstructure of a composite can make it more tolerant to defects and damage.

Chapter 6

Relaxing self-similarity constraints for more damage tolerance in composites

6.1 Introduction

Unlike most synthetic composites, naturally-occurring composites manage to achieve damage tolerance while using brittle constituents as building blocks [38]. To do so, most natural composites use discontinuous [14–16] and hierarchical [16,35,36] microstructures. However, most research on bio-inspired composites imposes self-similarity when designing hierarchical microstructures [25]. In a hierarchical microstructure, self-similarity imposes that, at each hierarchical level, the reinforcements are morphologically and mechanically similar (same shape and same layout), and only differ on the absolute value of a characteristic length (see Chapter 5). This is often a "default" choice to create hierarchical model systems, partially because it makes the microstructure easier to model, design and manufacture.

However, while self-similarity is often used in synthetic bio-inspired hierarchical microstructures, the literature suggests that non-self-similarity is often preferred in natural composites [35, 36, 45]. This can be due to the fact that non-self-similarity leads to more energy storage, more energy dissipation during failure, more resilience, and more damage tolerance in hierarchical materials [46].

For example, most sea shells exhibit reinforcements with different shapes and different layouts at each of their 3 to 4 hierarchical levels [36, 147, 148]. Bone is also not self-similar throughout its 7 levels of hierarchy [36], and displays different reinforce-

ment arrangements at the different hierarchical levels (aligned, woven, plywood-like, radial [35, 149], needle-shaped, plate-shaped [14]).

While the literature provides clear evidence that bio-inspired microstructures can make composites more damage tolerant, different authors have focused on different demonstrations of damage tolerance, e.g. withstanding diffuse damage (Chapter 5), presenting non-linear stress-strain curves [150, 151], dissipating energy before failure [150] and dissipating energy during failure [133]. Presenting permanent deformation and withstanding loading-unloading cycles stably [150] provides an overload warning once damage initiation occurs, and allows a structure to be unloaded safely after damage initiates.

HiBaM composites constitute one of the simplest model systems combining both discontinuities and hierarchies. Chapter 5, as well as previous work in the literature [25], proved their ability to increase damage tolerance compared to conventional continuous and discontinuous composites. However, most literature on HiBaM composites considers self-similar microstructures, so there is scope to explore the potential of non-self-similarity for this type of composite.

This chapter focuses on the effects of non-self-similarity on the stress-strain response and damage tolerance of hierarchical discontinuous CFRPs. This will be done by designing, manufacturing and testing HiBaM composites with and without self-similar microstructures, in order to assess the benefits of releasing the self-similarity constraints often imposed in the literature [25] and in Chapter 5.

The chapter is organised as follows: Sec. 6.2 identifies limits in the self-similar HiBaM design, and explains how novel non-self-similar hierarchical discontinuous microstructures can be developed and optimised using a numerical model. Sec. 6.3 describes the manufacturing process, and Sec. 6.4 describes the different testing methods employed and the results obtained. Sec. 6.5 discusses the advantages of non-self-similar microstructures over self-similar equivalents. Finally, Sec. 6.6 draws the main conclusions of the chapter.

6.2 Design of non-self-similar microstructures

6.2.1 HiBaM microstructures and modelling strategy

A self-similar HiBaM composite with two levels of hierarchy (see Fig. 6.1a) is the simplest model system for a discontinuous and hierarchical self-similar microstructure (see Chapter 5). The HiBaM composite consists of rectangular CFRP bricks used to form a simple (i.e. non hierarchical) BaM microstructure at a smaller scale (hereafter identified as level-0), which is itself used to form rectangular bricks at a larger scale

(hereafter identified as level-1) (see Fig. 6.1a). The 'mortar' in the microstructure is composed of a thin resin-rich layer of epoxy between neighbouring CFRP bricks, at both hierarchical levels, and will be hereafter referred to as 'matrix'.

Unit-cells of all microstructures to be defined in this chapter (see Sec. 6.2.3) will be modelled numerically with FE simulations, using Abaqus [141]. The microstructure will be realised experimentally using carbon/epoxy thin ply prepreg as level-0 bricks (see Sec. 6.3), which will therefore be modelled using orthotropic linear-elastic plane-stress elements and Hashin's failure criteria; the matrix (epoxy-rich interply region) will be modelled by cohesive elements (Chapter 5). The material properties of the carbon/epoxy thin ply prepreg used in this work are given in Tab. 6.1.

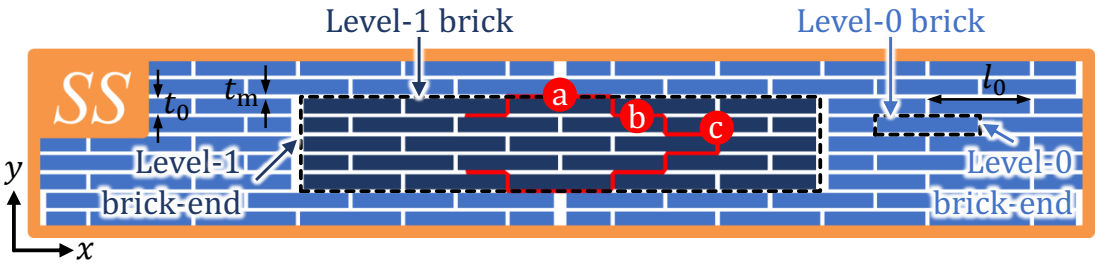
6.2.2 Mechanical response and limitations of the self-similar HiBaM microstructure

In the self-similar (*SS*) HiBaM microstructure (shown in Fig. 6.1a), the presence of hierarchies is achieved through the additional level-1 brick-ends when compared to the non-hierarchical BaM microstructure. These level-1 brick-ends are responsible for triggering damage initiation in the matrix between neighbouring level-1 bricks (Point ⓐ in Figs. 6.1a and 6.1c) (see Chapter 5); once initiated, this damage then propagates within the level-1 bricks, creating a staircase rhombus damage path along the matrix between level-0 bricks (Point ⓑ in Figs. 6.1a and 6.1c). This initiation and propagation of damage in the matrix leads to a non-linear stress-strain response, as shown in Fig. 6.1b.

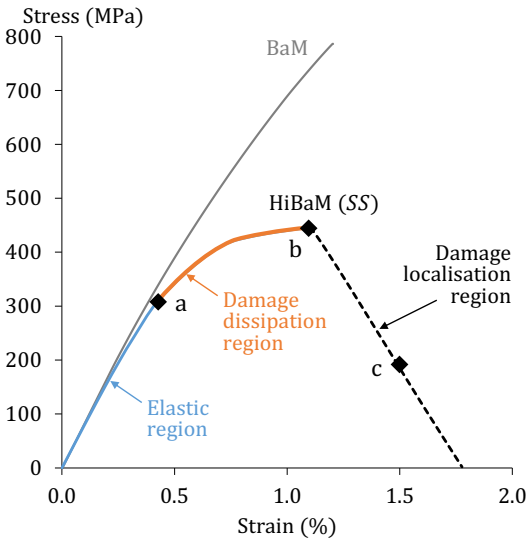
This *SS* hierarchical design ensures that damage is initiated and propagates in all level-1 bricks of the microstructure, before final failure occurs. As a result of this widespread diffuse damage during loading, a large amount of energy is dissipated stably via matrix damage throughout the microstructure, before failure (Fig. 6.1b) (Chapter 5).

Table 6.1: Material properties of the carbon/epoxy thin ply prepreg used in the models and the experiments (see Chapter 5). Superscripts 'b', 'm', and 'p' refer to the 'brick', 'matrix', and 'ply' properties respectively.

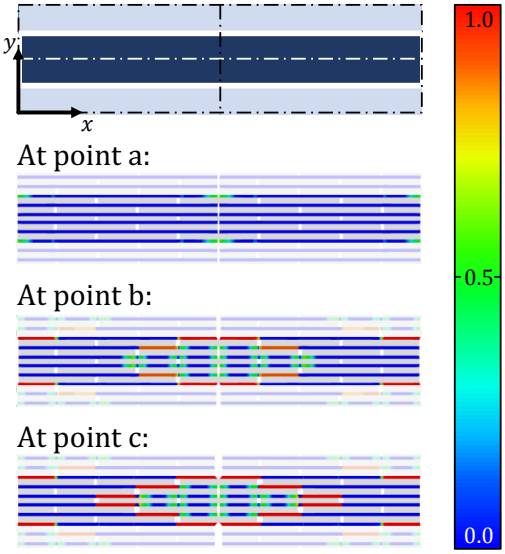
Property	Variable	Unit	Value
Prepreg ply thickness	t^{p}	µm	29
Level-0 brick thickness	t_0	µm	28
Thickness of the rich resin region between plies	t^{m}	µm	1
Fibre volume fraction in the ply	V^{f}	%	34
Longitudinal Young's modulus of the level-0 bricks	E^{b}	GPa	83.8
Longitudinal tensile strength of the level-0 bricks	X^{b}	MPa	1554
Matrix mode II fracture toughness	$\mathcal{G}^{\mathrm{m}}_{\mathrm{IIc}}$	kJ/m^2	0.90
Matrix shear strength	S^{m}	MPa	88.5



(a) The hierarchical *SS* microstructure with damage initiating at the end of neighbouring level-1 bricks ⓐ, and propagating between the level-0 bricks ⓑ within the level-1 brick, until final failure of the brick ⓒ.



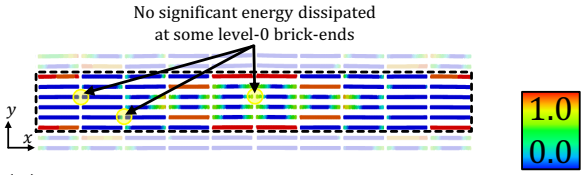
(b) Stress-strain curve of a HiBaM composite predicted numerically.



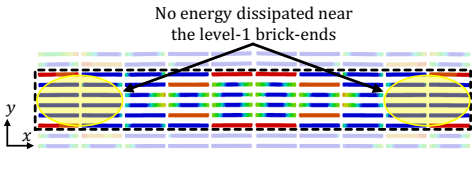
(c) Pattern of matrix damage (modelled as stiffness degradation) in the matrix within a level-1 brick, calculated numerically (mapped on 4 unit-cells for clarity).

Figure 6.1: The *SS* hierarchical microstructure (not to scale) is obtained by introducing discontinuities at two different hierarchical levels in the microstructure. Full details on the numerical model used to obtain the results shown in subfigures (b) and (c) are given in Chapter 5, and summarised in Sec. 6.2.1.

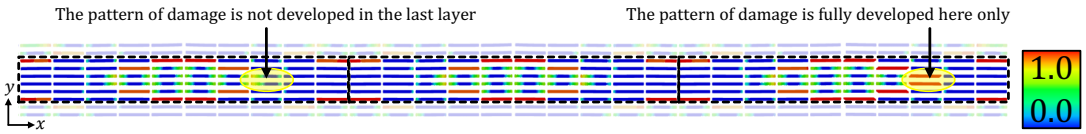
The size of the level-0 and level-1 bricks in the microstructure analysed in Fig. 6.1 have been optimised (see dimensions in Tab. 6.2), in order to ensure that level-0 bricks debond rather than breaking under tension, and that level-1 bricks are able to accommodate the rhombus shape of damage in the matrix without undergoing unstable premature delamination (see Chapter 5). However, this HiBaM microstructure is self-similar by design, meaning that both level-0 and level-1 bricks have the same rectangular shape, and all bricks within the same level have the same size. The question that this chapter aims to address is whether this microstructure can be improved further



(a) Matrix stiffness degradation within a level-1 brick, highlighting inactive level-0 brick-ends.



(b) Matrix stiffness degradation within a level-1 brick, highlighting large regions with undamaged matrix.



(c) Matrix stiffness degradation in 3 adjacent level-1 bricks, highlighting localisation of matrix damage in the level-1 brick on the right only.

Figure 6.2: Identification of different limits due to imposing self-similarity in HiBaM composites by looking at the damage in the matrix (shown as the stiffness degradation in the matrix predicted by numerical models) just before failure (i.e. at point II in Fig. 6.1b).

by relaxing the self-similarity constraints. This will result in the development of three non-self-similar (*NSS*) microstructures, to be presented in Secs. 6.2.3.1-6.2.3.3.

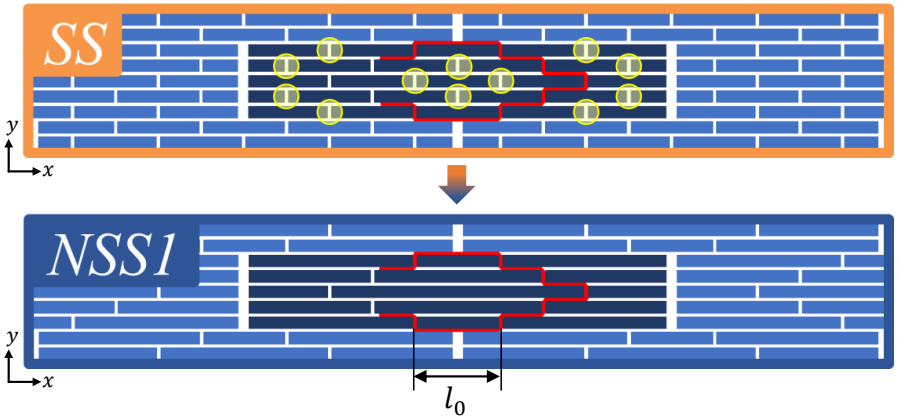
6.2.3 Design of NSS microstructures

6.2.3.1 NSS1: removing unnecessary brick-ends

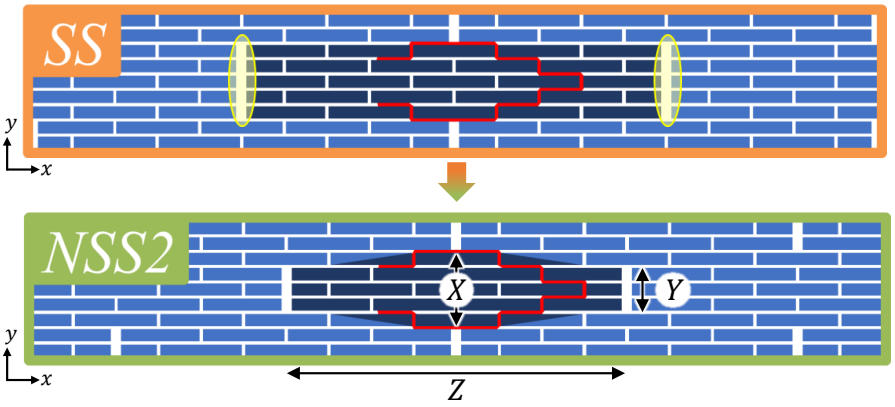
Fig. 6.2a shows the stiffness degradation of the matrix in a *SS* HiBaM level-1 brick and reveals that several level-0 brick-ends are not involved in the creation of the rhombus staircase pattern of matrix damage; these brick-ends do not contribute to a non-linear stress-strain response, nor to energy dissipation, and only obstruct stress paths and weaken the material. Therefore, a first *NSS* microstructure can be designed by removing these unnecessary level-0 brick-ends, and leaving only the ones required for the matrix damage to propagate along the desired rhombus path (see *NSS1* microstructure in Fig. 6.3a and Tab. 6.2).

6.2.3.2 NSS2: optimising level-1 brick shape

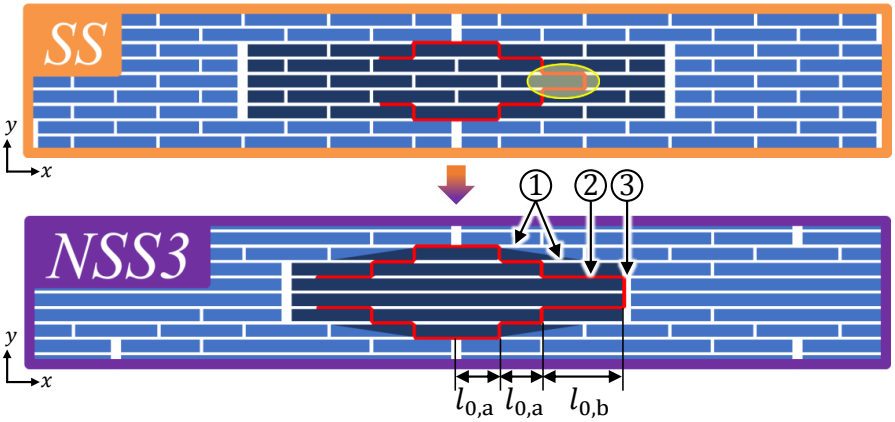
Fig. 6.1a shows that creating two levels of hierarchy in a HiBaM composite requires adding extra discontinuities to the material to create the level-1 brick-ends. These level-1 brick-ends are necessary to trigger stress concentrations on the neighbouring level-1 bricks, which initiates damage in the matrix in all level-1 bricks (Point ⓐ in



(a) The *NSS1* microstructure is obtained by removing unnecessary level-0 brick-ends.

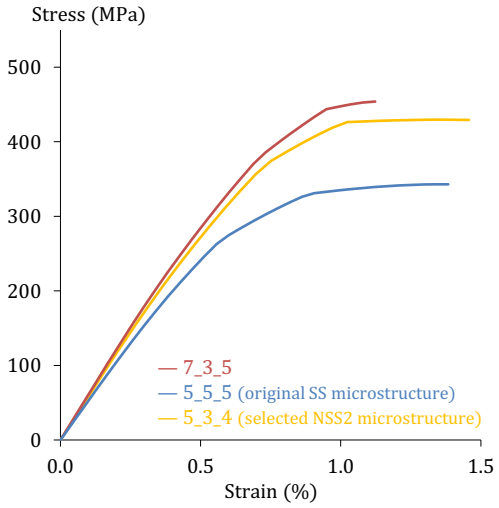


(b) The *NSS2* microstructure is obtained by reducing the size of the level-1 brick-ends and the length of the level-1 bricks, hence changing their shape from rectangular to rhombus.

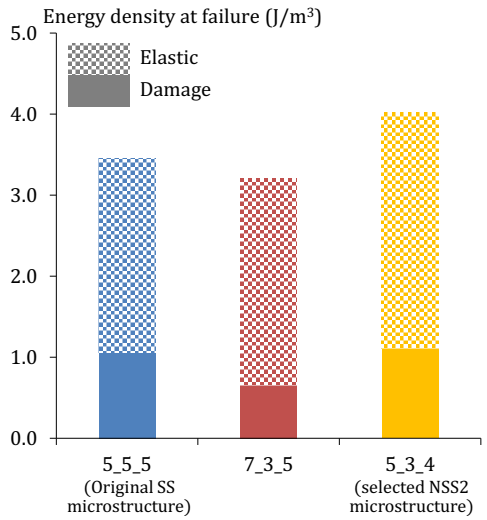


(c) The *NSS3* microstructure is obtained by combining the improvements from the *NSS1* and *NSS2* microstructure, and by strengthening (i.e. increasing the length and the thickness of) the central layer.

Figure 6.3: New *NSS* hierarchical microstructures (not to scale) designed by relaxing the self-similarity constraints imposed on the initial *SS* design (explained in Fig. 6.2 and highlighted here in yellow). For the sake of clarity, for each microstructure, the central level-1 brick is highlighted in a darker colour, and damage in the matrix is represented in red in that central level-1 brick only.



(a) Stress-strain curves for different level-1 brick shapes.



(b) Energy dissipated for different level-1 brick shapes.

Figure 6.4: Mechanical response predicted numerically for different level-1 brick shapes (keeping the length l_0 constant and equal to the nominal value given in Tab. 6.2). The specimen X_Y_Z is defined by the shape of the level-1 bricks: the height at the centre ($X \cdot t^{\mathrm{p}}$), the height at the brick-end ($Y \cdot t^{\mathrm{p}}$), and the length ($Z \cdot l_0$) (see Tab. 6.2 and Fig. 6.3b).

Fig. 6.1a), thus effectively leading to the non-linear response, energy dissipation and damage diffusion achieved by the *SS* HiBaM microstructure.

However, Fig. 6.2b shows that the large level-1 brick-ends in the *SS* HiBaM microstructure generate regions near the level-1 brick-ends where no energy is dissipated, and where the material carries virtually no stresses. This necessarily leads to a loss of stiffness and strength in the *SS* HiBaM microstructure, compared to the BaM microstructure.

This drawback can be overcome by reducing the size of level-1 brick-ends, in order to simultaneously (i) reduce the amount of material in the level-1 bricks which is not involved in the stress-transfer and failure mechanisms, and (ii) preserve the stress-concentrations needed to trigger matrix damage. Reducing the size of level-1 brick-ends effectively changes the shape of the bricks from rectangular to rhombus, which provides a better fit for the pattern of matrix damage observed in the *SS* HiBaM microstructure (Fig. 6.1), and allows for a more efficient packing of the microstructure.

Fig. 6.4 shows numerical results for a parametric study on the size and shape of rhombus level-1 bricks (see X, Y and Z in Fig. 6.3b). Fig. 6.4 shows that the design 5_3_4 (optimal *NSS2* design) provides the best combination of high strength and failure strain (Fig. 6.4a), and energy dissipated through damage (Fig. 6.4b).

Table 6.2: Geometry of the hierarchical microstructures. The prepreg ply thickness t^{p} is given in Tab. 6.1.

	Level-1 dimensions			Level-0 dimensions
Microstructure	Brick length	Height (at brick centre)	Height (at brick-end)	Brick length
SS	$5 \times l_0$	$5 \times t^{\mathrm{p}}$	$5 \times t^{\mathrm{p}}$	$l_0 = 460$ µm
NSS1	$5 \times l_0$	$5 \times t^{\mathrm{p}}$	$5 \times t^{\mathrm{p}}$	$l_0 = 460$ µm
NSS2	$4 \times l_0$	$5 \times t^{\mathrm{p}}$	$3 \times t^{\mathrm{p}}$	$l_0 = 460$ µm
NSS3 (Fig. 6.3c)	$4 \cdot l_{0,\mathrm{a}} + 2 \cdot l_{0,\mathrm{b}}$	$6 \times t^{\mathrm{p}}$	$4 \times t^{\mathrm{p}}$	$l_{0,\mathrm{a}} = 135$ µm $l_{0,\mathrm{b}} = 550$ µm

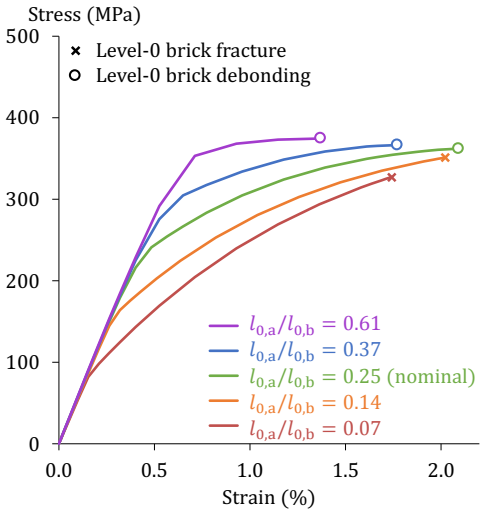
The optimised *NSS2* microstructure features level-1 bricks with a new shape, fitting the rhombus pattern of damage in the matrix, with smaller level-1 brick-ends and shorter level-1 bricks (see *NSS2* microstructure in Fig. 6.3b and Tab. 6.2). This microstructure keeps the same failure mechanism as the *SS* one, but allows for a better level-1 brick packing and a more efficient use of the material.

6.2.3.3 NSS3: strengthening the central level-0 brick

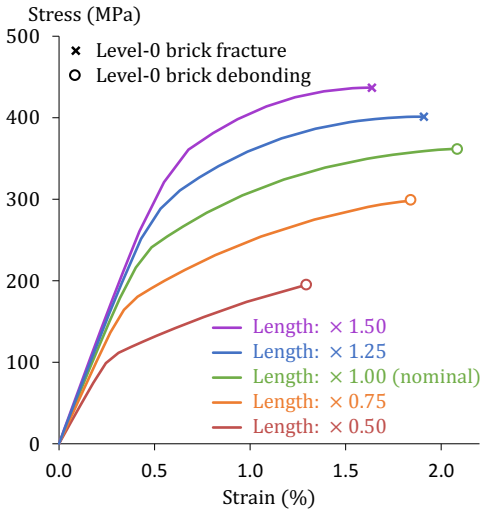
Fig. 6.2c shows that the self-similar microstructure does not completely remove the damage localisation but only delays it: damage initiates and propagates in each brick but failure occurs when damage localise in only one brick, where the matrix damage has reached the end of the last (central) brick. Moreover, the imperfections in the manufacturing process (see Sec. 6.3) often tend to aggravate this premature failure of the composite, accelerating the full propagation of matrix damage in some level-1 bricks when damage only just started propagating in other level-1 bricks (see Chapter 5).

Therefore, a new design was developed, aiming at delaying final localisation of damage and ensuring that a significant amount of damage would propagate in all bricks. To do so, the length of the central level-0 brick is increased until the end of the level-1 bricks. This also required increasing the thickness to avoid premature brick fracture (see *NSS3* microstructure in Fig. 6.3c and Tab. 6.2). Additionally, the features implemented in *NSS1* and *NSS2* are also applied in the *NSS3* design.

In the *NSS3* microstructure, the length of each level-0 brick will be tailored in order to maximise the failure strain. By performing a parametric study on the level-0 brick length shown in Fig. 6.3c, three main failure modes of the *NSS3* microstructure have been identified and are highlighted in Fig. 6.3c:



(a) Effect of varying the ratio $l_{0,a}/l_{0,b}$ (Fig. 6.3c) on the stress-strain curve of a *NSS3* unit-cell (keeping the level-1 brick length constant and equal to $2 \times (2 \cdot 135 + 550)$ µm).



(b) Effect of varying the level-1 brick length on the stress-strain curve of a *NSS3* unit-cell (keeping the ratio $l_{0,a}/l_{0,b}$ constant and equal to the optimal value found in Fig. 6.5a).

Figure 6.5: Stress-strain curves of the *NSS3* unit-cell calculated by the numerical model for different configurations of the microstructure.

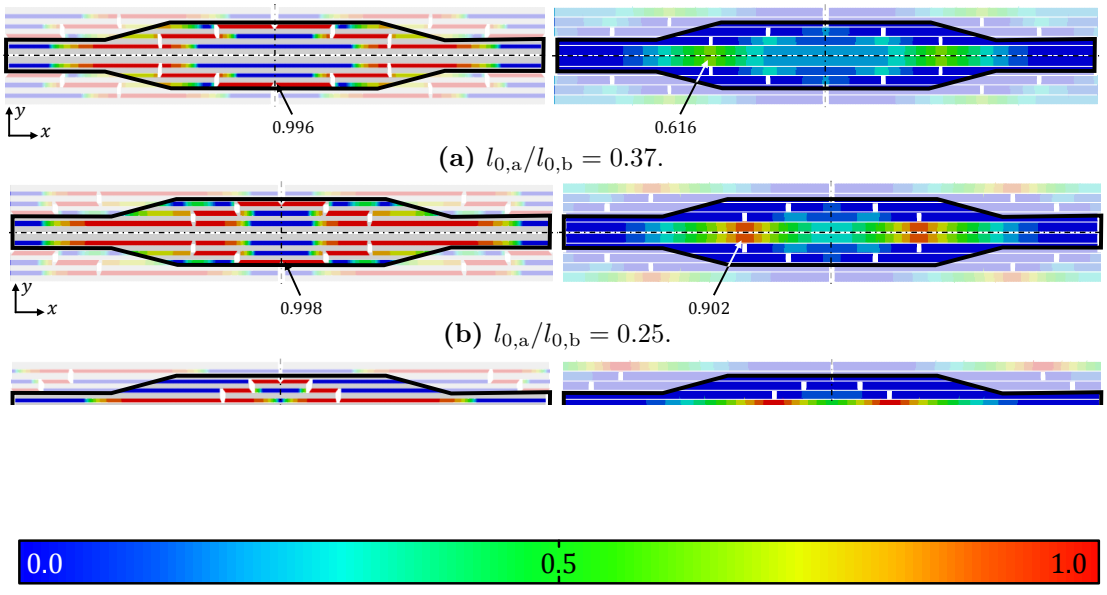


Figure 6.6: Numerical colour maps for three *NSS3* configurations. Left: stiffness degradation in the matrix. Right: Normalised longitudinal stress. The numbers drawn in each numerical map indicate the value and location of the highest stiffness degradation or normalised stress. (The thickness of the matrix layer has been increased on the left-hand side figures to improve the readability of the results.)

- Debonding of the overlaps between neighbouring level-1 bricks (see ① in Fig. 6.3c) occurs when the overlap length ($l_{0,\mathrm{b}} - l_{0,\mathrm{a}}$) becomes too short to transmit enough stress through shear of the matrix;
- Brick fracture (see ② in Fig. 6.3c) occurs in the central level-0 brick when $l_{0,\mathrm{b}}$ is increased above a critical length $l^*_{0,\mathrm{b}}$ at which the level-0 brick cannot sustain the amount of stress transmitted through shear;
- Debonding along the desired pattern (along the central level-0 brick, see ③ in Fig. 6.3c) occurs when the length $l_{0,\mathrm{b}}$ is below the critical length $l^*_{0,\mathrm{b}}$.

The desired failure mechanisms are ① and ③ in Fig. 6.3c, and lengths $l_{0,\mathrm{a}}$, and $l_{0,\mathrm{b}}$ are tailored to ensure that failure mode ③ and ② occur just before failure modes ①. The results of the parametric study on the microstructure of a *NSS3* unit-cell are given in Fig. 6.5.

For a given level-1 brick length $2 \times (2 \cdot l_{0,\mathrm{a}} + l_{0,\mathrm{b}})$, Fig. 6.5a suggests that there is an optimal ratio $l_{0,\mathrm{a}}/l_{0,\mathrm{b}}$ below which brick fracture occurs (leading to lower strength and lower failure strain), and above which brick debonding is triggered earlier (leading to lower failure strain). For this optimal ratio $l_{0,\mathrm{a}}/l_{0,\mathrm{b}}$, Fig. 6.5b shows that there is also an optimal scale above which brick fracture occurs and below which brick debonding occurs at lower stresses and strains.

Fig. 6.6 shows the matrix stiffness degradation and the normalised longitudinal stress in the level-0 bricks calculated numerically for 3 different *NSS3* microstructures studied in Fig. 6.5a. Fig. 6.6b shows that the optimal microstructure (ratio $l_{0,\mathrm{a}}/l_{0,\mathrm{b}} = 0.37$) allows for high stresses to be carried in the level-0 bricks (normalised stress equal to 0.9), like for longer ratios (Fig. 6.6c), while still largely diffusing damage in the matrix, like for shorter ratios (Fig. 6.6a).

One can notice that the optimisation described above is different from the optimisation of self-similar HiBaM composites (which was also used for *NSS1* and *NSS2*), for which only one length l_0 was adjusted, in order to ensure full propagation of the damage in the matrix.

6.3 Manufacturing

6.3.1 Manufacturing of hierarchical discontinuous composites

The four microstructures identified in Fig. 6.3 and Tab. 6.2 were manufactured using SkyFlex USN020A carbon/epoxy thin ply prepreg (see properties in Tab. 6.1), and the brick-ends were created by laser-cutting different patterns of micro-cuts in each ply in the xz-plane (see Chapter 5). All plies were then aligned using an alignment plate [133]

and laid-up in the y-direction to create the hierarchical discontinuous pattern visible in the xy-plane (see Fig. 6.3). Small shifts during the alignment process led to slight misalignments between neighbouring thin plies (hereafter referred to as "ply-shifts").

After curing the lay-up according to the prepreg manufacturer's specifications [142], 40 mm long (in the x-direction) and 0.30 mm wide (in the z-direction) specimens were cut; each specimen had 3 level-1 bricks along its length. The thickness of the specimens (in the y-direction) was given by the thickness of the cured plate, and small variations in the final volume fraction led to small variation in the specimens' thickness. Further details on the manufacturing methods are provided in Chapter 5.

6.4 Testing and results

6.4.1 Monotonic tensile testing

For each microstructure, a set of two specimens was tested in tension at a speed rate of 0.1 mm/min [145], using an optical strain gauge [144] covering the entire length of the pattern of micro-cuts in each specimen to track the strains. The stress-strain curves of the different microstructures are given in Fig. 6.7 (for fair comparisons, the stress-strain curves have been normalised to the same volume fraction (see Sec. 6.3)).

Additionally, three local optical strain gauges have been used to measure the stress-strain response of a *NSS3* specimen at three different locations along the length of the specimen (all three within the region with the pattern of micro-cuts); these regions were selected to capture either the failure site or the material away from the failure site. Results are shown in Fig. 6.8a.

6.4.2 Micro Digital Image Correlation

For one *NSS3* specimen, a speckle pattern was created to produce Digital Image Correlation (DIC) strain maps [152] which show, for each step of the tensile test, the local longitudinal strain ε_{11} along the entire specimen. Results are given in Fig. 6.8b.

6.4.3 Scanning Electron Microscopy

For each microstructure, a set of specimens was tested inside a SEM to observe the xy surface of the specimens during loading. Micrographs of representative surfaces of the *SS* and *NSS1* microstructures are shown in Fig. 6.9. Fig. 6.10 shows micrographs of a *NSS3* specimen.

6.4.4 Repetitive loadings

One *NSS3* specimen was tested under cyclic tension, using an optical strain gauge to track global strains. The cyclic test consisted of repetitive quasi-static loadings and unloadings of the specimen, reversing the loading at progressively higher stresses, until failure occurred. Results are shown in Fig. 6.11a.

6.5 Discussion

6.5.1 Tailorable non-linear stress-strain response

Fig. 6.7 shows that the *NSS1* specimens exhibited a higher stiffness and a higher strength than the *SS* ones. This result can be explained by looking at how the *NSS1* microstructure was created in Sec. 6.2.3.1: as expected, the removal of brick-ends identified as unnecessary in the *SS* microstructure helped the *NSS1* microstructure to partially recover the loss in stiffness and strength due to all level-0 brick-ends.

Moreover, Fig. 6.7 also shows that the *SS* and *NSS1* specimens failed at a similar strain, suggesting that the removal of the unnecessary level-0 brick-ends did not change the failure mechanism. This demonstrates that *NSS* microstructures preserve the hierarchical failure patterns observed in the *SS* microstructure.

Furthermore, Fig. 6.9 shows that, in the fracture surface of *NSS1* specimens, damage in the matrix follows perfectly the expected rhombus staircase pattern (Fig. 6.9b); this was not always the case for *SS* specimens (Fig. 6.9a), in which ply-shifts (see

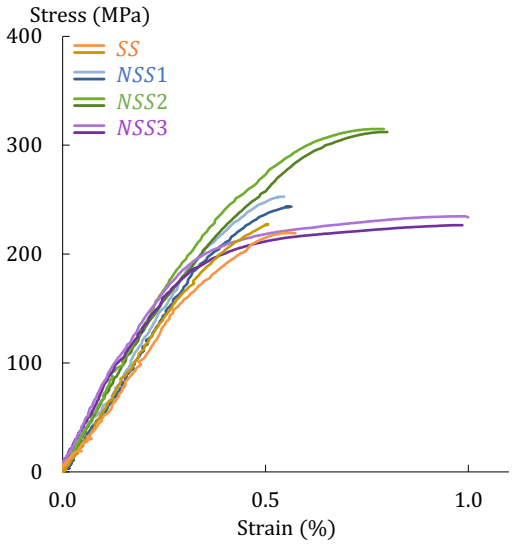
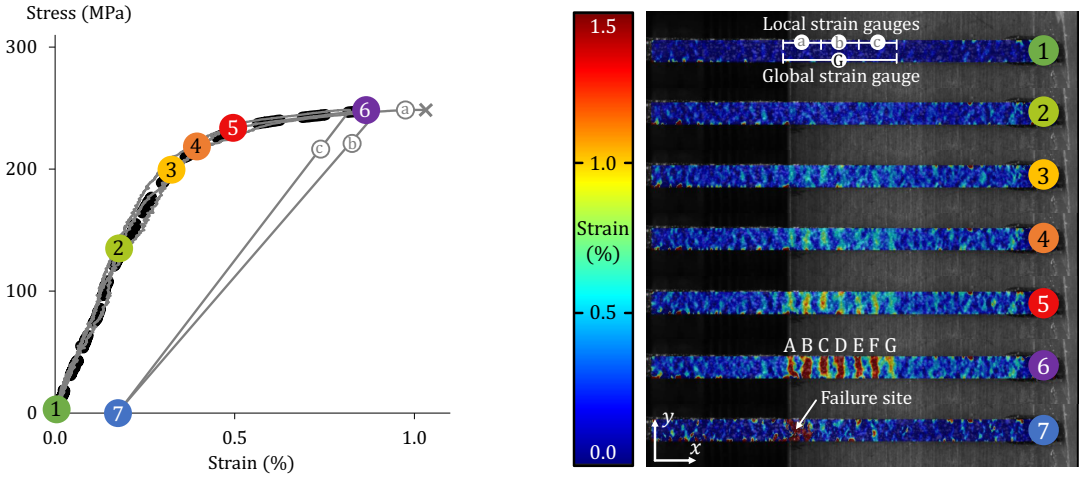


Figure 6.7: Stress-strain curves measured experimentally for *SS* and *NSS* HiBaM composites.



(a) Comparison between local and global SS curves of a *NSS3* specimen. ×: failure of the specimen in gauge section ⓐ.

(b) Strain map of a *NSS3* specimen for the different steps (in the global stress-strain response) shown in Fig. 6.8a.

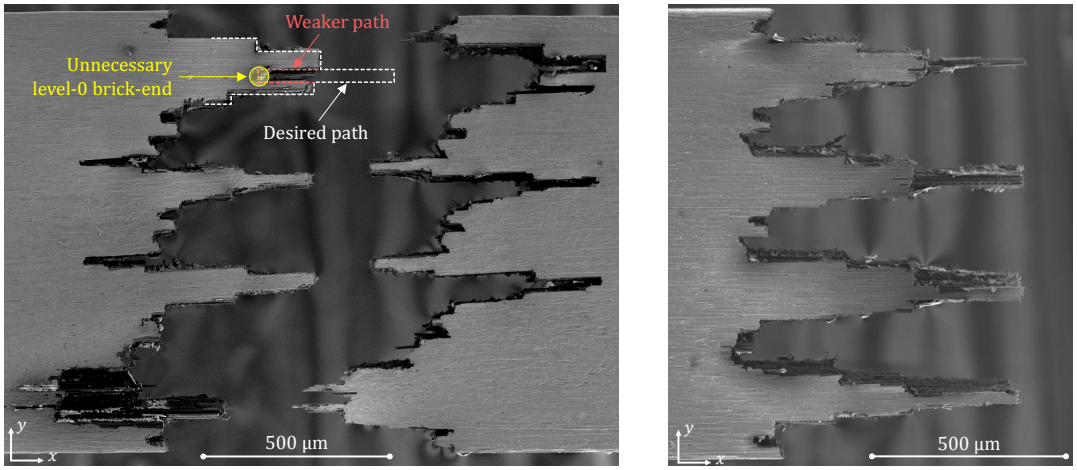
Figure 6.8: Evidence of spread deformation before failure, and permanent deformation after failure. Letters A to G in Fig. 6.8b (Step 6) represent the level-1 brick-end longitudinal locations (see Fig. 6.10).

Sec. 6.3) created weaker paths in the microstructure, which caused the real matrix damage pattern to be different from the designed one in some specimens (see Chapter 5). This suggests that the *NSS1* microstructure ensures that the damage pattern predefined by design is followed, as there are no other potentially weaker paths any more, making the composite more tolerant to manufacturing defects.

Looking now at the *SS* and *NSS2* microstructures (see Fig. 6.7), one can first notice that the better level-1 brick packing in the *NSS2* case results in (i) more level-1 bricks in the cross-section and smaller level-1 brick-ends, increasing the strength, and (ii) more level-1 bricks along the longitudinal direction, leading to more deformation and a higher failure strain. However, the failure mechanism remains the same in both microstructures, which explains why the shape of the stress-strain curve remains similar.

6.5.2 Permanent deformation and diffuse damage

Fig. 6.8a shows that the plateau observed in Fig. 6.7 in the global response of the *NSS3* microstructure is not due to localised strains at the final failure site only (captured by strain gauge ⓐ at Point ×), but to widespread deformation throughout the entire hierarchical microstructure, as the local stress-strain responses away from the failure site (in gauges ⓑ and ⓒ) also exhibit this plateau. This widespread deformation is due (i) to the opening of the level-1 bricks, and (ii) to the propagation of damage in between the level-0 bricks (see zoom-in in Fig. 6.10).



(a) Fracture surface of a *SS* specimen: weaker paths might be created by random ply-shifts, changing the morphology of the damage pattern in the matrix.

(b) Fracture surface of a *NSS1* specimen: the desired rhombus staircase path is the only path available for matrix damage to propagate.

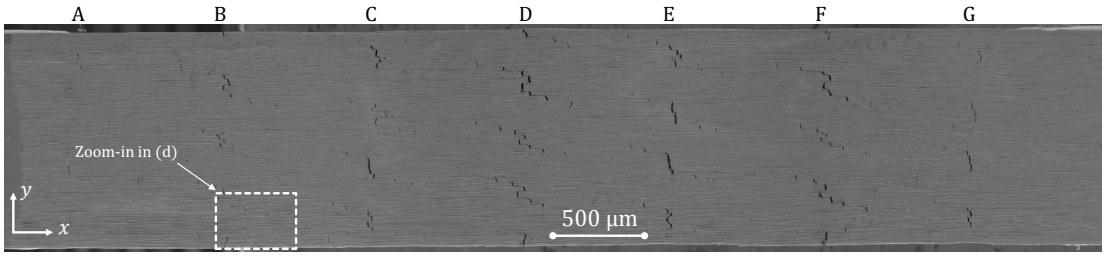
Figure 6.9: SEM images of the fracture surfaces of *SS* and *NSS1* specimens.

This damage diffusion is confirmed by micro-DIC performed on a *NSS3* specimen: the strain increases throughout the hierarchical microstructure until the very end of the stress plateau (see Steps 1 to 6 in Fig. 6.8b). In Step 6, which occurs just before final failure, it is still not obvious, from the strain map (Fig. 6.8b), where the specimen will fail. This demonstrates that the *NSS3* microstructure can successfully delay damage localisation in CFRPs, and provide damage warning before final failure, as diffuse damage and large deformations can be observed before final failure.

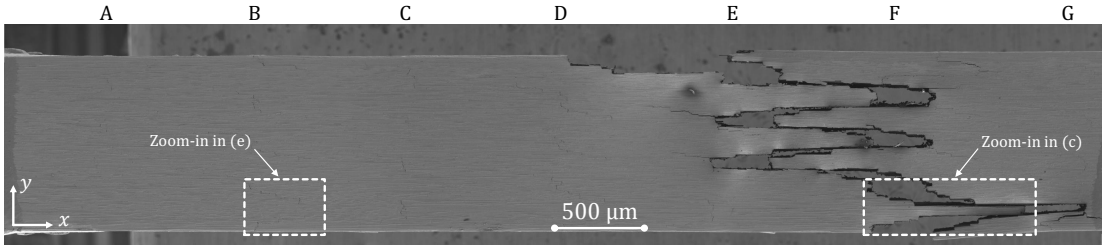
The opening of the level-1 bricks of the *NSS3* microstructure shown in Fig. 6.10 also explains why stripes of higher strain appear in the strain maps in Fig. 6.8b: the seven stripes of higher strain (A to G in Fig. 6.8b) correspond to the seven regions where level-1 brick-ends are located and open during tensile loading of the specimen (A to G in Fig. 6.10).

Moreover, Fig. 6.8a also shows positive residual strains away from the failure site after unloading the specimen (see Step 7 for gauges ⓑ and ⓒ), suggesting that the *NSS3* microstructure does not just exhibit a non-linear behaviour, but that permanent deformation does occur throughout the microstructure. This is explained by the fact that damage in the matrix (along the designed staircase pattern) is observed away from the failure site (see Fig. 6.10b, and zoom-in in Fig. 6.10e).

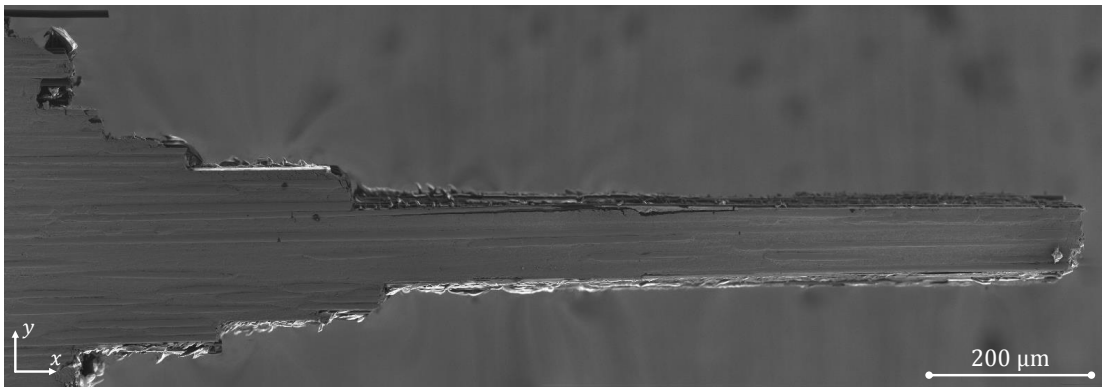
The energy dissipation mechanisms found in the *NSS3* specimen during loading in tension are the same as for the *SS* microstructure, namely (i) matrix/interface failure, (ii) fibre breakage, and (iii) fibre pull-out (see Chapter 5). However, the mains difference between the two microstructures is that *NSS3* specimens undergo much more



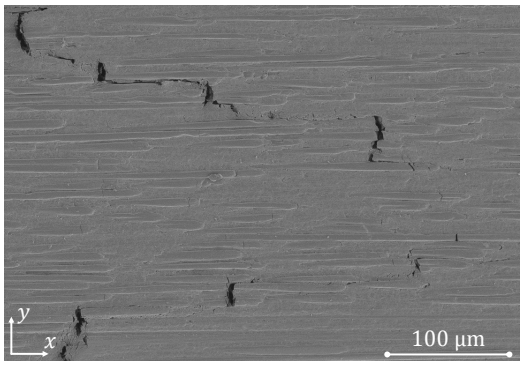
(a) Before failure (86% of maximal load): brick-ends open throughout the specimen and matrix damage propagates along the desired pattern (see zoom-in in Fig. 6.10d).



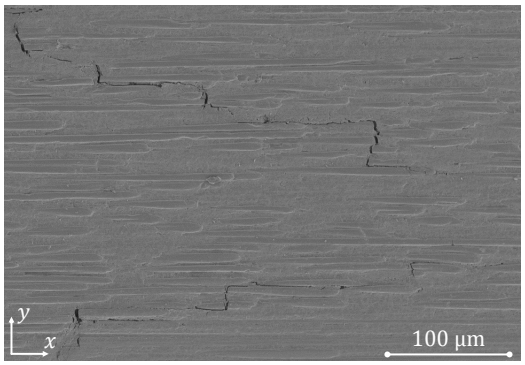
(b) After failure: permanent brick-end opening can be observed throughout the specimen (see zoom-in in Fig. 6.10e).



(c) Zoom on a broken level-1 brick at the failure site.



(d) Zoom on a damaged level-1 brick away from the failure site before failure (92% of maximal load).



(e) Zoom on a damaged level-1 brick away from the failure site after failure.

Figure 6.10: Diffuse damage during loading, and permanent deformation after failure, in *NSS3* specimens. Letters A to G in Figs. 6.10a and 6.10b represent the level-1 brick-end longitudinal locations.

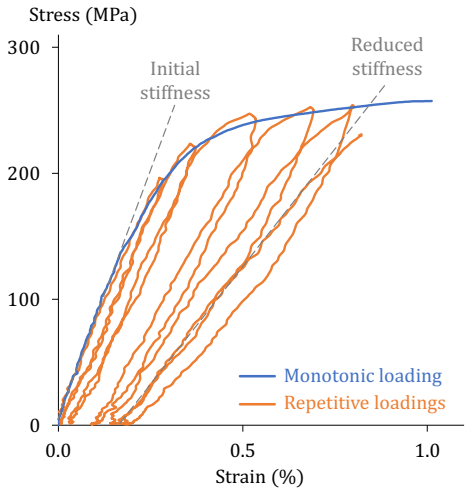
debonding before final failure occurs (see fracture surface in Fig. 6.10c); as a result, diffuse damage can be observed more clearly during the loading of *NSS3* specimens (Fig. 6.10d), suggesting that more energy is dissipated stably before failure.

6.5.3 Stable failure mechanism

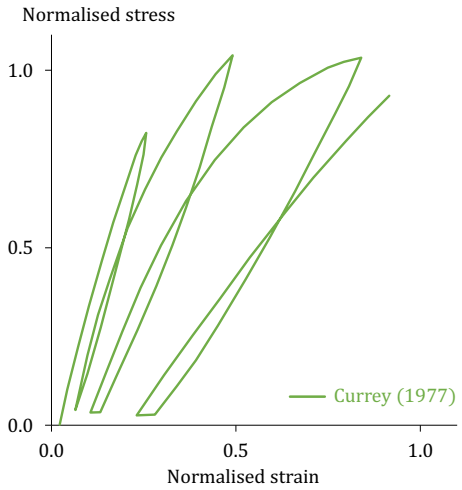
Fig. 6.11a shows that the *NSS3* microstructure can be successfully loaded and unloaded within the plateau region, suggesting that the damage mechanisms are stable. This is the case because the central level-0 bricks within the *NSS3* level-1 bricks have longer overlaps with the neighbouring material, and are therefore much harder to debond. As a result, most of the other level-0 bricks will debond throughout the microstructure – leading to a large increase of strain, and causing the observed plateau – before any of these central level-0 bricks debonds.

One can also notice that the permanent deformation after unloading increases with the number of loading cycles, up to the value observed in Fig. 6.8a (see Step 7), and that the stiffness of the *NSS3* specimen decreases with the number of cycles, suggesting that damage occurs in the microstructure during cyclic loadings.

Results from Fig. 6.11a are compared with repetitive tensile loading test performed on Nacre [32] (see Fig. 6.11b), as they share similarities in their microstructure, namely discontinuities and hierarchies. Interestingly, Figs. 6.11a and 6.11b show that both materials have a similar behaviour (both featuring a stress plateau, permanent deform-



(a) Stress-strain curve of repeated tensile loadings on *NSS3* composites.



(b) Normalised stress-strain curve of repeated tensile loadings on Pinctada margaritifera [32].

Figure 6.11: Demonstration of stable failure mechanism during loading in tension.

ation, stiffness reduction and small hysteresis loops), suggesting that similar damage mechanisms might be occurring in both microstructures during loading in tension.

6.6 Conclusions

This chapter studied the effect of relaxing self-similarity constraints on the microstructure of hierarchical brick-and-mortar composites with two levels of hierarchy. The following conclusions could be reached:

- Self-similarity of the reinforcing units at the two hierarchical levels is not necessary for hierarchical failure mechanisms to occur in hierarchical discontinuous composites. Moreover, removing the self-similarity constraint led to new microstructures with increased performance (strain, stress, damage diffusion) compared to the standard self-similar microstructure.
- Tailoring the shape of the level-1 bricks to the desired failure pattern allows for a more efficient brick-packing and promotes higher strength and failure strain, while also increasing damage dispersion and energy dissipation. Tailoring the geometry of level-0 bricks according to their location in relation to the damage path allows for more damage to be diffused stably before the final failure of the composite, and can be used to create a stable plateau in the stress-strain response.
- The damage tolerance of the new non-self-similar microstructures was demonstrated experimentally in various ways:
  - *Diffuse damage accumulation* was evidenced in micrographs showing widespread damage throughout the microstructure (both at the final failure site and away from the failure site) during loading. This diffuse damage was observed to a greater extent in non-self-similar microstructures than in self-similar microstructures, suggesting that the former dissipate more energy stably during the loading than the latter.
  - *Permanent deformation* was observed in micrographs taken after failure of specimens, and was measured during repeated tensile loading tests. Moreover, local measurements of the stress-strain response in the non-self-similar composite indicate that this permanent deformation occurs throughout the microstructure, which could not be observed in the self-similar microstructures.
  - A *stable plateau* in the stress-strain curve was demonstrated during repeated tensile loading tests; the non-self-similar specimens were successfully loaded and unloaded within the plateauing region, even after damage initiated.

Chapter 7

Conclusions

7.1 On modelling hybrid aligned discontinuous composites

Following from evidence in the literature of the potential of discontinuous and hybrid composites for structural applications, a virtual testing framework was developed in Chapters 2-4 to model the stress-strain response of aligned discontinuous and hybrid aligned discontinuous composites. The VTF is a set of semi-analytical models calculating the response of the composite at different scales (fibre, cross-section, specimen), which bridges the gap between over-simplified analytical models [99, 100, 119] and computationally expensive numerical models [128, 129].

The model developed in Chapter 2 focuses on aligned discontinuous composites and considers (i) a non-linear shear-lag approach to model the interaction (matrix/interface) between neighbouring fibres, (ii) Weibull distributions to capture the stochastic nature of fibre strength, adapted for loadings under non-uniform stress fields due to neighbouring fibre-ends, (iii) random locations of fibre-ends in the specimen, and (iv) unstable failure of the composite triggered by a critical cluster of damage.

A second model was developed in Chapter 3 to calculate the stiffness of HADCs. This model builds up on the model from Chapter 2 by considering interactions between fibres of different types, with different diameters and Young's moduli, but only focuses on the initial linear-elastic response of the composite.

The third part of the VTF, developed in Chapter 4, calculates the full stress-strain response of HADCs. In addition to the features used in the former two parts of the VTF, this model required calculating the stress-strain response of an interaction between different fibres while considering non-linearity in the matrix/interface.

All three parts of the VTF were successfully validated against results obtained through numerical models (developed for this purpose) and from experiments carried out in the literature. In particular, the VTF was able to capture the ductile/brittle responses of ADCs, and the brittle/pseudo-ductile response of HADCs.

7.2 On the understanding of the mechanics of hybrid aligned discontinuous composites

The results from Chapter 2 suggest that failure of ADCs depends on (i) the overlap length between fibres for short-fibre composites, and (ii) the fibre strength for long-fibre composites. The VTF was also used to identify critical sources of variability, and quantify the effect of that variability on the response of ADCs. The VTF showed that removing variability in the fibre-end location and fibre strength could increase the strength of aligned discontinuous composites by 20% to 30%.

Results from the VTF in Chapter 3 captured and explained the existence of a negative hybrid effect on the stiffness of HADCs: due to the asymmetry in the interaction between neighbouring fibres of different types, hybrid interactions are less efficient at transmitting stress through shear between the fibres. Moreover, the model demonstrated that this negative hybrid effect could not be captured by rules-of-mixtures, particularly for composites with (i) short fibres, (ii) a large difference in the stiffness of the two fibre types, and (iii) a high degree of intermingling, for which the hybrid effect is more pronounced.

The VTF also captured what is known in the literature as "the hybrid effect": the LE fibres break at higher strain when they are intermingled with HE fibres. Chapter 4 explains that HE fibres act as "crack arrestors" and delay the gradual fragmentation of LE fibres. In particular, Chapter 4 shows that the presence of discontinuities in hybrid composites enhance the importance of the shielding effect of HE fibres against the stress concentration of LE fibre-ends, which explains why larger hybrid effects could be calculated in HADCs than in continuous hybrid composites.

7.3 On the potential of hybrid aligned discontinuous composites

Results from virtual experiments performed with the VTF (Chapter 4) and physical experiments from the literature [73,84] both confirm the potential of ADCs and HADCs for structural applications. The introduction of discontinuities and hybridisation in composites enlarges the design spaces and allows for more material tailorability for

specific applications. In particular, HADCs, can provide ductility, damage tolerance, and damage warning, which are crucially lacking in current conventional composites.

Due to its analytical nature, the VTF was suitable for parametric studies and optimisation of the microstructures of ADCs and HADCs. In Chapter 2, the VTF showed that ADCs with a carefully selected fibre length could combine the stiffness and strength of long-fibre composites and the ductility of short-fibre composites. In Chapter 4, the VTF suggested that increasing the intermingling would delay the final failure of HADCs.

7.4 On the use of hierarchies in discontinuous composites

Although the concept of introducing hierarchies to improve damage tolerance of composites had already been studied in the literature [25, 153], it had been difficult to prove and study it experimentally. Chapter 5 provides a manufacturing process which enables to successfully manufacture hierarchical discontinuous composites using laser-micro-milled carbon/epoxy thin-plies.

Both the numerical model and the experimental results presented in Chapter 5 suggest that the introduction of hierarchies in discontinuous composites increases damage tolerance when loaded in tension: the presence of discontinuities and hierarchies promotes stable energy dissipation before failure, ensures damage diffusion throughout the specimen, and delays damage localisation in otherwise brittle composites.

Chapter 5 explains that such damage tolerance is enabled by a specific failure mechanism involving the different hierarchical levels: damage is initiated from features at a larger scale, but then propagates throughout the microstructure along paths created by features at the smaller scale. Therefore, each scale seems to have a different role, with the larger scale ensuring that damage is initiated throughout the composites, while the smaller scale actually dissipates damage.

7.5 On the role of self-similarity constraints on modelling and designing hierarchical discontinuous composites

Chapter 5 compared two different models to calculate the response in tension of hierarchical discontinuous composites, and showed that the assumption of self-similarity cannot be used even though the material being modelled was morphologically self-similar. This is because the failure mechanism of such composites involves interactions between the different hierarchical scales, which cannot be captured by homogenising material properties at different scales.

In Chapter 6, the self-similar constraint applied when designing the hierarchical microstructures of Chapter 5 was released, and new non-self-similar microstructures were produced. Results from numerical models and experiments showed that carefully tailored non-self-similar microstructures could exhibit higher stiffness, strength, strain at failure, non-linearity and damage diffusion than their self-similar equivalents.

7.6 Novelty

The VTF proposed in Chapters 2 to 4 is the first semi-analytical model in literature calculating the stress-strain response in tension of hybrid aligned discontinuous composites, accounting for (i) the full constitutive law of the matrix in shear, (ii) stochastic fibre strength and fibre breakage, (iii) stochastic fibre-end locations, (iv) stochastic intermingling of the two fibre types, and (v) a toughness-and-strength-based failure criterion.

Therefore, due to its computational efficiency, the model could also study the effect of variability and randomness (e.g. via Monte-Carlo analysis) to an extent which cannot be performed by numerical models today. Moreover, the VTF can capture and explain various mechanisms observed experimentally (such as hybrid effects, size effect, ...), which cannot be captured by simple analytical models.

In particular, for the first time in literature, the VTF considers that final failure of composites is not just fully strength-dominated or toughness-dominated, but a combination of both. In contrast, most models in literature [24, 61, 62] do not consider the toughness component. Although controversial, this failure mechanism has been observed experimentally: final failure occurs when a cluster of weaker/broken fibres reaches a critical size which triggers the catastrophic failure of the composite [64]. Moreover, this failure criterion was validated against experiments from the literature, and was able to successfully predict the final failure of ADCs and HADCs with different microstructures.

For the first time in literature, the VTF is able to identify the cluster responsible for final failure, and study its characteristics (Chapters 2 and 4). As a result, the VTF is able (i) to identify the sources of randomness causing failure for different microstructures, and (ii) to quantify the effect of randomness and variability on the stress-strain response of hybrid aligned discontinuous composites.

For the first time in the literature, the work in Chapters 5 and 6 demonstrates experimentally the potential of using hierarchical discontinuous microstructures to increase damage tolerance in CFRPs. While most existing composites localise damage, the designed hierarchical discontinuous composites are able to diffuse damage throughout the

microstructure, hence increasing damage energy dissipation before failure. Moreover, some of the proposed designs exhibit a stable stress-plateau in the stress-strain curve which cannot and had not been achieved yet in the literature for conventional aligned discontinuous microstructures.

Self-similar assumptions are often used for their convenience to either model or design hierarchical microstructures. In Chapter 5, the validity of such assumptions to model hierarchical microstructures was studied, and results showed that these assumptions are not always valid, even when the microstructure is morphologically self-similar. Moreover, Chapter 6 demonstrates that assuming self-similarity while designing hierarchical composites unnecessarily constrains the microstructure, and that releasing these constraints could lead to microstructures with higher failure strain, stiffness, or damage tolerance.

7.7 Impact

The first part of this work (Chapters 2 to 4) showed that sources of variability, such as stochastic fibre strength, random intermingling and fibre-end location, had a significant effect on the performance of discontinuous composites. This finding raises a need to better understand these effects. The models developed in this project are now being used in ongoing work carried out to quantify further these effects for the first time in literature [154].

Moreover, the model can now be used to support material design and provide guidelines to other research groups willing to develop/manufacture (hybrid) aligned discontinuous composites. In particular, the model has already been used: (i) to perform further virtual tests and explore the effects of different parameters on the stress-strain response of hybrid aligned discontinuous composites [155], (ii) by a research group from another department at Imperial College London working on improving fibre/matrix interface: the model was used to calculate the fibre length required to maximise the strength and ductility of discontinuous composites made of fibres with an improved interface [156], and (iii) in the HiPerDuCT program: the model was used to identify optimal hybrid microstructures to be manufactured [123].

More generally, the model developed is accurate, computationally efficient, robust, and can be used in industrial context to design microstructures for specific applications.

The second part of the work (Chapters 5 and 6) explored the limits of self-similarity. In particular, Chapter 5 explains why and when self-similarity should not be assumed while modelling hierarchical microstructures, and the given recommendations can help future works aiming at modelling hierarchical microstructures.

Chapter 6 shows the potential of using non-self similar microstructures, and paves the way for further works to create new non-self similar microstructures, aiming at increasing material properties such as damage tolerance.

Chapter 8

Further work

8.1 Optimising hybrid aligned discontinuous composites

Most of the work done in Chapters 2-4 considers randomly intermingled microstructures. However, new manufacturing methods now enable one to tailor the intermingling of different fibre types while creating hybrid specimens [123]. Therefore, the guidance provided in Chapter 4 on the effect of intermingling could support research to find optimal levels of intermingling in order to maximise material properties such as stiffness, ductility, and so on (some work on that topic has already started and is still in progress [123]).

More generally, such hybrid discontinuous composites exhibit an incredibly large design space. In this work, parametric studies were carried out on some individual parameters which could be optimised (such as the fibre length in Chapter 2). One work that could be now carried out with the model would be to design a method for a more general optimisation. The challenge here is to be able to optimise a microstructure with many input parameters. This could be carried out by using for example multiparametric optimisation [157, 158], genetic algorithms [159], or machine-learning [160, 161].

8.2 Extending the VTF for HADCs

The VTF presented in Chapters 2-4 focuses mainly on the response of HADC in tension. One clear improvement would be to extend the VTF to other loading cases. A first step could be to study the behaviour of aligned discontinuous composites under compression, by considering both fibre kinking and failure in shear of the matrix in an interaction between two fibres under compression. Bending loadings could then be

studied as a combination of tensile and compression loadings distributed throughout the cross-section of the virtual specimens.

The VTF presented in this work focuses on quasi-static loadings, and could also be improved by considering dynamic loadings such as high strain-rate tensile loadings, or impact loadings. One way to deal with high strain-rate would be to keep using the model as it is, but considering different matrix shear properties for different strain-rates, although this requires identifying how the matrix constitutive law changes with the strain-rate [162]. The main challenge to model impact loadings would consist of identifying analytically new boundary conditions (which for the moment are simply a uniform longitudinal displacement of the cross-section).

Composites have been found to suffer from cyclic degradation (e.g. reduction of stiffness and strength with the number of loading cycles) [163, 164], which restricts their application, especially for industries where fatigue is one of the main failure mechanisms [165]. Therefore, the VTF could be extended to incorporate fatigue, by considering the degradation of the matrix between neighbouring fibres under fatigue loading in a way similar to existing models for UD continuous composites [166].

Although the different models presented in Chapters 2-4 were first developed for discontinuous composites, the VTF could be extended to continuous composites, by considering an aligned discontinuous composites with infinitely long fibres. However, this would require modifications of the model to account for more fibre breaks (instead of just one per interaction) and to calculate the response of longer broken overlaps (see Sec. 2.2.3.2).

8.3 Hierarchical discontinuous composites

Chapter 6 showed the potential of releasing self-similar constraints. However, this comes with a widening of the design space which could be further explored to identify new microstructures. Tools such as genetic algorithms or machine-learning could help discover such microstructures.

The work presented in Chapters 5-6 focuses on modifying the longitudinal cross-section of UD CFRPs, but the microstructure remains similar through the thickness and could be seen as an "extended 2D" microstructure only, with anisotropic properties. Further work could be carried out to make it "fully 3D", for instance exploring features more similar to "nacre-like" platelets (e.g. hexagonal platelets). However, this requires modifying the manufacturing process to generate more complex shapes throughout the thickness of the specimen.

Chapters 5-6 studied the response of hierarchical discontinuous composites under tensile loading. Further work could be carried out to study the response (i) to high strain-rate, which tends to promote damage localisation, and (ii) to impact, which is a critical/relevant loading case for aeronautic industry for example. Such experimental validation would require designing new specimens with a geometry suitable for high-strain-rate or impact loadings.

The present work (Chapter 5-6) showed the potential of hierarchical discontinuous composites, but this experimental work remained at a laboratory scale. Further work could be carried out on investigating routes to scale-up the manufacturing processes to produce hierarchical discontinuous composites at an industrial scale. The main challenge here would be to produce hierarchical features at a large scale, which could be done by scaling up existing manufacturing processes for discontinuous composites [73], combining discontinuous fibres of different lengths, diameters or strengths (see for example [84]).

Bibliography

[1] J. Njuguna, ed., *Lightweight Composite Structures in Transport : Design, Manufacturing, Analysis and Performance*. Elsevier Science & Technology, 2016.

[2] C. Kaboglu, S. Pimenta, A. Morris, and J. P. Dear, "The effect of different types od core meterial on the flexural behaviour of sandwich composites for wind turbine blades," *Journal of Thermal Engineering*, vol. 3, no. 2, pp. 1102–1109, 2017.

[3] L. Mishnaevsky, J. Id, K. Branner, H. N. Petersen, J. Beauson, M. Mcgugan, and B. F. Sørensen, "Materials for Wind Turbine Blades: An Overview," *Materials*, vol. 10, pp. 1–24, 2017.

[4] L. Zhang, "The application of composite fiber materials in sports equipment," in *5th International Conference on Education, Management and Medicine*, pp. 450–453, 2015.

[5] G. J. Kennedy and J. R. R. Martins, "A Comparison of Metallic and Composite Aircraft Wings Using Aerostructural Design Optimization," in *12th AIAA Aviation Technology, Integration, and Operations (ATIO) Conference and 14th AIAA/ISSM*, pp. 1–31, American Institute of Aeronautics and Astronautics, 2012.

[6] V. Faivre and E. Morteau, "Damage tolerant composite fuselage sizing, characterization of accidental damage threat," *Airbus Tech Mag (FAST)*, vol. 48, pp. 10–16, 01 2011.

[7] "The research requirements of the transport sectors to facilitate an increased usage of composite materials. Part I: The Composite Material Research Requirements of the Aerospace Industry," Tech. Rep. June, EADS Deutschland GmbH, Corporate Research Centre, 2004.

[8] S. Sharma, *Sandwich steels for crash energy absorption applications*. PhD thesis, University of Warwick, 2014.

[9] W. Zhou, J. Lin, T. A. Dean, and L. Wang, "Feasibility studies of a novel extrusion process for curved profiles: Experimentation and modelling," *International Journal of Machine Tools and Manufacture*, vol. 126, pp. 27 – 43, 2018.

[10] K. Zheng, J. Lee, W. Xiao, B. Wang, and J. Lin, "Experimental investigations of the in-die quenching efficiency and die surface temperature of hot stamping aluminium alloys," *Metals*, vol. 8, no. 4, 2018.

[11] H. Saidpour, M. Barikani, and M. Sezen, "Mode-II interlaminar fracture toughness of carbon/epoxy laminate," *Iranian Polymer Journal*, vol. 12, no. 5, pp. 389–400, 2003.

[12] F. Barthelat and R. Rabiei, "Toughness amplification in natural composites," *Journal of the Mechanics and Physics of Solids*, vol. 59, no. 4, pp. 829–840, 2011.

[13] S. M. M. Valashani and F. Barthelat, "A laser-engraved glass duplicating the structure, mechanics and performance of natural nacre," *Bioinspiration & Biomimetics*, vol. 10, no. 2, pp. 1–11, 2015.

[14] J. Y. Rho, L. Kuhn-Spearing, and P. Zioupos, "Mechanical properties and the hierarchical structure of bone," *Medical Engineering and Physics*, vol. 20, pp. 92–102, 1998.

[15] R. Menig, M. Meyers, M. Meyers, and K. Vecchio, "Quasi-static and dynamic mechanical response of Haliotis rufescens (abalone) shells," *Acta Materialia*, vol. 48, pp. 2383–2398, 2000.

[16] F. Barthelat and D. Zhu, "A novel biomimetic material duplicating the structure and mechanics of natural nacre," *Journal of Materials Research*, vol. 26, no. 10, pp. 1203–1215, 2011.

[17] G. Czél, S. Pimenta, M. R. Wisnom, and P. Robinson, "Demonstration of pseudo-ductility in unidirectional discontinuous carbon fibre/epoxy prepreg composites," *Composites Science and Technology*, vol. 106, pp. 110–119, 2015.

[18] M. R. Piggott and M. Ko, "Aligned short-fibre reinforced thermosets: experiments and analysis lend little support for established theory," *Composites Science and Technology*, vol. 48, pp. 291–299, 1993.

[19] M. Grossman, F. Bouville, F. Erni, K. Masania, R. Libanori, and A. R. Studart, "Mineral Nano-Interconnectivity Stiffens and Toughens Nacre-like Composite Materials," *Advanced Materials*, pp. 1–7, 2017.

[20] P. Feraboli, F. Gasco, B. Wade, S. Maier, R. Kwan, W. Salmon, A. Masini, L. Deoto, and M. Reggiani, "Lamborghini "forged composite" technology for the suspension arms of the setso elemento," no. September 2010, pp. 1–13.

[21] S. Pimenta and S. T. Pinho, "Recycling carbon fibre reinforced polymers for structural applications: Technology review and market outlook," *Waste Management*, vol. 31, no. 2, pp. 378–392, 2010.

[22] M. L. Longana, N. Ong, H. Yu, and K. D. Potter, "Multiple closed loop recycling of carbon fibre composites with the HiPerDiF method," *Composite Structures*, vol. 153, pp. 271–277, 2016.

[23] H. L. Cox, "The elasticity and strength of paper and other fibrous materials," *British Journal of Applied Physics*, vol. 3, pp. 72–79, 1952.

[24] S. Pimenta and P. Robinson, "An analytical shear-lag model for brick-and-mortar composites considering non-linear matrix response and failure," *Composites Science and Technology*, vol. 104, pp. 111–124, 2014.

[25] H. Gao, B. Ji, I. L. Jager, E. Arzt, and P. Fratzl, "Materials become insensitive to flaws at nanoscale: lessons from nature.," *Proceedings of the National Academy of Sciences of the United States of America*, vol. 100, no. 10, pp. 5597–5600, 2003.

[26] N. Abid, M. Mirkhalaf, and F. Barthelat, "Discrete-element modeling of nacre-like materials: Effects of random microstructures on strain localization and mechanical performance," *Journal of the Mechanics and Physics of Solids*, vol. 112, pp. 385–402, 2018.

[27] B. Bar-on and H. D. Wagner, "Mechanical model for staggered bio-structure," *Journal of the Mechanics and Physics of Solids*, vol. 59, no. 9, pp. 1685–1701, 2011.

[28] Y. Swolfs, L. Gorbatikh, and I. Verpoest, "Fibre hybridisation in polymer composites: A review," *Composites Part A: Applied Science and Manufacturing*, vol. 67, pp. 181–200, 2014.

[29] H. Yu, M. L. Longana, M. Jalalvand, M. R. Wisnom, and K. D. Potter, "Pseudo-ductility in intermingled carbon / glass hybrid composites with highly aligned discontinuous fibres," *Composites Part A: Applied Science and Manufacturing*, vol. 73, pp. 35–44, 2015.

[30] C. C. Chamis and R. F. Lark, "Hybrid composites - state-of-the-art review: analysis, design, application and fabrication," in *Ann. Structural Dynamics and Materials Conf.*, pp. 1–56, 1977.

[31] L. N. Phillips, "The hybrid effect - does it exist?," *Composites*, pp. 7–8, 1976.

[32] J. D. Currey, "Mechanical properties of mother of pearl in tension," *Royal Society publishing*, vol. 196, pp. 443–463, 1977.

[33] A. P. Jackson, J. F. V. Vincent, and R. M. Turner, "The Mechanical Design of Nacre," *Proceedings of the Royal Society B: Biological Sciences*, vol. 234, pp. 415–440, 1988.

[34] H. M. Yao and H. J. Gao, "Multi-scale cohesive laws in hierarchical materials," *International Journal of Solids and Structures*, vol. 44, pp. 8177–8193, 2007.

[35] S. Weiner and H. D. Wagner, "The material bone: Structure-Mechanical Function Relations," *Annual Review of Materials Research*, vol. 28, pp. 271–298, 1998.

[36] Z. Zhang, Y.-W. Zhang, and H. Gao, "On optimal hierarchy of load-bearing biological materials.," *Proceedings. Biological sciences / The Royal Society*, vol. 278, no. September 2010, pp. 519–525, 2011.

[37] G. Mayer, "Rigid Biological Systems as Models for Synthetic Composites," *Science (New York, N.Y.)*, vol. 310, pp. 1144–1148, 2005.

[38] X. Wei, T. Filleter, and H. D. Espinosa, "Statistical shear lag model Unraveling the size effect in hierarchical composites," *Acta Biomaterialia*, vol. 18, pp. 206–212, 2015.

[39] F. Barthelat, A. K. Dastjerdi, and R. Rabiei, "An improved failure criterion for biological and engineered staggered composites.," *Journal of the Royal Society, Interface / the Royal Society*, vol. 10, no. December 2012, pp. 1–10, 2013.

[40] P. Pingle, J. Sherwood, and L. Gorbatikh, "Properties of rigid-line inclusions as building blocks of naturally occurring composites," *Composites Science and Technology*, vol. 68, pp. 2267–2272, 2008.

[41] L. Gorbatikh, S. V. Lomov, and I. Verpoest, "Original mechanism of failure initiation revealed through modelling of naturally occurring microstructures," *Journal of the Mechanics and Physics of Solids*, vol. 58, no. 5, pp. 735–750, 2010.

[42] H. Gao, "Application of fracture mechanics concepts to hierarchical biomechanics of bone and bone-like materials," *International Journal of Fracture*, vol. 138, pp. 101–137, 2006.

[43] S. M. Mirkhalaf, F. M. A. Pires, and R. Simoes, "Determination of the size of the Representative Volume Element (RVE) for the simulation of heterogeneous polymers at finite strains," *Finite Elements in Analysis and Design*, vol. 119, pp. 30–44, 2016.

[44] R. Piat and E. Schnack, "Hierarchical material modeling of carbon / carbon composites," *Carbon*, vol. 41, pp. 2121–2129, 2003.

[45] B. Achrai and H. D. Wagner, "Micro-structure and mechanical properties of the turtle carapace as a biological composite shield," *Acta Biomaterialia*, vol. 9, no. 4, pp. 5890 – 5902, 2013.

[46] B. An, X. Zhao, and D. Zhang, "On the mechanical behavior of bio-inspired materials with non-self-similar hierarchy," *Journal of the Mechanical Behavior of Biomedical Materials*, vol. 34, pp. 8–17, 2014.

[47] K. Brandt, M. F. H. Wolff, V. Salikov, S. Heinrich, and G. A. Schneider, "A novel method for a multi-level hierarchical composite with brick-and-mortar structure," *Scientific Reports*, vol. 3, pp. 1–8, 2013.

[48] W. Weibull, "A statistical distribution function of wide applicability," *Journal of Applied Mechanics*, pp. 293–297, 1951.

[49] J. Kabelka, L. Hoffmann, and G. W. Ehrenstein, "Damage Process Modeling on SMC," *Journal of Applied Polymer Science*, vol. 62, pp. 181–198, 1996.

[50] J. K. Wells and P. W. R. Beaumont, "The toughness of a composite containing short brittle fibres," *Journal of Materials Research*, vol. 23, pp. 1274–1278, 1988.

[51] Y. T. Zhu, W. R. Blumenthal, and T. C. Lowe, "The tensile strength of short fibre-reinforced composites," *Journal of Materials Science*, vol. 32, pp. 2037–2043, 1997.

[52] Y.-C. Gao, Y.-w. Mai, and B. Cotterell, "Fracture of fiber-reinforced materials," vol. 39, pp. 550–572, 1998.

[53] J. K. Kim and Y. W. Mai, "Stress transfer in the fibre fragmentation test. Part II: Multiple fibre composites," *Journal of Materials Science*, vol. 30, pp. 3024–3032, 1995.

[54] H. Huang and R. Talreja, "Numerical simulation of matrix micro-cracking in short fiber reinforced polymer composites: Initiation and propagation," *Composites Science and Technology*, vol. 66, pp. 2743–2757, 2006.

[55] X. Wei, M. Naraghi, and H. D. Espinosa, "Optimal length scales emerging from shear load transfer in natural materials: application to carbon-based nanocomposite design," *ACS Nano*, vol. 6, no. 3, pp. 2333–2344, 2012.

[56] H. J. Böhm, F. G. Rammerstorfer, and E. Weissenbek, "Some simple models for micromechanical investigations of fiber arrangement effects in MMCs," *Computational Materials Science*, vol. 1, pp. 177–194, 1993.

[57] E. Weissenbek and F. G. Rammerstorfer, "Influence of the fiber arrangement on the mechanical and thermo-mechanical behavior of short fiber reinforced MMCs," *Acta Metallurgica et Materialia*, vol. 41, no. 10, pp. 2833–2843, 1993.

[58] S.-Y. Fu and B. Lauke, "Effects of fiber length and fiber orientation distributions on the tensile strength of short-fiber-reinforced polymers," *Composites Science and Technology*, vol. 56, pp. 1179–1190, 1996.

[59] E. Trujillo, D. Perremans, L. Osorio, A. W. V. Vuure, J. Ivens, and I. Verpoest, "Characterization of unidirectional discontinuous bamboo fibre-epoxy composites," in *ECCM16*, pp. 1–7, ECCM16, Seville, Spain, Jun 2014.

[60] D. Hull and T. W. Clyne, *An Introduction to Composite Materials*. Cambridge Solid State Science Series, Cambridge University Press, 1996.

[61] T. Okabe, T. Motani, M. Nishikawa, and M. Hashimoto, "Numerical simulation of microscopic damage and strength of fiber-reinforced plastic composites," *Advanced Composite Materials*, vol. 21, no. 2, pp. 147–163, 2012.

[62] T. Okabe, T. Sasayama, and J. Koyanagi, "Micromechanical simulation of tensile failure of discontinuous fiber-reinforced polymer matrix composites using Spring Element Model," *Composites Part A: Applied Science and Manufacturing*, vol. 56, pp. 64–71, 2014.

[63] S. Pimenta and P. Robinson, "An analytical model for the mechanical response of discontinuous composites," in *ICCM-19*, pp. 1–9, ICCM-19, Montral, Canada, Jul-Aug 2013, 2013.

[64] A. E. Scott, M. Mavrogordato, P. Wright, I. Sinclair, and S. M. Spearing, "In situ fibre fracture measurement in carbon epoxy laminates using high resolution computed tomography," *Composites Science and Technology*, vol. 71, no. 12, pp. 1471–1477, 2011.

[65] D. Dugdale, "Yielding of steel sheets containing slits," *Journal of the Mechanics and Physics of Solids*, vol. 8, no. 2, pp. 100 – 104, 1960.

[66] M. R. Piggott, "Theoretical estimation of fracture toughness of fibrous composites," *Journal of Materials Science*, vol. 5, pp. 669–675, 1970.

[67] V. M. Karbhari and W. D. J., "Constituent scale and property effects on fibre-matrix debonding and pull-out," *Journal of Materials Research*, vol. 26, pp. 5888–5898, 1991.

[68] H.-Y. Liu, X. Zhang, Y.-w. Mai, and X.-x. Diao, "On steady-state fibre pull-out. II: Computer simulation," *Composites Science and Technology*, vol. 59, pp. 2191–2199, 1999.

[69] S. Kari, H. Berger, and U. Gabbert, "Numerical evaluation of effective material properties of randomly distributed short cylindrical fibre composites," *Computational Materials Science*, vol. 39, pp. 198–204, 2007.

[70] W. Leclerc, P. Karamian, A. Vivet, and A. Campbell, "Numerical evaluation of the effective elastic properties of 2D overlapping random fibre composites," *Technische mechanik*, vol. 32, pp. 358–368, 2012.

[71] M. Nishikawa, T. Okabe, and N. Takeda, "Periodic-cell simulations for the microscopic damage and strength properties of discontinuous carbon fiber-reinforced plastic composites," *Advanced Composite Materials*, vol. 18, pp. 77–93, 2009.

[72] R. P. Harrison, K. Loosemore, and I. Milne, "Assessment of the integrity of structures containing defects," in *Central Electricity Generating Board*, 1977.

[73] H. Yu, K. D. Potter, and M. R. Wisnom, "A novel manufacturing method for aligned discontinuous fibre composites (High Performance-Discontinuous Fibre method)," *Composites Part A: Applied Science and Manufacturing*, vol. 65, pp. 175–185, 2014.

[74] S. Pimenta and S. T. Pinho, "An analytical model for the translaminar fracture toughness of fibre composites," *Journal of the Mechanics and Physics of Solids*, vol. 66, pp. 78–102, 2014.

[75] E. J. Corat, L. D. R. Cardoso, and M. C. B. Carvajal, "Effect of the CVD parameters on the fiber tensile strength of carbon fibers using single-fiber tensile test after carbon nanotubes growth," in *INPE*, São José dos Campos, 2015.

[76] W. Liu, S. Zhang, B. Li, F. Yang, W. Jiao, L. Hao, and R. Wang, "Improvement in interfacial shear strength and fracture toughness for carbon fiber reinforced epoxy composite by fiber sizing," *Polymer Composites*, pp. 1–7, 2014.

[77] S. Yumitori, Y. Arao, T. Tanaka, K. Naito, and K. Tanaka, "Increasing the interfacial strength in carbon fiber / polypropylene composites by growing CNTs on the fibers," in *Wit Trans Model Sim*, pp. 275–284, 2013.

[78] D. T. Burn, *Long Discontinuous Carbon Fibre / Polypropylene Composites for High Volume Automotive Applications*. PhD thesis, University of Nottingham, 2016.

[79] N. Toyama and J. Takatsubo, "An investigation of non-linear elastic behavior of CFRP laminates and strain measurement using Lamb waves," *Composites Science and Technology*, vol. 64, pp. 2509–2516, 2004.

[80] T. W. J. de Geus, R. H. J. Peerlings, and M. G. D. Geers, "Microstructural topology effects on the onset of ductile failure in multi-phase materials," *International Journal of Solids and Structures*, vol. 67-68, pp. 326–339, 2015.

[81] L. S. Sutherland, R. A. Shenoi, and S. M. Lewis, "Size and scale effects in composites: I. Literature review," *Composites Science and Technology*, vol. 59, pp. 209–220, 1999.

[82] M. R. Wisnom, "Size effects in the testing of fibre-composite materials," *Composites Science and Technology*, vol. 59, pp. 1937–1957, 1999.

[83] A. Kelly and W. Tyson, "Tensile properties of fibre-reinforced metals: Copper/tungsten and copper/molybdenum," *Journal of the Mechanics and Physics of Solids*, vol. 13, pp. 329–350, 1965.

[84] H. Yu, M. L. Longana, M. Jalalvand, M. R. Wisnom, and K. D. Potter, "Hierarchical pseudo-ductile hybrid composites combining continuous and highly aligned discontinuous fibres," *Composites Part A: Applied Science and Manufacturing*, vol. 105, pp. 40–56, 2017.

[85] M. L. Longana, H. Yu, M. Jalavand, M. R. Wisnom, and K. D. Potter, "Aligned discontinuous intermingled reclaimed/virgin carbon fibre composites for high performance and pseudo-ductile behaviour in interlaminated carbon-glass hybrids," *Composites Science and Technology*, vol. 143, pp. 13–21, 2017.

[86] J. Henry, S. Pimenta, H. Yu, and M. L. Longana, "Prediction of mechanical properties of hybrid discontinuous composites," in *Proceedings*, pp. 1–7, ECCM17, Munich, Germany, Jun-Jul 2016.

[87] Y. Swolfs, *Hybridisation of self-reinforced composites: modelling and verifying a novel hybrid concept*. PhD thesis, KU Leuven, 2015.

[88] J. Summerscales and D. Short, "Carbon fibre and glass fibre hybrid reinforced plastics," *Composites*, vol. 9, no. 3, pp. 157–166, 1978.

[89] N. Pan and R. Postle, "The tensile strength of hybrid fibre composites: a probabilistic analysis of the hybrid effect," *Philosophical Transactions of the Royal Society A*, vol. 354, pp. 1875–1897, 1996.

[90] S. Tsai and J. Melo, *Composite Materials Design and Testing: Unlocking Mystery with Invariants*. Composites Design Group, Department of Aeronautics & Astronautics, Stanford University, 2015.

[91] S.-Y. Fu and B. Lauke, "The elastic modulus of misaligned short-fiber-reinforced polymers," *Composites Science and Technology*, vol. 58, pp. 389–400, 1998.

[92] J. C. Halpin, "Effects of Environmental Factors on Composite Materials," tech. rep., Air Force Materials Lab Wright-Patterson AFB OH, 1969.

[93] Z. Hashin and B. W. Rosen, "The elastic moduli of Fiber-Reinforced materials," *Journal of Applied Mechanics*, vol. 31, no. 63, pp. 223–332, 1964.

[94] M. Ibnabdeljalil and W. Curtin, "Strength and reliability of fiber-reinforced composites: Localized load-sharing and associated size effects," *International Journal of Solids and Structures*, vol. 34, no. 21, pp. 2649–2668, 1997.

[95] T. Okabe, H. Sekine, K. Ishii, M. Nishikawa, and N. Takeda, "Numerical method for failure simulation of unidirectional fiber-reinforced composites with spring element model," *Composites Science and Technology*, vol. 65, no. 6, pp. 921–933, 2005.

[96] T. Okabe, N. Takeda, Y. Kamoshida, M. Shimizu, and W. Curtin, "A 3D shear-lag model considering micro-damage and statistical strength prediction of unidirectional fiber-reinforced composites," *Composites Science and Technology*, vol. 61, no. 12, pp. 1773–1787, 2001.

[97] A. R. Sanadi and M. R. Piggott, "Interfacial effects in carbon-epoxies. Part 1: Strength and modulus with short aligned fibres," *Journal of Materials Science*, vol. 20, pp. 421–430, 1985.

[98] S. Sihn, R. Y. Kim, K. Kawabe, and S. W. Tsai, "Experimental studies of thin-ply laminated composites," *Composites Science and Technology*, vol. 67, no. 6, pp. 996–1008, 2007.

[99] V. V. Vasiliev and E. Morozov, *Advanced Mechanics of Composite Materials and Structural Elements*. Elsevier Science, 3 ed., 2013.

[100] M. Jalalvand, G. Czél, and M. R. Wisnom, "Damage analysis of pseudo-ductile thin-ply UD hybrid composites - a new analytical method," *Composites Part A: Applied Science and Manufacturing*, vol. 69, pp. 83–93, 2014.

[101] G. Czél, S. Pimenta, M. R. Wisnom, and P. Robinson, "Demonstration of pseudo-ductility in unidirectional discontinuous carbon fibre/epoxy prepreg composites," *Composites Science and Technology*, vol. 106, pp. 110–119, 2015.

[102] A. R. Bunsell and B. Harris, "Hybrid carbon and glass fibre composites," *Composites*, vol. 5, pp. 157–164, 1974.

[103] M. J. Pitkethly and M. G. Bader, "Failure modes of hybrid composites consisting of carbon fibre bundles dispersed in a glass fibre epoxy resin matrix," *Journal of Physics D: Applied Physics*, vol. 20, pp. 315–322, 1987.

[104] T. Kishi, M. Enoki, and H. Tsuda, "Interface and strength in ceramic matrix composites," *Materials Science and Engineering: A*, vol. 143, pp. 103–110, 1991.

[105] T. A. Godfrey, "A micromechanical model for extension of a tightly packed bundle of aligned short fibres," *The Journal of The Textile Institute*, vol. 99, pp. 101–109, 2008.

[106] S. E. Sanborn and J. H. Prévost, "Discrete modeling of crack bridging by a discontinuous platelet with a controlled interface," *International Journal of Solids and Structures*, vol. 45, pp. 5059–5073, 2008.

[107] Y. L. Chen, B. Liu, X. Q. He, Y. Huang, and K. C. Hwang, "Failure analysis and the optimal toughness design of carbon nanotube-reinforced composites," *Composites Science and Technology*, vol. 70, pp. 1360–1367, 2010.

[108] J. A. Nairn and M. S. Mohammadi, "Numerical and Analytical Modeling of Aligned Short Fiber Composites including Imperfect Interfaces," *Composites Part A: Applied Science and Manufacturing*, vol. 77, pp. 26–36, 2015.

[109] C. M. Landis and R. M. McMeeking, "A shear-lag model for a broken fiber embedded in a composite with a ductile matrix," *Composites Science and Technology*, vol. 59, pp. 447–457, 1999.

[110] R. K. Chintapalli, S. Breton, A. K. Dastjerdi, and F. Barthelat, "Strain rate hardening: A hidden but critical mechanism for biological composites?," *Acta Biomaterialia*, vol. 10, pp. 5064–5073, 2014.

[111] S. E. Szczesny and D. M. Elliott, "Incorporating Plasticity of the Interfibrillar Matrix in Shear Lag Models is Necessary to Replicate the Multiscale Mechanics of Tendon Fascicles," *Journal of the mechanical behavior of biomedical materials*, vol. 40, pp. 325–338, dec 2014.

[112] S. E. Szczesny and D. M. Elliott, "Interfibrillar shear stress is the loading mechanism of collagen fibrils in tendon," *Acta biomaterialia*, vol. 10, pp. 2582–2590, jun 2014.

[113] P. W. Manders and M. G. Bader, "The strength of hybrid glass/carbon fibre composites - Part 2 A statistical model," *Journal of Materials Science*, vol. 16, no. 8, pp. 2246–2256, 1981.

[114] T. Hayashi, "On the improvement of mechanical properties of composites by hybrid composition," in *Proc 8th Intl Reinforced Plastics Conference*, pp. 149–52, 1972.

[115] G. Kretsis, "A review of the tensile, compressive, flexural and shear properties of hybrid fibre-reinforced plastics," *Composites*, vol. 18, no. 1, pp. 13–23, 1987.

[116] H. Fukuda, "An advanced theory of the strength of hybrid composites," *Journal of Materials Science*, vol. 19, pp. 974–982, 1983.

[117] C. Zweben, "Tensile strength of hybrid composites," *Journal of Materials Science*, vol. 12, pp. 1325 – 1337, 1977.

[118] H. Fukunaga, T.-W. Chou, and H. Fukuda, "Strength of Intermingled Hybrid Composites," *Journal of Reinforced Plastics and Composites*, vol. 3, pp. 145–160, 1984.

[119] J. Aveston and A. Kelly, "Tensile first cracking strain and strength of hybrid composites and laminates," *Philosophical Transactions of the Royal Society A*, vol. 294, pp. 519–534, 1980.

[120] H. Yu, M. L. Longana, G. Grail, S. Pimenta, P. Robinson, M. R. Wisnom, and K. D. Potter, "Aligned short fibre composites with nonlinear behaviour," in *ICCM-20*, pp. 19–24, ICCM-20, Copenhagen, Denmark, Jul 2015.

[121] K. Naito, Y. Tanaka, J.-m. Yang, and Y. Kagawa, "Tensile properties of ultrahigh strength PAN-based , ultrahigh modulus pitch-based and high ductility pitch-based carbon fibers," *Carbon*, vol. 46, pp. 189–195, 2008.

[122] "ASTM D3039 / D3039M-14, Standard Test Method for Tensile Properties of Polymer Matrix Composite Materials," standard, ASTM International, West Conshohocken, PA, 2014.

[123] J. Finley, H. Yu, M. Longana, S. Pimenta, M. Shaffer, and K. Potter, "Exploring the pseudo-ductility of aligned hybrid discontinuous composites using controlled fibre-type arrangements," *Composites Part A: Applied Science and Manufacturing*, vol. 107, pp. 592 – 606, 2018.

[124] G. Czél, S. Pimenta, M. R. Wisnom, and P. Robinson, "Demonstration of pseudo-ductility in unidirectional discontinuous carbon fibre/epoxy prepreg composites," *Composites Science and Technology*, vol. 106, pp. 110–119, 2015.

[125] H. Lei, Z. Zhang, and B. Liu, "Effect of fiber arrangement on mechanical properties of short fiber reinforced composites," *Composites Science and Technology*, vol. 72, pp. 506–514, 2012.

[126] G. Liu, B. Ji, K. C. Hwang, and B. C. Khoo, "Analytical solutions of the displacement and stress fields of the nanocomposite structure of biological materials," *Composites Science and Technology*, vol. 71, no. 9, pp. 1190–1195, 2011.

[127] K. D. Jones and A. T. DiBenedetto, "Fibre fracture in hybrid composite systems," *Composites Science and Technology*, vol. 51, pp. 53–62, 1994.

[128] S. Banerjee and B. V. Sankar, "Mechanical properties of hybrid composites using finite element method based micromechanics," *Composites Part B: Engineering*, vol. 58, pp. 318–327, 2014.

[129] A. A. J. M. Peijs and J. M. M. De Kok, "Hybrid composites based on polyethylene and carbon fibres Part 6: Tensile and fatigue behaviour," *Composites*, vol. 24, pp. 19–32, 1993.

[130] S. M. Mirkhalaf and F. Barthelat, "A laser-engraved glass duplicating the structure, mechanics and performance of natural nacre," *Bioinspiration & Biomimetics*, vol. 10, pp. 1–11, 2015.

[131] F. Narducci and S. T. Pinho, "Exploiting nacre-inspired crack deflection mechanisms in CFRP via micro-structural design," *Composites Science and Technology*, vol. 153, pp. 178–189, 2017.

[132] R. Mirzaeifar, L. S. Dimas, Z. Qin, and M. J. Buehler, "Defect-Tolerant Bioinspired Hierarchical Composites : Simulation and Experiment," *Acta Biomaterialia*, vol. 1, pp. 295–304, 2015.

[133] G. Bullegas, S. T. Pinho, and S. Pimenta, "Engineering the translaminar fracture behaviour of thin-ply composites," *Composites Science and Technology*, vol. 131, pp. 110–122, 2016.

[134] V. S. Romanov, S. V. Lomov, I. Verpoest, and L. Gorbatikh, "Can carbon nanotubes grown on fibers fundamentally change stress distribution in a composite?," *Composites Part A: Applied Science and Manufacturing*, vol. 63, pp. 32–34, 2014.

[135] G. Dai and L. Mishnaevsky, "Fatigue of multiscale composites with secondary nanoplatelet reinforcement: 3D computational analysis," *Composites Science and Technology*, vol. 91, pp. 71–81, 2014.

[136] W. Xia, J. Song, Z. Meng, C. Shao, and S. Keten, "Designing multi-layer graphene-based assemblies for enhanced toughness in nacre-inspired nanocomposites," *Molecular Systems Design & Engineering*, vol. 1, pp. 40–47, 2016.

[137] T. Kanit, S. Forest, I. Galliet, V. Mounoury, and D. Jeulin, "Determination of the size of the representative volume element for random composites : statistical and numerical approach," *International Journal of Solids and Structures*, vol. 40, pp. 3647–3679, 2003.

[138] C. Pelissou, J. Baccou, Y. Monerie, and F. Perales, "International Journal of Solids and Structures Determination of the size of the representative volume element for random quasi-brittle composites," *International Journal of Solids and Structures*, vol. 46, pp. 2842–2855, 2009.

[139] B. Haghpanah, R. Oftadeh, J. Papadopoulos, and A. Vaziri, "Self-similar hierarchical honeycombs," *Proceedings of the Royal Society of London A: Mathematical, Physical and Engineering Sciences*, vol. 469, no. 2156, pp. 1–19, 2013.

[140] S. Pimenta and S. T. Pinho, "Hierarchical scaling law for the strength of composite fibre bundles," *Journal of the Mechanics and Physics of Solids*, vol. 61, pp. 1337–1356, 2013.

[141] *ABAQUS/Standard User's Manual, Version 6.9*. Simulia, 2009.

[142] Skyflex, *USN020A carbon/epoxy prepreg technical datasheet*. 2015.

[143] L. Mishnaevsky, "Hierarchical composites: Analysis of damage evolution based on fiber bundle model," *Composites Science and Technology*, vol. 71, no. 4, pp. 450–460, 2011.

[144] iMetrum, *iMetrum LTD - Non Contact Precision Measurement*. Simulia, 2018.

[145] Deben, *Deben UK Ltd., in-situ tensile testing*. 2013.

[146] Z. Q. Zhang, B. Liu, Y. Huang, K. C. Hwang, and H. Gao, "Mechanical properties of unidirectional nanocomposites with non-uniformly or randomly staggered platelet distribution," *Journal of the Mechanics and Physics of Solids*, vol. 58, no. 10, pp. 1646–1660, 2010.

[147] X. Li and Z. Huang, "Unveiling the formation mechanism of pseudo-single-crystal aragonite platelets in nacre," *Physical Review Letters*, vol. 102, no. 7, p. 075502, 2009.

[148] A. G. Checa, J. H. E. Cartwright, and M. U. Willinger, "Mineral bridges in nacre revisited," 2012.

[149] P. Weiss and W. Ferris, "Electronmicrograms of larval amphibian epidermis," *Experimental Cell Research*, vol. 6, no. 2, pp. 546 – 549, 1954.

[150] J. D. Fuller and M. R. Wisnom, "Ductility and pseudo-ductility of thin ply angle-ply CFRP laminates under quasi-static cyclic loading," *Composites Part A: Applied Science and Manufacturing*, vol. 107, pp. 31–38, 2018.

[151] M. R. Wisnom, J. D. Fuller, P. Suwarta, and G. Czél, "Repeated Tensile Loading of Thin-Ply Pseudo-Ductile Laminates," in *ASC, 30th technical conference*, East Lansing, MI, US, Sept 2015, September 2015.

[152] J. Blaber, B. Adair, and A. Antoniou, "Ncorr: Open-Source 2D Digital Image Correlation Matlab Software," *Experimental Mechanics*, vol. 55, no. 6, pp. 1105–1122, 2015.

[153] F. Barthelat, H. Tang, and P. D. Zavattieri, "On the mechanics of mother-of-pearl: A key feature in the material hierarchical structure," *Journal of the Mechanics and Physics of Solids*, vol. 55, pp. 306–337, 2007.

[154] J. Finley, J. Henry, S. Pimenta, and M. Shaffer, "The influence of variability and defects on the structural performance of complex composite microstructures," in preparation, 2018.

[155] A. Jalan, "Virtual Testing of Hybrid Discontinuous Composites," tech. rep., Imperial College London, 2018.

[156] F. De Luca, *Fibre-Reinforced Composites with Nacre-Inspired Interphase: A Route Towards High Performance Toughened Hierarchical Composites*. PhD thesis, 2016.

[157] L. F. Domínguez, D. A. Narciso, and E. N. Pistikopoulos, "Recent advances in multiparametric nonlinear programming," *Computers and Chemical Engineering*, vol. 34, pp. 707–716, 2010.

[158] J. Leverenz, M. Xu, and M. M. Wiecek, "Multiparametric optimization for multidisciplinary engineering design," *Structural and Multidisciplinary Optimization*, vol. 54, pp. 795–810, 2016.

[159] J. H. Holland, *Adaptation in Natural and Artificial Systems: An Introductory Analysis with Applications to Biology, Control and Artificial Intelligence*. Cambridge, MA, USA: MIT Press, 1992.

[160] S. Shalev-Shwartz and S. Ben-David, *Understanding Machine Learning: From Foundations to Algorithms*. Cambridge University Press, 2014.

[161] I. Witten and E. Frank, *Data Mining: Practical Machine Learning Tools and Techniques*. Morgan Kaufmann series in data management systems, Morgan Kaufman, 2005.

[162] P. Pawel, "Investigating ductile composites at high strain rates," tech. rep., Imperial College London, 2017.

[163] E. K. Gamstedt and R. Talreja, "Fatigue damage mechanisms in unidirectional carbon-fibre-reinforced plastics," *Journal of Materials Science*, vol. 34, no. 11, pp. 2535–2546, 1999.

[164] M. Quaresimin, L. Susmel, and R. Talreja, "Fatigue behaviour and life assessment of composite laminates under multiaxial loadings," *International Journal of Fatigue*, vol. 32, no. 1, pp. 2 – 16, 2010. Fourth International Conference on Fatigue of Composites (ICFC4).

[165] S. M. O. Tavares and P. M. S. T. de Castro, "An overview of fatigue in aircraft structures," *Fatigue & Fracture of Engineering Materials & Structures*, 2017.

[166] M. Alves and S. Pimenta, "A computationally-efficient micromechanical model for the fatigue life of unidirectional composites under tension-tension loading," *International Journal of Fatigue*, in press, 2018.

[167] R. Sharma, "Measuring the fracture toughness of aligned discontinuous composites," tech. rep., Imperial College London, 2018.

[168] A. Kaddour, M. Hinton, P. Smith, and S. Li, "Mechanical properties and details of composite laminates for the test cases used in the third world-wide failure exercise," *Journal of Composite Materials*, vol. 47, pp. 2427–2442, 2013.

[169] Y. Arai, "Pitched-based Carbon fiber with low modulus and high heat conduction," tech. rep., Nippon Steel, 2001.

Appendix A

Correction factors for the Weibull strength distribution of fibres in a discontinuous composite

The fibre strength distribution used in the model (Eq. 2.9) contains a correction factor, C_{length}, which accounts for a difference between the length of the fibres used to measure the strength (l_{r}) and the length of the fibres in the composite (l^{f}). In addition, the fibres in the composites are allowed to break four times, for which four values of strength are needed; consequently, the fibres are considered to be divided in four elements of equal length $l^{\text{f}}/4$, and therefore the length-scaling factor of the Weibull distribution for fibre strength is

$$C_{\text{length}} = \frac{l^{\text{f}}}{4 \cdot l_{\text{r}}}. \tag{A.1}$$

The set of four strengths generated for each fibre is sorted, and each fibre (i, j) is initially affected the lowest value of the set. During the simulation, each time that fibre (i, j) breaks, its strength is updated to the next smallest value of the set (see Sec. 2.2.4.4).

The other correction factor in the fibre strength distribution, C_{shape}, accounts for the shape of the stress fields seen by the fibres, which is uniform during the measurement of fibre strengths, but has stress concentrations in discontinuous composites. Therefore, a representative case of the stress field $\sigma^{\text{f}}_{ij}(x)$ along a fibre in the discontinuous composite – where the four neighbouring fibre-ends are evenly spaced – is considered. The survival probability $\mathcal{S}_{\text{shape}}$ of a fibre (i, j) under a complex stress field $\sigma^{\text{f}}_{ij}(x)$ similar to the one shown in Fig. 2.2 is given by [140]

$$\ln\left[\mathcal{S}_{\text{shape}}\right] = \frac{1}{l^{\text{f}}} \cdot \int_{x=0}^{l^{\text{f}}} \left(\frac{\sigma_{ij}^{\text{f}}(x)}{\sigma_0} \right)^m \mathrm{d}x, \tag{A.2}$$

where the integral is calculated numerically, and m and σ_0 are respectively the shape and scale parameters of the original single-fibre strength Weibull distribution; note that, because the scale parameter σ_0 was measured at the length l_{r}, the survival probability S_{shape} refers to a fibre of length l_{r} as well.

The result found numerically for $\mathcal{S}_{\text{shape}}$ can be compared to the analytical result ($\mathcal{S}_{\text{uni}}$) given for a uniform stress field $\sigma_{ij}^{\text{f}}(x) = \hat{\sigma}_{ij}^{\text{f}}$, and a correction factor C_{shape} is calculated to account for the shape of the complex stress field: assuming that the survival probability of the fibre under a complex stress field can be expressed in the form $\ln\left[\mathcal{S}_{\text{shape}}\right] = C_{\text{shape}} \cdot \ln\left[\mathcal{S}_{\text{uni}}\right]$, the shape parameter is then defined by

$$C_{\text{shape}} = -\ln\left[\mathcal{S}_{\text{shape}}\right] \cdot \left(\frac{\sigma_0}{\hat{\sigma}_{ij}^{\text{f}}} \right)^m, \quad \text{where} \quad -\left(\frac{\hat{\sigma}_{ij}^{\text{f}}}{\sigma_0} \right)^m = \ln\left[\mathcal{S}_{\text{uni}}(\hat{\sigma}_{ij}^{\text{f}}) \right]. \tag{A.3}$$

Appendix B

Toughness estimation of aligned discontinuous composites

To estimate the fracture toughness (or critical energy release rate) of an aligned discontinuous composite, let us start by assuming a perfectly-plastic matrix (with strength S^{m}) so that the maximum stress carried by a fibre with minimum overlap δl is [83]

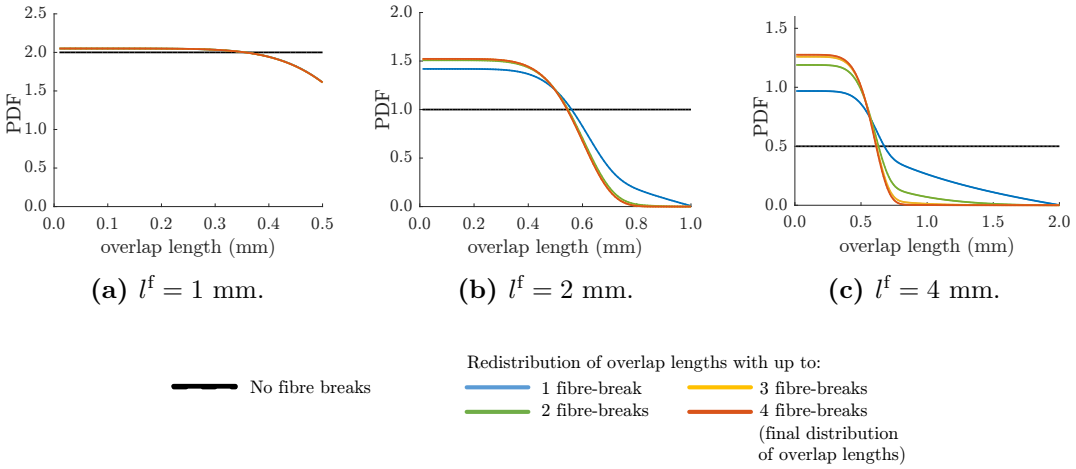
$$\hat{\sigma}^{\mathrm{f}} \approx \frac{4 \cdot S^{\mathrm{m}} \cdot \delta l}{\phi^{\mathrm{f}}}. \tag{B.1}$$

Consequently, one can then define the survival probability of an overlap of length δl as:

$$S_{\mathrm{L}}(\delta l) = \exp\left(-C_{\mathrm{length}} \cdot C_{\mathrm{shape}} \cdot \left(\frac{4 \cdot S^{\mathrm{m}} \cdot \delta l}{\phi^{\mathrm{f}} \cdot \sigma_0}\right)^m\right), \tag{B.2}$$

where C_{length} and C_{shape} are derived in App. A.

Then, because a fibre always fails at the same location as the end of one of its four neighbours (at a location x_{break} defined in Eq. 2.12), a fibre break always creates one overlap of length $\delta l = 0$ with one of the four neighbouring fibres. In addition, the minimum overlap lengths between the broken fibre and the three other neighbouring fibres can be recalculated: when a fibre breaks within the shortest shear-lag segment of an interaction, the new length of the shortest overlap generated will be uniformly distributed between zero and the length of the initial shear-lag segment. This principle can be applied recursively every time a fibre breaks to generate the probability density function) of overlap lengths PDF(δl) (Fig. B.1). For this model, the assumption of a square packing implies that each fibre can break up to four times.



(a) $l^{\mathrm{f}} = 1$ mm. **(b)** $l^{\mathrm{f}} = 2$ mm. **(c)** $l^{\mathrm{f}} = 4$ mm.

Figure B.1: Probability density function of minimum overlap lengths for discontinuous composites with different initial fibre lengths (the infinite peaks at $\delta l = 0$ are not shown in the plots).

Moreover, the work of debonding W_{deb} and pull-out W_{po} for an overlap of length δl are given by

$$W_{\mathrm{deb}} = \frac{\pi \cdot \phi^{\mathrm{f}}}{4} \cdot \mathcal{G}^{\mathrm{m}} \cdot \delta l \quad \text{and} \quad W_{\mathrm{po}} = \frac{\pi \cdot \phi^{\mathrm{f}}}{4} \cdot \tau_{\mu} \cdot \frac{\delta l^2}{2}. \tag{B.3}$$

Therefore, normalising the dissipated work by the cross-section of an overlap $\pi \cdot {\phi^{\mathrm{f}}}^2/(8 \cdot V^{\mathrm{f}})$, the toughness components g are defined as

$$g_{\mathrm{deb}} = \frac{2 \cdot V^{\mathrm{f}}}{\phi^{\mathrm{f}}} \cdot \mathcal{G}^{\mathrm{m}} \cdot \delta l \quad \text{and} \quad g_{\mathrm{po}} = \frac{V^{\mathrm{f}}}{\phi^{\mathrm{f}}} \cdot \tau_{\mu} \cdot \delta l^2. \tag{B.4}$$

Finally, combining the toughness components with the probability density functions of the overlap lengths, the toughness of the composite is calculated by summing the components of debonding and pull-out as follows:

$$\mathcal{G}_{\mathrm{crit}} = \int_{\delta l=0}^{l^{\mathrm{f}}/2} (g_{\mathrm{deb}} + g_{\mathrm{po}}) \cdot \mathrm{PDF}(\delta l) \cdot \mathrm{d}\delta l. \tag{B.5}$$

This method was validated against experiments where discontinuous Compact Tension (CT) specimens were tested in order to (i) measure experimentally the toughness of aligned discontinuous composites, and (ii) observed fracture surfaces of the broken CT specimens to identify the different failure mechanisms [167].

Appendix C

Derivation of the Young modulus from the non-hybrid BaM model

In the non-hybrid BaM model [24], the remote stress and strain applied to the composite and the stress and strain fields in the platelets and matrix are given by

$$\sigma^{\infty} = \frac{\Delta\sigma_{\mathrm{L}}}{2}, \tag{C.1a}$$

$$\varepsilon^{\infty} = \frac{\Delta\sigma_{\mathrm{L}}}{2\cdot E} + \frac{t^{\mathrm{m}}\cdot\gamma_{\mathrm{L}}}{2\cdot L} = \Delta\sigma_{\mathrm{L}}\cdot\left[\frac{1}{2\cdot E} + \frac{t^{\mathrm{m}}}{2\cdot L}\cdot\frac{\gamma_{\mathrm{L}}}{\Delta\sigma_{\mathrm{L}}}\right], \tag{C.1b}$$

$$\Delta\sigma(x) = \Delta\sigma_0\cdot\cosh(\lambda\cdot(x-x_0)) + \frac{2}{\lambda\cdot T}\cdot\tau_0\cdot\sinh(\lambda\cdot(x-x_0)), \tag{C.1c}$$

$$\gamma(x) = \gamma_0 + \frac{\tau_0}{G^{\mathrm{m}}}\cdot[\cosh(\lambda\cdot(x-x_0))-1] + \frac{\Delta\sigma_0}{\lambda\cdot t^{\mathrm{m}}\cdot E}\cdot\sinh(\lambda\cdot(x-x_0)). \tag{C.1d}$$

Moreover, because the matrix is in the linear-elastic subdomain along the entire overlap, $x_0 = 0$, $\Delta\sigma_0 = 0$ and $\tau_0/G^{\mathrm{m}} = \gamma_0$; therefore, Eq. C.1 can be simplified and leads to

$$\Delta\sigma_{\mathrm{L}} = \Delta\sigma(L) = \Delta\sigma_0\cdot\cosh(\lambda\cdot L) + \frac{2}{\lambda\cdot T}\cdot\tau_0\cdot\sinh(\lambda\cdot L), \tag{C.2a}$$

$$\gamma_{\mathrm{L}} = \gamma(L) = \gamma_0\cdot\cosh(\lambda\cdot L) + \frac{\Delta\sigma_0}{\lambda\cdot t^{\mathrm{m}}\cdot E}\cdot\sinh(\lambda\cdot L), \tag{C.2b}$$

$$\frac{\gamma_{\mathrm{L}}}{\Delta\sigma_{\mathrm{L}}} = \frac{\lambda\cdot T}{2\cdot G^{\mathrm{m}}\cdot\tanh(\lambda\cdot L)}. \tag{C.2c}$$

Therefore, using $\lambda = \sqrt{2\cdot G^{\mathrm{m}}/(T\cdot t^{\mathrm{m}}\cdot E)}$, Eq. C.1b becomes

$$\varepsilon^{\infty} = \frac{\sigma^{\infty}}{E}\cdot\left(1 + \frac{1}{L\cdot\lambda\cdot\tanh(\lambda\cdot L)}\right). \tag{C.3}$$

Finally, the Young's modulus of the composite is given by

$$E_{\mathrm{BaM}}(T,E) = \frac{\sigma^{\infty}}{\varepsilon^{\infty}} = \frac{E}{1+\frac{1}{\lambda\cdot L\cdot\tanh(\lambda\cdot L)}}, \qquad \text{where} \quad \lambda = \sqrt{\frac{2\cdot G^{\mathrm{m}}}{t^{\mathrm{m}}\cdot E\cdot T}}. \tag{C.4}$$

Appendix D

Derivation of rules-of-mixtures

D.1 Continuous-fibre RoM

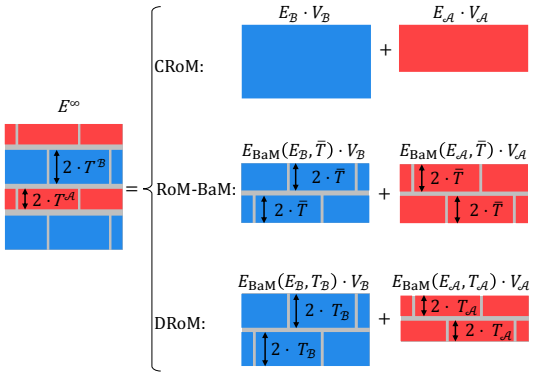
The standard rule-of-mixtures predicts the modulus of a hybrid composite with a linear combination of the Young's moduli of the two types of inclusion ($E_{\mathcal{A}}$ and $E_{\mathcal{B}}$), as shown in Fig. D.1a. This neglects the brick-and-mortar architecture of the composite.

D.2 RoM for brick-and-mortar

In order to account for the BaM architecture, one can assume that the overall Young's modulus of the hybrid composite is a linear combination of the two Young's moduli of the non-hybrid BaM composites, each consisting of only one platelet type ($\mathcal{A}$ or $\mathcal{B}$), with the same average platelet thickness $\bar{T}$ (see Eq. C.4). Therefore, the overall Young's modulus calculated with this rule-of-mixtures (named $E^{\mathcal{C}}_{\text{RoM-BaM}}$ in the results) takes into account the discontinuous nature of the platelets, although it does not account for differences in platelet thickness while calculating the two Young's moduli of the non-hybrid BaM (see Fig. D.1b).

D.3 Discontinuous-fibre RoM

A third rule-of-mixtures (named $E^{\mathcal{C}}_{\text{DRoM}}$ in the results) considers the actual thickness of each platelet type when calculating the Young's moduli of the two non-hybrid BaM composites; this means that, instead of using $T_{\mathcal{A}} = T_{\mathcal{B}} = \bar{T}$ and doing a linear interpolation (as done in Sec. D.2), the DRoM calculates the Young's moduli of the two non-hybrid BaM considering the actual thicknesses of the platelets ($T_{\mathcal{A}} \gtreqless T_{\mathcal{B}}$) in the hybrid BaM for each value of $\Delta T/\Sigma T$ (see Fig. D.1c).



$$E^{\mathcal{C}}_{\mathrm{CRoM}} = E_{\mathcal{A}} \cdot V^{\mathcal{A}} + E_{\mathcal{B}} \cdot V^{\mathcal{B}} \tag{D.1a}$$

$$E^{\mathcal{C}}_{\mathrm{RoM\text{-}BaM}} = E_{\mathrm{BaM}}(\bar{T}, E_{\mathcal{A}}) \cdot V^{\mathcal{A}} + E_{\mathrm{BaM}}(\bar{T}, E_{\mathcal{B}}) \cdot V^{\mathcal{B}} \tag{D.1b}$$

$$E^{\mathcal{C}}_{\mathrm{DRoM}} = E_{\mathrm{BaM}}(T_{\mathcal{A}}, E_{\mathcal{A}}) \cdot V^{\mathcal{A}} + E_{\mathrm{BaM}}(T_{\mathcal{B}}, E_{\mathcal{B}}) \cdot V^{\mathcal{B}} \tag{D.1c}$$

Figure D.1: Definition of the different rules-of-mixtures (CRoM, RoM-BaM and DRoM), and the corresponding equations to calculate the Young's modulus of the hybrid BaM composite.

Appendix E

Validation of the analytical model for HyBaM composites against FE simulations

The analytical model for hybrid BaM composites has been validated using 2D plane stress FE simulations (see Fig. E.1). For each simulation, the platelets are defined as isotropic-linear-elastic materials with Young's moduli $E_{\mathcal{A}}$ and $E_{\mathcal{B}}$ and Poisson's ratio $\nu_{\mathcal{A}} = \nu_{\mathcal{B}} = 0$. The matrix is also defined as an isotropic-linear-elastic material with a Young's modulus $E^{\mathrm{m}} = 2 \cdot G^{\mathrm{m}} \cdot (1 + \nu^{\mathrm{m}})$ and a Poisson's ratio $\nu^{\mathrm{m}} = 0.5$. Three elements have been used through the thickness of each platelet in order to validate the shear-lag assumption of thin layers.

The simulations are run with Abaqus Standard solver [141], and the remote load P^{∞} and displacement u^{∞} were collected to find the overall Young's modulus of the

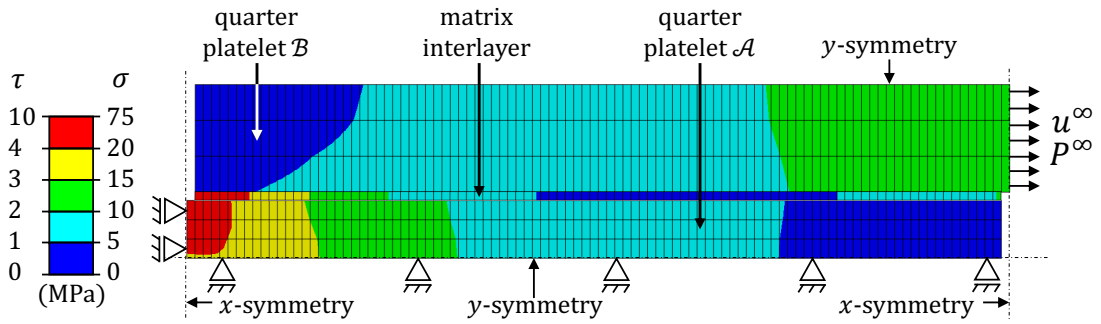


Figure E.1: Example of the FE geometry, mesh and boundary conditions used to validate the analytical model for hybrid BaM composites. The model represents the unit-cell shown in Fig. 3.1b for one particular configuration (defined in Tab. 3.2, and with $L = 1$ mm, $\frac{\Delta T}{\Sigma T} = 0.3$ and $\frac{\Delta E}{\Sigma E} = 0.2$).

hybrid BaM composite:

$$E_{\mathrm{FE}}^{\mathrm{c}} = \frac{\sigma_{\mathrm{FE}}^{\infty}}{\varepsilon_{\mathrm{FE}}^{\infty}} = \frac{P^{\infty}/\Sigma T}{u^{\infty}/(2 \cdot L)}. \tag{E.1}$$

The FE results are displayed in Fig. 3.5a, and show good agreement with the results from the analytical model.

Appendix F

Modelling of fibre misalignment

To analyse the effect of fibre misalignment, let us consider a hybrid discontinuous composite with a fibre volume fraction V^{f} (and $V^{\mathrm{m}} = 1 - V^{\mathrm{f}}$), fibre-$\mathcal{A}$ volume ratio $V^{\mathcal{A}}$ and fibre-$\mathcal{B}$ volume ratio $V^{\mathcal{B}}$ (with $V^{\mathcal{A}} + V^{\mathcal{B}} = 1$). The reduced stiffness matrix $\mathbf{Q}_{ij}$ of a ply with all fibres perfectly aligned in the longitudinal direction is given by:

$$\mathbf{Q}_{ij} = \begin{bmatrix} Q_{11} & Q_{12} & 0 \\ Q_{12} & Q_{22} & 0 \\ 0 & 0 & Q_{66} \end{bmatrix}, \text{ where } \begin{cases} Q_{11} = E_{11}^2/(E_{11} - \nu_{12}^2 \cdot E_{22}), \\ Q_{12} = \nu_{12} \cdot E_{11} \cdot E_{22}/(E_{11} - \nu_{12}^2 \cdot E_{22}), \\ Q_{22} = E_{11} \cdot E_{22}/(E_{11} - \nu_{12}^2 \cdot E_{22}), \\ Q_{66} = G_{12}, \end{cases} \tag{F.1}$$

where E_{11} is the longitudinal Young's modulus, calculated by the model described in Sec. 3.3; the other stiffness constants are defined (using the rule-of-mixtures and input

Table F.1: Inputs parameters used to calculate the reduced stiffness matrix (values estimated from literature [168, 169]). The fibre volume fraction is set to $V^{\mathrm{f}} = 30\%$.

Parameter	E_{11} (GPa)	E_{22} (GPa)	G_{12} (GPa)	ν_{12} (-)
Matrix	4.0	4.0	1.5	0.35
Glass	73	73	30	0.2
HSC	225	20	27	0.2
HMC	860	7	32	0.2

values in Tab. F.1) as

$$\begin{cases} E_{22} &= 1/(V^{\mathrm{f}} \cdot V^{\mathcal{A}}/E_{22,\mathcal{A}} + V^{\mathrm{f}} \cdot V^{\mathcal{B}}/E_{22,\mathcal{B}} + V^{\mathrm{m}}/E_{22}^{\mathrm{m}}), \\ G_{12} &= 1/(V^{\mathrm{f}} \cdot V^{\mathcal{A}}/G_{12,\mathcal{A}} + V^{\mathrm{f}} \cdot V^{\mathcal{B}}/G_{12,\mathcal{B}} + V^{\mathrm{m}}/G_{12}^{\mathrm{m}}), \\ \nu_{12} &= V^{\mathrm{f}} \cdot V^{\mathcal{A}} \cdot \nu_{12,\mathcal{A}} + V^{\mathrm{f}} \cdot V^{\mathcal{B}} \cdot \nu_{12,\mathcal{B}} + V^{\mathrm{m}} \cdot \nu_{12}^{\mathrm{m}}. \end{cases} \tag{F.2}$$

The coefficients of the stiffness matrix $Q'_{ij}(\theta)$ in the off-axis system rotated by an angle θ can be calculated from the coefficients of the reduced stiffness matrix by using classical laminate theory [90, 91]:

$$\begin{Bmatrix} Q'_{11}(\theta) \\ Q'_{22}(\theta) \\ Q'_{12}(\theta) \end{Bmatrix} = \begin{Bmatrix} m^4 & n^4 & 2 \cdot m^2 \cdot n^2 & 4 \cdot m^2 \cdot n^2 \\ n^4 & m^4 & 2 \cdot m^2 \cdot n^2 & 4 \cdot m^2 \cdot n^2 \\ m^2 \cdot n^2 & m^2 \cdot n^2 & m^4 + n^4 & -4 \cdot m^2 \cdot n^2 \end{Bmatrix} \times \begin{Bmatrix} Q_{11} \\ Q_{22} \\ Q_{12} \\ Q_{66} \end{Bmatrix}, \tag{F.3}$$

where $m = \cos(\theta)$ and $n = \sin(\theta)$.

The overall laminate stiffness matrix $\bar{Q}_{ij}$ of a composite with a fibre orientation distribution defined by the probability density function $g(\theta)$ is then calculated by

$$\bar{Q}_{ij} = \int_{\theta_{\min}}^{\theta_{\max}} Q'_{ij}(\theta) \cdot g(\theta) \mathrm{d}\theta, \tag{F.4}$$

and the overall Young's modulus of the composite is given by

$$\bar{E}_{11} = \frac{\bar{Q}_{11} \cdot \bar{Q}_{22} - \bar{Q}_{12}^2}{\bar{Q}_{22}}. \tag{F.5}$$

This method was validated against a composite layup section model available in Abaqus [141], and was used to predict the results shown in Fig. 3.7 (Chapter 3), in order to compare the results of the model against experiments accounting for fibre misalignment.

Appendix G

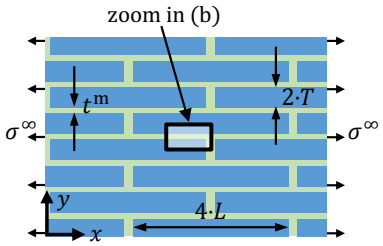
Extension of the brick-and-mortar model for non-linear-elastic bricks

The aim of this appendix is to summarise how the existing model for single-level BaM composites with hybrid brick types (Chapters 2-4) was extended for non-linear-elastic bricks, as mentioned in Chapter 5.

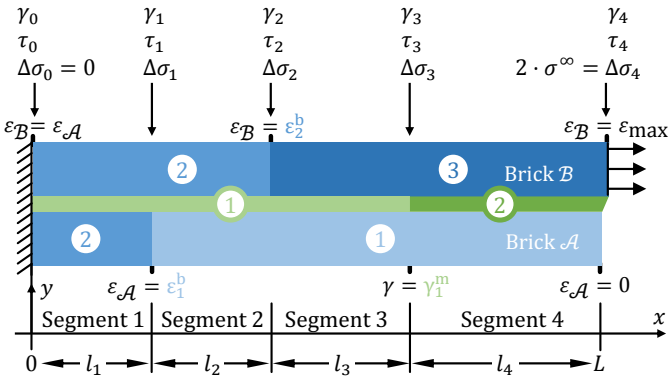
The current model considers a composite with perfectly staggered bricks (see Fig. G.1a, and zoom on the unit-cell in Fig. G.1b). The matrix has a bilinear response in shear (with material properties showed in Tab. 5.2), and the bricks have a non-linear response in tension; both responses are approximated by piecewise-linear stress-strain curves, as exemplified in Fig. G.1c for the matrix, and in Fig. G.1d for the bricks.

According to a 1-dimensional shear-lag mechanism (in which there are no through-the-thickness stress gradients within a brick or matrix layer), the matrix will transfer shear-stresses between each pair of neighbouring bricks, along the overlap between brick-ends. Along each brick, tensile stress will therefore increase from the brick-ends (where the stress is set to zero) to the centre of the brick (where the stress is maximum), as shown in Fig. G.1b. This non-homogeneous stress state in the bricks, combined with their piecewise non-linear tensile response, means that different *segments* of one brick along the overlap will have different tangent stiffnesses (as exemplified in Fig. G.1b).

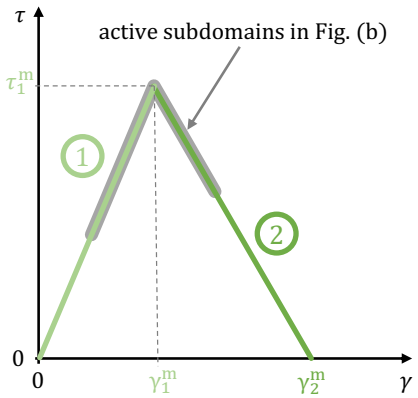
The brick half-overlap shown in Fig. G.1b (of length L) can be regarded as a series of 4 segments; let us for example focus on Segment 2. In Segment 2, brick $\mathcal{A}$ is in Subdomain 1 (with tangent stiffness E_1 and stress $\sigma_{\mathcal{A}}(\varepsilon_{\mathcal{A}}) = E_1 \cdot \varepsilon_{\mathcal{A}} + \sigma_1^0$), brick $\mathcal{B}$ is in Subdomain 2 (with tangent stiffness E_2 and stress $\sigma_{\mathcal{B}}(\varepsilon_{\mathcal{B}}) = E_2 \cdot \varepsilon_{\mathcal{B}} + \sigma_2^0$), and



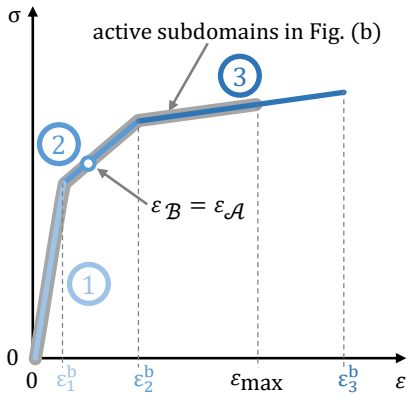
(a) BaM structure.



(b) Overlap between two non-linear-elastic bricks. The different colours represent the different piecewise linear subdomains which are active in the overlap, as identified in Figs. G.1c and G.1d



(c) Example of a matrix piecewise-linear constitutive law (with 2 subdomains).



(d) Example of a brick piecewise-linear constitutive law (with 3 load-bearing subdomains).

Figure G.1: Overview of the extension of the hybrid BaM model (Chapters 3-4) to BaM composites with non-linear-elastic bricks.

the matrix is in Subdomain 1 (with tangent stiffness G_1^m). Using a method similar to the one developed for hybrid bricks (Chapters 3-4) yields the following governing differential equation for the shear-lag stress transfer in Segment 2 in Fig. G.1b:

$$\frac{d^2\Psi(x)}{dx^2} = \text{sign}\left[G_1^{\text{m}}(\gamma)\cdot\tilde{E}_{12}\right]\cdot\lambda_{12}^2\cdot\Psi(x),$$

$$\text{where}\begin{cases} \lambda_{12} &= \sqrt{\frac{2}{T\cdot t^{\text{m}}}\cdot\left|\frac{G_1^{\text{m}}(\gamma)}{\tilde{E}_{12}}\right|}, \\ \Psi(x) &= \Delta\sigma(x) + \frac{\sigma^{\infty}\cdot\Delta E_{21} - \sigma_2^0\cdot E_1 + \sigma_1^0\cdot E_2}{\bar{E}_{12}}, \\ \Sigma E_{12} &= E_1 + E_2, \\ \Delta E_{21} &= E_1 - E_2, \\ \bar{E}_{12} &= \Sigma E_{12}/2, \\ \tilde{E}_{12} &= \frac{2\cdot E_1\cdot E_2}{E_1+E_2}, \end{cases} \tag{G.1}$$

and where $\Delta\sigma(x)$ is the stress difference $\sigma_{\mathcal{B}}(x) - \sigma_{\mathcal{A}}(x)$ along the overlap.

For each Segment $k = \{1, 2, 3, 4\}$ in the overlap in Fig. G.1b, an equation similar to Eq. G.1 can be defined and solved in a way similar to that proposed in Chapter 4 for hybrid bricks, and the values of γ_k, τ_k and $\Delta\sigma_k$ (defined in Fig. G.1b) can be calculated from γ_{k-1}, τ_{k-1} and $\Delta\sigma_{k-1}$. This allows for the stress-strain responses of each segment to be calculated successively; finally, the stress-strain response of the whole overlap is obtained by combining the response of the 4 segments in series.

This analysis was presented for the particular case of subdomains and segments shown in Fig. G.1, but it can be extended to any generic case using the same methodology as proposed in Chapter 4 for hybrid brick-and-mortar composites.